Human and eco-toxicological impacts of organometallic halide perovskites

THÈSE N^{O} 7595 (2017)

PRÉSENTÉE LE 17 MARS 2017

À LA FACULTÉ DES SCIENCES DE BASE
LABORATOIRE DE PHYSIQUE DE LA MATIÈRE COMPLEXE
PROGRAMME DOCTORAL EN BIOTECHNOLOGIE ET GÉNIE BIOLOGIQUE

ÉCOLE POLYTECHNIQUE FÉDÉRALE DE LAUSANNE

POUR L'OBTENTION DU GRADE DE DOCTEUR ÈS SCIENCES

PAR

Ryma Iness BENMESSAOUD

acceptée sur proposition du jury:

Prof. M. Dal Peraro, président du jury
Prof. L. Forró, Prof. H. Lashuel, directeurs de thèse
Dr A. Bahinski, rapporteur
Dr B. Schmid, rapporteur
Prof. A. Radenovic, rapporteuse

ÉCOLE POLYTECHNIQUE
FÉDÉRALE DE LAUSANNE

Suisse
2017

Failure isn’t the end, it’s just part of the success. Quitting is the end.
— Unknown

To my parents,
To Yaz, Saly, Hamid, Isma,
To Sam.

Abstract

Solar radiation currently represents the most important source of renewable energy. Existing technologies to collect and distribute solar energy are expensive, difficult to manufacture, non-recyclable and not very cost-effective. Recent advances in physics and materials engineering have pointed to photovoltaic (PV) perovskites (or $CH_3NH_3MI_3$, where M=Pb, Sn) as the future solution for sustainable energy because of their simple fabrication procedure, low price, and high efficiency. Several companies are already building perovskites-based PV devices for commercialization in the near future. Nevertheless, perovskites contain heavy metals, and safety concerns during PV fabrication and transportation have not yet been addressed, not to mention recycling, and environmental hazards in case of any failure of large-area solar panels. This dissertation documents my investigation of the potential health and environmental effects of perovskites. I have performed a "zoom-in approach" on human cells to study gene expression and biochemical changes, and a "zoom-out approach" *in vivo* to investigate toxicity at an organism level. The time frame during which living cells can be manipulated on the same substrate is short, therefore we selected concentrations in the range of $50-200\mu g/ml$ (from 80 to 400 μM)) to observe a measurable effect *in vitro*. These concentrations may seem relatively high, however, an accidental exposure scenario with such concentrations may occur during material fabrication if safety measures are not taken properly.

In the *in vitro* study using human cells, I have discovered not only a dose- and time-dependent response to perovskites exposure, but also a cell-type dependent effect. Within 24 hours following perovskites exposure, neuronal cells died whereas lung cells became giant and polynucleated. Complementary assays showed that mitochondria were heavily damaged, with an increase in their activity when compared to untreated cells. Furthermore, genome profile studies showed many differences in gene expression levels. Extra analysis identified the co-regulated gene networks rather than individual coding genes, which indicated that some pathways critical to basic cellular functions were heavily affected by perovskite exposure (such as regulation of the metabolism, cell division, cell signaling etc.).

To understand more thoroughly, I applied the Scanning Fourier Transform Infrared Microspecrometry (S-FTIRM) to study cell toxicity. This has never been done before. I investigated the biochemical changes displayed on infrared absorption spectra. The results are complementary to other techniques, which makes the use of S-FTIRMS applicable to real-time toxicity studies because of its submolecular sensitivity and high-resolution.

I also explored the eco-toxic effects of photovoltaic perovskites on small model organisms: fruit flies (*Drosophila melanogaster*) and nematodes (*Caenorhabditis elegans*). In both models, life span and organism development were reduced by the exposure. Moreover, the fertility of

young adults was drastically affected.
My *in vitro* and *in vivo* studies showed that $CH_3NH_3PbI_3$ and $CH_3NH_3SnI_3$ are acutely and chronically toxic compounds. The obtained results are conclusive, and encourage the scientific community not only to conduct further tests on more complex organisms, but to first search for novel solutions with non-toxic properties.

Keywords

Photovoltaic halide perovskites, solar energy, health hazard, toxicity, cytotoxicity, eco-toxicity, apoptosis, mitochondrial stress, gene profiling, small organism, Fourier transform Infrared spectroscopy.

Résumé

Le rayonnement solaire représente, de nos jours, la source la plus importante des énergies durables. En revanche, les technologies actuelles permettant de collecter et redistribuer l'énergie solaire sont coûteuses, difficiles à fabriquer, non-recyclables et peu rentables. Les avancées récentes en physique et en science des matériaux ont prodigué aux pérovskites photovoltaïques (ou $CH_3NH_3MI_3$, où M=Pb, Sn) la réputation de solution du future pour les énergies renouvelables. Ceci, notamment, grâce à la simplicité et rapidité de fabrication de panneaux contenant des pérovskites, leur prix avantageux, et leur haute efficacité à convertir l'énergie solaire. Plusieurs entreprises industrialisent d'ores et déjà des panneaux photovoltaïques contenant des pérovskites pour une commercialisation dès 2018. Cependant, ces pérovskites contiennent des métaux lourds, et les questions de sécurité pendant la fabrication et le transport des panneaux n'ont pas encore été considérées, tout comme leur recyclage et les enjeux environnementaux lors de brisure d'installations de grande surface. La présente thèse documente mes recherches sur les impacts potentiels des pérovskites photovoltaïques sur la santé de l'Homme et de l'environnement. J'ai utilisé une approche *in vitro* pour « zoomer » sur les conséquences des pérovskites sur les cellules, leur expression génétique, et leur état biochimique, ainsi qu'une approche *in vivo* pour observer les effets sur un organisme entier (*Drosophila melanogaster* et *Caenorhabditis elegans*). Nous avons sélectionné des concentrations entre 50 et 200 μg/ml (équivalentes à 80-400 μM), dans le but d'évaluer les effets mesurables *in vitro*. Ceci, parce que le lapse de temps où des cellules vivantes peuvent être manipulées sur un même substrat est court (Maximum 10 jours). Ces concentrations peuvent paraître relativement élevées, néanmoins, un tel scénario d'exposition accidentelle est très probable pendant la phase de fabrication dans un laboratoire où les mesures de sécurité ne seraient pas respectées. Dans l'étude *in vitro* sur des cellules humaines exposées aux pérovskites, j'ai découvert non seulement un effet dépendant de la dose et du temps d'exposition, mais aussi une réponse propre à chaque type cellulaire. Vingt-quatre heures après exposition, les cellules neuronales sont mortes d'apoptose par voie mitochondriale, contrairement aux cellules pulmonaires devenues géantes et polynucléaires. Des essais complémentaires ont révélé que leurs mitochondries ont été sévèrement endommagées avec une hausse d'activité. De plus, des études que j'ai mené sur le profil génétique ont montré des différences au niveau de l'expression de certains gènes. Des analyses approfondies ont permis d'identifier des réseaux de gènes co-régulés impliqués dans des voies de signalisation importantes pour certaines fonctions vitales des cellules, qui ont été perturbées par l'exposition au $CH_3NH_3PbI_3$ (comme la régulation du métabolisme, la division cellulaire, signalisation cellulaire etc.) Pour une meilleure compréhension, j'ai appliqué pour la première fois la Microspectrométrie à balayage Infrarouge à Transformée de

Fourier (S-FTIRM) pour une étude de toxicité sur des cellules fixées ou vivantes. J'ai exploré les changements biochimiques sur des spectres d'absorption infrarouge, et les résultats ont été complémentaires à ceux obtenus par des techniques conventionnelles. Ceci fait de la S-FTIRM une methode applicable aux études de toxicité *in vitro* en temps réel, notamment grâce à sa sensibilité et sa haute-résolution. J'ai aussi étudié les effets écotoxiques des pérovskites photovoltaïques sur des petits organismes modèles : la mouche des fruits, ou du vinaigre (*Drosophila melanogaster*) et les nématodes (*Caenorhabditis elegans*). Dans les deux modèles, j'ai observé une baisse dans la durée de vie et dans la croissance des organismes, ainsi qu'une perturbation drastique de la fertilité de jeunes adultes. Mes études *in vitro* et *in vivo* démontrent que $CH_3NH_3PbI_3$ et $CH_3NH_3SnI_3$ sont toxiques de manière aiguë et chronique. Les résultats obtenus sont concluants et encouragent la communauté scientifique à établir des tests sur des organismes plus complexes, et surtout à chercher de nouvelles solutions pour les énergies vertes.

Mots-clés

Pérovskites halogénés photovoltaïques,energie solaire, Risques pour la santé, toxicité, cytotoxicité, écotoxicité, apoptose, stress mitochondrial, profile génétique, petit organism, Spectroscopie infrarouge à transformée de Fourier

Contents

Prologue

The increasing world population presents new challenges. One of the most severe is its increasing demand for energy, which is accompanied by an increasing awareness for environmental concerns like pollution and health hazards that deteriorate quality of life, and present long-term dangers for humanity. This energy challenge is accentuated by the rapid reduction of fossil energy resources and the disgrace of nuclear energy following the Chernobyl and Fukushima disasters. Today there is a strong tendency to turn towards clean energy sources like solar energy or hydrogen as fuel. But the efficient conversion of these energy sources into electricity requires new concepts, efficient technology and, especially, new materials. With the advent of nanoscale research (popularly called nanoscience) there has been tremendous progress in new materials and nanostructures, which improve solar energy conversion, hydrogen storage, and the design of efficient fuel cells. The history of the use and production of asbestos, however, teaches us that all promising new materials should be tested for health hazards before their large-scale application. My PhD program seeks to address this issue: starting with testing the toxicity of a novel molecular system called Metal-Organic-Frameworks (abbreviated MOFs), and switching to a hybrid organic lead halide perovskite (a class of materials) which has demonstrated remarkable progress in solar energy conversion over the last four years (Figure 1).

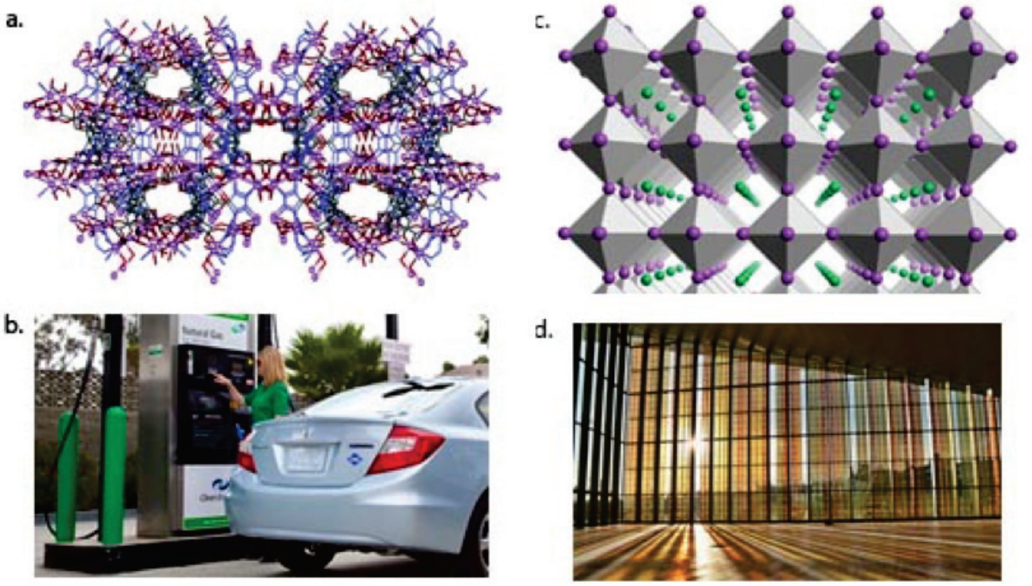

Figure 1 – a) Illustration of the crystal structure of MOFs; b) Possible application of MOFs for hydrogen storage for cars equipped with fuel cells; c) Sketch of the crystal structure of the photovoltaic perovskite, and d) and their foreseen application in large scale photovoltaic panels like shown here (source: google image gallery).

By examining only the list of keywords, I was exposed to: solar energy, conversion, novel materials, health hazard, gene profiling, toxicity etc. This shows that the research program I was following in my PhD training was interdisciplinary, and involved a close collaboration between biologists, chemists, material scientists and physicists.

Being a biologist by training, I joined professor László Forró at the Laboratory of Physics of Complex Matter, where besides physics, there is a strong emphasis on materials synthesis and a permanent questioning and concern about the toxicity of novel materials. This was the case previously for carbon nanotubes, titanium dioxide nanowires, graphene, just to mention a few. In this laboratory, I learnt concepts like solubility, ionic radii, stoichiometry, infrared spectroscopy, principal component analysis and many more. To be able to investigate and understand the potential impact of novel materials on human health, I needed to perform the in vitro and in vivo toxicity studies in dedicated laboratories. Therefore, I initially collaborated with Professor Beat Schwaller at the Department of Medicine in Fribourg, and later on in the Laboratory of Molecular Neurobiology and Neuroproteomics of my co-supervisor and mentor Professor Hilal Lashuel. Some of the test measurements I performed were at synchrotron light sources in the United States, France and Switzerland. During these four years, on daily basis, I was "commuting" between biology, physics and chemistry. I was more than motivated to be proactive whenever facing a scientific difficulty, and to discuss with other scientists. This is how I progressed during my PhD in a multidisciplinary research by collaborating with over 15 laboratories. I was not annoyed for a single moment and it has been an exciting period of my life.

I will now share a few words about the materials: MOFs launched in the 90's by Omar Yaghi and collaborators[130,233] , who emphasized their high-porosity and their suitability for gas storage.[24,231] Since then, the fields of application have extended to catalysis,[191] optics,[219] magnetism,[123] ferroelectrics,[99] and even drug delivery.[30,107,142] BASF is already producing MOFs in large quantities. At the time I started my PhD training, not much was known about their toxicity. At the time I started my PhD training, not much was known about their toxicity. However, as my project progressed, another compound, the perovskite methylammonium lead iodide ($CH_3NH_3PbI_3$, hereafter $MAPbI_3$) stole the spotlight. In a photovoltaic device configuration, this compound has shown an astonishing increased efficiency. It is being picked-up by many research groups, and already at the beginning of 2016, its light conversion efficiency was shown to reach an unprecedented 22%. Furthermore, the material is found to be promising in other applications like bright and cheap light emitting diodes lasing at a relatively low pumping threshold, in thermoelectrics, and is proven to be an excellent photodetector. Many research laboratories are focusing on this material and in the case for my PhD program, $MAPbI_3$ represents the core of my dissertation.

The chemical formula of the compound contains lead, which has been known for many years to be toxic. We are exposed to lead everyday: burning coal releases lead into the atmosphere, we have lead-containing pipes, paints, batteries, etc. Across the globe, it is a general aim to reduce or eliminate lead as much as we can. This is, for example, why leaded gasoline has been banned. Concerning the photovoltaic perovskite, it is important to understand the stabil-ity of the material, especially that of the devices, and how one can protect from the release of Pb into the environment. It is very likely that researchers will not give up studying $MAPbI_3$ simply because of the lead content, since the energy conversion benefit is too high. But a ques-tion worth pondering is why exactly is this material so efficient, and is there perhaps another material with similar performances but composed of non-toxic elements? The photovoltaic community supposes that $MASnI_3$ might be a good alternative, because tin is not harmful to the organism. But this is still more a conjecture than a fact. Therefore, I have included this compound in my research, as well.

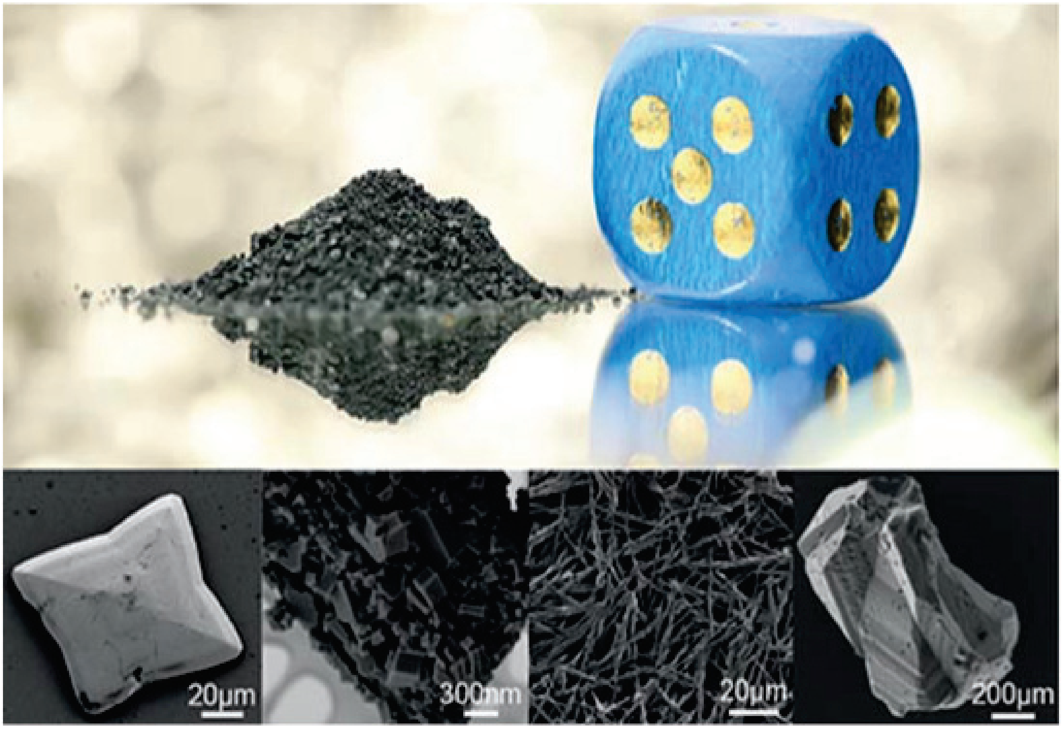

Figure 2 – Different forms, different appearances of $CH_3NH_3PbI_3$ material: they can be bulk crystals, platelets, wires of micron and nanometer size and tiny crystals. Their shape and size is relevant in physical measurements.A typical quantity used for one toxicity study (assay) is shown in the upper panel, the scale is given by the dice. In this case the shape of the crystals is not important, since they will be dissolved in water or physiological liquids.

How did I do my investigations? The crystallites of the material (Figure 2) were dissolved in water or in physiological fluids and administrated to cultured cells, or to living small organisms at various concentrations. I then monitored the observed phenotypic changes in a time-dependent manner. The biological models used for this work are cell-based (neuronal and lung cells) and small model organisms (fruit flies and nematodes). The first goal was to better understand the effect of $MAPbI_3$ at the cellular level. Despite the intense research to investigate the circumstances and the mechanisms of lead toxicity over the past 20 years,[80] there are still many unknowns. For example, I found that lung cells respond differently to con-tact with the material than neurons do (the latters die while the formers do not). Why? I had to “zoom” into the cells to study the molecular changes, including the genome profile, caused after exposure to perovskites. This necessitated a special technique, and from an enormous data set I managed to identify the subcellular structures or molecules that are affected in treated cells.

As these fine details became clearer, I had to “zoom out” to see what these changes meant for a living organism of a different complexity, such as Drosophila melanogaster or Caernorhabdi-tis elegans, which are the gold standards for many biological tests (Figure 3). Such manipulations required a lot of patience. For example, in the case of Drosophila, I had to inspect eggs, larvae, and adults by gender. In some cases I tracked the emergence of young adults to be able to quickly separate virgin females before mating. All these tasks were done on large populations in order to assess toxicity at various concentrations, for different time-points. Each independently repeated 3 times for biological replicate. Sometimes, I was dreaming flies!

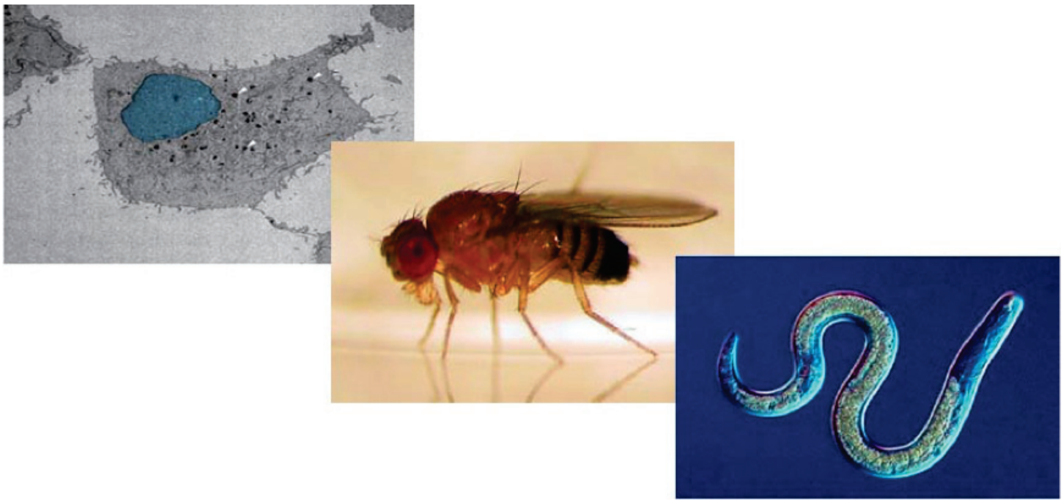

Figure 3 – Illustration of the living organism by increasing complexity which were tested against $CH_3NH_3PbI_3$ exposure: single cell, D. melanogaster and C.elegans. (source: google image gallery)

This detailed endeavor is documented within the pages of this dissertation. In chapter I, I provide highlights on the use of perovskite materials for energy purposes, introduce technology vs. toxicology by presenting some toxicity cases, and also give a detailed outline on the PhD work. Chapter II reports on the physico-chemical characterization of the material. Chapter III contains some findings on the in vitro toxicity of the perovskites: from the whole cell to the signaling pathway to the genome. Chapter IV describes a new and non-conventional approach to follow the toxicity of compounds: infrared microspectroscopy. This chapter also covers some of the findings on perovskites toxicity. Chapter V presents what happens at a whole or-ganism level when exposed to $MAPbI_3$ and its counterpart $MASnI_3$. Finally, all the key results of this PhD work are summed up in chapter VI, where I discuss their impacts and provide some outlooks.

This is the journey of my four and half years towards a PhD. I appreciated every challenge, which helped to develop my personal, professional and scientific skills, as well as all my colleagues who contributed to the accomplishment of this project.

1

State of the art

1.1 A growing need for energy

The world's population has more than doubled since the 1960s and continues to grow by approximately 1.1% annually.[76] According to a recent report from the United Nations' department of economic and social affairs, the world's population is estimated to reach 9.7 billion in 2050[214] and the distribution is illustrated in (Figure 1.1. Thereafter, the demographic growth is expected to keep rising, exceeding 10 billion at the end of the century. This ascending trend will certainly be accompanied by an increase in energy demand.

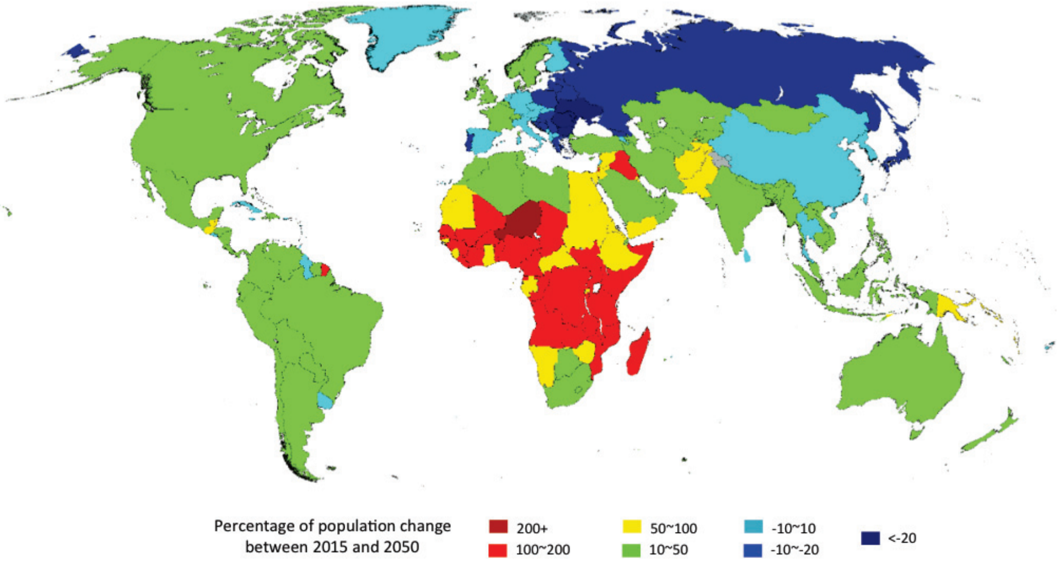

Figure 1.1 – Projected population growth between 2015 and 2016 by the united nations (With permission from the United Nations[214]).

It should be stressed that the world's total energy demand is twofold. For example, after the oil is extracted, it has to be refined and transported long distances to gas stations (upstream energy), then used for many purposes (downstream energy). Therefore, most of the consumed energy needs an upstream energy supply. Institutions such as the International Energy Agency (IEA), the Energy Information Administration (EIA) and the European Environment Agency (EEA) publish energy-related reports periodically. They help to frame current energy issues and to encourage the community to find solutions. In 2013, the IEA published the world energy consumption by type of power source which showed that fossils (oil, coal, and natural gas) were the most frequently used fuels (Table 1.1).[17]

Fossil fuels have been used extensively worldwide for centuries, causing not only oppressive geopolitical conflicts, but also extremely deleterious human[64] and environmental[215] effects. As for nuclear power, its exploitation for energetic purposes began in 1951 in the United States during the Cold War,[133] where president Eisenhower spoke about "atoms for peace".

Source of energy	Percentage
Oil	31.3
Coal	28.6
Natural gas	21.2
Biofuels and waste	10.3
Nuclear	4.8
Hydro	2.4
Other [2]	1.4

[1] World includes also international aviation and marine bunkers.

[2] Other includes geothermal, solar, wind, heat, etc.

Table 1.1 – Distribution of the world[1] final energy consumption by source in 2013.[17]

The United States (U.S.) Department for Energy assured that nuclear power would generate a "future electricity too cheap to meter".[14] Nuclear powerplants spread to many countries, satisfying the increasing energy demand, especially during the oil crisis when atomic power represented a good alternative to fossil energy. In the 60's, however, a few accidents occurred in the U. S. and the Soviet Union, raising local opposition amongst members of the scientific community who began to express their concerns.[47, 182] Following the Three Mile Island (1979) and Chernobyl (1988) accidents, nuclear energy production started to decrease; contingent to this were rising economic costs (related to extended construction times due to regulatory changes and pressure-group litigation). Moreover, falling fossil fuel prices made nuclear power plants under construction less attractive.[74] Later on though, the prices of fossil fuels rose, and concerns about greenhouse gas emission limits encouraged a nuclear renaissance.[228] This came to a halt, however, with the Fukushima Daiichi nuclear disaster in 2011 that brought about a one-year moratorium on nuclear power development. Today, some countries (Belgium, Germany, Spain and Switzerland) are phasing-out nuclear power, and Italy is the only country that has closed all of its functioning nuclear plants and withdrawn all plans to build new facilities. At the same time, the use of hydropower and other renewable energies have grown at a rate faster than any other time in history during the last 15 years. This indicates that the international community is concerned with environmental and security issues. Recently, there has been a large increase in international agreements and national energy action plans, such as the EU 2009 Renewable Energy Directive,[4] or more lately on December 2015, the United Nations Climate Change Conference COP21,[61] which negociated a worldwide agreement on the reduction of global warming and pollution. A significant trend that has come out following the COP21 is the promotion of solar panels. The International Solar Alliance (ISA)[213] was launched by Narendra Modi during the COP21 gathering of "sunshine countries" to develop the conversion of solar energy into electricity. On June 30, 2016 the World Bank announced a project to accelerate the mobilization of finances for solar energy exploitation by investing more than US $1 trillion that will be needed by 2030 to meet ISA's goals for the massive deployment of affordable solar energy.[6]

1.2 History of photovoltaics

The sun is the world's non-exhaustible renewable source of energy. However, barely 0.1% of the world's energy production comes from solar photovoltaics. The reason why the sun is insufficiently utilized is because of the limits that photovoltaic technology still faces. The first solar cell prototype was developed in 1954; as of today we have three generations of solar cells (Table 1.2). Unfortunately, none of them combines both high power-conversion efficiency and low production costs. In the following subsections, the historical development of solar panels will be briefly reviewed.

1.2.1 Evolution of engineered materials in photovoltaics

Nowadays, Si-based (1st generation) technology represents 90% of the photovoltaic market versus 10% for thin film (2nd generation) technology.[197] It is important to note that different semiconducting materials (CdTe, $CuInGaSe_2$ (CIGS) and GaAs) have contributed to the development of second generation solar panels.[166] Each of these materials has been engineered to increase light conversion efficiency. The cost of such technologies remains expensive because of the high purity grade requirements of the silicon and thin films.

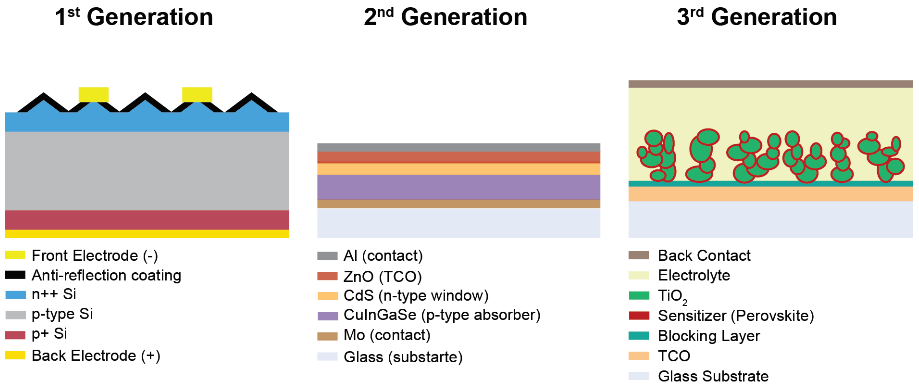

1st generation	2nd Generation	3rd Generation
Si- based technology Large pn junction diode Up to 25% efficiency 90% market	CdTe, CIGS, GaAs pn junction thin film Up to 29% efficiency 10% market	DSSC, Nanotechnology based No pn junction Up to 10-12% efficiency 0% market

Table 1.2 – Summary of the main characteristics of the three solar cell generations.[93]

Figure 1.2 represents the evolution over time of the efficiency of certain technologies (a more detailed chart can be found on the website of the National Renewable Energy Laboratory (NREL), Golden, CO) .[3] The chart shows that efficiency improvements within the same generation is due to progress in processing of engineered novel materials (ENMs). For example, in thin film technology, different materials were competing over 25 years to show a maximum efficiency of 3.9% to 20.1%. The third generation of photovoltaics integrate multiple technologies. One of them is the dye-sensitized solar cell, also known as a Graetzel-cell, which over two decades of development has reached a conversion efficiency of 12% .[236] But a real revolution in this generation of photovoltaic devices started in 2009 [121] with the use of methylammonium lead iodide ($CH_3NH_3PbI_3$, hereafter $MAPbI_3$), which has a perovskite structure.

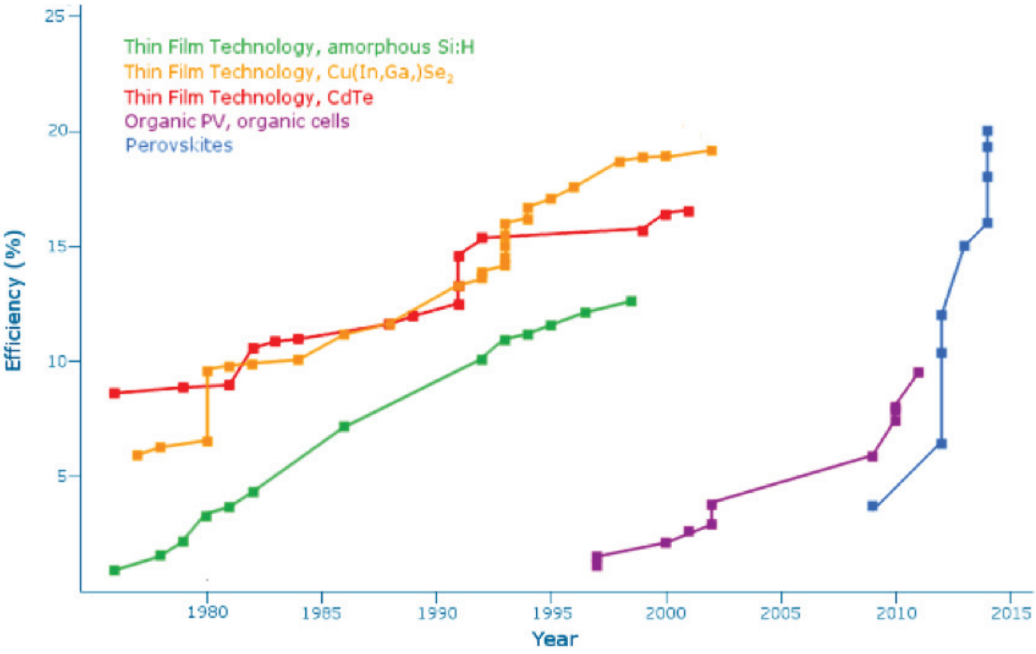

Figure 1.2 – The evolution of certain solar cell efficiencies for different photovoltaic technologies. (Chart simplified from the NREL[3]).

1.2.2 The revolution of hybrid halide perovskites

Perovskites are natural minerals that were discovered in Russia's Ural Mountains, and named after the mineralogist Lev Perovski. Their general formula of composition is ABX_3. Even synthesized compounds (not minerals) having this formula are called perovskites. The first explored perovskite was calcium titanium oxide ($CaTiO_3$) in 1839, and coincidentally that same year, Edmond Becquerel discovered the photovoltaic effect. Nevertheless, perovskites entered the field of photovoltaics only in 2009 with $MAPbI_3$. This hybrid perovskite was first synthetized by D. Weber[224] in 1978 with some other sister compounds having different dimensionalities. They were studied mostly in an optoelectronics context by Mitzi Miura and collaborators, and later by many other scientists. Kojima and his collaborators [121] have reported that $MAPbI_3$ might be interesting for photovoltaic applications because it has shown an efficiency of 3.8%. Three years later, a historical paper was published by Lee et al.,[126] which shook the scientific community working in photovoltaics: over a short amount of time, the efficiency of $MAPbI_3$ literally jumped to 10.9%. Since then, and again in a short amount of time, many researchers have improved the perovskites technology (Figure 1.2). Due to these efforts, the perovskite-based solar cell technology has been developped over the last four years by optimizing all the constituents of a device: the processing of the perovskite, the hole and the electron conducting layers and the contacts. Its efficiency has improved tremendeously. To date there is no other solar cell technology that has been developed so rapidly, with efficiencies growing from 3.9% to 22.1% in just 7 years.

Nonetheless, the photovoltaic-perovskite fever faces challenges: i) Long- and short-term stability of the material greets the photovoltaic community with skepticism. ii) Sensitivity of the material to temperature changes and water vapour makes the devices prone to rapid degradation. For this reason, the group of H. Snaith replaced the organic hole transport material with polymer-functionalized single-walled carbon nanotubes (SWNTs) embedded in an insulating polymer matrix .[97] With this structure, they observed a delay in device degradation. However, no long-term studies and comprehensive encapsulation techniques have been demonstrated yet for perovskite solar cells. iii) The heavy metal content in perovskite solar cells addresses potential health and environmental hazards.

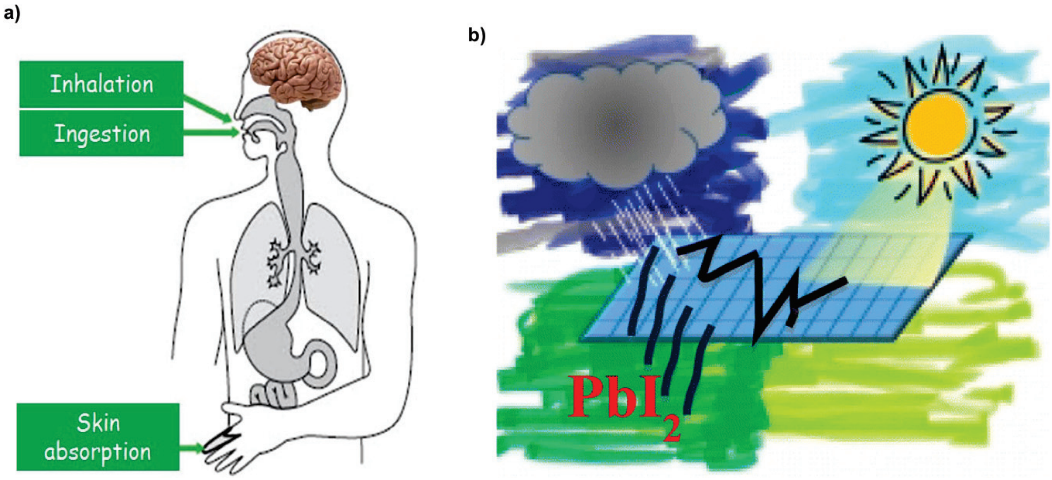

Figure 1.3 – Examples of the health hazards related to the photovoltaic perovskite a) contacts during synthesis and manipulation and b) its release into the environment after device failure (with permission from the Royal society of chemistry .[11,156]

Not only is human exposure during device production and handling a concern, but its release into soil and waterways after a failure of large area solar cells also represents major health and environmental risks, especially due to a potential thermal shock or damaged encapsulation.

The initial material is powder-like, and during the device fabrication, small particles can be accidentally inhaled, ingested or absorbed by the skin (see Figure 1.3 a.). After device production, transport, and mounting, it is likely that serious health and environmental hazards can be caused (see (Figure 1.3 b.), especially because of the instability of the light harvester, which contains heavy metals. The different routes of exposure and their potential consequences will be discussed in the next subsections.

1.3 Routes of exposure

Before discussing the potential toxicity of $MAPbI_3$, the various routes of human exposure have to be mentioned. Exposure may come through direct contact with humans during synthesis and manipulation (occupational) as well as through its release into the environment (environmental). It is important to note that these considerations are valid for most ENMs that are used in large-scale applications, regardless of their size or their scientific field of interest.

1.3.1 Sources of pollution and exposure

The diagram in Figure 1.4 gives a more general picture of the pollution cycle related to engineered materials in any field. During the manufacturing processes (waste discharge, storage and transportation) materials at any scale may leak into the atmosphere or to the ground leading to further transport and diffusion. Engineered materials may also penetrate the soil and groundwater through farming and husbandry applications such as pollution remediation or pesticide use. Like other pollutants, they are capable of environmental and adverse health effects above certain concentrations in the air, drinking water, or food chain.

Once released into the environment, these materials can spread into many ecosystems and cause deleterious effects. Under certain conditions at workplaces, the engineered materials may be inhaled in significant amounts. Also, nanoscale-sized particles may enter more easily into the body than larger particles.[45]

1.3.2 Endogenous pathways of exposure

Respiratory paths represent the main route of exposure to humans for any airborne material.[51] The lungs, where the total area of airways including alveoli represents approximately 143 m^2,[87] are continuously exposed to airborne particles. Aerosols penetrate the nose, and if they are soluble, they can reach the brain *via* the mucus surrounding the olfactory system (Figure 1.5 a.). Otherwise they cross the trachea, encounter the alveolar epithelium and the mucus, or the lining fluid of the lumen (Figure 1.5 b.). Once in the lungs, the deposit of particles may either be cleared by macrophages and monocytes, or penetrate the interstitium to encounter

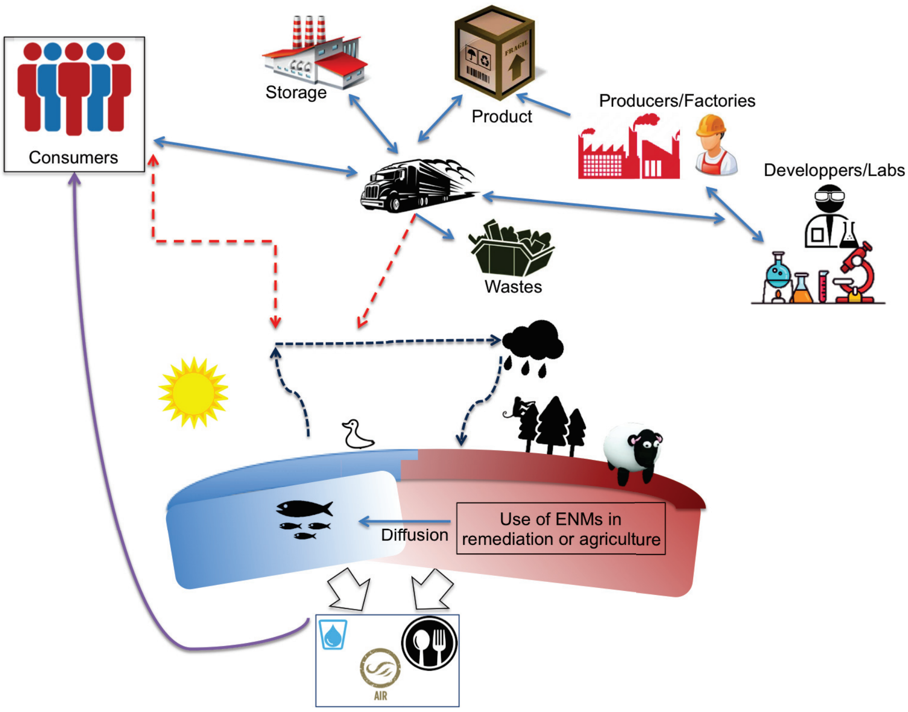

Figure 1.4 – The various sources and cycles of exposure to engineered materials are valid for the photovoltaic perovskite, as well.

fibroblasts, endothelial cells and other immune cells in the connective tissue, before they can potentially be transported into the blood circulation.[156]

The biokinetics of inhaled small particles after deposition has been quantified using microscopic and macroscopic techniques in rodents. In general, non-soluble microparticles, with a diameter of 0.5 - 10 μm, remain on the epithelium in airways and alveoli, and are accessible to branchoalveolar lavage, and at least the same can be expected for nanoparticles.[88] The clearance of deposited particles in the respiratory tract is made possible *via* two processes: a) physical translocation of particles by different mechanisms and b) chemical clearance processes and leaching. Chemical dissolution of biosoluble particles occurs either in the lipidic or hydrophilic environment both in the intracellular and extracellular fluids. Soluble components can undergo absorption, diffusion or binding to proteins and to other subcellular structures. They may also be cleared into blood or lymphatic circulation. Chemical clearance for soluble materials can happen at any location within the three regions of the respiratory tract (nasopharyngeal, tracheobronchial and alveolar, (Figure 1.5) depending on local extracellular and intracellular conditions (biochemical composition of the fluid, pH etc.). In contrast, a number of diverse processes involving physical translocation of inhaled particles exist in the respiratory tract and are different in the three regions. This part is discussed in the context of various toxicity studies in the following section, where toxicity regulations, most frequent

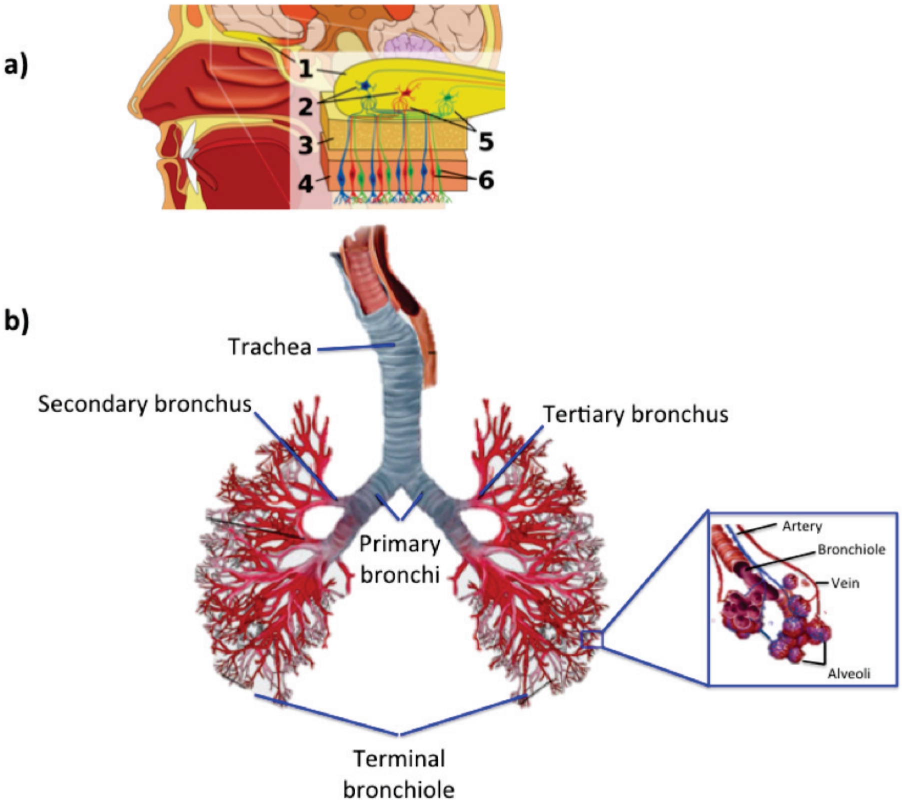

Figure 1.5 – Exposure of humans to ENMs through the respiratory paths: a) Human olfactory system; 1. Olfactory bulb, 2. Mitral cells, 3. Bone, 4. Nasal epithelium, 5. Glomerulus, 6. Olfactory receptor neurons. (source: Image gallery modified). b) Human bronchi system (source: organsofthebody.com modified)

ENMs and their chronic and acute consequences in human exposure will be reviewed.

1.4 The importance of toxicity studies of ENMs

Engineered materials are attracting a lot of attention not only because of their tunable properties (as seen in 1.1), but also in order to evaluate their potential environmental and health hazards. Epidemiological studies have shown a positive correlation between the level of particulate air pollution and increased morbidity and mortality rates; respiratory diseases are associated with the number of ambient ultrafine particles inhaled. In the following subsections, we will discuss the historical case of asbestos, and the current regulations for novel materials.

1.4.1 A historical case study: Asbestos

Asbestos is the most famous non-soluble material that gained much attention, first because of its desirable physical properties, but then because of its high toxicity. The silicate mineral is fibrillar and has been mined for more than 4000 years. Details on the historical use and development in applications can be found in appendix A of this dissertation. The very first observation of asbestos toxicity was found in a letter addressed by Pliny the Younger (61-113 AD),[86] and the second one appeared in the 16th century but was forgotten until 1898 when a letter by Lucy Deane, an inspector of factories in the UK, signaled a concern. A year later, Dr. Montague Murray reported a death related to chronic exposure to asbestos via inhalation.[184,211] Toxicity studies for asbestos started after serious epidemiological cases, and accidents were documented at workplaces. Scientists discovered that the dangers related to asbestos arose mainly when the fibers become airborne and inhaled. Because of the small size of the fibers, lungs cannot expel them. All types of asbestos fibers are toxic to humans and animals, and consequent exposure results in asbestosis or mesothelioma (the most common diseases). Mossman and Churg[145] documented that asbestosis and other lung cancers have been reported primarily in asbestos workers with long-term exposure at high concentrations. In the same paper, they considered instead a long latency period (the time taken between exposure and appearance of the illness) as being inversely proportional to exposure level. An examination of various epidemiological studies about dose-and-time response of the different forms of asbestos was shown to have a linear or square relationship for all the respiratory cancers.[104] Today, asbestos is no longer traded or used. The lessons learned from this story are not about the mining, manufacture and uses of a dangerous product. There are hundreds of companies selling products more dangerous than asbestos—such as deadly chemicals, poisons or explosives—with thriving employees and customers. The lesson is not even the recurrent failure of companies to act after concrete proof of damage to workers' health. Instead, what should be learnt is that warnings were not enough to prevent the tragedy. What might have prevented the asbestos situation is if toxicity studies had begun before accidents and illnesses were documented. Therefore, advances in novel materials should be accompanied by accurate toxicological research and their industrial applications accompanied by relevant regulations.

1.4.2 Current regulation aspects

The use of engineered materials in Europe, especially at the nanoscale, is free of any strict regulation or approval.[10] For example, the European Commission (EC) obliges manufacturers to mention the use of engineered materials including nanomaterials. However, potential reactivity and other hazardous properties are not properly regulated. In the U.S., The Food and Drug Administration (FDA) has not established regulatory definitions of "nanotechnology," "nanomaterial," "nanoscale," or other related terms.[157] In June 2014, the FDA issued industry guidelines entitled, "Considering Whether an FDA-Regulated Product Involves the Application of Nanotechnology.", which describes that a product involving the application of technology is considered FDA-regulated when: "(1) a material or end product is engineered to have at least one external dimension, or an internal or surface structure, in the nanoscale range (approximately 1 nm to 100 nm), and (2) whether a material or end product is engineered to exhibit properties or phenomena, including physical or chemical properties or biological effects, that are attributable to its dimension(s), even if these dimensions fall out-side the nanoscale range, up to one micrometer (1,000 nm)". Just like its counterpart in Europe, the FDA requires proper labeling for engineered material excipients of up to 1000 nm in a final product. Another example comes out of cosmetics, in which the ingredients (other than color additives) are FDA-regulated but no approval is required before their commercialization.[153]

Additionally, the Environmental Protection Agency (EPA) in the U.S. gathers environmental and health safety data, and needs exposure testing that can be used to set inventories[216] and then suggests a regulation. However, manufacturers are not obligated to apply for EPA guidance. The absence of strict regulations and lack of approvals in the application of engineered mate-rials at any scale (bulk, micro or nano) is probably due to both the absence of an official classification and a lack of toxicological studies. This dissertation focuses on the promising photovoltaic perovskites, because their energy conversion efficiency has significantly improved within few years, which led some industrials, such as Dysol, Oxford PV and Nesli, to rapidly exploit them as a sustainable, cheap, and "clean" solution for solar power harvesting.

1.4.3 Toxicity of the materials used for solar panels

In terms of the currently available photovoltaic solar panels on the market (as seen in section 1.2 History of photovoltaics and Figure 1.2), TiO_2, CdTe, $CuInGaSe_2$ (CIGS) and GaAs are the materials to be considered in toxicity evaluation and safety measures. A short review on their toxicity is presented in the following sub-sections.

Titanium dioxide

Titanium dioxide represents the highest total production volume of pigments worldwide.[15] It has been used to provide whiteness and opacity to various products (paints, papers, foods, toothpastes etc.). TiO_2 can also be found in skin care products (sunscreens), and has been used in the second generation of solar cells Figure 1.2. The latter represents 10% of all solar panels on the market.

Titanium dioxide dust, when inhaled, has been classified by the International Agency for Research on Cancer (IARC)[75] as an IARC Group 2B carcinogen, meaning it is possibly carcinogenic to humans.[227] The findings of the IARC are based on the discovery that high concentrations of powdered and ultrafine titanium dioxide dust cause respiratory tract cancer in rats when exposed by inhalation and intratracheal instillation.[210] The series of biological steps that trigger lung cancer in rats (e.g. particle deposition, impaired lung clearance, cell injury, fibrosis, mutations and ultimately cancer)[235, 238] were considered by IARC as relevant to employees with exposures to titanium dioxide dust. Concerns about the safety of using nanoparticle sized titanium dioxide has been criticized because the mechanism by which TiO_2 may cause cancer is unclear. However, many studies have focused on the cellular and *in vivo* uptake of TiO_2, and it has been demonstrated that ultrafine TiO_2 particles have a significantly greater pulmonary potency for inflammatory response than larger TiO_2 ones, and that this response is accompanied by an increased interstitial access of these particles.[155] This argument convinced the brand “Dunkin’ Donuts” in the United States to switch to bulky titanium dioxide in its powdered sugar donuts.[140] However, public pressure forced the brand to drop the use of TiO_2 in food.[111]

Different studies have shown that nano-sized TiO_2 translocates along the lung to the blood stream then disperses into different organs (Skin, heart, liver, spleen and lung).[154, 165, 165, 230] In vitro studies showed how cellular toxicity of TiO_2 at the molecular level results from the interaction between TiO_2 nanoparticles and the lysosomal compartment.[238] The dermal sorption of TiO_2 in the epidermis and dermis were observed by the daily application of sunscreens containing micro- and nanosized TiO_2 to subjects for 2 to 6 weeks.[203] Puccetti et al. have published the layer distribution of nanoTiO_2 within the human skin,[177] and under sunlight illumination, nano-sized TiO_2 internalized in skin cells, oxidative stress was catalyzed and DNA was damaged.[73]

In 2009, Wu and collaborators evaluated the penetration profile and potential toxicity of TiO_2 nanoparticles *in vitro* and *in vivo* via a dermal route.[230] The results showed for the first time how—after chronic dermal exposure—materials of various size could penetrate the skin and reach different organs to induce tissue damage and trigger oxidative stress. This latter significantly increases MDA levels (malondialdehyde, a marker for oxidative stress) and decreases SOD activities (superoxide dismutase, Enzyme that catalyzes the superoxide radical into O_2 or H_2O_2) in the penetrated tissues. This paper warned the community about dermal toxicity with topical application of nano-sized TiO_2 for a prolonged period, and how its association with free radical generation, oxidative stress, and collagen depletion can pose a risk to human health after dermal exposure over a relatively long time period. Research focusing on the carcinogenicity of different particle sizes of titanium dioxide has led the US National Institute for occupational Safety and Health (NIOSH)[150] to recommend two separate exposure limits: 1) fine TiO_2 particles are set at an exposure limit of 2.4 mg/m^3, 2) ultrafine TiO_2 are set at an exposure limit of 0.3 mg/m^3, as time-weighted average concentrations up to 10 $hours$ a day for a 40-hour work week.[149] These recommendations are in agreement with the scientific findings showing how smaller titanium dioxide particles are more likely to pose carcinogenic risk than the larger ones.

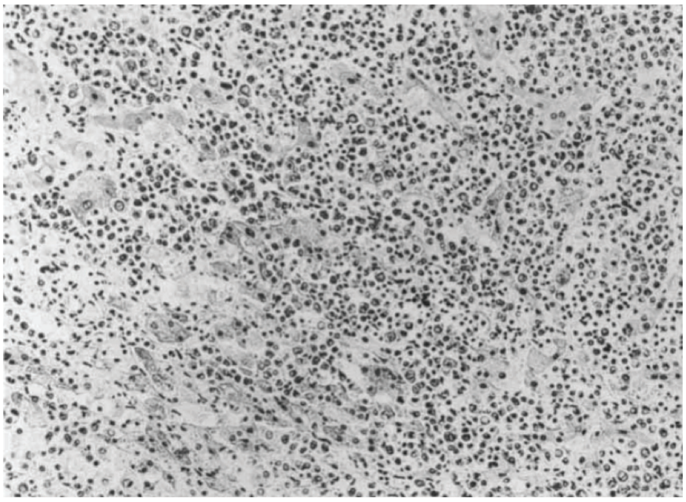

Figure 1.6 – Liver tumor (malignant lymphoma) of a hamster after intratracheal instillation of GaAs for 15 $weeks$.[159]

Gallium Arsenide, Cadmium Telluride, Cupper Indium Gallium Selenide

Pulmonary toxicity Acute toxicity studies of GaAs, when administered by instillation to the trachea of rats, reported the solubility and dose-related increases in blood levels of arsenic, and gallium in the blood was not detected.[221] A single delivery of 100 mg/kg of GaAs particles resulted in a dose-dependent increase in lung wet weight associated with acute pulmonary inflammation and pneumocyte hyperplasia after two weeks.[222] Furthermore, the same group documented that smaller-sized GaAs particles induced more serious acute pulmonary lesions including a marked inflammatory response and a mild pulmonary fibrosis. In their previous studies, they showed a more rapid onset of arsenic toxicity with larger GaAs particles.[223] At 18 days following injection of 100 mg/kg GaAs, marked body weight loss, lung weight increase, moderate seropurulent pneumonia, and type II pneumocyte hyperplasia were also evidenced.[91]

Regarding the chronic toxicity, weekly treatment of hamsters with GaAs particles by repetitive intratracheal injections, for 15 weeks, resulted in survival reduction and pulmonary inflammation although no tumors occurred over a 2-year observation period.[159] On the other hand, GaAs inhalation caused an increased incidence of both benign and malignant lung tumors in female rats, which had been exposed to 0.01, 0.1, or 1.0 mg/m^3 of GaAs particles for 2 years, but not in male rats.[152] In addition to GaAs, Tanaka et al.[205] reported that indium arsenide ($InAs$ 1.27 mg/kg) triggered pulmonary lesions across a 2-year observation period. The same molar amounts significantly suppressed body weight gain in hamsters compared to controls.

Pneumonia, alveolar or bronchiolar cell hyperplasia, pulmonary proteinosis-like lesions, and metaplastic ossification in the lung were observed in InAs-treated animals.

Testicular toxicity Following intratracheal administration in rats and hamsters of 7.7 mg/kg of GaAs particles twice a week for 8 $weeks$, Omura et al.[161, 163] showed a decrease in sperm count, an increase in abnormal sperm in the epididymis, and degeneration of late elongated spermatids at the post-spermiation stages. The same group observed testicular damage, including testicular spermatid retention and epididymal sperm reduction in hamsters.[162] Moreover, InAs produced definitive testicular damage to hamsters in a long-term study[164] because injection of indium twice a week for 8 weeks in hamsters decreased reproductive organ weight and caudal sperm count, and caused severe histopathologic lesions in the testis.

Circulatory system When the toxicological effects of semiconductor materials containing arsenic are evaluated, not only has the toxicity of arsenic been a main focus but also research into whether the other constitutive elements may be toxic as well. In hamsters treated with 7.7 mg/kg of InAs, the serum arsenic concentration was approximately 0.4 μM during the entire observation period of 88 weeks, showing little change. Serum indium levels after injection were about 7.62 μM and these levels decreased gradually until the end of the observation period. In a subchronic study[204] in which twice the dose of InAs was administered intratracheally, indium serum level was about the same amount injected. However, 0.4 μM of arsenic was detected in the serum, which might be the maximum concentration to remain in the serum of hamsters when InAs particles were given intratracheally, regardless of varied treatment protocols. Therefore, the presence of these two elements in the blood might be responsible for the damages observed in pulmonary and testiculary systems.

Toxic effects on other organs When gallium-containing semi-conductors were intraperitoneally injected into rodents, the survival was reduced and different tumors significantly developped[204](Figure 1.6). Toxicity in kidneys was also clearly evidenced[91] after exposure of 50, 100, or 200 mg/kg of GaAs, where mitochondrial swelling was observed in renal proximal tubule cells. Furthermore, inhibition of γ-aminolevulinic acid dehydratase (ALAD, a precursor of hemoproteins) was also observed in the blood, kidney, and liver in a dose-dependent manner. Some reports documented the potential immunotoxicity of GaAs particles in both *in vitro* and *in vivo* model systems.[48, 192, 193] Oral administration of GaAs resulted in impairment of the heme synthesis and immune system.[81, 82]

Toxicity of hybrid materials for future energy-related applications

Metal Organic Frameworks (MOFs) are hybrid materials with a porous structure[130, 233] suitable for many applications[30, 99, 106, 107, 123, 191, 219] including medicine, optoelectronics, but also gas storage (namely hydrogen). BASF is already producing them on an industrial scale. Thus far, only a few reports have focused on the question of toxicity involving MOFs for medical applications. Couvreur and colleagues, who promoted MOFs in medecine, examined the toxicological effects of iron carboxylate MOFs both *in vitro* and *in vivo* and tested the effects of acute or subacute exposure to very high doses (up to 220 mg/kg) of three different iron carboxylate MOFs administered intravenously to rats. They found no observable toxicity and reported that these iron carboxylate MOFs were rapidly sequestered by the liver and spleen, biodegraded and directly eliminated through the urine or feces without causing obvious toxicity.[31] Another study, however, looking at the toxicity of MOF containing zinc reported a disrupted cellular zinc homeostasis and down-regulation of GAP-43 protein.[178] Nonetheless, the health hazards of MOFs for applications other than for drug delivery remain unexplored. The core of this dissertation is on the toxicity of hybrid halide perovskites because such studies has not been done yet. Concerns about their potential hazards rose primarily because of the lead content,[11, 100] and so the photovoltaic community is currently interested in replacing Pb by Sn, another heavy metal. At the same time, many reports on the toxicity of tin have to be considered, since the metal triggers tumor formation in the lungs, infertility by downregulation of sperm creatine kinase, skin and retinal irritation, heavily affects the hematological system as well as kidney cells and interferes with neurotransmitters.[33, 40, 44, 89, 113, 127, 132, 198] Exposure to tin may be dietary[40] (by consumption of food stored in unlacquered tin cans) or occupational[33] (by inhalation, skin contact, and eye contact in the workplace). The Swiss Occupational Safety and Health Administration (OSHA) has set the legal permissible exposure limit for tin exposure in the workplace as 2 mg/m^3 over an 8-hour workday.[65] Heavy metals mainly harm the body by creating an imbalance between the production of free radicals and the body's ability to repair free radical damage. When applied to photovoltaics, the perovskite layer (containing Pb or Sn) is neither thermally stable nor in a water-rich environment; one of the main degradation products could be Lead iodide (PbI_2) and Tin iodide (SnI_2). Both halides are available in the market and several reports documenting their negative effects together with regulations about their use are summarized in safety data sheets.[8, 176] PbI_2 has been found to be a carcinogen causing irreversible damage to fertility, respiration and digestion. It is cumulative and very toxic to aquatic organisms and the environment.[8] At the molecular level, it interacts with sulfhydryl groups, impacting various enzymes, receptors and proteins. It also interferes with metabolic pathways in mitochondria, and in systems that regulate cellular energy and metabolism. It causes activation/inactivation of many enzymes via its competing effects with other cations, notably calcium, ferrous iron, and zinc. Lead inhibits several enzymes involved in heme synthesis, and impairs erythrocyte membrane stability, causing anemia.[37] SnI_2 is also acutely and chronically destructive. It impairs vision, skin, lungs and the digestive system.[65] The toxicity of the entire perovskite materials has not been documented at all before this dissertation. A detailed outline of the toxicity of photovoltaic lead and tin halide perovskites will follow in the next paragraphs of this chapter.

1.5 Motivation and objectives of the study

Figure 1.7 shows the number of publications on materials developed for photovoltaic application versus the number of published studies on their hazards. For the last 20 years, there has been little research on the potential toxicity of novel materials when we compare the advances in material science and engineering. Today, approximately 170 $publications$ warn the scientific community about the potential hazards of photovoltaic materials, which represents less than 0.8% of the total number of publications on photovoltaic materials. Clearly, there is a need for toxicological research. We contribute to this effort with a detailed toxicity study on two novel photovoltaic light harversters: methylammonium lead and tin iodide perovskites. These two compounds will soon join the market of photovoltaic solar panels (in 2018 according to Oxford PV, Dyesol and Nesli companies). If no robust studies on these promising compounds are published, no specific regulations will be able to handle the manufacture, amount, use and recycling of the fabricated solar panels.

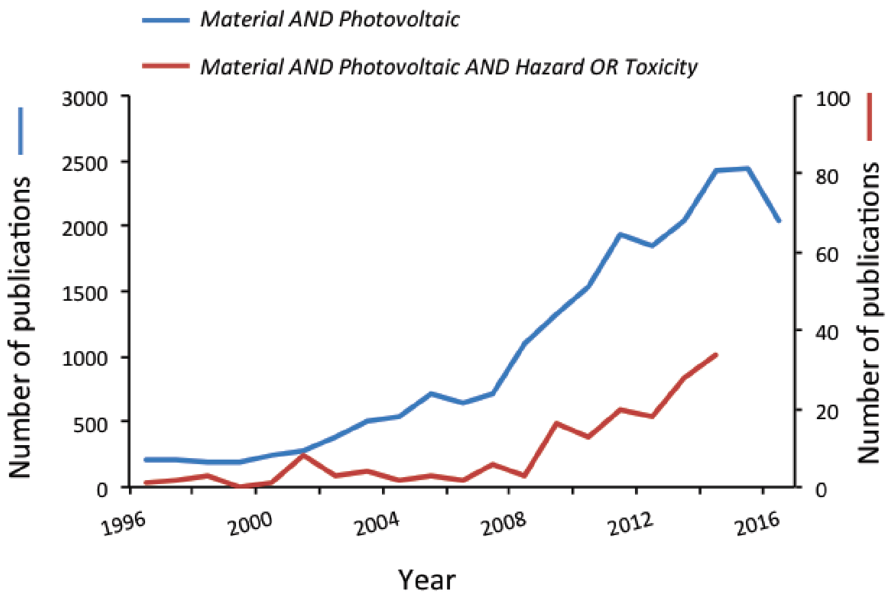

Figure 1.7 – Chart representing the number of publications over the last 20 $years$ on materials for photovoltaic application (left axis) versus the number of publications reporting hazards or toxicity of the same materials (right axis). Research done November 3^{rd}, 2016 on Scopus with the keywords “Material AND Photovoltaic”, and “Material AND Photovoltaic AND Hazard OR Toxicity”.

1.5.1 Study design

The overall design of this study starts with the physical/chemical characterization of the studied material with its molecular environment. Various microscopic and spectroscopic techniques were used. In addition, the solubility of the photovoltaic perovskites was evaluated in a time- and dose-dependent approach in water and physiological media. Human neuroblastoma and lung epithelial cells were selected according to section 1.3.2. The cellular uptake was monitored using specific protocols and the phenotypical, physiological and molecular effects were tracked accurately using standard protocols. The chemical and structural changes induced by exposure of human cells to perovskites were also observed with a very efficient and uncommon technique: infrared microspectroscopy using synchrotron radiation. The toxic effects of perovskites were also studied at the organism level. The use of small model organisms, *Drosophila melanogaster* and *Caenorhabditis elegans*, represents an important step before studying toxicity on more complex animal models.

1.5.2 Characterization of hybrid halide perovskites

$MAPbI_3$ was synthetized using the method described by Poglitsch and Weber[172] in organic solvents. The elemental composition of the obtained crystallites was analyzed using Xray diffraction and the presence of lead and iodine was confirmed and the atomic percent ratio Pb:I was found to be 25:75. Lead- and tin-containing perovskites were synthesized at various shapes and sizes (Figure 1.8); a powder-like material was used for the toxicity study reported in this dissertation. Prior to assessing their hazards, perovskite was added to water and physiological solutions and characterized using spectroscopic analytical chemistry. The results of the material characterization will be detailed in chapter 2.

1.5.3 Administration of perovskites to various biological model systems

Cellular models

The lungs are regarded as one of the main portals of entry for tiny particles, something which underscores the importance of pulmonary toxicity evaluation. The first barrier that the inhaled particles encounter, when deposited on conducting airways or the alveolar region, is the epithelium. If the particles are soluble in the nasal mucosa, they are conducted to the brain via the neuronal receptors of the olfactory system or via the nerve endings embedded in the tracheobronchial region through the afferent vagal nerves Figure 1.5. Consequently, we targeted the toxicity study on human lung epithelial cells and human neuroblastoma cell lines. The importance of cell lines lies in their ability to provide a renewable source of cells for repeated studies. Unlike *in vivo* tests, cellular studies make it possible to identify

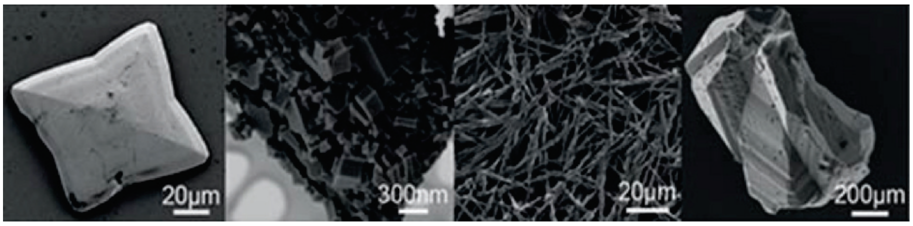

Figure 1.8 – Scanning electron micrographs of the photovoltaic perovskite crystals synthesized in our laboratory in different sizes and shapes.

the biological pathways and mechanisms involved in toxic reactions observed on a whole organism. In vitro tests can be used to rapidly determine important parameters influencing toxicity, such as dose; exposure time; isolation of specific pathways etc. In order to mimic the occupational exposure to photovoltaic perovskites dust and byproducts, test particles were added to a cell culture medium using short-term sonication. We tested various doses *in vitro*, from 5 to 1000 $\mu g/ml$, in order to probe the most significant range of concentration to observe a traceable effect within a significant time-lapse in the cellular study. We will present the methodology of administering the perovskites to our cellular models, the performed assays in examining different cellular processes and we will also discuss the corresponding results. These *in vitro* studies on human cells provided a preliminary understanding of the first signs of perovskites toxic effects. However, using cell derived from cancer cells is often subject to debate because they reflect the properties of their original cancers. For this reason, we also worked with primary cultures from mice as a substitute for human cells. Other disadvantages include a mismatch in doses, lack of engagement of the complete biological responses in a whole organ and lack of validation against *in vivo* effects. Therefore, we selected model animals to observe the effects of perovskites on a whole organism and to compare the results with our *in vitro* data.

***in vivo* models**

In vivo testing remains a crucial step for evaluating the relevance of *in vitro* findings. Although genetic differences are responsible for the unicity of subspecies or individuals within the same species, there are multiple genetic and proteic similarities between them. For this reason, *in vivo* studies have the potential to offer better insights into the toxicity and potential diseases caused by a material and eventually serve to find the right medication. The most used animal models are rodents because 85% of their protein-coding regions are identical to humans'. Moreover, both rodents and humans often suffer from the same diseases, react similarly to infection and injury as well as control their body chemistry using similar hormones. Therefore, research on rodents has contributed significantly to advance modern medicine. In the 17^{th} century, the use of vertebrates and mammalian models in the laboratory raised concerns because of vivisection. Since then, ethical guidelines, laws for animal testing and the animal welfare act are significantly emphasized. One alternative to vertebrates are small organisms. They represent good biological models and do not require ethical approval. With their small size, they are easy to handle, inexpensive to buy and maintain, and produce many offspring in a short period of time. Consequently, we have also assessed the toxicity of $MAPbI_3$ and $MASnI_3$ on small organism models, namely *Drosophila melanogaster* (or the fruit fly) and *Caenorhabditis elegans* (or the earthworm). A description of the models and details on experimentation can be found in chapter 5. In vivo, we used the same doses as *in vitro* tests suspended in the animals' food (bacteria for the worms and yeast/grapefruit for the flies). This administration method makes it possible to monitor both the toxicity by ingestion, and also by skin contact and breathing since flies and worms are in direct contact with their food, and have a thin permeable skin through which oxygen penetrates.

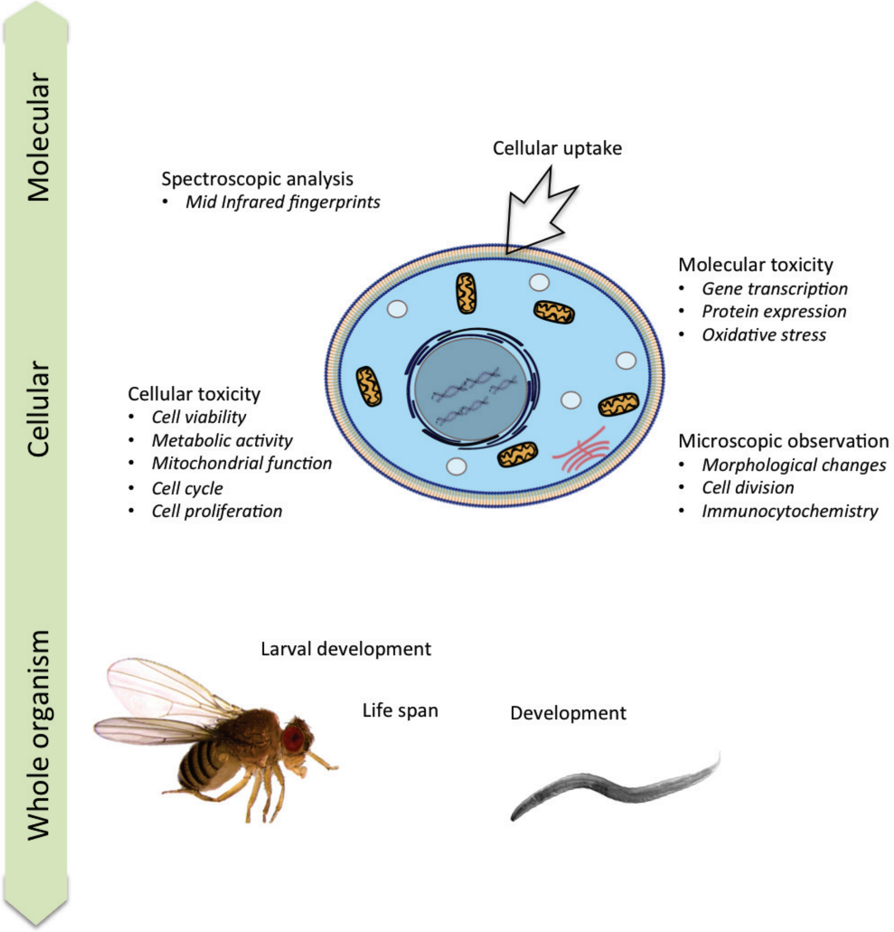

Figure 1.9 – Illustration of the strategy in my dissertation to study the toxicity of photovoltaic perovskites: at the cellular and molecular levels (zoom-in) and at the living organism level (zoom-out) approach

1.5.4 Thesis objectives

In this dissertation, the main goal was the toxicity study of perovskites before their large-scale commercialization in the next-generation of solar panels. The study started by the chemical characterization of the material, which allowed understanding its behaviour in a humid environment. Next, we used a battery of assays to assess the degree to which perovskites can damage living cells and their subcellular mechanisms. In addition to cellular studies, effects on a whole organism were also evaluated using small model organisms. Figure 1.9 and the following specific aims summarize the main achievements of this thesis.

Specific aim 1: Chemical characterization of the photovoltaic hybride perovskites and improvement of the experimental set up to use them for toxicity evaluation. Size and shape of the materials were characterized using electron microscopy. Moreover, analytical chemistry methods were used to determine their behavior in solution, which helped the design of toxicity experiments. This specific aim was achieved within the first year of my PhD.

Specific aim 2: For toxicity assessment *in vitro*, we targeted accidental exposure to the solid material, by inhalation, to select the cellular models. We reproduced this scenario of exposure *in vitro* on neuronal cells (SH-SY5Y human cell line and murine primary hippocampal neurons), and on human lung epithelial cells (A549). These cells were grown and exposed to perovskites at different concentrations and during various time points. We first evaluated the plasma membrane integrity, caspases activity (programmed cell death markers) to assess the overall state of cells over perovskite administration. Then, we investigated the subcellular mechanisms from intracellular uptake, to cell cycle to mitochondrial function, before analyzing the gene expression profile following perovskite exposure. We have also used IR spectroscopy under synchrotron illumination to elucidate the biochemical fingerprints of perovskites' toxicity. This sophisticated method was employed for the first time to conduct toxicity studies.

Specific aim 3: A third independent specific aim consisted on evaluating the toxicity of perovskites on an entire model organism, namely, *Drosophila melanogaster* (or the fruit fly) and *Caenorhabditis elegans*. We first focused on the impact of perovskites on the life span of young adults, then focused on the impacts on their fertility, and development of their progeny.

In the following chapters, we present the experimental procedures, results and conclusions towards achieving those specific aims.

2

Characterization of $MAPbI_3$ and $MASnI_3$ in solution

2.1 Overview of the studied photovoltaic materials

The development of organo-metal halide perovskites represents one of the top ten science breakthroughs of 2013.[13] They are a promising class of compounds[126] used for making highly efficient photovoltaic solar cells because of their high photon to electron conversion efficiency, low material and manufacturing costs, and the simplicity of their device architectures. Indeed, over the past three years, these materials have shown a record improvement of efficiency[3, 126, 234] (see chapter I). In general, all novel materials destined for large-scale commercial applications should be tested for health hazards, and this is especially important for these perovskites because of their heavy metal content (Pb, Sn). The condition *sine qua non* for any toxicity screening strategy is a detailed and comprehensive physico-chemical characterization of the tested material. A chemical characterization is crucial for correlating the materials' characteristics with any measured biological/toxicological responses. The health hazard of photovoltaic perovskites is amplified by the fact that they are unstable and degrade in a humid environment: they may be easily dissolved in water and physiological liquids. This chapter deals with a detailed analytical investigation of the starting powder compound in aqueous environments.

2.2 Shape and size of the $MAPbI_3$ and $MASnI_3$ materials

$MAPbI_3$ and $MASnI_3$ can be synthesized, depending on the purpose of their use, into various forms: big crystals, nano-crystals, thin films, nanowires, or quantum dots Figure 2.1. All these forms are the result of a solution-based process described by Poglitsch and Weber.[172]

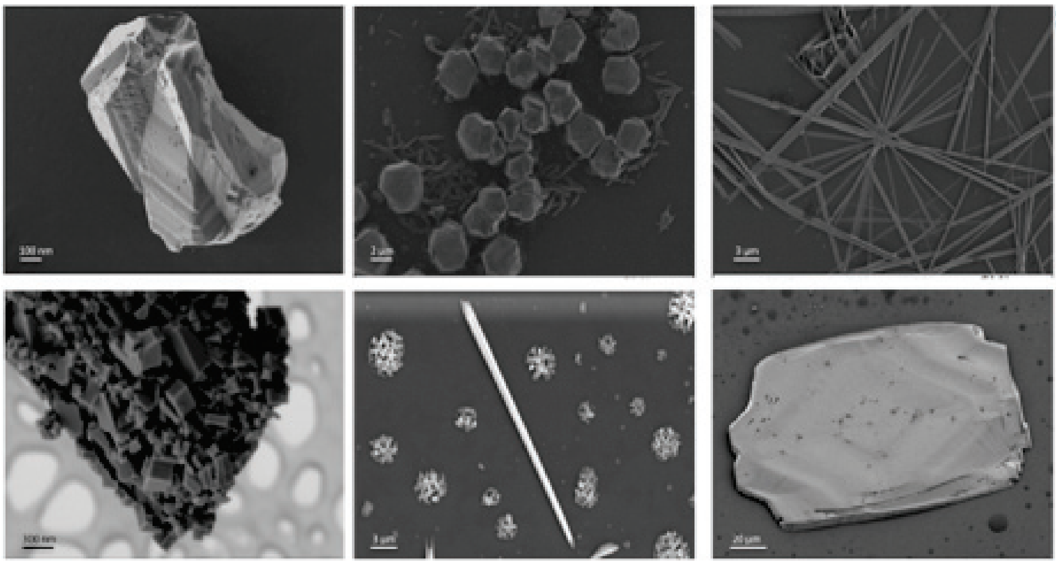

Figure 2.1 – SEM micrographs showing the morphology of a typical polycrystalline perovskite based films implemented in high performance perovskite solar cells.

In this study, we used a powder composed of microcrystalline species since this is more abundant and easier to synthesize. As a first step towards assessing the potential toxicity of $MAPbI_3$ and $MASnI_3$, it is important to conduct a quantitative assessment of their volatility and stability in an aqueous environment with respect to chemical and microbial degradation. It is well known that $MAPbI_3$ and $MASnI_3$ have a hygroscopic character, *i.e.* they are sensitive to moisture and decompose into their water-soluble constituents. Therefore, in a health hazard investigation, the shape and size do not play a role since the material is dissolved.

2.3 The behavior of the photovoltaic perovskites in solution

We determined the solubility of $MAPbI_3$ and $MASnI_3$ polycrystalline powder in deionized water (close to outdoor environmental conditions) as well as in two types of cell culture media (DMEM and DMEM:F12) which mimic the fluid conditions of the human body. The perovskite powder was dispersed into these liquids at different concentrations (from 50 $\mu g/ml$ to 100 mg/ml). The starting step of the perovskite dissolution was identical in deionized water and in the cell culture media, where the initial powder turned instantly to a silver-grey and then a white solid precipitate. After a few minutes in water, the latter dissolved completely at the lowest concentration, and the process was faster for the $MASnI_3$ compound.

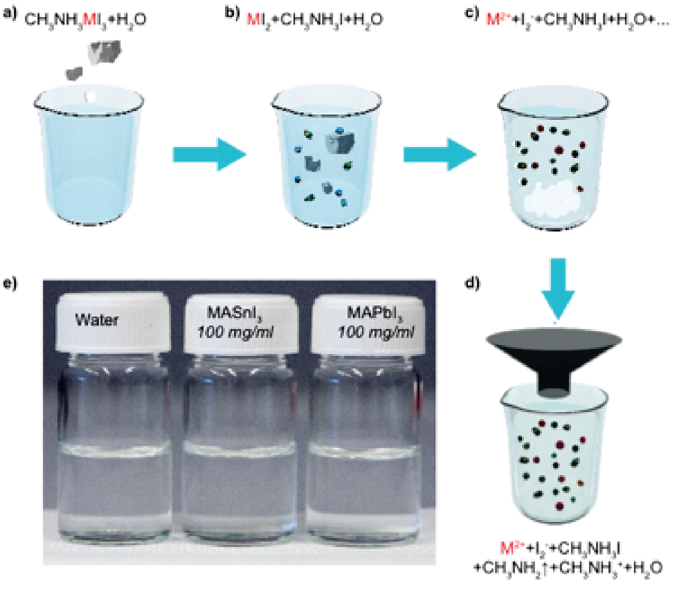

Figure 2.2 – The methylammonium metal (M: Pb or Sn) perovskite in water for analytical chemistry evaluation. The different steps of the solution preparation in water at a high dose (100 mg/ml): The polycrystalline powder was suspended in water (a); dissolution of the perovskite material started instantly (b). After several hours, a white/yellow precipitate formed but disappeared after 4 days (c). This solution was filtered for elemental analysis (d); Pictures of the perovskites-containing water solutions after one week before filtration (e).

At the highest dose, a clear and transparent liquid was obtained in deionized water after

4 days, indicating that the $MASnI_3$ or $MAPbI_3$ was completely dissolved (Figure 2.2). In a cell culture medium, the initially silver-grey colored $MAPbI_3$ or $MASnI_3$ decomposed into a solid, white-yellow precipitate and water-soluble methyl ammonium iodide derivatives within a few seconds. Importantly, altered dissolution mechanisms were observed after longer soaking times (Figure 2.3). The white precipitate remained present in the $MAPbI_3$ solution, even 30 days post-preparation, while opaque flakes appeared in the $MASnI_3$ solution. The next characterization steps were focused on the precipitate and the filtered solution independently. The related experimental procedure and results are discussed in the following paragraphs.

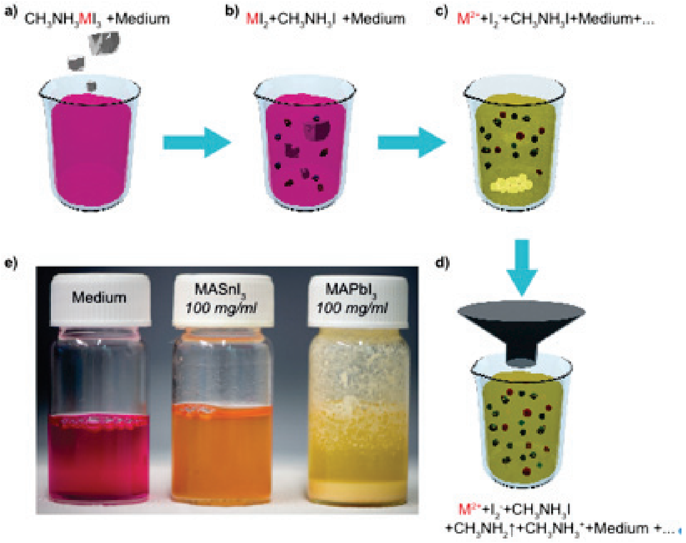

Figure 2.3 – The methylammonium metal (M: Pb or Sn) perovskite and its preparation for the toxicity tests. The different steps of the solution preparation in the cell culture medium (DMEM) at a high dose (100 mg/ml): The polycrystalline powder was suspended in DMEM (a); dissolution of the perovskite material started instantly (b). After several hours, in the $MAPbI_3$ solution, the majority of the Pb^{2+} ions formed a white/yellow solid deposit, whereas in the $MASnI_3$ solution, some Sn^{2+} ions precipitated into transparent flakes (c). The solutions were filtered for elemental analysis and cellular administration (d). Pictures of the perovskites-containing solutions after one week before filtration (e).

2.4 Analysis of perovskites in aqueous environment

The structure of the perovskite presented in Table 2.1 shows the octahedral building block and the organic cation. The atomic distribution of the perovskite components is estimated according to the chemical formula. For example, $MAPbI_3$ has a molecular weight percentage of lead, iodine and methylamine of 33.42, 61.41 and 5.17%, respectively. In the same way, $MASnI_3$ has a percentage of tin, iodine and methylamine in the total molecular weight of 22.34, 71.63 and 6.04%, respectively. In the next section, we present an analysis of the $MAPbI_3$ and $MASnI_3$ by-products after filtration.

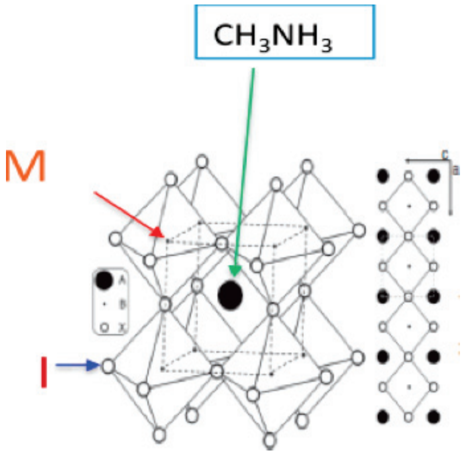

$MAPbI_3$ content	Atomic mass (A.U.)	Percentage (%)	$MASnI_3$	Atomic mass (A.U.)	Percentage (%)
Lead (Pb)	207.20	33.42	Tin (Sn)	118.71	23.34
Iodide (I_3)	380.70	61.41	Iodide (I_3)	380.70	71.63
Methylammonium (CH_3NH_3)	32.08	5.17	Methylammonium (CH_3NH_3)	32.08	6.04
Total ($MAPbI_3$)	619.98	100	Total ($MAPbI_3$)	531.49	100

Table 2.1 – Chemical structure and molecular weight distribution of the pervoskite $CH_3NH_3MI_3$ (M: Metal, Pb or Sn)

2.4.1 Analysis of the precipitates

The precipitates formed in the $MAPbI_3$ and $MASnI_3$ solutions were lyophilized and grinded before analysis. The elemental composition of the $MAPbI_3$ and $MASnI_3$ crystallites and their solid decomposition by-products were analyzed using Energy-dispersive X-ray spectroscopy (EDX). The measurements were done with an X-MAX EDS detector mounted at a 35-degree take-off angle with a SATW window. EDS spectra were taken at a working distance of 8.5 mm with 20 keV accelerating voltage and a current held at 200 pA. The results revealed that the white deposit that appeared in the $MAPbI_3$ solution is composed of a mixture of lead (II) hydroxide, lead (II) carbonate, and lead (II) phosphate compounds (Table 2.2), which were formed by the reaction of Pb^{2+} with the carbonate, phosphate and hydroxide anions of the cell culture medium (the full composition of the cell media can be found in the appendix).

On the other hand, the flakes formed in the $MASnI_3$ solution contained mainly iodine, oxygen and carbon complexes of tin (Table 2.3). These compounds were formed by the reaction of Sn^{2+} with the carbonate and hydroxide anions of the cell culture medium. According to the elemental composition analysis of the precipitate, tin ions do not seem to form complexes with phosphates, but instead they likely precipitate with sodium in a hydroxide form.

a

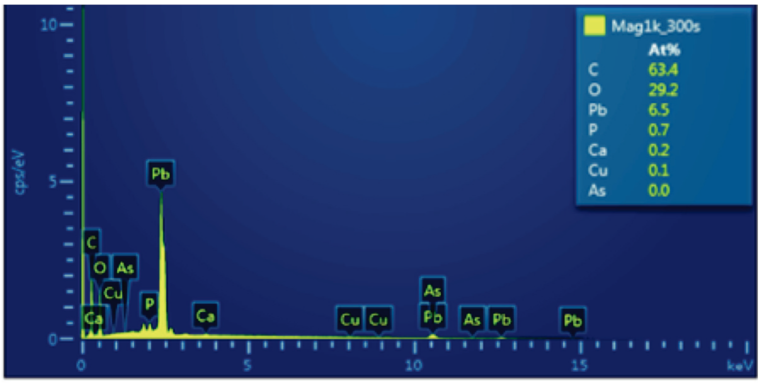

b

Element	Line Type	Apparent Concentration	k Ratio	Wt%	Wt% Sigma
C	K series	5.52	0.05521	29.26	0.27
O	K series	6.41	0.02157	17.98	0.19
P	K series	0.75	0.00420	0.79	0.03
Ca	K series	0.13	0.00119	0.26	0.04
Cu	K series	0.15	0.00146	0.27	0.09
As	L series	0.03	0.00017	0.05	0.06
Pb	M series	28.54	0.26563	51,39	0.27
Total				100.00	

Table 2.2 – Elemental analysis of the white/yellow solid precipitate formed by reacting $MAPbI_3$ powder with the cell culture medium (DMEM). (a) The elemental composition of the solid decomposition by-products of the $MAPbI_3$ dispersed in the cell culture medium were analysed using Energy-dispersive X-ray spectroscopy (EDX); (b) The elemental analysis revealed that the white, solid precipitate contains significant amounts of Pb. Ca and P. The yellow/white solid precipitate is presumably a mixture of lead (II) hydroxide, lead (II) carbonate, and lead (II) phosphate compounds, which were formed by the reaction of Pb^{2+} with the carbonate, phosphate and hydroxide anions of the cell culture media.

2.4.2 Analysis of the filtered solution

Elemental composition

The $MAPbI_3$ and $MASnI_3$ solutions in deionized water and the cell culture media were analyzed using Inductively Coupled Plasma Optical Emission Spectroscopy (ICP-OES, Shimadzu ICPE-9000). From a stock solution (about 30 mg/ml), aliquots were taken at various time points (1-30 days), diluted at the desired concentrations and filtered using 220 nm pore cellulose filters (Merck Millipore, Switzerland). The metal and iodine concentrations of the clear solutions were measured three times. Analytical chemistry by ICP-OES was used to detect the metal ions and iodine in a filtered solution of the perovskite. However, this method cannot distinguish between soluble elements or particles smaller than 220 nm (i.e. filter pore size). The concentrations of the perovskite filtrates were determined after a preliminary screening of cell viability in a dose-time response using microscopy (detailed in the next chapter). Con-

a

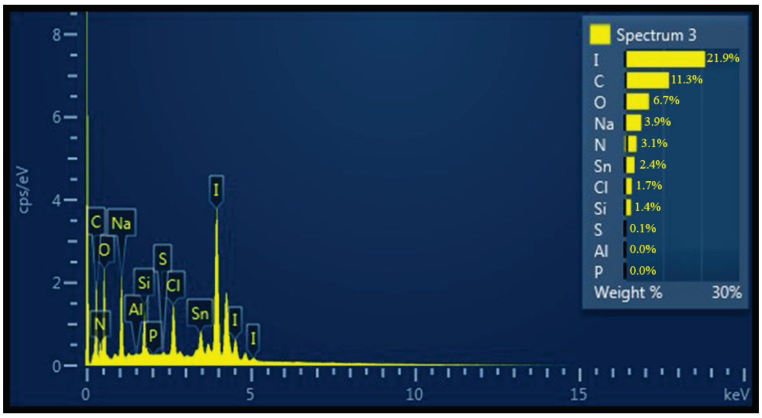

b

Element	Line type	Apparent Concentration	k Ratio	Wt%	Wt% Sigma
C	K series	3.44	0.03435	11.55	0.23
O	K series	4.93	0.01657	6.24	0.12
P	K series	-0.02	-0.00012	-0.02	0.02
N	K series	3.55	0.00631	3.03	0.55
Sn	K series	2.15	0.02149	2.52	0.07
Na	L series	2.92	0.01232	4.28	0.06
Al	M series	0.03	0.00024	0.05	0.02
Si	K series	1.17	0.00930	1.55	0.03
S	K series	0.08	0.00065	0.08	0.02
Cl	L series	1.67	0.01459	1.76	0.03
I	M series	17.44	0.17440	21.06	0.14
Total			52.12		

Table 2.3 – Elemental analysis of the flakes formed by reaction $MASnI_3$ powder with cell culture medium (DMEM). a) The elemental composition of the solid decomposition by products of the $MASnI_3$ dispersed in cell culture medium were analyzed by Energy dispersive X-ray spectroscopy (EDX); (b) The elemental analysis revealed that the precipitate contains significant amounts of Sn, Ca and P. The yellow/white solid precipitate is presumably a mixture of lead (II) hydroxide, lead (II) carbonate, and lead (II) phosphate compounds, which were formed by the reaction of Pb^{2+} with the carbonate, phosphate and hydroxide anions of the cell culture media. Note that the toxicity effect of this solid precipitate is out of the scope of the present study.

sequently, we targeted concentrations of $50, 100\ and\ 200\ \mu g/ml$ of $MAPbI_3$ and $MASnI_3$, which were administrated to cell cultures on time scales extended to a few days. For simplicity, the nominal $MAPbI_3$ concentration is used on the histograms and figures.

The recorded concentration value of lead, tin and iodine in the filtered solutions were subtracted from the initial concentration before filtration using Table 2.1. For example, a $MAPbI_3$ solution of 100 $\mu g/ml$ before filtration contains 33.42 $\mu g/ml$ of Pb. The filtered solution

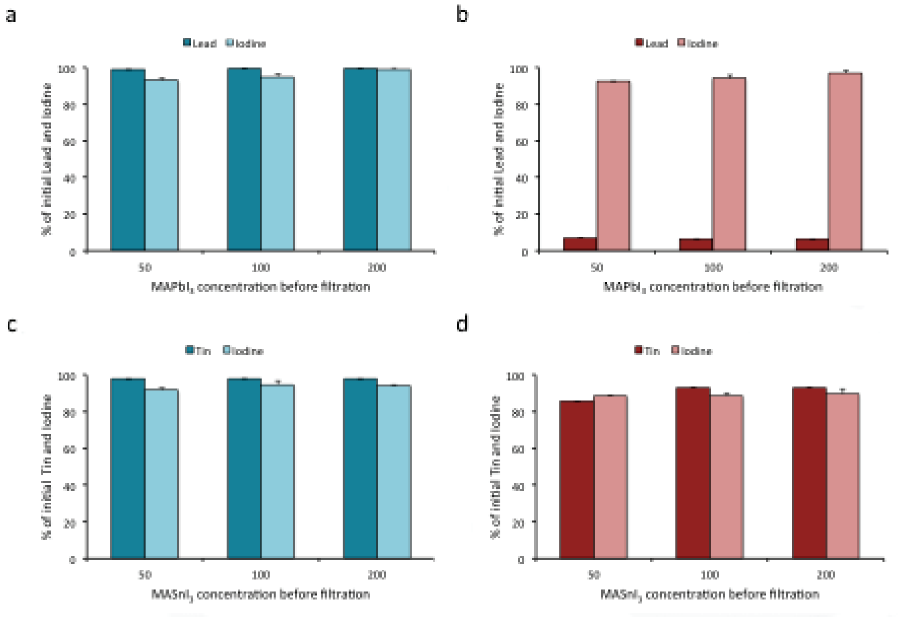

Figure 2.4 – The elemental analysis of the $MAPbI_3$ and $MASnI_3$ solutions after one week incubation at RT and filtration at 220 nm. Concentration levels of lead and iodine in the $MAPbI_3$ solution in water (a) and in the DMEM cell culture medium (b); and the concentration levels of the $MASnI_3$ solution in water (c) and in the DMEM cell culture medium (d). All the histograms show an average of 3 independent repeats. Bars are means +/- S.D.

analysed by ICP-OES contains only 2.07 $\mu g/ml$ of lead; which means 6.19% of the initial lead passes through the filter and is detected. This analysis was done for iodine, tin and lead at different concentrations. As seen in Figure 2.4 a and c, when the buffer is water, both perovskite solutions contain between 80 and 90% of the initial metals in the filtrate. However, more than 90% of the initial iodine and 6% of the initial lead are recovered in the filtered cell culture medium (Figure 2.4 b). Methylamine is known to be soluble[181] in a water-rich environment and cannot be quantified using elemental analysis due to the presence of carbon, hydrogen and nitrogen, which are light elements. This result is in accordance with the precipitate analysis by EDS in section 2.4.1, where the precipitate was found to be mainly composed of Pb complexes. The solution of $MASnI_3$ in the cell culture medium shows a higher content of tin and iodine when filtered (Figure 2.4 d). The quantification of both elements by ICP-OES in the filtered DMEM is similar to the initial concentration before filtration. This result suggests that the flake precipitate observed in (Figure 2.3 e) contains only a little amount of tin compounds as well.

pH assessment

Most mammalian cell lines grow well in media at a pH between 7 and 7.8, depending on the cell type, and physiological pH is critical for cellular function. Aside from the protondriven membrane transporters in cellular membranes and organelles, proper protein and lipid interactions are dependent upon the available charges of the cytosolic atoms and molecules. The pH in a cell culture can deviate from the optimum ranges in static cultures inside the incubator because of the build-up of acidic metabolic metabolites by cultures that have grown too dense or too long in the same medium. Generally, cell culture media are formulated for a specific CO_2 gas level in the incubator (5% or more), but the ambient atmosphere is far lower in CO_2 (less than 1%). This leaves cultured cells in carbonic-based buffered media exposed to pH changes during cell handling ambient conditions. If the pH varies significantly ($pH<6.6$ or $pH>8.3$), the acidic and alkaline environments become toxic to the cells and unbalance growth.[59] When conducting in vitro toxicity studies, it is very important to determine whether the studied material influences the pH of the solution where the biological model is being cultured. In this study, pH was probed in the solution where a maximum dose was administered to the cells (200 $\mu g/ml$). The results in different cell culture media are reported in Table 2.4.

	Media only	Media + $MAPbI_3$ (200 $\mu g/ml$)	Media + $MASnI_3$ (200 $\mu g/ml$)
DMEM	7.31	7.53	7.45
DMEM;F12	7.69	7.85	7.72
Neuronal primary culture medium	7.46	7.48	7.51

Table 2.4 – pH of the $MAPbI_3$ and $MASnI_3$ solutions in cell culture media.

The cell culture media used in this study have a pH between 7.3 and 7.7. When $MAPbI_3$ and $MASnI_3$ perovskites were added, very little change was observed. Overall, the pH remains in a physiological range after administration of the perovskites.

2.5 Conclusions on the chemical characterization of $MAPbI_3$ and $MASnI_3$

The perovskites used in this study are powder-like and polycrystalline. Size and shape do not matter in toxicity assessment, since the material is soluble in both water and physiological media. The results of our characterization confirm the instability of the perovskite in an aqueous environment. In water, the starting material degrades very fast and in less than one week the solution becomes transparent. After filtration, analytical chemistry revealed that almost 100% of the initial content of iodine and lead remain in the filtrate. We assume that the material is completely water-soluble. When a cell culture medium was used as a buffer, a precipitate was observed even after a long soaking period: a solid white precipitate in the $MAPbI_3$ solution and opaque flakes in the $MASnI_3$ solution. Elemental analysis showed the presence of metal ions in both precipitates but in much lower concentration for Sn. Consequently, in the filtered solution the concentration of Pb ions was much lower than that of Sn. The marked differences in the behavior of $MAPbI_3$ and $MASnI_3$ in water and cell culture media clearly demonstrate that the physico-chemical properties of these materials and their potential environmental impact can be modulated through different parameters (temperature, pH and chemical environment dependent equilibrium of soluble and solid forms). For this reason, the toxic properties of not only the filtered solutions but also the powder-like material were evaluated on human lung epithelial cells (A549), and neuronal cells (SH-SY5Y, and murine primary hippocampal neurons). The effects of $MAPbI_3$ and $MASnI_3$ exposure were measured using flow cytometry, fluorogenic and colorimetric assays, immunocytochemistry (ICC) and transmission electron microscopy (TEM). The combination and complementarity of these assays made it possible to assess the effect of the photovoltaic perovskites on cellular properties, metabolic activity, morphology and viability. Interestingly, the two cell types (brain and lung) responded in radically different ways to exposure to the perovskites. The details of these observations are discussed in the next chapter.

3

In vitro toxicity of the photovoltaic halide perovskites

Chemical characterization is a very important step in the study of potential toxicity of any material of interest. The previous chapter discussed the solubility of the organometallic perovskites in aqueous environments and in physiological solutions. This instability already indicates that cells are exposed to the hydrated ions or the precipitate. I have shown that the methyl ammonium lead halide, $CH_3NH_3PbI_3$ (hereafter $MAPbI_3$) and methyl ammonium tin halide or $CH_3NH_3SnI_3$ (hereafter $MASnI_3$) are completely dissolved in water while in physiological solution an important part of the metallic ions form precipitates mainly composed of carbonate, hydroxide and phosphate. In this chapter, we address the consequences of exposure of cell cultures to the filtered solution and to the formed precipitate of the two perovskites. We also report on time- and dose-dependent cytotoxicity and on the cell-type dependent responses. The choice of cellular models was done by taking into consideration the following properties of accidental inhalation: $MAPbI_3$ and/or $MASnI_3$ may start a dissolution process inside the nasal mucosa and penetrate the brain through the olfactory nerves. Furthermore, airborne particles of the perovskites follow the respiratory path and deposit on the epithelium. For this reason, the *in vitro* toxicity studies of the photovoltaic perovskites $MAPbI_3$ and $MASnI_3$ focused mainly on two human cell lines: neuroblastoma cells (SH-SY5Y) and lung mesothelioma cells (A549). It should be noted that the assays reported in this section were conducted on cell lines derived from cancerous cells that can divide indefinitely. These cytotoxic tests represent good models for initial studies aimed at understanding the mechanisms of action of the perovskite compounds after accidental inhalation.

3.1 Cellular effect of MAPbI$_3$ and MASnI$_3$

Our first approach towards assessing the toxicity of perovskites consisted in observing SH-SY5Y and A549 cells upon exposure to perovskites using bright field microscopy, and the compounds induced serious damages to the cells. Next, we exposed cells to the precipitates or to the filtered solution only. In this section, we explain how the material is likely to reach the targeted cellular models used for this study, and we show the results of our observations.

3.1.1 The precipitate

In the scenario where the photovoltaic perovskite airborne particles are inhaled, body fluids in the respiratory pathways degrade the material. The formed precipitate may reach the alveoli and deposit on the epithelial layer and is not likely to penetrate the brain. To mimic such a scenario *in vitro*, perovskite powder was incubated during 5 days with cell culture medium and the formed precipitate was left for sedimentation overnight, the medium was then aspired and replaced with 50% methanol in water. The precipitate was lyophilized overnight in vials capped with perforated parafilm. The obtained powder was then administered to the epithelial lung cells at 50, 100 and 200 $\mu g/ml$. The dose response of cellular exposure to the precipitated perovskites was evaluated using bright field microscopy after 3 days (Figure 3.1).

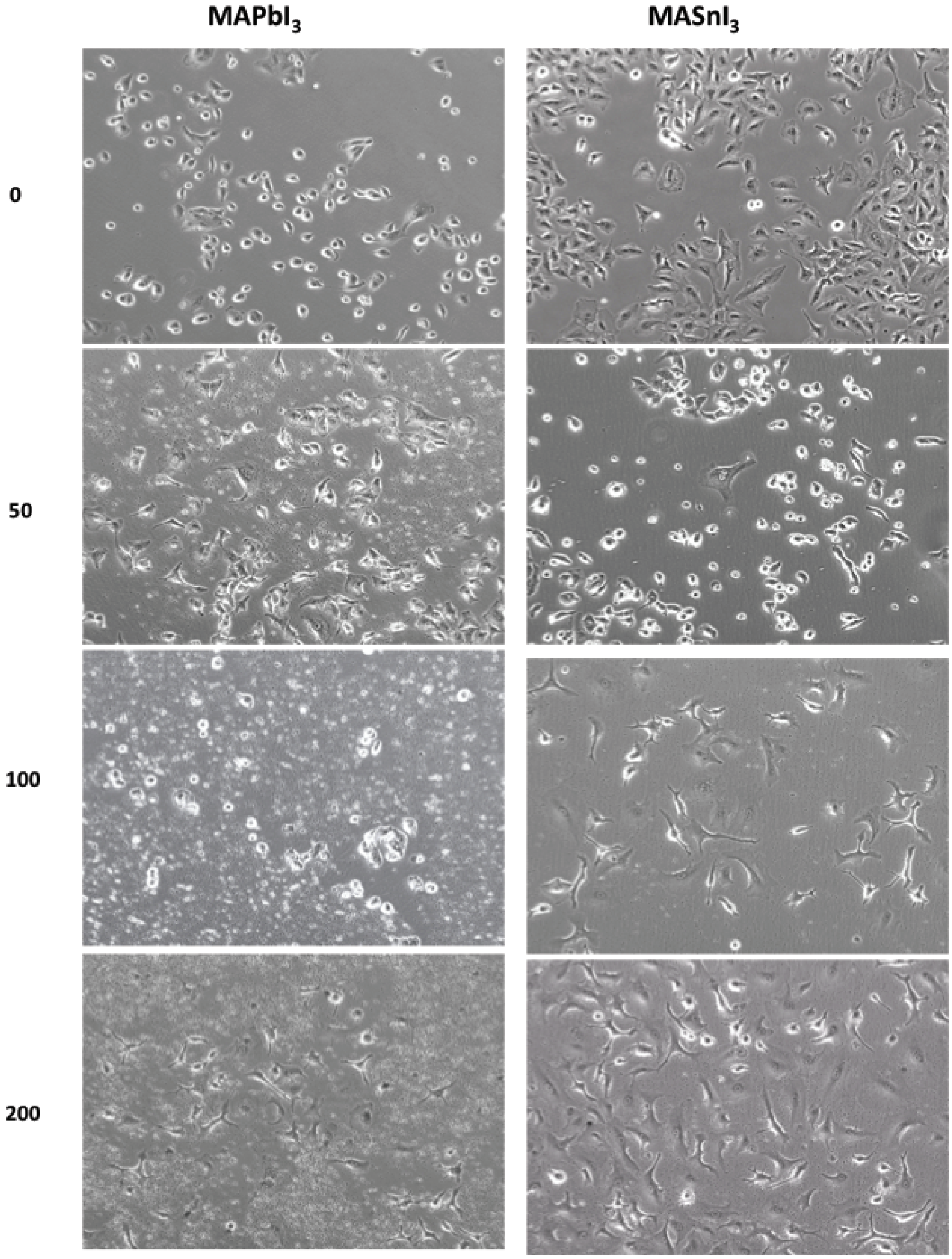

Figure 3.1 – Bright field microscopy images of A549 lung cells following exposure to increasing concentrations of the precipitate of $MAPbI_3$ and $MASnI_3$ after 3 days.

Morphology of the human lung epithelial A549 cells is affected over the treatment with

$MAPbI_3$ and $MASnI_3$, some cells become giant and polynucleated within 3 days of exposure, and their number has not changed much. This observation is emphasized when the dose is increased. It has to be mentioned that the human neuroblastoma SH-SY5Y cells were not treated by the precipitates insoluble compounds can neither reach the brain *via* the olfactory system located in the nose, nor cross the blood-brain-barrier after deposition in the lungs, therefore neurons are unlikely to be directly exposed to the insoluble perovskite precipitates.

3.1.2 The filtered solution

The soluble part of the material, which stays in ionic form, is likely to reach the brain through the olfactory system. In the same way, particles may also reach the lungs where chemical dissolution can happen in the pleural mucus. This scenario was mimicked *in vitro* by exposing human SH-SY5Y and A549 cell lines to the filtered solutions of $MAPbI_3$ or $MASnI_3$ (shown in appendix C). Bright field images of the cells (Figure 3.2) showed the same effects observed for A549 cells exposed to the precipitates (Sub-section 2.4.1): The morphology was heavily affected by the exposure, some cells become giant and display more than one nucleus, and their confluence slightly decreased after 5 days. On the other hand, SH-SY5Y cells suffer the treatment in a different way: cells tend to shrink and float following the exposure. These observations are clearly more pronounced with an increasing concentration.The next step consisted in quantifying living cells. To do so, we used a counting Neubauer chamber (see details in appendix C) and the results are plotted as a percentage of total non-treated cells in Figure 3.3.

After 5 days of culture, the non-treated A549 cells reached confluency whereas the density of cells exposed to $MAPbl_3$ or $MASnI_3$ decreased significantly in a dose-dependent manner (Figure 3.3). For example, exposure at 100 $\mu g/ml$ of $MAPbI_3$ induced a decrease of over 80% in viable SH-SY5Y cells, and around 60% in A549 cells. The confluence decrease is more striking in the neuronal cell line, and stronger when cells are exposed to $MASnI_3$ perovskite.

As exposure of the cell lines to perovskites (either the precipitates or the filtered solution) results in major changes in morphology and confluence, we sought to investigate the integrity of the plasma membrane after treatment to understand the cellular response.

3.2 Cell membrane disruption

The cell membrane is a phospholipid bilayer with embedded proteins that separates the internal from external environments of the cell. It is mainly involved in protecting the cell from the surroundings but also in adhesion, cell signaling, controlling the ionic and molecular

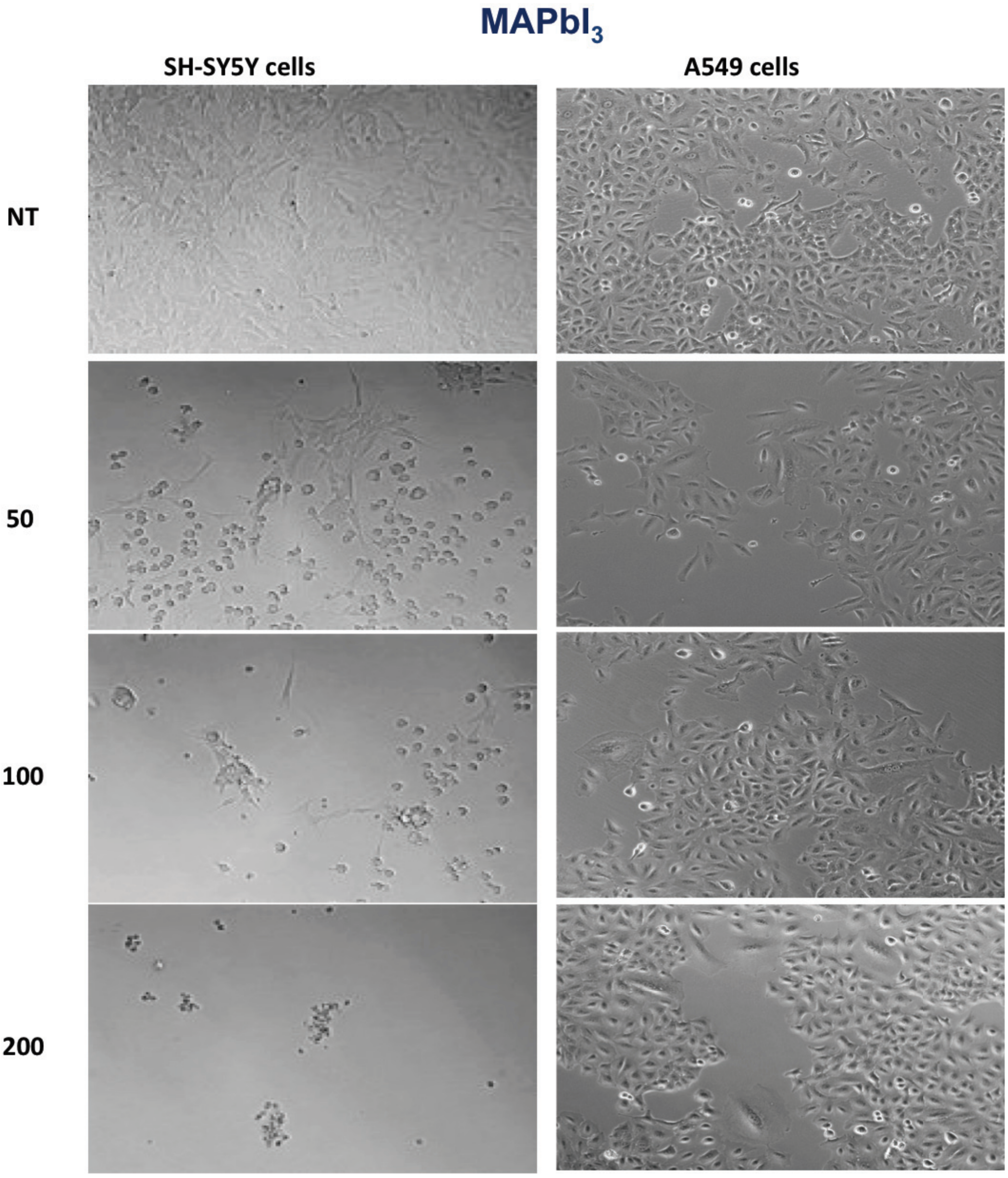

Figure 3.2 – Bright field images of SH-SY5Y neuroblastoma cells and A549 lung epithelial cells exposed to $MAPbI_3$ filtered solution during 5 days.

traffic and many other processes. An external cellular stress may result in damage to the cell membrane. Full function may return to cells but in some cases a degree of injury will remain. Depending on the extent of injury, the cellular response may be adaptive, and where possible, homeostasis is restored. Electrolyte balance is highly regulated by the cell membrane and serious disturbances may lead to severe adverse effects. Cell death occurs when the severity of the injury exceeds the cell's ability to repair itself.[22]

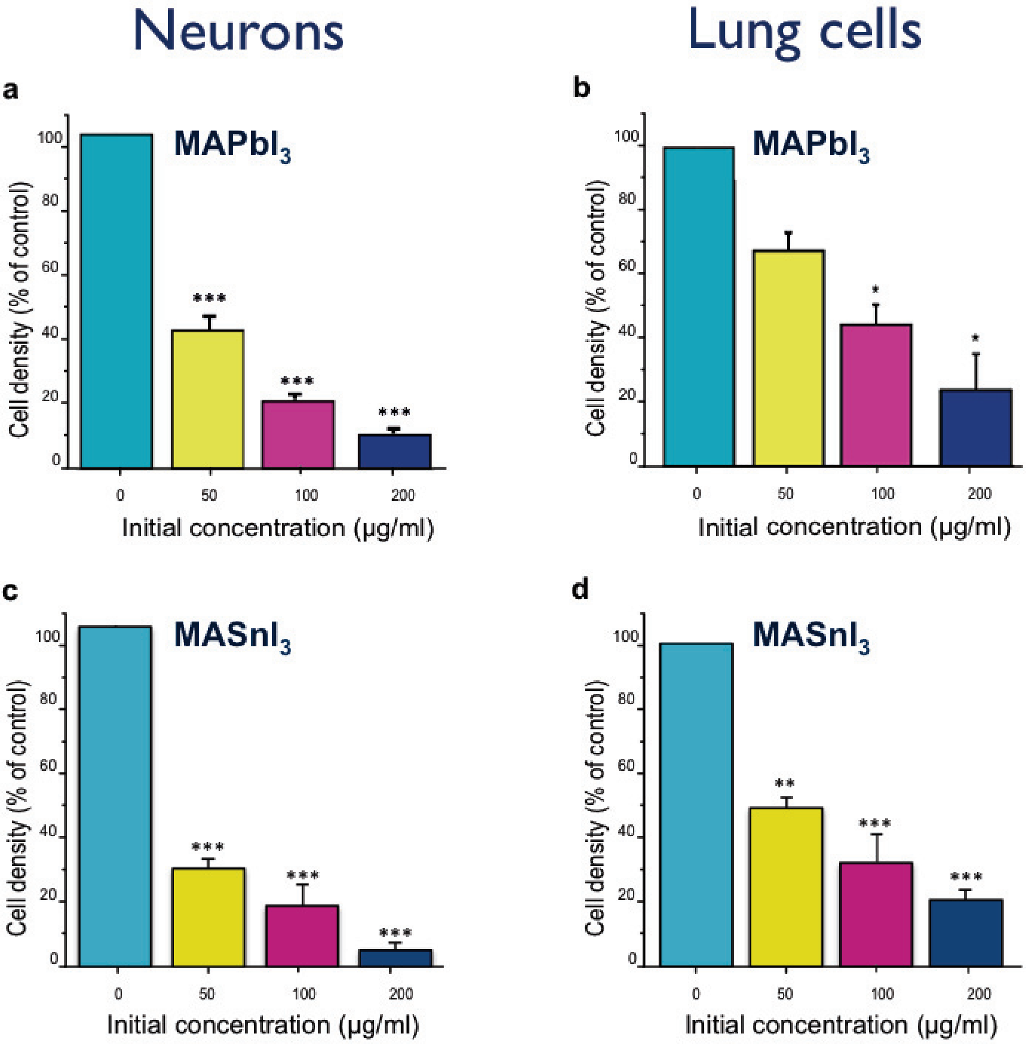

Figure 3.3 – Quantification of living cells upon exposure to $MAPbI_3$ and $MASnI_3$ filtered solutions in SH-SY5Y neuroblastoma cells (a, c), and in A549 lung epithelial cells (b, d). All the histograms show an average of at least 3 independent repeats (each condition in triplicate). Bars are means ± S.D. One-way ANOVA test followed by a Tukey-Kramer post-hoc test were performed (non-treated vs. $MAPbI_3$ or $MASnI_3$ treated conditions), *p<0.01, **p<0.005, ***p<0.0005.

In this section, we present the assessment of cell membrane state upon exposure of cells to the photovoltaic $MAPbI_3$ and $MASnI_3$ filtered solutions. We evaluated the time and concentration dependent effects on the cell membrane by dye exclusion method using Sytox green (SG, a specific fluorescent marker that penetrate the cells when the plasma membrane is disrupted) and flow cytometry. Flow cytometry is a high-throughput analysis technique used in cell counting, cell sorting and markers detection. Flow cytometers are able to analyze several thousand particles (in this study, cells) every second, and can actively separate and isolate particles having specified properties. The cell suspension is sucked by a syringe into a sheath stream carrying and aligning single cells through the light beam for sensing (generally lasers at different wavelengths). A detector converts not only analogue measurements of forward-scattered light (FSC) and side-scattered light (SSC) –which inform about the size and granularity– but also the dye-specific fluorescence signals into digital signals. The data generated by flow cytometers can be plotted in one dimension (histograms of fluorescence of specific markers), or in two-dimensional dot plots or even in three-dimensions. The regions in the plots can be sequentially separated based on the fluorescence intensity, the FSC and the SSC, by creating subsets called "gates". In our study, the precipitate of the material in solution represented an artifact in data analysis because the deposited particles were counted and sorted in the flow as cells. Since the precipitate of the material produces the same effect on epithelial cells as the filtered solution, only the latter one was considered in further analysis to avoid false positive or negative counts and contamination.

3.2.1 Methodology of membrane integrity assessment

SH-SY5Y cells and A549 cells were plated in 24 well plate. The following day, the original culture medium was removed from the cells and replaced by medium spiked with increasing concentrations of $MAPbI_3$ or $MASnI_3$ (50, 100 and 200 $\mu g/ml$). After 1, 3, 5 or 7 days of exposure, cell death was quantified using the vital dye Sytox Green (SG), which only penetrates in cells with damaged plasma membrane. The supernatant and adherent cells were collected at each indicated time point. After 5 min of centrifugation at 250 g, cells were re-suspended in PBS containing SG at a final concentration of 330 nM. Cells were then analyzed (20'000 events per condition were counted) by flow cytometry using Accuri C6 (BD Biosciences, Switzerland). SG emission was collected in Fl1 channel and FlowJo software (Treestar, USA) was used for subsequent analysis. Hippocampal primary neurons were plated in 96 well plates. After 2 weeks of culture, the original culture medium was removed from the cells and replaced by medium spiked with increasing concentration of $MAPbI_3$ or $MASnI_3$ (of 50, 100 and 200 $\mu g/ml$). Cell death was quantified as previously described by Mahul-Mellier et al.[19] using the vital dye exclusion method using Sytox Green (SG, Life Technology, Switzerland), a membrane impermeable dye which will enter only in cells with damaged plasma membranes after 3, 10, 17 and 25 days of exposure to perovskite solutions. Briefly neuronal cells were washed three times with PBS before being incubated with SG at a final concentration of 330 nM. After 15 minutes of incubation, cells were washed twice with PBS and fluorescence was quantified by using Tecan infinite M200 Pro plate reader (Tecan, Switzerland) with respective excitation and emission wavelengths of 487 nm and 519 nm.

3.2.2 Results on the membrane disruption of neuronal cells

In this part, the reported histograms show the percentage of SG positive cells being the cells with a damaged plasma membrane. The membrane disruption of SH-SY5Y cells is shown in Figure 3.4 (a, b). The results show a time-and-concentration-dependent toxicity of $MAPbI_3$ and $MASnI_3$. Exposure of SH-SY5Y cell line to $MAPbI_3$ or $MASnI_3$ at a concentration as low as 50 $\mu g/ml$, was sufficient to trigger significant damage to the cell membrane (from 10 to 30% of SG-positive cells in treated conditions) after 7 days, whereas at the highest concentration (200 $\mu g/ml$) of perovskites more than half of the SH-SY5Y cell population suffered the exposure 3 days after incubation with the perovskite solution, and almost all of them did not resist the treatment after 7 days. Once again, the Tin-containing perovskite had a stronger effect than its lead counterpart. To validate our findings we next investigated the effect of perovskites in the differentiated mice hippocampal primary neurons. These neurons have the advantage to spontaneously differentiate in their growth cell culture medium after two weeks in culture[34] allowing long term toxicity studies (up to four weeks). The treatment with perovskites was added to the cell culture medium of the primary hippocampal neurons at various concentrations and up to 25 days. Figure 3.4(c, d) shows that $MAPbI_3$ also induced cell membrane injury in a time- and concentration-dependent manner in these primary cells. The striking effect on neuronal health observed by bright field microscopy and consistently confirmed by SG uptake is subject to viability evaluation. We will cover this part in the next section.

3.2.3 Results on the integrity of lung epithelial cells

Figure 3.4 (e, f) shows the absence of Sytox Green uptake by A549 cells upon perovskites exposure. This result suggests that the plasma membrane integrity of lung epithelial cell line is not compromised over the treatment. Details on flow cytometry dot plots analysis are shown in appendix C.

These studies on plasma membrane show that the response of cells to exposure to perovskites is cell type-dependent. The membrane of neuronal cells (primary neurons or neuroblastoma cells) get damaged, therefore the soluble material can easily penetrate the cells. On the other hand, the membrane of lung cells remains intact, since it is impermeable to SG. Considering the phenotypical changes observed previously, we next sought to explore whether the material is internalized into A549 cells.

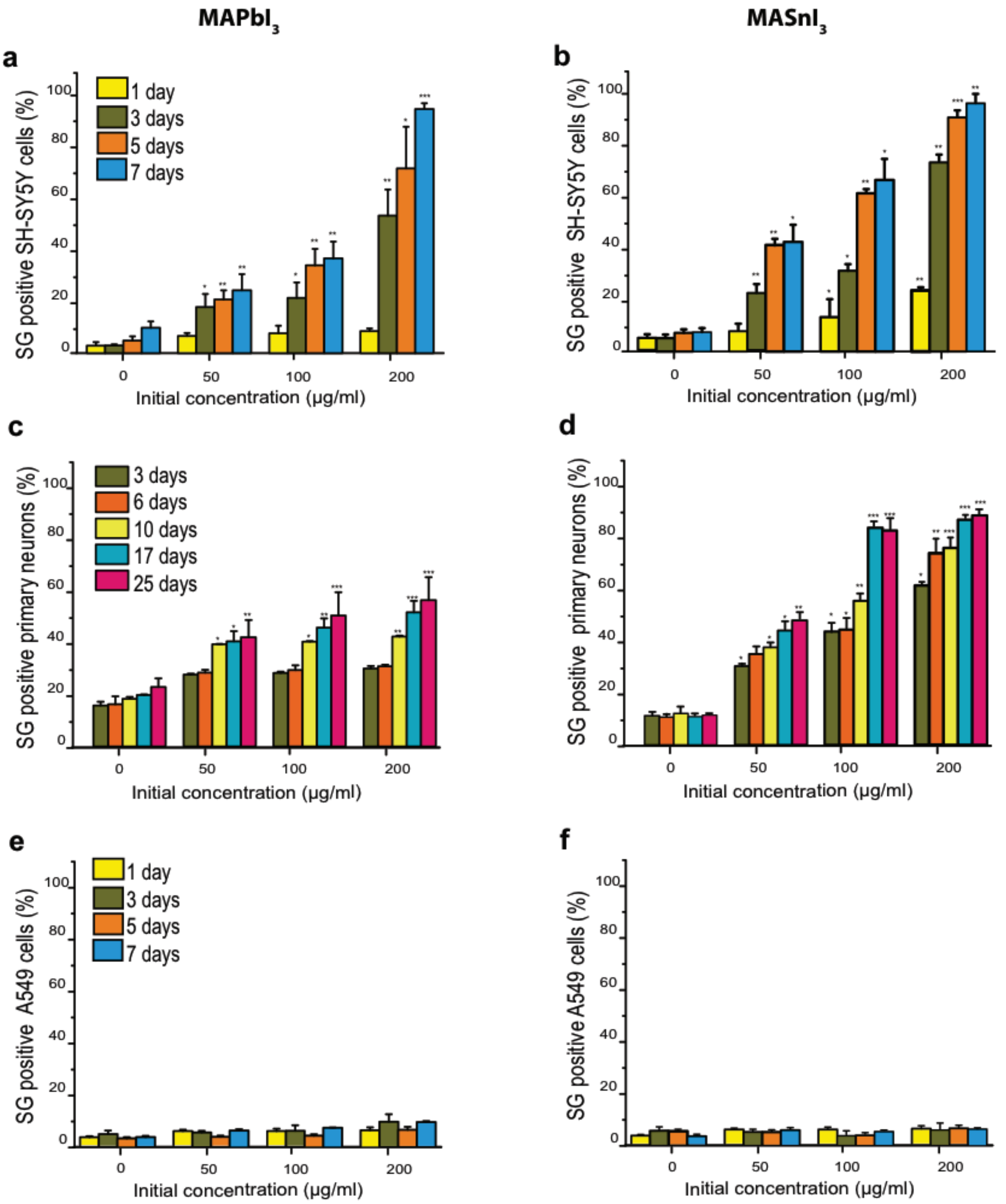

Figure 3.4 – Plasma membrane disruption quantified by Sytox green uptake upon $MAPbI_3$ and $MASnI_3$ treatments. Neuronal cells: Human SH-SY5Y cell line (a, b) and mice primary hippocampal neurons (c, d), and Human lung epithelial cell line (e, f). All the histograms show an average of at least 3 independent repeats (each condition in triplicate). Bars are means ± S.D. One-way ANOVA test followed by a Tukey-Kramer post-hoc test were performed (non-treated vs. $MAPbI_3$ or $MASnI_3$ treated conditions), *p<0.01, **p<0.005, ***p<0.0005.

3.3 Cellular uptake of the perovskites

The dissolved ions, especially Pb^{2+}, can get easily into the cells *via* the calcium channels. These channels have 24 times higher permeability for lead than for calcium ions,[237] and once inside the cytoplasm they can start their deleterious effects. However, if larger ionic complexes are created, or precipitates form, their internalization happens differently. Cells internalize extracellular material by a mechanism called endocytosis. In order to be taken up into cells and subcellular targets, extracellular material must first be able to cross the plasma membrane in the spatio-temporal dimension.

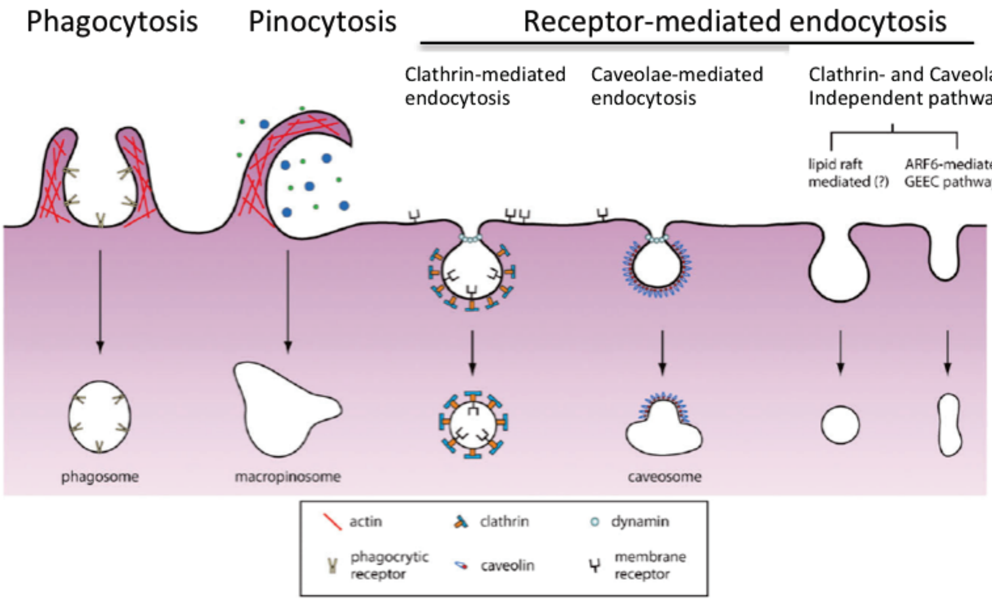

Figure 3.5 – Pathways described by L. T. Chou and colleagues of the cellular uptake regulating the signaling routes and cargo transport. Each pathway is mechanistically distinct and highly regulated at the molecular level.[57] (with permission from the Royal Society of Chemistry).

There is an increasing number of pathways of internalization so far grouped into three main mechanisms (Figure 3.5): 1. Phagocytosis; 2. Pinocytosis and 3. Receptor-mediated endocytosis. Some scientists subdivide the endocytosis pathways into those that are Clathrin-(CLT)-dependent and those that are CLT-independent.[57] For cytotoxicity studies, an understanding of the cellular uptake mechanisms would be crucial to determine how they modulate the signaling pathway and the subsequent molecular response of the cell.[108,114,196,207] CLT-mediated endocytosis is the most understood pathway of receptor-mediated endocytosis. In this pathway, ligand binding triggers the recruitment of receptors to CLT through adaptor proteins. CLT then polymerizes, driving the invagination of the pit, which is eventually released into the cytoplasm through the scission of the enzyme Dynamin (DYN). Therefore, there is the CLT-dependent/DYN-dependent and the CLT-dependent/DYN-independent pathways. The latter is mediated by primary carriers called clathrin-independent carriers (CLICs), which fuse to form tubular early endocytic compartments called Glycosylphosphatidylinositol enriched endosomal compartments (GEECs).[169] This process is highly complex given that more than 50 different proteins can be found in CLT-coated pits.[146,187] On the other hand, many other forms of endocytosis exist, including Caveolae- or lipid-raft dependent endocytosis. Caveloae are a special form of lipid rafts on the plasma membrane of many cell types more specifically in endothelial, epithelial cells and adipocytes. These structures are rich in proteins and lipids and have several functions in signal transduction including endocytosis.[26] Caveolins were shown to form and maintain caveolae and also lead to a local morphological change of the membrane in presence of extracellular material to be internalized.[170] Although various signaling pathways have been identified in external material uptake by cells, we currently understand little about the membrane trafficking principles of endocytic routes. In our cellular models, the uptake of the non-soluble precipitates of the $MAPbI_3$ and $MASnI_3$ perovskites was probed by the inactivation of CLT and DYN by siRNA transfection. We also used a control siRNA of a viral protein (VSVG) which is not expressed in mammalian cells to show that the effect is not induced by the transfection process. In the next subsections, we report the used protocol for such silencing and show how the CLT/DYN-silenced cells interact with $MAPbI_3$ and $MASnI_3$.

3.3.1 Methodology to assess the cellular uptake

A549 cells were plated in 6-well platess at a confluence of 60%. After cellular adherence to the plate's substrate (3-4 hours later), the original culture medium was removed and replaced by a lipofectamine transfection buffer containing the diluted siRNA for CLT, a mix of DYN1/DYN2 (50/50) or VSVG prepared according to the manufacturer's protocol (can be found in appendix C). Cells were incubated at 37°C for two days so that the genes coding for CLT and DYN are silenced, then rinsed three times with PBS before being trypsinized and transferred to 24 well plates, where they were treated with 100 $\mu g/ml$ of $MAPbI_3$ or $MASnI_3$. The treatment was 3 days long. For this reason and to avoid hyper-confluence after treatment, plating was initially performed in 6 well plates, because the total time for cells preparation was 5 days (2 days incubation with siRNA and 3 days of exposure to perovskites). At 3 days post-treatment, the phenotype of cells was verified using bright field microscopy, then gene silencing was verified by immunoblotting against CLT and DYN using Western Blot (WB). Briefly, cells were harvested using trypsin and gently centrifuged before rinsing with cold PBS and re-suspension in the lysis buffer (see protocol of lysis buffer preparation in the appendix C). Cells were incubated on ice for 20 min in a rocking plate, then centrifuged 20 min at 12'000 rpm at 4°C. We quantified the total protein concentration in the supernatant using bicinchoninic acid (BCA) assay and we kept it for WB analysis. (Protocol in the appendix C).

3.3.2 Results of the cellular uptake

To confirm the knockdown of CLT and DYN genes using siRNA transfection, we immunoblotted the cell lysate using antibodies against CLT and DYN proteins. Figure 3.6 shows the corresponding WB where Actin is used as a loading control, and the silencing of CLT (about 150 kDa) and DYN (about 90 kDa) is clearly obvious in both cell lines. No knockdown is seen in the non-transfected (nt) or VSVG (-vsvg) controls.

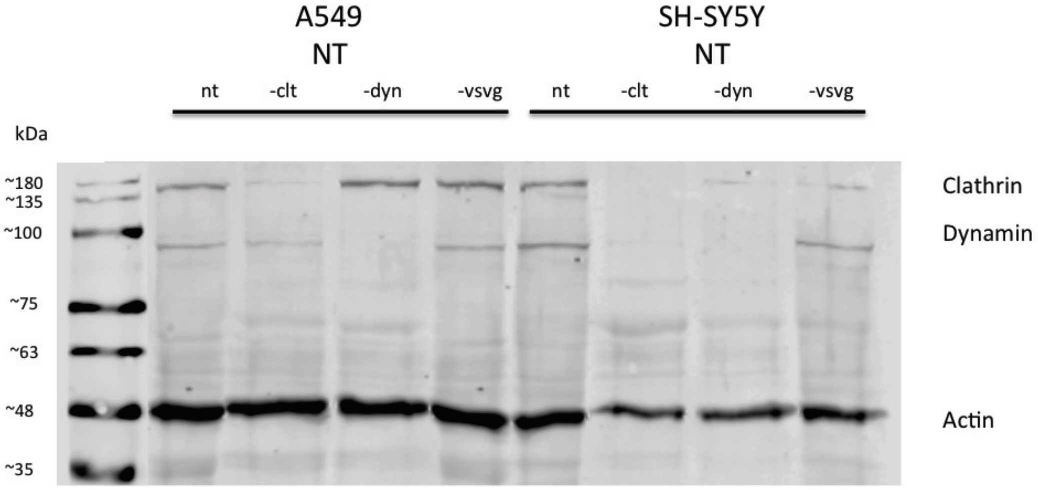

Figure 3.6 – In vitro validation for the CLT/DYN silencing by Western Blot in non-treated (NT) A549 and SH-SY5Y cell lines.

Now that we know that our silencing is efficient, we can see whether DYN or CLT have a role in perovskite uptake. As seen in Figure 3.7, bright field microscopy images distinctly exhibit the A549 cells' phenotype 3 days post treatment with 100 $\mu g/ml$ of $MAPbI_3$ and $MASnI_3$. In the left panels, non-treated cells are shown (labeled NT), whereas cells treated with $MAPbI_3$ are presented in the medium panels, and the ones treated with $MASnI_3$ in the right panels. CLT inactivation (upper row) did not alter the consequences of treatment with perovskites (i.e. giant cell, polynucleation) as compared to the VSVG control. On the other hand, when DYN was silenced (intermediate row), the outcome changed because the cells did not display an increase in size and nuclei number, and seem healthier when treated with the perovskites as compared to CLT-silenced cells.

These findings suggest that DYN might be important for cellular response to perovskite exposure, but also contributes to the cellular uptake of the material because the perovskites did not have an effect on the cells since they could not gain entry due to the silencing of dynamin.

Although subsequent pathways of endocytosis still need to be demonstrated, our data on membrane integrity and endocytosis clearly show that the material is internalized into the neuronal and lung cells. With this finding, we are going now to focus on the cellular and

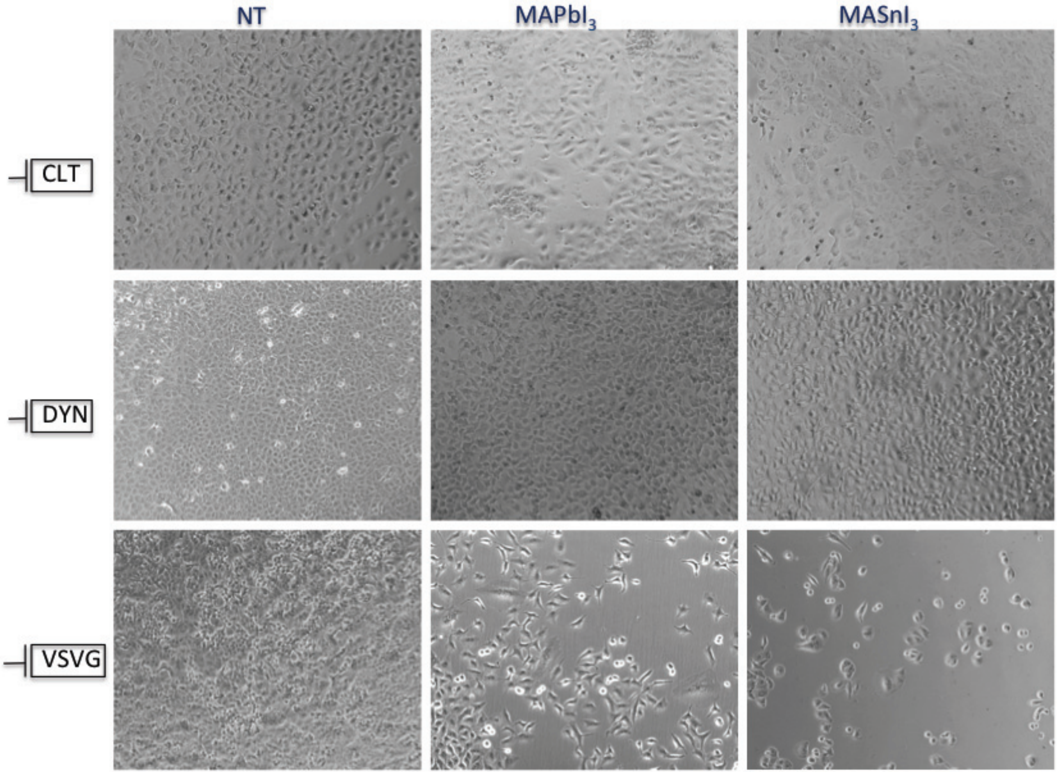

Figure 3.7 – Bright field microscopy images of A549 cells reporting the phenotype after gene silencing by siRNA transfection of Clathrin (CLT), Dynamin I & II (DYN), and a viral protein (VSVG) as a negative control, 3 days post-treatment with $MAPbI_3$ or $MASnI_3$ perovskites.

molecular pathways involved in the phenotypical changes observed previously, starting with cell survival quantification.

3.4 Viability assessment

Several factors from the internal or the external environment called stimuli can trigger cell death. This may be the result of the natural process of old cells being renewed, or may result after an injury, a stress or death of the organism in which the cells are part of. Two types of cell death are indexed: Programmed cell death (PCD), including apoptosis, necroptosis and autophagy, and non-physiological cell death, including necrosis and mitotic catastrophe.[84, 167] The effects observed on our cellular models, especially neuronal cells, led us to investigate whether cell demise occurs upon treatment with perovskites and which subcellular and molecular pathways are involved. Our strategy included the use of flow cytometry by dye exclusion method to detect the apoptosis precursors: the caspase family. Caspases are protease enzymes playing essential role in PCD (Figure 3.8).

Caspases activation means that cell death is programmed and apoptosis-like. Technical

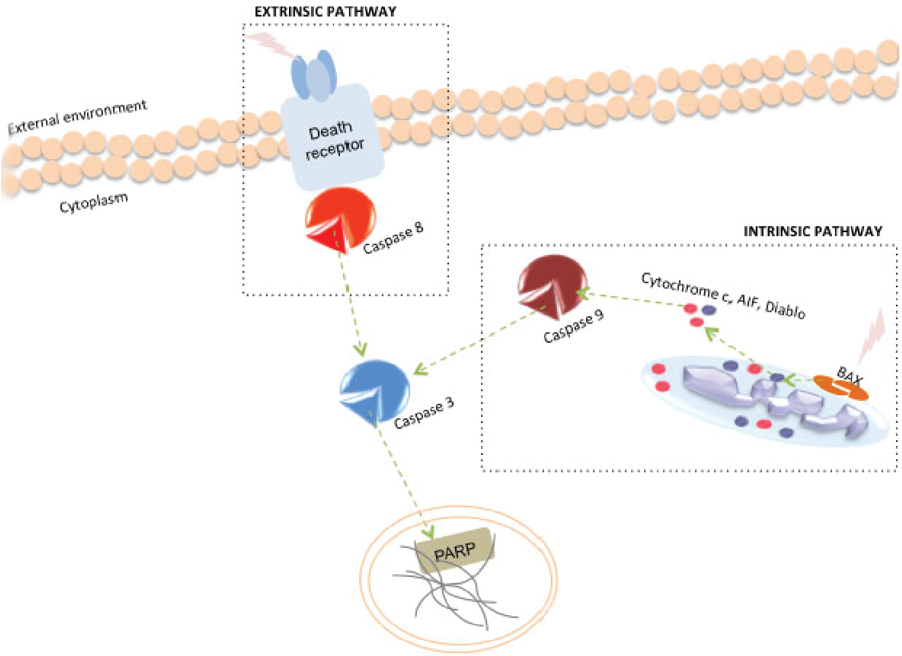

Figure 3.8 – Simplified illustration of the caspase family cascade inducing programmed cell death *via* the extrinsic and the intrinsic pathways. In summary, when an external stress is sensed by the "death receptors" on the plasma membrane (such as TNFR1, TRAIL etc.), caspase 8 is recruited and activates caspase 3. The latter stimulates nuclear enzymes (ICAD, PARP and helicases) to start the degradation of DNA and to launch apoptosis process. In the case of internal stress signals (oxidative stress, ischemia etc.), the mitochondrial receptors (BAX, tBid, Bak...) are stimulated and release pro-apoptotic factors that activate caspase 9. The latter induces the activation of caspase 3 which initiates apoptosis.[78]

details are provided in the following sub-section, and the analysis method consisted in double plotting the histograms of fluorescence of Propidium iodide (PI), a vital dye, with the one of the caspase-fluorescein. This double plot is then divided into 4 regions (Figure 3.9): Caspase-negative and PI-negative cells are considered as healthy; Caspase-positive and PI-positive cells are considered as apoptotic cells; Caspase-negative and PI-positive cells are considered as necrotic cells, Caspase-positive and PI-negative cells represent the cells that undergo PCD.

3.4.1 Methodology of the viability tests

SH-SY5Y cells and A549 cells were plated in 24 well plates. The following day, the original culturing medium was removed from the cells and replaced by medium spiked with increasing concentrations of $MAPbI_3$ or $MASnI_3$ (50, 100 and 200 $\mu g/ml$). Caspases activity in living cells was quantified using CaspaTagTM fluorescein caspase 3, 8 or 9 activities kit (Enzo life sciences, Switzerland). These fluorogenic kits used specific Fluorochromes peptide Inhibitors of Caspases (FLICA). These probes passively enter the cells and bind irreversibly to the active caspases. After 5 days of exposure to perovskite solution, SH-SY5Y and A549 cells were har-

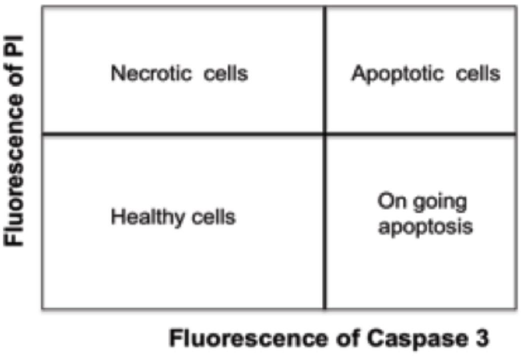

Figure 3.9 – Schematic illustration of the dot plot of Propidium iodide vs. caspase 3 obtained by flow cytometry. The non-fluorescent cells are considered as healthy; the caspase-positive cells (two quadrants in the right position) represent cells undergoing apoptosis-like cell death; and the PI-positive caspase-negative cells (upper quadrant in the left position) are dead cells with necrosis.

vested and incubated for one hour at 37°C with FAM-DEVD-FMK (caspase 3), FAM-LETD-FMK (caspase 8) or FAM-LEHD-FMK (caspase 9) and with the vital dye Propidium Iodide (PI) in accordance with the supplier's instructions. Fluorescein emission was analyzed by flow cytometry [Accuri C6 (BD Biosciences)] in Fl1 channel and PI emission was collected in Fl3 channel. FlowJo software was used for subsequent analysis. For hippocampal primary neurons, cells were plated in 96 well plates. After two weeks of growth, the original culture medium was removed from the cells and replaced by medium spiked with increasing concentrations of $MAPbI_3$ or $MASnI_3$ (50, 100 and 200 $\mu g/ml$). Neurons were washed 3 times with PBS and incubated for 30 minutes at 37°C with FAM-DEVD-FMK (caspase 3), FAM-LETD-fmk (caspase 8) or FAM-LEHD-fmk (caspase 9) in accordance with the supplier's instructions. Fluorescein emission was quantified by using Tecan infinite M200 Pro plate reader (Tecan, Switzerland) with respective excitation and emission wavelength of 487 nm and 519 nm.

3.4.2 Results of neuronal cells survival when exposed to perovskites

We sought to investigate the molecular mechanisms by which the perovskite-filtered solutions induced death in our cellular models. Using fluorogenic assays combined with flow cytometry, we observed that caspase 3, a key enzyme involved in the execution phase of apoptosis, was significantly activated in SH-SY5Y cells exposed for 5 days to $MAPbI_3$ (Figure 3.10 a, green bars) and $MASnI_3$ (Figure 3.10b., green bars). In order to elucidate the $MAPbI_3$-mediated apoptotic pathways, we monitored the activation of the caspase 8, a key initiator caspase activated by the extrinsic/death receptors pathway, and the caspase 9, a key initiator caspase activated by the intrinsic/mitochondrial pathway. The blue bars in Figure 3.9 a, b, show a concentration-dependent caspase 9 activation in SH-SY5Y cells treated for 5 days with $MAPbI_3$ or $MASnI_3$. No increase in caspase 8 activity was observed under the same conditions (Figure 3.9 a, b, red bars). This finding suggests that apoptosis in SH-SY5Y cells is triggered through the mitochondrial pathway. These quantifications were made through the analysis and double gating of the dot plots shown in Figure 3.11.

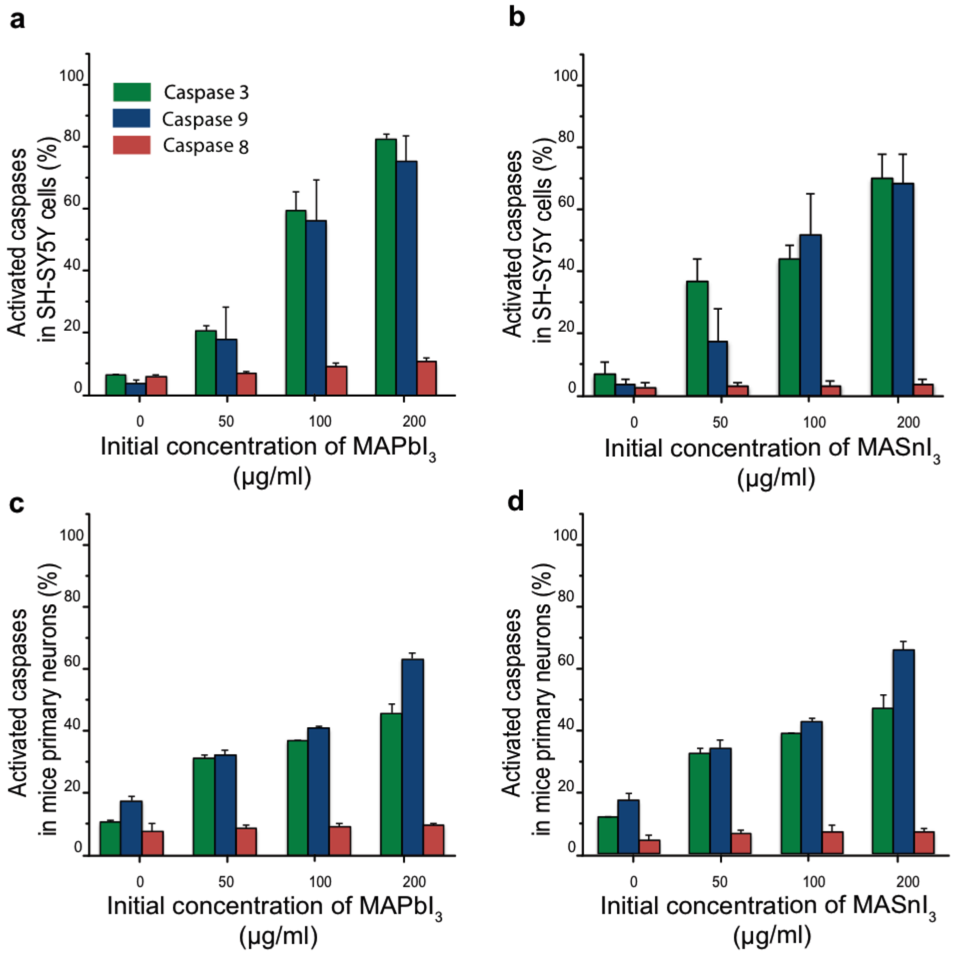

Figure 3.10 – $MAPbI_3$ and $MASnI_3$ induce intrinsic apoptosis neuronal cells. The cells were plated in 24 well and treated with increasing concentrations of perovskite solutions (50, 100 and 200 $\mu g/ml$), and cell death was quantified by flow cytometry using fluorogenic assays. The apoptotic pathways activated by the perovskite solutions were identified by measuring the caspase 3, caspase 9 and caspase 8 activities after 5 days of treatment; in human SH-SY5Y cell line (a, b) and in mice primary hippocampal neurons (c, d). All the histograms show an average of at least 3 independent repeats (each condition in triplicate). Bars are means ± S.D. One-way ANOVA test followed by a Tukey-Kramer post-hoc test were performed (non-treated vs. $MAPbI_3$ or $MASnI_3$ treated conditions), *p<0.01, **p<0.005, ***p<0.0005.

The specific activation of the caspase 3 (Green bars) and the caspase 9 (Blue bars) together with the absence of caspase 8 (Red bars) in Figure 3.10 c, also confirmed the initiation of the intrinsic apoptotic pathway in the differentiated hippocampal primary neurons, when exposed to the solution of the photovoltaic perovskites, as already monitored in SH-SY5Y cells. The dot plots in Figure 3.11show the fluorescence of FLICA-Caspase 3 and propidium iodide in SH-S5Y5 cells exposed to $MAPbI_3$ using flow cytometry. The dot plots are divided into 4 quadrants (Q1, Q2, Q3 and Q4) that show the respective distribution expressed as a percentage of the healthy cells [negative for PI and for caspase 3 activity (Q4)], the cells undergoing apoptosis but not yet dead [negative for PI but showing caspase 3 activity (Q3)], the apoptotic dead cells [positive for PI and for caspase 3 activity (Q2)] or the necrotic dead cells [positive for PI but negative for caspase 3 activity (Q1)]. The overall meaning of these plots confirms that necrotic cell death was not induced in SH-S5Y5 cells when exposed to perovskite. Under these conditions, the cells died *via* apoptotic signaling pathways. We have obtained the same result upon $MASnI_3$ treatment.

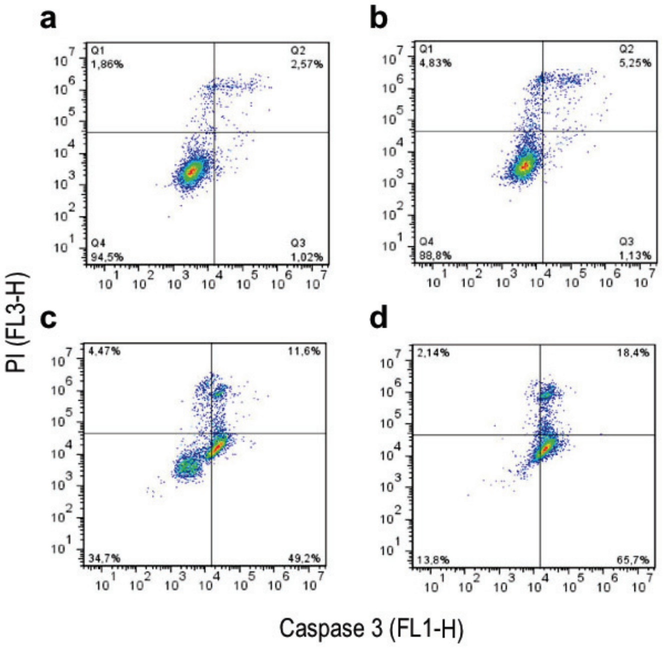

Figure 3.11 – Two-dimensional flow cytometry dot plots (Propidium iodide and Caspase 3) of the SH-SY5Y cell line. a) Non-treated (negative control) cells; or cells exposed to $MAPbI_3$ at b) 50 $\mu g/ml$, c) 100 $\mu g/ml$, and d) 200 $\mu g/ml$. $MAPbI_3$ does not induce necrotic cell death in SH-S5Y5 or in A549 cells.

3.4.3 Results of lung cells survival when exposed to perovskites

Exposure of A549 cell line to $MAPbI_3$ and $MASnI_3$ perovskite filtered solutions did not activate the caspases cascade (Figure 3.12). This result suggests that PCD is not initiated upon perovskite treatment, which is consistent with the bright field images that did not show visible toxicity and with the absence of SG uptake reported in section 3.1.2, which shows that the plasma membrane of A549 cells is not compromised over treatment with the filtered solution of perovskites. These results were extracted from the double gating in dot plots shown in Figure 3.13, that also shows the absence of death by necrosis following exposure to perovskites. The phenotypical changes observed using bright field microscopy in subsection 3.1.2 were then quantified to estimate the consequence of the exposure.

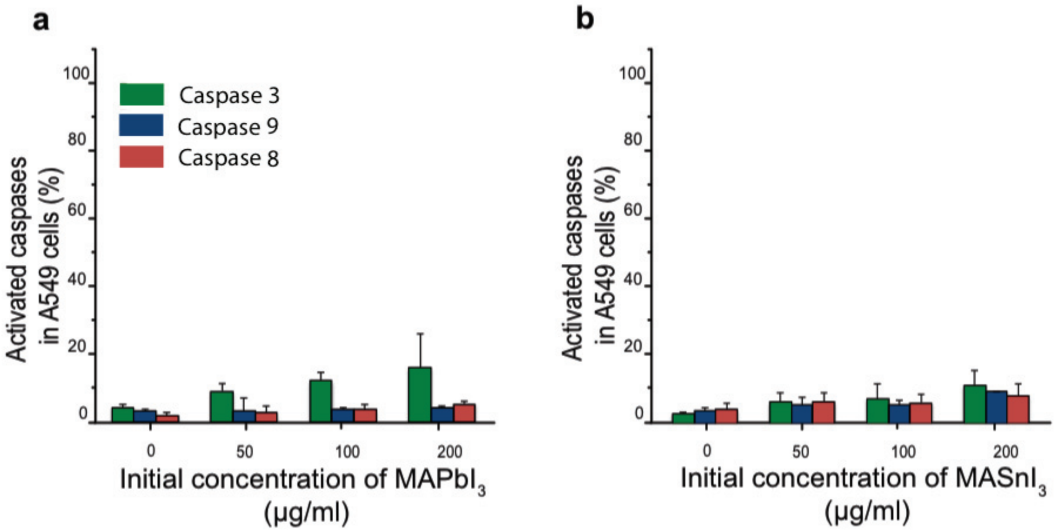

Figure 3.12 – $MAPbI_3$ and $MASnI_3$ do not induce cell demise by apoptosis in A549 human lung epithelial cells. The cells were treated with increasing concentrations of $MAPbI_3$ or $MASnI_3$ (50, 100 and 200 $\mu g/ml$) and the cellular toxicity was evaluated using flow cytometry (a). A549 cells were harvested after 1, 3, 5 or 7 days post-treatment and stained with SG. Cell death level is expressed as the percentage of cells with compromised cell membrane (SG positive cells) to the total cell number (b) A549 cells were harvested 5 days post-treatment and caspase 3 (green), caspase 9 (blue) and caspase 8 (red) activities were measured using fluorogenic assays. All the histograms show an average of at least 3 independent repeats (each condition in triplicate). No significance was observed.

3.4.4 Quantification of the morphological changes

To quantify the morphological changes induced by $MAPbI_3$ or $MASnI_3$ treatment, A549 cells were plated in 24-well plates. The following day, the original culture medium was removed from the cells and replaced by medium spiked with increasing concentrations of $MAPbI_3$ or $MASnI_3$ (50, 100 and 200 $\mu g/ml$) during 5 days. A549 cells were imaged using an EVOS bright field microscope (Life Technologies). The respective sizes and shapes of the cells were analyzed using FIJI[186] software (NIH, Bethesda, MD, USA).

Interestingly, imaging by bright field optical microscopy (Figure 3.14 a) revealed a heterogeneous population of cells with different morphologies. The non-treated cells exhibited a homogeneous triangle-shape with an average size ranging from 15 to 20 μm, typical of epithelial cells. After 5 days of exposure to MAPbl3, we observed different populations in terms of morphology (Figure 3.14): the overall size of some cells significantly increased ("giant cells", $size > 50\ \mu m$) with a round-shaped aspect. Some cells were stretched and acquired an elongated morphology ("elongated cells", $width < 7\ \mu m$). These changes were sometimes accompanied by an increase in the number of nuclei (more than one per cell). Once again, treatment with $MASnI_3$ induced a more pronounced change in cell morphology, since $at 100\ \mu g/ml$, over 20% of A549 cells were giant and polynucleated whereas $MAPbI_3$ altered the phenotype of less than 15% of A549 cells. This experiment was done independently three

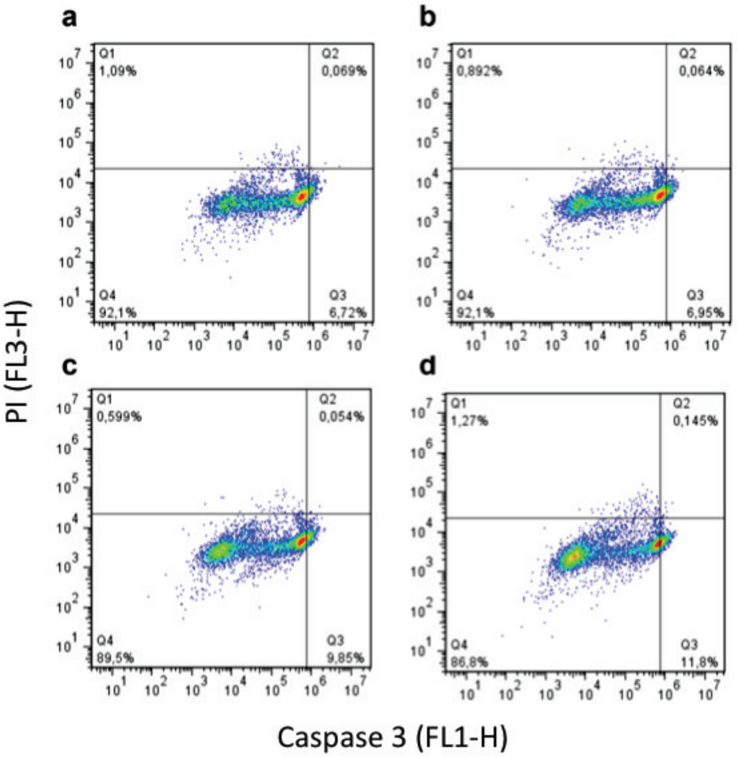

Figure 3.13 – Two-dimensional flow cytometry dot plot (Propidium iodide and Caspase 3) of the A549 cell line. a. Non-treated (negative control) cells; or cells exposed to $MAPbI_3$ at 50 $\mu g/ml$ (b), 100 $\mu g/ml$ (c) and 200 $\mu g/ml$ (d). $MAPbI_3$ does not induce necrotic cell death in A549 cells.

times yielding to the same observation. One could hypothesize that the decrease in cell density and increase in cell size together with the change in the number of nuclei are due to an altered cell division cycle. To verify this hypothesis, we performed various assays on the cell cycle upon $MAPbI_3$ and $MASnI_3$ exposure to A549 cells. The experimental procedures and results will be discussed in the following section.

3.5 Cell division under $MAPbI_3$ or $MASnI_3$ exposure

The organization and apparent function of microtubules in cultured mammalian cells vary markedly as the cell cycle progresses from interphase to mitosis and back to interphase again. During cell division, the genetic material has to be correctly segregated into the daughter cells.[239] This is achieved through the formation of a dedicated bipolar structure called the mitotic spindle, which involves a profound remodeling of the microtubule network. This reorganization of the cytoskeleton is very complex and depends on many proteins, enzymes and other parameters reviewed recently by di Pietro et al.[67] However, tubulin and actin are the main cytoskeletal proteins that play a central role in the structure and function of dividing

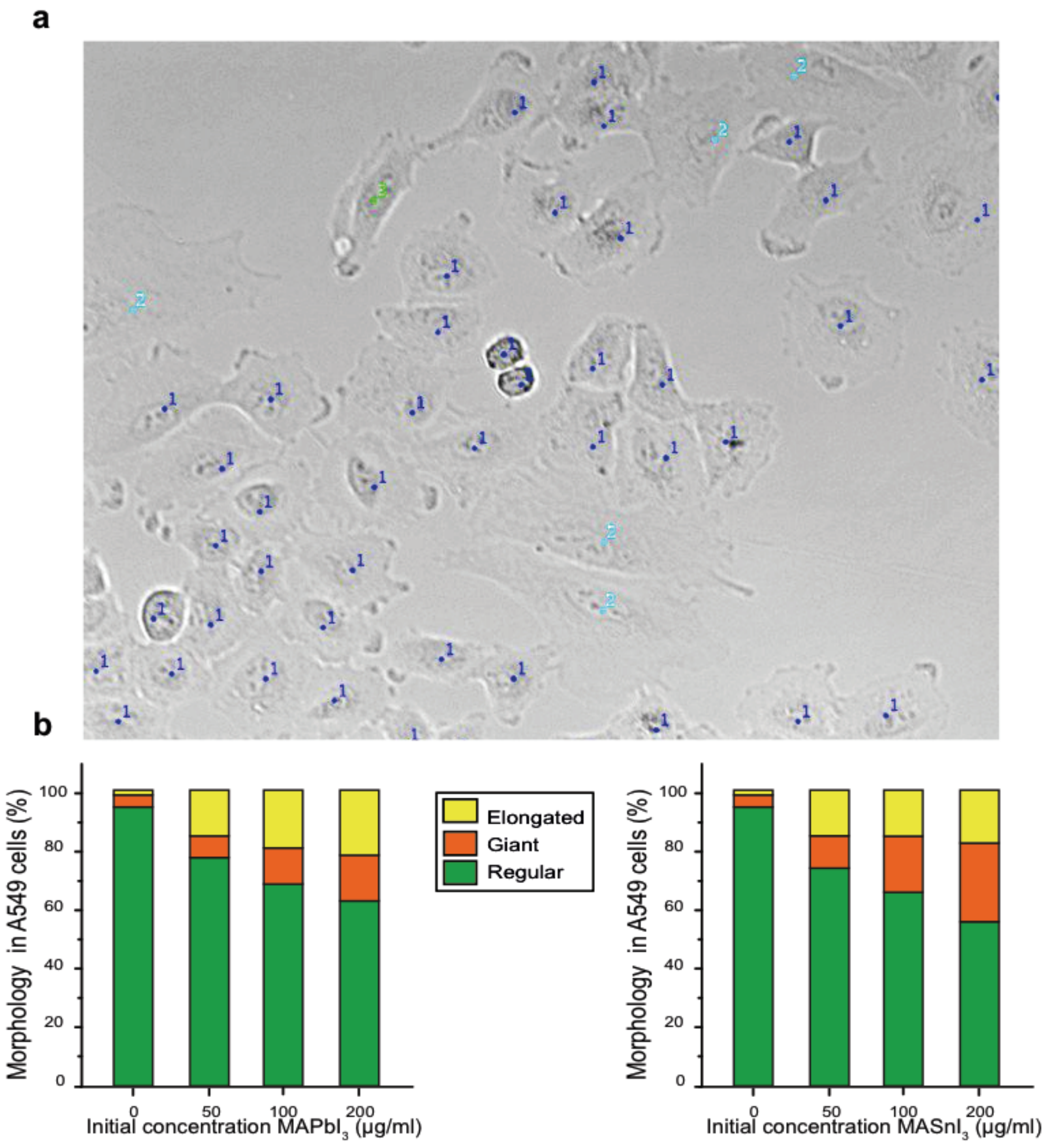

Figure 3.14 – Quantification of the phenotypical changes observed on A549 cells: a) Example of bright field microscopy image of cells exhibiting regular (1), giant (2) and elongated (3) cells, and their quantification when exposed to $MAPbI_3$ (b) or $MASnI_3$ (c) after 5 days using FIJI software and the cell counter plugin.

cells.[50, 139] Their organization in a network orchestrates the mitotic spindle, where actin distribution is in the region of the cleavage groove, while tubulin clusters in a fibrous spindle between the daughter cells.[50] Although the cytoplasmic content is strongly involved in the process of cell division, the nuclear state is also very critical. Cells at different stages of the cell cycle can also be distinguished by their DNA content. As they contain two copies of each chromosome at G1 phase (diploid cells) and this content is doubled during the S-phase. Experimentally, the DNA content can be determined by incubation of cells with a fluorescent dye that binds to DNA, followed by analysis of the fluorescence intensity of individual cells using flow cytometers.[60] In this section, we will show how $MAPbI_3$ and $MASnI_3$ perovskite solutions affect some pathways involved in regulating the cell cycle and the kinetics of cell division in A549 cells.

3.5.1 The cytoskeleton arrangement revealed by immunocytochemistry (ICC)

Experimental procedure for ICC

A549 cells were seeded at 20% confluence onto glass coverslips coated with poly-L-lysine (Life Technologies). After adhesion, cells were treated with $MAPbI_3$ at a final concentration of 200 $\mu g/ml$. After 5 days, they were washed 3 times with PBS (Phosphate Buffer Saline) and then fixed in 4% PFA (paraformaldehyde, Sigma-Aldrich) for 20 min at RT. After blocking with 3% BSA (Bovine Serum Albumin) in 0.1% Triton X-100 mixed with PBS (PBST) for 30 minutes at RT, cells were incubated with the rabbit anti-ß-tubulin primary antibody for two hours at RT. The cells were rinsed five times in PBST and subsequently incubated with the secondary anti-mouse Alexa488 at a dilution of 1/800 in PBST and with the labelled phalloidin AF594 at a dilution of 1/1000 in PBST. The cells were washed five times in PBST and incubated 30 minutes at RT in DAPI at 2 $\mu g/ml$, before mounting in polyvinyl alcohol mounting-medium with DABCO. The cells were then examined with confocal laser-scanning microscope (LSM 700, Zeiss) with a 40x objective and analyzed using Zen software (Zeiss).

Results of ICC

A549 cells proliferate rapidly, a population, in average, doubles after 1.5 days. Before immunostaining with actin and tubulin antibodies, cells were plated at 20% confluency then exposed to $MAPbI_3$ and $MASnI_3$ for 5 days. Figure 3.15 shows the immunostained cells after 5 days for non-treated cells (upper panel), and cells exposed to $MAPbI_3$ and $MASnI_3$ (lower panels). There is no difference in the effect of the two perovskites on cytoskeleton rearrangement. In the control condition, the population of cells reached confluency. The presence of two nuclei in very few non-treated cells is a normal observation in cancer cell lines. Interestingly, the organization of actin and tubulin was not affected by the exposure to the perovskites after 5 days, suggesting that there is no major difference in cell division between treated and untreated cells. Nevertheless, we observe once again that treated cells do not reach high confluency and their size and shape are heavily affected. This observation led us to investigate other molecular pathways that regulate the cell cycle, namely the DNA content.

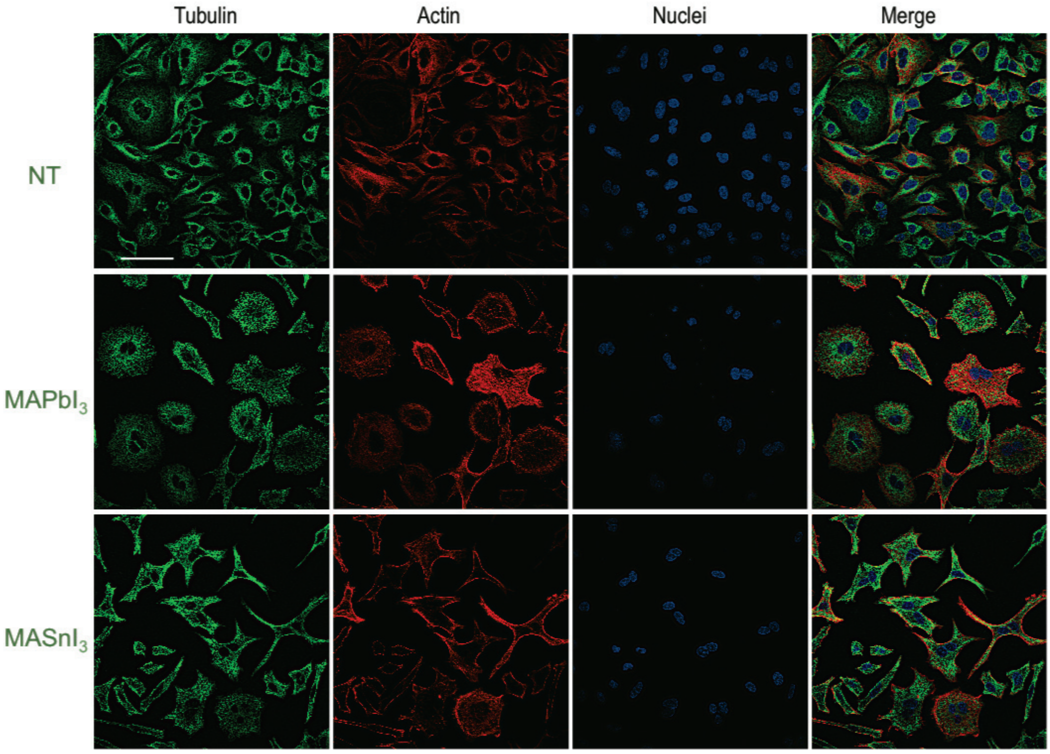

Figure 3.15 – Morphological changes caused by $MAPbI_3$ in A549 human lung epithelial cells. Cells were treated during 5 days with 200 $\mu g/ml$ of $MAPbI_3$, and $MASnI_3$. Tubulin and actin distribution was analyzed by immunostaining ß-tubulin (green), actin (red) and nuclei using DAPI (blue), then imaged using confocal microscopy. Non-treated condition is shown on the top panel and treated cells on the panels below. $Scale\ bar$ = 100 μm.

3.5.2 Cell cycle following perovskites exposure studied by flow cytometry

Experimental procedure

Quantification of the cell cycle distribution of A549 cells A549 cells were plated in 24-well plates. The following day, the original culture medium was removed from the cells and replaced with a medium spiked with increasing concentrations of $MAPbI_3$ or $MASnI_3$ (50, 100 and 200 $\mu g/ml$). After 5 days of exposure, the cell cycle was analyzed using propidium iodide staining (PI) (Life Technologies) that binds to DNA. Cells were harvested using the classical trypsin (Life Technologies) procedure. After 5 minutes of centrifugation at 200 g at 4°C, cells were suspended in ice-cold buffer, gently mixed then added to an equal volume of cold absolute ethanol and stored at 4°C for 24 hours. Cells were then centrifuged for 10 minutes at 200 g and washed with cold PBS. The pellets were resuspended in cold PBS containing 0.1 % (v/v) Triton X-100 (Sigma-Aldrich) and 0.4 % (v/v) 5 $\mu g/ml$ PI (which allows the cellular DNA content staining). Cell cycle distribution was analyzed (15'000 events per condition were measured) by flow cytometry using Accuri C6 (BD Biosciences). PI emission was collected in Fl2 channel and FlowJo software (Treestar) was used for subsequent analysis.

Quantification of the cell proliferation kinetics of A549 cells A549 cells were plated in 24-well plates and the medium was replaced by PBS containing CFSE (Life Technologies), a proliferation dye that penetrates every mammalian cell and diffuses passively into each daughter cell. The final concentration of 5 μM and left for 1 minute at 37°C then rinsed with PBS and left in complete medium overnight. The following day, medium was removed from the cells and replaced with a medium spiked with increasing concentrations of $MAPbI_3$ and $MASnI_3$ (50, 100 and 200 $\mu g/ml$). After 0, 1, 3 and 5 days of exposure, treated and non-treated A549 cells were harvested using trypsin procedure and PI was added to the cells suspension. Cell proliferation capacity was then analysed (15'000 events per condition were measured) by flow cytometry using Gallios instrument (Beckman Coulter). CFSE emission was collected in Fl1 channel and Kaluza software (Beckman Coulter) was used for subsequent analysis.

Results on the cell cycle study and the proliferation capacity tracking

We have shown previously that perovskites exposure induces a decrease in cell density in A549 accompanied by a strong change in their phenotype. Moreover, these effects do not involve the activation of cell death pathways in lung cells. We have also shown that actin and tubulin networks do not suffer the treatment even 5 days post-exposure to $MAPbI_3$. In this part, we present the results of DNA quantification obtained by flow cytometry. Figure 3.16 shows the quantification of cells, based on their DNA content, in the cell cycle phases : sub-G1 (growth phase after the mitosis), S (DNA replication or synthesis phase) and G2 (phase of cell maturation before division). We observe that the distribution of cell cycle phases is similar between the non-treated and treated cells with various concentrations of $MAPbI_3$ and $MASnI_3$ after 5 days. As the procedure of this assay infers nuclei isolation, the result reports the DNA content per nucleus and not per cell. This is the reason why quantification of DNA appears the same between treated and non-treated cells. Nonetheless, this test suggests that the cell cycle phases are not altered upon exposure to $MAPbI_3$ or $MASnI_3$, we therefore sought to investigate the proliferation capacity using other methods.

The kinetics of proliferation were assessed by measuring the fluorescence intensity of the Carboxy-Fluorescein Succinimidyl Ester (CFSE) dye by flow cytometry. This dye diffuses passively into cells and its intensity decreases by half after every cell division cycle. The results in Figure 3.17 show the fluorescence intensity of CFSE normalized to non-treated cells after 5 days of exposure for increasing concentrations of $MAPbI_3$ or $MASnI_3$. Cells exposed to the highest concentration of $MAPbI_3$ show a CFSE fluorescence intensity that is 2.3 times higher than non-treated cells, and in the case of $MASnI_3$ this factor is even higher. We can also appreciate the dose-dependent increase of the fluorescence intensity of CFSE. This result suggests that division kinetics have decreased in perovskites-treated cells, which is the reason for their slower proliferation and low density after 5 days likewise.

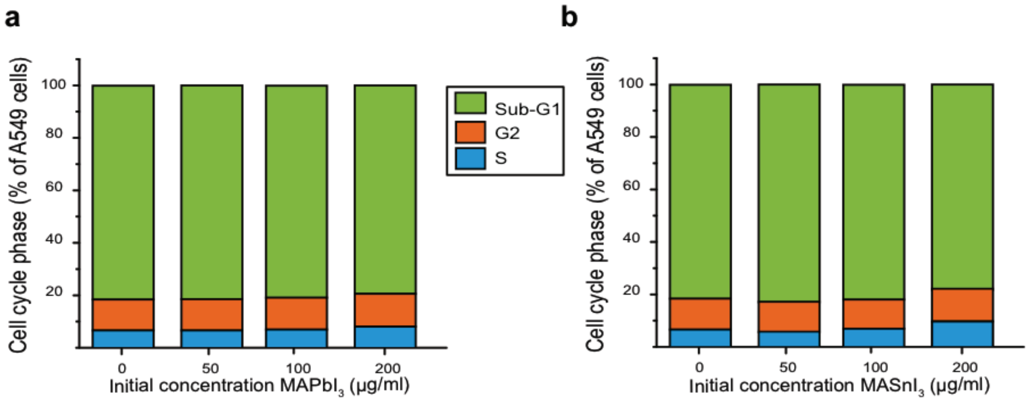

Figure 3.16 – Cell cycle distribution of A549 cells upon exposure to perovskites. Cells were treated during 5 days with increasing concentrations of $MAPbI_3$ or $MASnI_3$ (50, 100 and 200 $\mu g/ml$), their DNA was stained with propidium iodide (PI) and sub-G1, S and G2 phases distribution were assessed by flow cytometry: the histograms show the distribution of sorted cells based on their DNA content which did not change even at the highest concentration of perovskites.

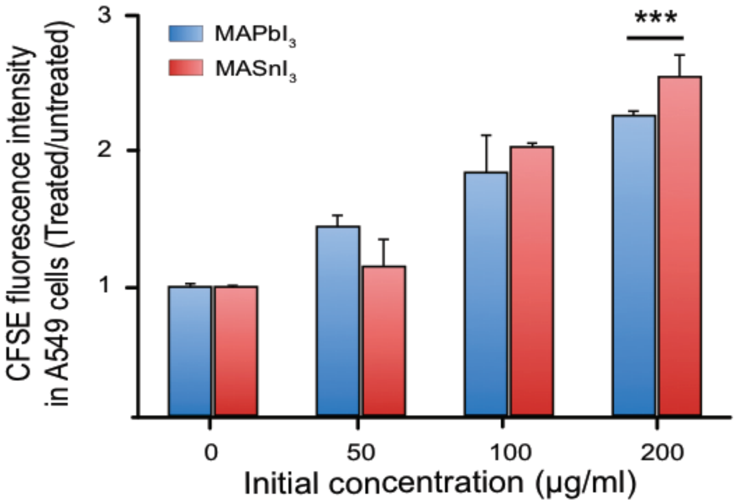

Figure 3.17 – Proliferation kinetics changes caused by the photovoltaic perovskites in A549 human lung cells: 5 days after treatment with increasing concentrations (50, 100 and 200 $\mu g/ml$) of $MAPbI_3$ (blue) or $MASnI_3$ (red), the proliferation capacity of A549 cells was assessed by acquiring the fluorescence intensity of CFSE using flow cytometry. The intensity in treated cells is normalized to the non-treated ones. All the histograms show an average of at least 3 independent repeats (each condition in triplicate). Bars are mean ± S.D. One-way ANOVA test followed by a Tukey-Kramer post-hoc test were performed (non-treated vs treated conditions), ***<0.0005.

To gain more detailed insight into the molecular and cellular basis of $MAPbI_3$-induced cellular dysfunction, we examined the real-time effect of $MAPbI_3$ and $MASnI_3$ on Geminin and Cdt1, two complexes involved in the regulation of the cell cycle.

3.5.3 Probing damages in real-time using live imaging

In addition to being regulated at the transcriptional and post-translational levels, the cell cycle is also controlled by ubiquitin (Ub)-mediated proteolysis of two complexes, that function as a feedback inhibitor for one another, *via* a ligase-mediated process. The two ligase activities oscillate reciprocally during the cell cycle from late mitosis (M) and G1 phases to the S and G2 phases[18, 151, 183] Geminin and Cdt1 are the direct substrates of the ligase activities in cell cycle proteolysis, and are thus produced only once per division. This carefully regulated process ensures that replication occurs only once in a cell cycle. Due to cell cycle-dependent proteolysis, protein levels of Geminin and Cdt1 oscillate inversely. In 2008, A. Miyawaki et al.[183] fused the ligases substrates to GFP and RFP to develop dual-colour fluorescent probes that indicate whether individual live cells are in G1 phase or S/G2/M phases (Figure 3.18).

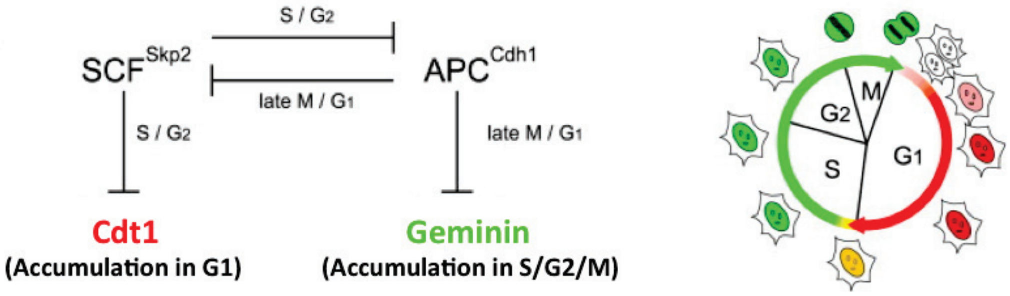

Figure 3.18 – Illustration of a fluorescent indicator for cell-cycle progression: Cell-cycle regulation by the production of Cdt1 and Geminin maintains bistability between G1 and S/G2/M phases (left panel). A fluorescent probe that labels individual G1 phase nuclei in red and S/G2/M phase nuclei green (right panel). (From Miyawaki et al.[183] in Cell, with permission from Elsevier).

In the G1 phase of the cell cycle, geminin is proteolysed and only Cdt1 tagged with RFP may be visualized, thus cells in the G1 phase emit red fluorescence and can be imaged. On the other hand, when in the S, G2, and M phases, Cdt1 is degraded and only geminin tagged with GFP remains, therefore cells become green and can be imaged in these phases. During the G1/S transition, as Cdt1 levels decrease and geminin levels increase, both proteins are present in cells, resulting in the superposition of GFP and RFP at the same time, thus cells appear yellow. On the other hand, after mitosis cells might remain in G0 phase, where no fluorescence in emitted. In this part, we report the live-assay in our cellular model exposed to $MAPbI_3$ or $MASnI_3$ and we explain the experimental procedure together with the results.

Live imaging methodology

A549 cells were plated at 13′000 $cells/cm^2$ in glass chambers (IBIDI, Germany) coated with poly-L-lysine. After adhesion, cells were treated with 100 $\mu g/ml$ of $MAPbI_3$ or $MASnI_3$. We then stained the nuclei in blue using Hoechst33343 (Thermo Fisher) and used the Bacmam 2.0

Premo Fucci cell cycle sensor (Thermo Fisher, Switzerland) according to the manufacturer's protocol.[9] Live imaging was performed during 48 hours every 20 minutes, for treated and non-treated cells, using an inverted Olympus Cell-R coupled with a CCD camera. We used FIJI software for image analysis.

Live imaging results

We examined cell cycle progression in A549 cells exposed to $MAPbI_3$ or $MASnI_3$ after transfection with fluorescent, ubiquitination-based cell cycle indicator (Fucci) using live imaging. After 24 h and 48 h, non-treated cells proliferated as clusters maintaining cell-cell adhesion with their neighbors (Figure 3.19, upper panels). The high proliferation rate of these cells was evidenced by the large fraction of cells with green nuclei. However, when cells were exposed to $MAPbI_3$ (Figure 3.19 intermediate panels), a change in fluorescence could hardly be observed over time. In the case of $MASnI_3$ exposure, only the blue-stained nuclei were observed, indicating that Cdt1 and geminin proteins are not expressed and therefore cells remained in G0 phase. Additionally, the cells' density was not changed (Figure 3.19 lower panels). This observation is in accordance with the results obtained from the proliferation capacity assay using CFSE (Section 3.5.2) witnessing a slower cell cycle. In combination with these cellular labeling techniques, we next examined the subcellular ultrastructures using electron microscopy. In the next sub-section, we will present a detailed procedure on how we obtained high-resolution micrographs of the cytoplasmic content of A549 cells exposed to perovskites.

3.6 The utrastructural effects revealed by Transmission Electron Microscopy (TEM)

3.6.1 Materials and methods for TEM

A549 cells were grown on plastic coverslips (Thermanox) coated with poly-L-lysin. The following day, the original culture medium was removed and replaced by a medium spiked with 100 $\mu g/ml$ of $MAPbI_3$. After 5 days of exposure, cells were fixed using 4% paraformaldehyde during 10 minutes and washed five times with PBS. Cells were post-fixed with 1% osmium tetroxide reduced with 1.5% (w/v) potassium ferrocyanide in 0.1 M sodium cacodylate buffer pH 7.4 for 40 min followed by 1% osmium tetroxide, then washed using double-distilled water and enblock stained with 1% (w/v) uranyl acetate in water for 40 min. Brief wash with water was followed by dehydration in graded alcohol series (2 × 50%, 1 × 70%, 1 × 90%, 1 × 95%, and 2 × 100%) for 3 min in each change. Then the cells were gradually infiltrated in the Durcupan resin diluted with ethanol (1:2, 1:1, and 2:1) for 30 min each dilution and in fresh pure resin for

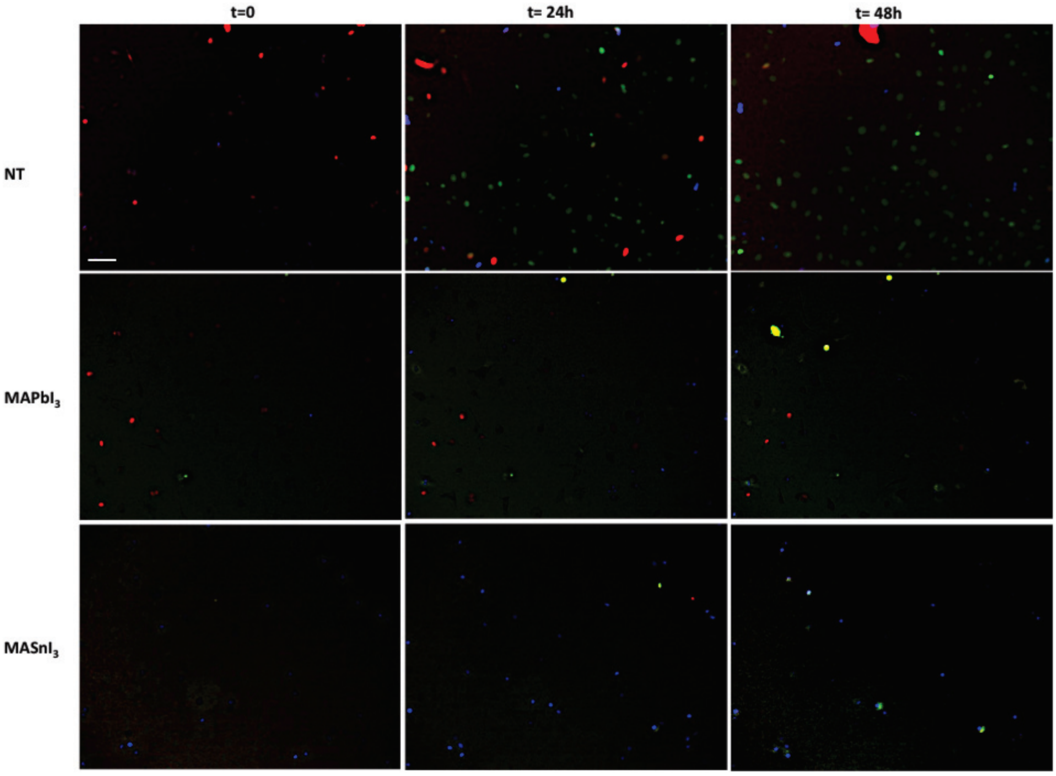

Figure 3.19 – Live A549 cells stained with Hoechst and premo Fucci during 24 and 48h: Non treated (upper panels), 100 μm of $MAPbI_3$ (intermediate panels), and 100 μm of $MASnI_3$ (lower panels). $Scale\ bar = 100\ \mu m$. The full videos can be found at http://go.epfl.ch/NT_A549_Live for non treated cells, http://go.epfl.ch/L100_A549_Live for 100 μm $MAPbI_3$ treated cells, and http://go.epfl.ch/Sn100_A549_Live for 100 μm, $MASnI_3$ treated cells

1 hour. Finally, the cells were sandwich embedded. The 13 mm diameter Teflon ring, 1 mm thick, was placed on the glass slide coated with mold separating agent and the inner volume was filled with Durcupan resin and covered with the coverslips, cells facing down. The sandwich was then placed in the 65°C oven to polymerize and cure the Durcupan resin overnight. The plastic coverslip was removed from the cure resin block by alternation between immersing into liquid nitrogen and hot water until departed from the resin block. Cells were marked on the resin surface using pulsed laser of dissection under microscope (Leica LMD, Leica Microsystems). Selected cells were cut off from the resin disk by single edge razor blade, glued to dummy resin block with superglue and the cutting face was trimmed using ultramicrotome (Leica Ultracut UCT, Leica Microsystems) and glass knife. Ultrathin sections (50-60 nm) were cut with the diamond knife (DiATOME, Biel, Switzerland) and collected onto single slot (2 mm) copper grids coated with formvar plastic support films. Sections were contrasted with uranyl acetate and lead citrate and examined using Tecnai Spirit TEM (FEI, Netherlands) equipped with a bottom mounted 4k × 4k Eagle CCD camera controlled by TIA acquisition software (FEI, Netherlands).

3.6.2 Results of TEM

As shown previously, treatment with $MAPbI_3$ resulted in an increased size of cells, multiple nuclei and a decrease in cellular density. Imaging with electron microscopy offers a high-resolution visualization of the subcellular structures. In Figure 3.20 a, we can see a non-treated A549 cell exhibiting a regular shape, we can also appreciate the presence of lamellar bodies, small secretory organelles that store lung surfactants to protect the cell against extra cellular material[188] After exposure to $MAPbI_3$ (Figure 3.20 b), the density of lamellar bodies increases and the multiple nuclei present in the treated cells did not show any ultra-structural defects with well-preserved nuclear membrane and also present multiple nucleoli. However, the most striking effect of $MAPbI_3$ treatment was observed on the mitochondrial compartment. The non-treated cells showed typical ultrastructure of the mitochondrial cristae organization (Figure 3.20 c, light green), whereas cells treated with $MAPbI_3$ exhibited severely damaged mitochondria (Figure 3.20 d, dark green for damaged mitochondria). The size of mitochondria in these cells increased dramatically and the intra-mitochondrial space became highly dilated with severe damage to the cristae organization. These results suggest that $MAPbI_3$ induces adverse effects on the mitochondrial function of A549 cells. To verify this statement, we measured the mitochondrial function using several assays.

3.7 Alteration of the mitochondrial function after exposure to perovskites

A mitochondrion is an organelle found in the cytoplasm of almost all eukaryotic cells. They have been described as "the powerhouse of the cell" because they generate most of the cell's supply of adenosine triphosphate (ATP), the source of chemical energy.[53] Moreover, mitochondria are essential in regulating the vital cellular functions such as signaling, cellular differentiation, cell survival, cell death, cell cycle and cell growth.[141] Their size ranges between 0.75 and 3 μm in diameter.[226] In humans, mitochondria are composed of the outer membrane, the intermembrane space, the inner membrane, the cristae and the matrix. These compartments carry out specialized functions orchestrated by the means of different mitochondrial proteins (615 in mitochondria from cardiac cells).[206] DNA can also be found inside mitochondria showing substantial similarities to bacterial genome.[27] The density of mitochondria per cell varies considerably depending on the cell type, the tissue and the species. In this section, we report the mitochondrial activity of A549 cells exposed to $MAPbI_3$ or $MASnI_3$ using the standard MTT assay.[179] We have also investigated the mitochondrial membrane potential that we compared to the total mass of mitochondria using the Mitotracker test coupled with flow cytometry.

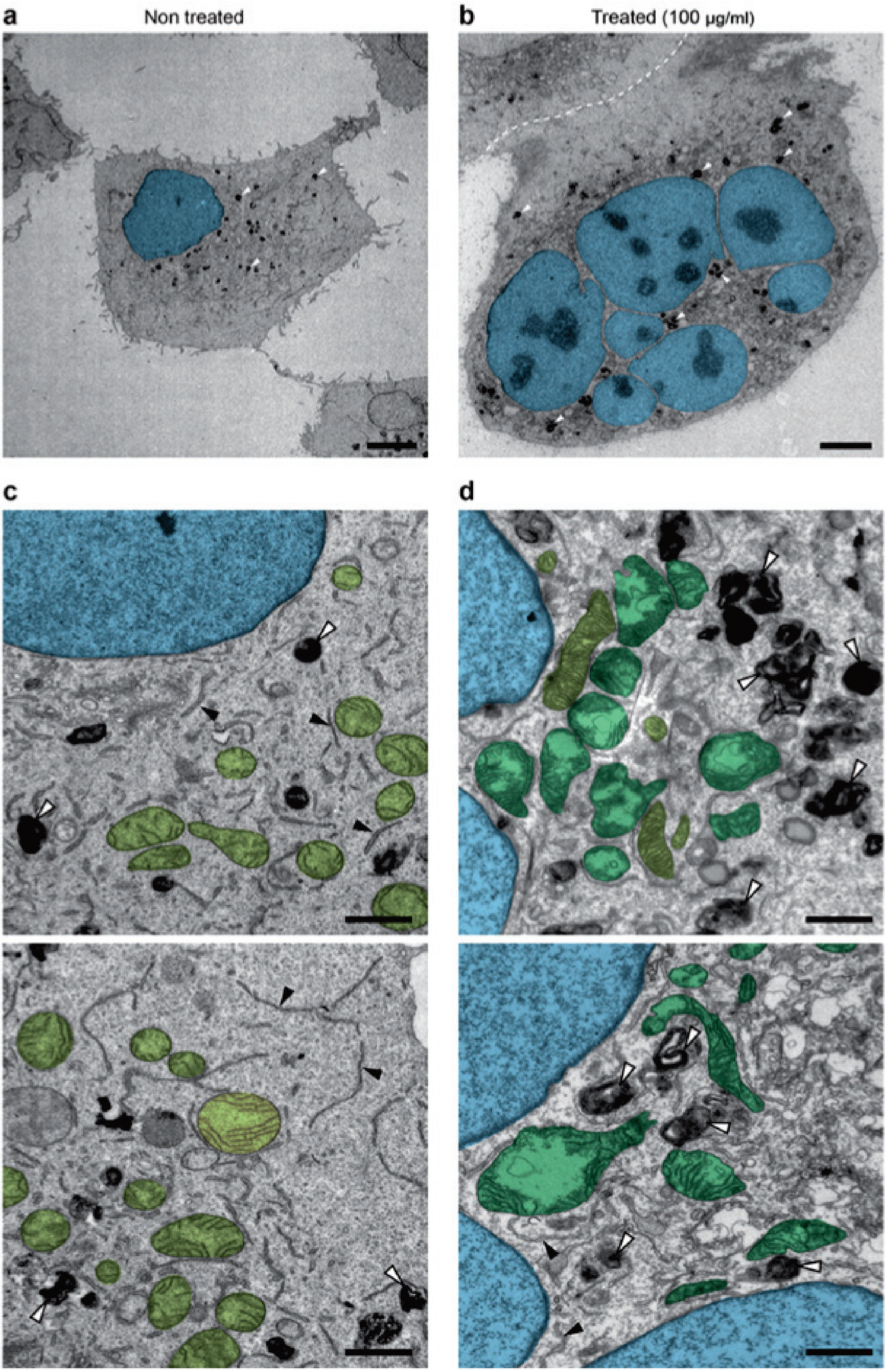

Figure 3.20 – Ultrastructural analysis by EM of A549 cells. (a) Low magnification electron micrograph of the non-treated A549 cells. A typical cellular morphology is shown with single nucleus (blue) well preserved nuclear membrane and multiple nucleoli and lamellar bodies (LB; white arrows);

(b) Changed morphology of the A549 cells upon the treatment with $MAPbI_3$ nanoparticles. Low magnification overview image of the large "giant" multinucleated cell containing 7 nuclei and significantly increased number of lamellar bodies depicted by white arrows; (c) Two characteristic higher magnification images of the normal mitochondrial (green) morphology with typical cristae organization, tubular organization of the endoplasmic reticulum (black arrowheads) together with lamellar bodies (white arrows); (d) Two characteristic higher magnification images demonstrating the severe damage of the mitochondria, particularly their increased size compared to the non-treated A549 cells and highly dilated intra-mitochondrial space and reduced cristae organization. The lamellar bodies (white arrows) and tubular organization of the endoplasmic reticulum are marked (black arrowheads). Scale bars: 5 μm in a and b; 1 μm in c and d.

3.7.1 Experimental methodology for the mitochondrial assays

The MTT assay

A549 cells were plated in 24-well plates. The following day, the original culture medium was removed from the cells and replaced by medium spiked with increasing concentrations of $MAPbI_3$ or $MASnI_3$ (50, 100 and 200 $\mu g/ml$). Metabolic activity of the cells was measured using the tetrazolium derivative 3-[4,5- dimethylthiazol-2-yl]-2,5-diphenyl tetrazolium bromide (MTT) assay. This colorimetric assay based on the capacity of the healthy cells to reduce MTT (Sigma Aldrich, Switzerland) in a purple formazan product. Briefly, after the indicated days of exposure to $MAPbI_3$, 5 mg/ml MTT was added to the different cell cultures. After 3 hours of incubation, the culture medium was aspired and replaced by 100 μl or 20 μl (respectively in 24 or 96 well plates) of DMSO (Sigma-Aldrich). The levels of formation of formazan products were quantified by using Tecan infinite M200 Pro plate reader (Tecan). Absorbance of the converted dye was measured at a wavelength of 570 nm with background subtraction at 630–690 nm. Normalization to the number of counted cells had to be performed, in order to take into account both the changes in proliferation and the confluence of A549 cells and thus to fit the measured MTT absorption to the relative mitochondrial activity.

The mitotracker assay

A549 cells were plated in 24 well plates. The following day, the original culture medium was removed from the cells and replaced by medium spiked with 100 $\mu g/ml$ of $MAPbI_3$ or $MASnI_3$. After 5 days of exposure, the membrane potential $\Delta\Psi_m$ was analyzed using the fluorochrome MitoTracker Red (CMXRos) dye, and the overall mass of mitochondria was quantified using the fluorochrome MitoTracker Green. In short, CMXRos is a dye which passively enters in living cells and that is selectively taken up and retained in mitochondria depending on $\Delta\Psi_m$, whereas MitoTracker Green can passively diffuse through the plasma membrane and once inside the cells, this dye selectively binds to the lipids of the mitochondria and fluoresces regardless the mitochondrial membrane potential. Therefore MitoTracker Green allows the overall measurement of the mitochondrial mass. After 5 days of exposure to $MAPbI_3$, cells were resuspended and incubated for 20 minutes at 37°C with CMXRos and MitoTracker Green in accordance with the supplier's instructions. Mitotrackers emission was analyzed by flow cytometry [Accuri C6 (BD Biosciences)] in Fl2 channel for the CMXRos and in Fl1 channel for the MitoTracker Green, 30'000 events per condition were measured. FlowJo (Treestar) was used for subsequent analysis.

3.7.2 Results of the mitochondrial assays

In the previous sub-section we demonstrated with TEM the adverse effect of $MAPbI_3$ on the mitochondrial structure. Here we present how these effects are translated into the mitochondrial activity. A549 cells were exposed to $MAPbI_3$ and $MASnI_3$ during 5 days, and their metabolic activity was examined using 3-(4,5-dimethylthiazol-2-yl)-2,5-diphenyltetrazolium bromide MTT assay normalized to the cells confluence. We found a clear increase in mitochondrial activity (Figure 3.21 a) in a time- and dose-dependent manner. Moreover, The tin-compound has a more radical effect on the increase in metabolic activity. We then compared the mitochondrial membrane potential ($\Delta\Psi_m$) in the non-treated and treated cells by measuring the capacity of Mitotracker Red CMXRos to be taken up and retained into the mitochondria. Figure 3.21 (b, c) shows a significant increase of the membrane potential $\Delta\Psi_m$ in the cells exposed to $MAPbI_3$ or $MASnI_3$. This observation is in accordance with the MTT result. Nonetheless, the overall mass of the mitochondria, assessed using the Mitotracker green FM and flow cytometry, was also slightly increased in the treated cells.

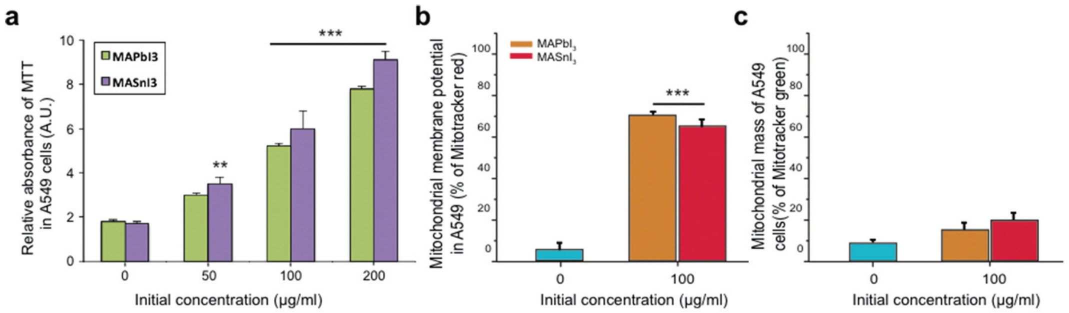

Figure 3.21 – Effect of $MAPbI_3$ and $MASnI_3$ on the mitochondrial function of A549 cells. A549 cells were treated with increasing concentrations of $MAPbI_3$ and $MASnI_3$ ($50,\ 100\ and\ 200\ \mu g/ml$) and their mitochondrial activity was evaluated. (a) MTT assay after 1, 3, 5 and 7 days of exposure to $MAPbI_3$ and $MASnI_3$ showing increasing metabolic activity normalized to the number of counted cells; (b) Mitochondrial membrane potential ($\Delta\Psi_m$) was assessed in non-treated and treated cells (100 $\mu g/ml$ of $MAPbI_3$ and $MASnI_3$) at 5 days post-treatment. Cells were stained by Mitotracker Red CMXRos and analyzed by flow cytometry. These results corroborate with the increased mitochondrial activity seen in a; (c) Overall mass of mitochondria was measured in non-treated and treated cells (100 $\mu g/ml$ of $MAPbI_3$ or $MASnI_3$) at 5 days post-treatment. Cells were stained with Mitotracker Green and analyzed by flow cytometry. All the histograms show an average of at least 3 independent repeats (each condition in triplicate). Bars are means ± S.D. One-way ANOVA test followed by a Tukey-Kramer post-hoc test were performed (non-treated vs treated conditions), **p<0.005 and ***<0.0005.

The effects of $MAPbI_3$ and $MASnI_3$ on human lung epithelial cells were markedly different compared to the neuronal cells. In summary, the photovoltaic perovskites do not induce cell death of A549 cells but heavily affect their phenotype, proliferation kinetics and the mitochondrial structure and function. Considering that the molecular mechanisms of the perovskites toxicity still need to be elucidated, we decided to inspect the genome profile of cells exposed to $MAPbI_3$ and compared it to the non-treated cells. In the next part of this chapter, we will introduce the gene expression methods and present our preliminary data.

3.8 Study of the toxicity effect of MAPbI$_3$ by genome profiling

To have a better insight on the microscopic changes inside A549 cells induced by perovskite exposure, I have zoomed in further more by doing a genome profiling, and performed this study only by the $MAPbI_3$. The profile of gene expression contains the global picture of cellular state and can be useful for discerning the mechanisms by which chemical compounds invoke toxic effects. The human genome contains around 20'000 genes coding for 30'000 proteins and hundreds of thousands of peptides.[119] Because of the redundancy in regulations of many genes, identifying individual markers that are responsible of a specific toxic effect can be challenging. In light of this complexity, new methods have been developed for studying the levels of genes expression at high-throughput. Among them DNA microarray,[173] a technology that measures the relative activity of specific target genes. In this technology, the sample (mRNA) is reverse-transcribed into cDNA and injected into a biochip where a collection of microscopic single-strand DNA spots are attached to a solid surface. Each DNA spot is a probe that has the capability to hybridize the target cDNA. The advent of next-generation sequencing has made RNA sequencing (or RNA-seq)[220] a digital alternative to microarrays. This technology quantifies total RNA in a biological sample at a given moment of time, including mRNA, small RNA (miRNA, tRNA) and taking into account the post-transcriptional modifications and the spliced transcripts. We chose the use of RNA-seq to analyze the continually changing transcriptome of A549 cells exposed to $MAPbI_3$ versus non-exposed cells (Figure 3.22). RNA-seq method is more sensitive than the conventional micro-array sequencing approach, and allows transcriptome mapping and quantification.

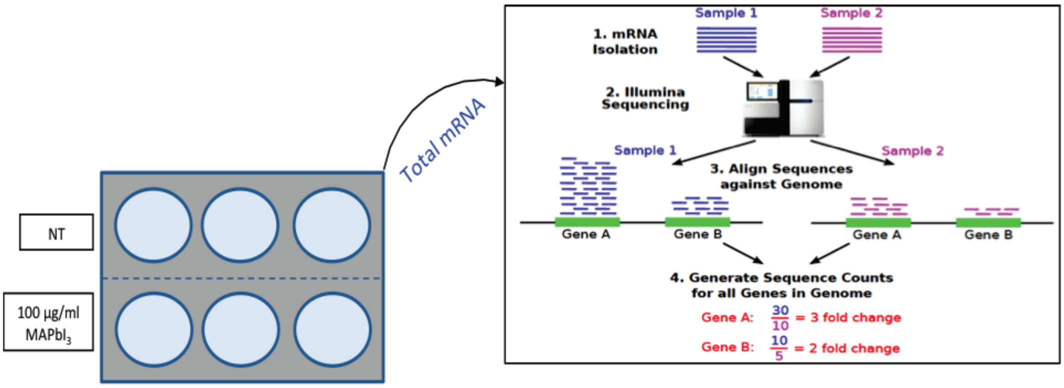

Figure 3.22 – Illustration of the genome profiling study: A549 cells were treated with $MAPbI_3$ at 100 $\mu g/ml$ during 3 days, then total mRNA was isolated and sequenced using Illumina machine. The sequence was then aligned against human genome to probe the gene expression changes.

3.8.1 Experimental procedure

Samples preparation for genome profiling

A549 cells were plated in a 6-well plate at 40% confluency. The following day, the original culture medium was removed from the cells and replaced by medium containing 100 $\mu g/ml$ of $MAPbI_3$. At 6 hours and 3 days, mRNA was isolated from treated and non-treated cells using RNeasy mini kit (Qiagen, Switzerland) following the manufacturer's protocol.[12] Quality and quantity measurements of extracted RNA was done using NanoDrop2000 (Thermo Scientific), and wells were poured together to reach 1 μg of total RNA from the same condition.

RNA-seq approach

The purity and quality of the reads was trimmed with Cutadapt version 1.3,[136] and seq_crumbs (v. 0.1.8). Reads were aligned against Homo sapiens version GRCh38 genome using STAR[69] (version 2.4.0f1). The number of read counts per gene locus was summarized with HTSeq-count[25] version 0.6.1, using H. sapiens GRCh38 Ensembl version 76 gene annotation. Quality of the RNA-seq data alignment was assessed using RSeQC[219] version 2.3.7. Reads were also aligned to the H. sapiens GRCh38 Ensembl version 76 transcriptome using STAR and the estimation of the isoforms abundance was computed using RSEM[129] version 1.2.16.

Statistical and differential analysis

RNA samples from treated and non-treated cells were prepared independently in duplicate. Statistical data analysis was performed for genes in R (R version 3.1.2). Genes with low counts were filtered out according to the rule of 1 count per million (cpm) in at least one sample. Library sizes were scaled using TMM normalization (EdgeR v 3.8.5) and log-transformed with limma (R version 3.22.4). Statistical quality controls were performed through pairwise sample correlations, clustering and sample PCA (principle component analysis) using transformed data. Differential expression was computed using LIMMA by fitting data into a linear model and extracting the contrast in two groups according to the time point. A moderated t-test was used for the comparison. Adjusted p-values have been computed for each comparison by the Benjamini-Hochberg (BH) method, controlling for false discovery rate (FDR).

Signaling pathways analysis

After the LIMMA, a gene set enrichment analysis (GSEA) and pathway analysis were performed using GAGE and R. To do so, the log2 Fold Change (FC) of the comparison between treated and non-treated samples was considered. Next we analyzed the gene ontology (GO) enrichment for a gene set compared to the totality of genes. The latter is annotated in 3 main classes: molecular function, cellular component and biological process. We selected biological process since it includes the global cellular mechanisms with details on the molecular functions and localization inside the cell. We also used TopGO (topology-based Gene Ontology scoring), an R library, to analyze statistically gene sets. We used a standard Fisher statistical test because it uses the count of genes belonging to each GO term in the whole human genome versus the selected gene list in order to calculate a gene enrichment score. The GO terms are ranked by their p-value.[41] To analyze the gene set and the signaling pathways, Ensembl gene ID were converted into Entrez-gene ID. Then we used the Generally Applicable Gene-set Enrichment (GAGE) method to link the known regulatory signaling pathways from differential gene expression, and by connecting some KEGG published pathways with the phenotypic conditions Treated *versus* Non-treated. It allows getting a systemic approach of the points leading to different phenotypes (Treated *versus* Non-treated). Unlike the SPIA strategy focusing on a limited number of differentially expressed genes (cutoff-based), GAGE focuses on sets of related genes (log2FC). One GAGE advantage is that sometimes coordinated gene expression changes that are not significant according to our thresholds (adjusted p-value > 0.05) can have a major pathway impact. With GAGE, we can have two different approaches for pair–wise comparison between samples (LL/TT and LLTT/HEC): based on Log2FC or on the per gene statistics (t-student test paired samples). That is to say, GAGE uses sample wise fold change as per gene score/statistics in gene set test. We assume that gene set test on log2FC data is not as powerful and sensitive as the GAGE pair-wise comparison scheme. However, this experiment was done only in duplicate (two samples per condition). It seems that there is not enough samples in each condition to have a powerful t-student test. We run GAGE to infer gene sets (or pathways) that are significantly perturbed comparing to all the considered genes . GAGE compares expression level of a gene set to the whole set background. We select the KEGG pathways that have a p value<0.05. In order to complete the GAGE results, we decided to use another approach. The idea is to find pathways specifically associated to the gene set that we consider as differentially expressed (DE), or a cutoff-based approach, or to find pathways associated to our data (gene set statistically found). As the algorithms are different, they can give complementary outcomes. Nevertheless the common pathways resolved by the two methods are the ones modified by the perovskite treatment. We have also used another bioinformatics method called SPIA or Signaling Pathway Impact Analysis. This analytical method combines the classical pathway enrichment analysis of a gene set and compares it to the gene background within two biological conditions. SPIA uses the log2 fold change and predefines sets of DE genes. We chose to apply the thresholds adjusted pvalue <0.05 for a statistical significance. The next section will present the analyzed outcomes and discuss the preliminary impact of $MAPbI_3$ on the genome of A549 cell line.

3.8.2 Gene profiling results

We performed RNAseq at the genomic technologies facility (GTF) at the university of Lausanne.[7] Common RNA fragmentation and other manipulations were made prior library production, processing and alignment. We generated a table including referenced genes and their specific fold change (FC) over exposure to $MAPbI_3$. Up-regulated genes have a positive value of the FC and the down-regulated ones have a negative FC value. The preliminary results of the toxic effects of perovskites on the genome profile of A549 cells are presented in this part.

	Total	sum > 0	In analysis
antisense	5408	3749	610
lincRNA	7403	4278	605
processed transcript	530	372	135
protein coding	19924	18162	13005
sense intronic	909	708	104
sense overlapping	189	151	42
Totals	34363	27420	14501

Table 3.1 – Number of genes measured by HTSeq method.

Quality control report

A global quality control report can be found in appendix C and includes alignment metrics, gene body coverage profiles and read density over annotated regions. In summary, it shows high number of total reads sequenced for all samples varying between 35 to 50 million of reads and high percentage (> 99%) of aligned reads to the genome. Very low percentage of reads mapping RNA sequences (< 1%) as expected for poly-A selection protocol and low percentage of mitochondrial sequences (< 1%). Mapped reads are principally located in CDS regions of the genome and they account for 29 to 41 million of reads. Gene body coverage profiles are of very good quality and similar across samples.

Differential expression analysis

Differential expression was computed with LIMMA by fitting data into a linear model and extracting the contrast in treated versus non-treated conditions according to the time point 6 hours or 3 Days. The number of genes measured by biotype category (HTSeq)[25] are presented in Figure 3.1 where "Total" represents all genes to which the read counts were mapped; "Sum>0" are the genes that have at least 1 read count in at least 1 sample; and "In_analysis" stems for the genes that have at least 1 count per million in at least 1 sample.

From this outcome, we extracted the number of genes found with significant differential expression using the False Discovery Rate procedure (FDR) at a cut-off of 0.05 and a fold change >2. The results are summed up in Figure 3.2; where the background noise is very present below 0.05 of FDR in the 6 hours time point in treated *versus* non-treated conditions. Therefore, we considered the data only for the time point 3 days, and also for a FC>2 to make sure that the changes in gene expression due to exposure to $MAPbI_3$ are at lease 2 fold.

These analysed data are generated from duplicates, they need to be normalized and correlated among them before a more detailed comparison. As seen in Figure 3.23, pairblots, PCA and the quality score boxplots show that data are well normalized and the correlation is good between treated and non-Treated cells after 3 days. These results report that the quality of our

Group	Comparison	FDR<0.05			FDR<0.05 Fold changes > 2		
		ALL	UP	DOWN	ALL	UP	DOWN
6 hours	Treated 6h vs. NT 6h	0 (FDR 10%)					
3 days	Treaded 3d vs. NT 3d	281	237	44	239	201	38

Table 3.2 – Number of genes with a significant DE and FDR cut-off 0.05.

samples are very good and suggest that their corresponding RNA-seq raw data are comparable. Therefore, based on the transcripts, we proceeded on analyzing the potential networks that could be altered by exposure to the Pb-containing perovskite.

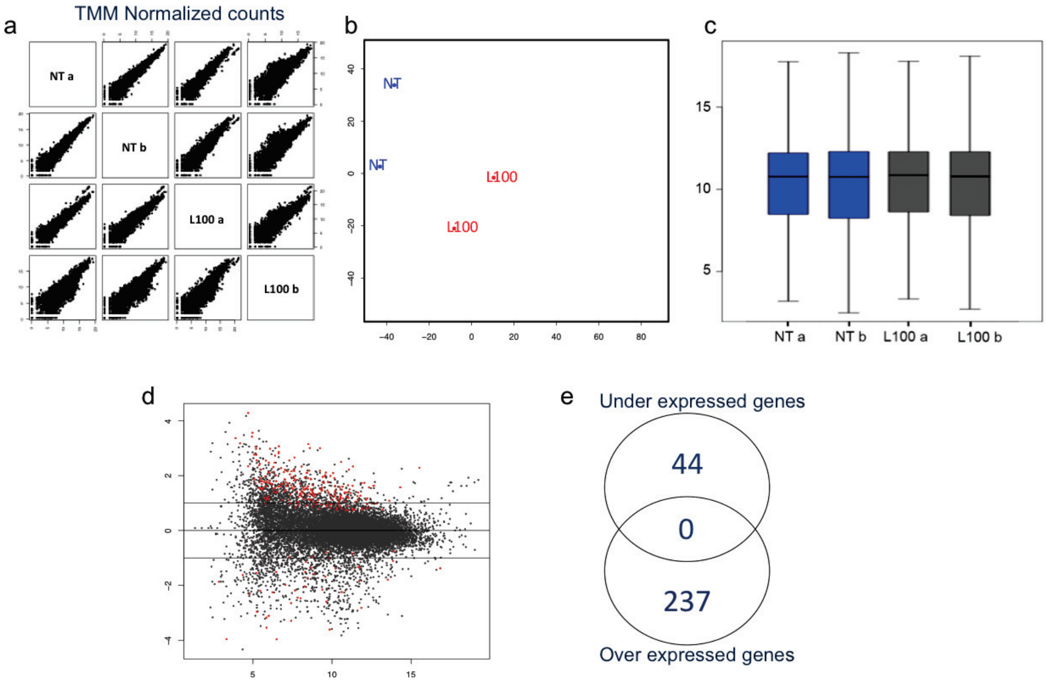

Figure 3.23 – Quality control of the RNA samples from A549 cells before analysis of the gene profile. a) Pairplot, b) PCA, c) Quality score boxplots, to verify the correlation among duplicates, and to normalize the samples. d) Maplot to distinguish between affected transcripts, and e) number of over- and under-expressed genes.

Signaling pathways analysis

The transcriptome mirrors the genes being actively regulated, and therefore reflects the expression profile. Since it is considered as a precursor for the proteome, we identified the co-regulated gene networks rather than individual coding genes^{190} that are up- or down-regulated in our samples. The first approach in identifying the potential signaling networks, where $MAPbI_3$ might interfere, is gene set enrichment (or GSEA) by taking into account the log2FC, this method is commonly called GAGE. Next we investigated the gene ontology (GO) and

Strategy	Description	Advantage	Disadvantage
GAGE KEGG	This method verifies if specific gene sets are significantly differentailly expressed (DE) versus background. Outcome: pathways associated to the data.	• based on log2 fold change (as per gene score) or on the t-test statistics per gene (t-student test paired sample). • Gage infer gene sets	Gene set test on log2FC data is not as powerful and sensitive as the GAGE pair wise comparison scheme. However, there are only two samples in each condition (Treated and Non-Treated).
SPIA KEGG Pathway topology	• Test over representation of DE genes • Combines pNDE hypergeometrical model and perturbation of the pathway pERT Outcome: pathways associated to the User Gene set.	• Take into account log2FC • Take into account Pathway topology • We chose the set of differentially expressed genes (pvalue < 0.05)	User Gene set. Only 2 pathways with pGFWER<0.05. No significant pathways for DE genes with adjusted pvalues < 0.05
GO Hypergeometric	Gene ontology hypergeometric enrichment. This method reflects the pathways and larger processes made up of the activities of multiple gene products.	One can choose the set of differentially expressed genes (adjusted pvalue<0.05).	• Expression value not taken into account • User Gene set
REACTOME Hypergeometric	This method is an hypergeometric model to assess whether the number of selected genes associated with reactome pathway is larger then expected.	Complementary results to KEGG. We chose the set of differentially expressed genes (adjusted pvalue<0.05).	Expression value not taken into account User Gene set

Table 3.3 – Summary of the four methods used in this study to analyze the RNAseq data a short description of the main characteristics of each method is given, as well as the advantages and the inconveniences in the present study.

then analysed the signaling pathway impact (SPIA). A comprehensive table compares these methods and sums up their advantages and inconveniences (Figure 3.3). By descriminating the data, we have found around 23 down-regulated and 17 up-regulated pathways following the exposure of $MAPbI_3$. Among them: the cell cycle protein network, DNA replication, RNA transport, mismatch repair and adherens junction. Figure 3.24 shows an example of pathway where the signaling cascade of proteins and peptides involved in regulating the cell cycle are affected: the mRNA of almost all the actors significantly undergo a fold change greater than 2: down-regulation (green boxes), or up-regulation (red boxes). Some of the other affected pathways mentioned previously are presented in appendix C.

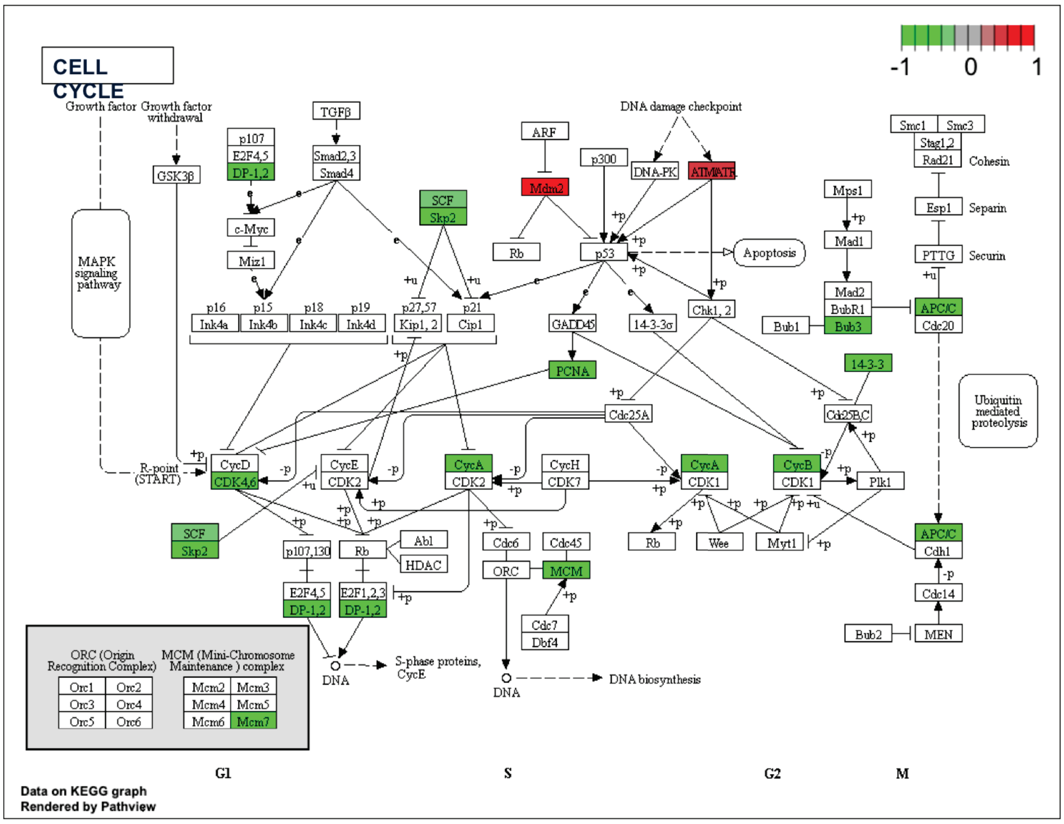

Figure 3.24 – Cell cycle down-regulated pathway at the transcriptome level of Treated vs. Non-Treated A549 cells exposed to $MAPbI_3$ for 3 days.

In summary, this genome profiling study exposed the effects of perovskites on gene expression, with the spotlight on transcripts. Computation and model fitting of the results allowed to identify changes in subcellular signaling pathways. Although the results are conjectures, because they are based on the profile of expressed genes, they are clearly in line with our previous findings, and shed light on the microscopic mechanisms of toxicity. Nevertheless, for a complete picture, further investigation on protein expression levels is needed.

3.9 Discussion and main conclusions of the *in vitro* study

The discovery of the $MAPbI_3$ perovskite as a cheap and extremely efficient material to convert sunlight to electricity represents a major breakthrough in the development of photovoltaic cells. However, one serious drawback of its large scale exploitation is its lead content that raises major concerns[94] about its potential toxicity during device production, handling and disposal. Replacement of Pb by Sn is an option widely accepted whithin the photovoltaic community. However, in this field nothing is granted, one has to check the consequences of exposure both to $MAPbI_3$ and $MASnI_3$ before large-scale production. The toxicity of the entire perovskite materials has not been documented at all before this dissertation.The group of Conings[32] claimed to report the toxic effects of Pb- and Sn-based perovskites, however they showed in their publications hazards related to PbI_2 and SnI_2. Both halides are available in the market with safety data sheets adocumenting their negative effects together with regulations about their use.[8, 176] Moreover, they study very high concentrations of PbI_2 and SnI_2, which are not realistic in an exposure scenario. In this chapter I have presented the *in vitro* results of our zoom-in approach of perovskites' toxicity. In our study, we observed that when $MAPbI_3$ or $MASnI_3$ are dispersed in cell culture media, a part forms a precipitate, while the other stays in solution (6% of Pb, 85% of Sn and 90% of I, see Chapter 2). Methylamine is known to be highly soluble in a water-rich environment.[181] In this study, we considered the soluble part of the perovskite only. Herein, we showed that $MAPbI_3/MASnI_3$ perovskites penetrate our cellular models and cause a time-and-dose-dependent toxicity in both SH-SY5Y neuroblastoma cell line and in differentiated mice primary hippocampal neurons. In both neuronal cell types, they damaged the plasma membrane and triggered apoptotic cell death *via* the activation of the mitochondrial/intrinsic pathway signaled by caspase 9. The heavy metal could be the main cause of this effect since it is known to depolarize cells mitochondria resulting in cytochrome c release, caspases activation, and apoptosis.[206, 226] In humans, a blood lead $level > 0.1\ \mu g/ml$ is considered to be elevated even though clinical symptoms are rarely seen below 0.6 $\mu g/ml$ in chronic poisoning.[28] Moreover, *in vivo*, the accumulation of lead in the organism amplifies the toxic effect. In our *in vitro* cellular studies the effect of accumulation was substituted by the increased concentration. Remarkably, in the case of epithelial cells such as A549 human lung cells, exposure to the perovskites did not result in cell death, but the proliferation rate decreased without cell cycle arrest leading to severe morphological changes and significant increase in the mitochondrial mass and activity. Upon exposure to $MAPbI_3$, A549 cells became giant and polynucleated; their mitochondria showed an unusual polymorphic arrangement of the cristae. Lead ions are known to enter some cells through calcium channels, then bind to calmodulin (with a higher affinity than calcium) which alters enzyme activities, gene transcription and cell signaling.[90, 124] On the other hand, methylamines are also known to inhibit protein turnover resulting in a modification the cells' DNA and RNA content.[96] The solubility of $MAPbI_3$ could be at the origin of the polynuclearity and the modified mitochondria. Paradoxically, the metabolic activity rate produced by the mitochondria increased significantly in response to $MAPbI_3$ and $MASnI_3$ exposure, whereas cell proliferation kinetics and confluency decreased. At first sight, this observation seems controversial but as the cells become giants and escape death, they must expand their energy production for survival. Mitochondria are essential regulators of metabolism, stress responses, cell survival and cell death.[85] One reason for the different response of the lung and neuronal cells to $MAPbI_3$ and $MASnI_3$ exposure might be the presence of lamellar bodies in the former ones and their absence in the latter cells. These structures are naturally present in the cytoplasm of mucosal cells; they are part of the cellular protective mechanisms against environmental influences[188] of the lung alveoli. A549 cells exposed to $MAPbI_3$ show an increase in the number of lamellar bodies in the cytoplasm. A similar increased number of lamellar bodies was observed in epithelial cells exposed to single-walled carbon nanotube exposure.[66] The cell survival strategies involve countless coordinated physiological and genetic changes that serve to escape cell demise.[174] It seems that one of these strategies consists of increasing the number of lamellar bodies, which have a protective function. Genome profiling of treated and non-treated cells provide a preliminary understanding of the cellular mechanisms underlying the differences in cellular toxicity and cellular phenotypes observed in A549 cells. The analyzed transcriptome given by RNA sequencing provides a significant hint on the observed effects following exposure to $MAPbI_3$ and confirms the outcomes of molecular and cellular biology assays performed using immunoblotting, microscopy, FACS and/or specific probes. The genome profiling was run in duplicate not only due to the high cost of the assay but also to the high reliability and reproducibility for technical and biological replicates.[58,147] However, validating data might be necessary to ensure that the analysis is operating on clean and correct genes or molecular networks. Validation of the candidates obtained using RNA-seq can be confirmed in the future by cheap and conventional tests at the mRNA level. Specific primers of the gene-candidates obtained from the RNA-seq test should be designed for reverse transcription-polymerase chain reaction (RT-PCR). RT-PCR is a routinely used technique in molecular biology to amplify targeted DNA sequences (*via* their primers) and then quantify them at a specific time point after exposure to the material. This assay (from RNAseq to RT-PCR) should also be done on cells exposed to $MASnI_3$. Validation could also be performed at the protein level for quantification and comparison with the bioinformatics data. Cells exposed to $MAPbI_3$ or $MASnI_3$ should be lysed and the total protein content extracted. Specific antibodies against the protein-candidates (related to the transcript analysed by RNAseq) should reveal by immunoblotting the actual change in protein content. This *in vitro* study is alarming, and suggests: 1) reconsidering the use of $MAPbI_3$ as a light harvester, 2) revisiting replacement of Pb by Sn, 3) finding alternative materials less toxic for “green energy” collection, 4) to the scientific community to understand the necessity of toxicity study for each novel material before its large-scale production and industrialization.

4

Identification of the biochemical fingerprints of perovskites toxicity by Infrared spectroscopy

The released ions after PV perovskites dissolution (Pb^{2+}, Sn^{2+} etc.) are chemically very active, and can enter easily into cells through calcium channels. Moreover,they are able to interact with proteins, lipids and DNA, and potentially catalyze chemical reactions. During these processes,

changes within the cell in biochemical activity or conformation of proteins and polypeptides may occur. Infrared (IR) spectroscopy is able to finely detect such fingerprints of toxicity, and this feature of IR is frequently used e.g. in detecting the hallmarks of neurodegenerative diseases, but it is the first time that it applied in a toxicity study. My goal was to zoom-in further at the microscopic level in order to detect the biochemical changes following exposure of cells to $MAPbI_3$ and $MASnI_3$. Since the approach is radically new to the field of toxicity, I separated it in a new chapter. For a better understanding of the working principles of the technique, first I give a short introduction to it.

4.1 Introduction to IR spectroscopy

Within molecules, the covalent bonds between atoms are in a constant state of vibration at specific temperatures. The energy required to stretch or bend a bond corresponds to the infrared (IR) region of the electromagnetic spectrum (typically between 1 meV and 1 eV). Consequently, IR spectroscopy is used mainly to differentiate between bond types.[79] By a technique, called Fourier-transform infrared spectroscopy (FTIR), one can find the main components of vibrational frequencies, which for historical reasons are expressed in units of cm^{-1} (8000 cm^{-1} corresponds to 1 eV). In a molecule with two atoms of mass m1 and m2 the frequency of vibrations could be expressed as:

$$f = \frac{1}{2\pi}\sqrt{\frac{k}{\mu}} \tag{4.1}$$

Where μ is the reduced mass $\frac{m_1 m_2}{m_1+m_2}$, and k is the strength of the chemical bonds between the two atoms. If the atomic vibrations result in an electrical dipole moment, light is absorbed at the characteristic frequency of the vibration. In other words, when IR illuminates a complex matter, like a cell or a protein or DNA, one could detect the absorption spectrum of the IR light.

A typical experimental configuration of IR absorption and a biological spectrum are depicted in Figure 4.1. The advantage of FTIR is that it detects all the components at the same time. Bending and stretching vibrations of functional groups have spectral fingerprints in specific regions and thus provide a diagnostic by compound class. In the case of organic and biochemical compounds, the corresponding bands appear in the region 1000-4000 wavenumbers (cm^{-1}). Figure 4.1 displays a spectrum of a single human neuroblastoma cell in which the IR signature of the biochemical content can be observed. In this spectrum, each peak represents the vibrational frequency of a cellular biochemical component. The variation in absorption intensity or in the wavenumber (energy) of the spectral peaks brings information about the biochemical and structural changes in the sample. The main spectral features observed in the cell with their associated assignments are represented in Figure 4.1.

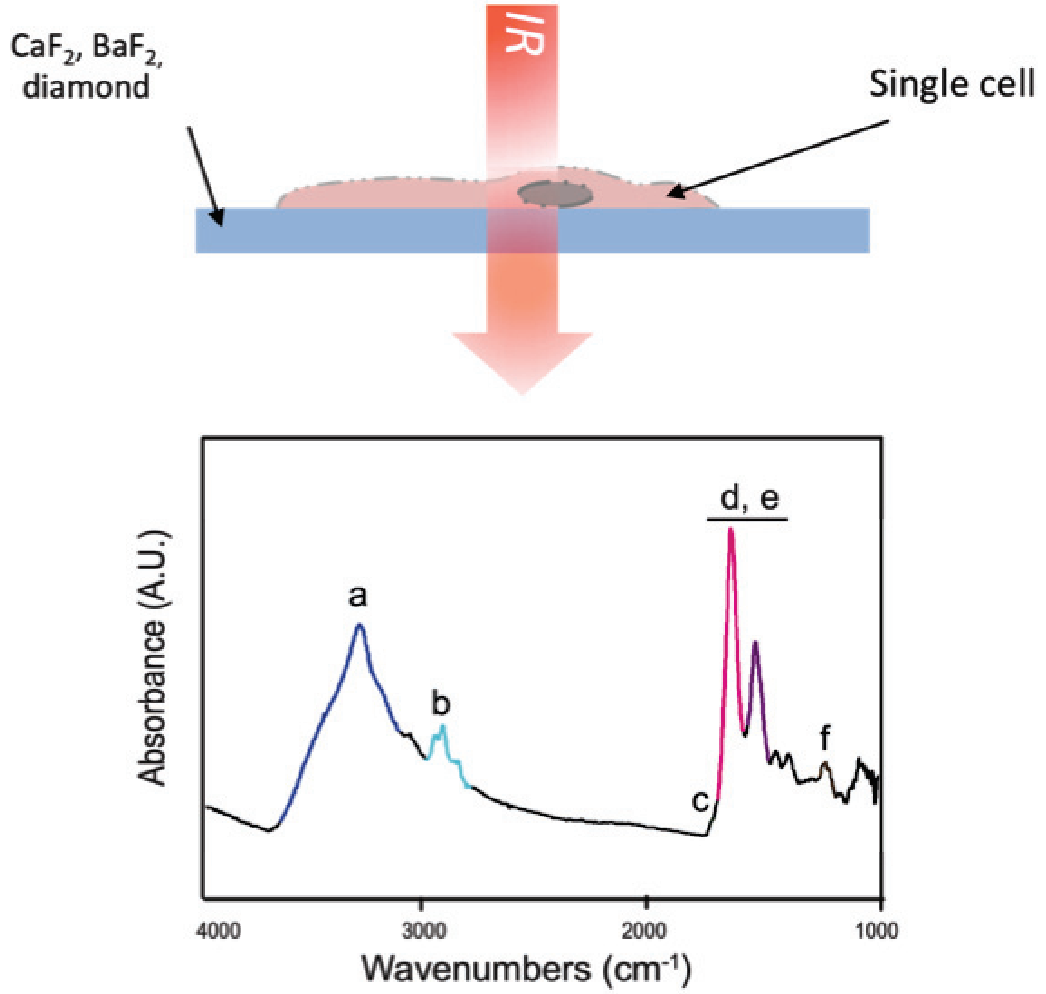

Figure 4.1 – Typical Fourier transformed infrared spectrum recorded for a single human neuroblastoma cell over a 7x7 μm aperture. The cell was grown on a CaF_2 window. For the assignment of the vibrational modes: a. N-H and O-H stretching; b. Aliphatic C-H stretching; c. C=O stretching; d. Amid I stretching; e. Amid II stretching; f. PO^{2-} asymmetric stretching. The details of these assignments can be found in Figure 4.1

Evaluation of an IR spectrum consists on identifying the chemical details in a sample based on the measured vibrational frequencies. The value of the characteristic frequencies depend not only on the chemical bond (covalent or not), whether the vibration is symmetric or asymmetric (bending of the bonds), but also on the environment. The vibrational frequencies of a sample measured by IR can provide valuable information on the non-local structure of molecules (e.g. folding, unfolding of a protein), as well.

Generally, the source of IR is a black body radiation of a glowing SiC rod (also called Globar source, for “glowing bar”). It is less efficient in the far infrared region since the intensity of the emission falls with the fourth power of the wavelength (Wiener-law). Therefore, such equipment has a very limited spatial resolution, which prevents the exploitation of fine and short spectral peaks. To overcome this problem, another source of IR light called synchrotron radiation (SR) can be used. The light is generated when electrons are accelerated in a ring, confining the charges by bending magnets, and undulators give additional acceleration to them.

	Wavenumber	Biological assignments
a	3300 cm^{-1} (gray arrow)	Originates from both the N–H and O–H bonds present in water traces, polysaccharides, carbohydrates and proteins.
b	$2995-2800\ cm^{-1}$ (green arrow)	arises from the symmetric and asymmetric stretching modes of the carbon – hydrogen bond in methylene (CH_2) and methyl (CH_3) group mainly present in lipids and protein.
c	$1740-1725\ cm^{-1}$ (blue arrow)	the resulting shoulder is attributed to the contributions of the carbonyl ester group (>C=O) in non-hydrogen bonded and hydrogen-bonded states respectively, found in phospholipids.
d,e	The two absorption peaks at 1650 and 1545 cm^{-1}	correspond to the intensity of Amide I (orange arrow) and Amide II (dashed gray arrow) respectively. Amide I originates from the C=O hydrogen bonded stretching vibrations. The Amide II peak, is also representative of a protein-based structure, and arises from C-N stretching and C-NH bending vibrations.
f	The bands at 1240 and 1085cm^{-1}	originate mainly from asymmetric phosphate (asPO^{2-}, red arrow) and symmetric phosphate (sPO^{2-}, dotted gray arrow) stretching vibrations, respectively. They are attributed to the phosphodiester groups of nucleic acids from DNA. These two bands are also attributed to the C-O-P stretching modes present in phosphorylated lipids or proteins.

Table 4.1 – Assignment of the main IR features in biological spectra.[71,143,200,225]

SR offers many advantages as compared to the Globar source, because the spectral range is broader and the high intensity photon beam allows accurate experiments.[72] Moreover, its naturally high brilliance and polarization allows the study of very small biological samples, like individual cells or scanned tissues with small aperture size. One might consider that the high brilliance is a disadvantage in measurement of biological samples because it could induce thermal heating which could damage the biological specimen. Nonetheless, M.C. Martin et al. conducted a study on temperature fluctuations over acquisition time and have shown a maximum local rise of temperature under IR synchrotron irradiation of 0.5 ± 0.2°K.[137] Consequently, Synchrotron-based FTIR microspectroscopy (or S-FTIRM) can be considered as a powerful non-destructive tool to probe bio-systems to monitor the chemical changes without using labels. In addition, when SR is used in a scanning mode, it offers the possibility to generate a vibrational map of cells or tissues, to display the chemical content in 3D and in a submicron high-stability.[143] In the next parts of this chapter, I discuss the methods and a few results on fixed and living cells following exposure to $MAPbI_3$. The S-FTIRM experiments were conducted using SR at the Swiss Light Source (SLS), Villigen, Switzerland; the Brookhaven National Laboratory, New York, USA, and at the Source Optimisée de Lumière d'Énergie Intermédiaire du LURE (SOLEIL), Gif-Sur-Yvette, France. The three laboratories are equipped with synchrotron radiation, and we used the mid-infrared range to investigate the biochemical fingerprints of $MAPbI_3$ and $MASnI_3$ toxicity on single cells. A major drawback is not solved yet in the application of IR spectroscopy: when studying living cells in a native physiological environment, strong water absorption frequencies in the mid-IR range prevent the access to some regions of interest. For this reason, biological samples are usually fixed and desiccated before acquisition of IR spectra in order to obtain resolvable data. Nevertheless, in the last part of this chapter, I report my attempt to study living cells in a liquid environment.

4.2 Use of IR to assess toxicity fingerprints on fixed samples

4.2.1 Experimental conditions

Samples preparation

SH-SY5Y and A549 Cells were maintained as previously described in chapter III. In this part, cells were plated on calcium fluoride (CaF_2) optical windows transparent for IR light (Crystran, UK) at a density of 20'000 cells. 5 days before administration to cells, $MAPbI_3$ and $MASnI_3$ powders were suspended at concentrations of 50, 100 and 200 $\mu g/ml$ in preheated culture medium. Solutions were prepared at RT and vortexed under laminar flow. They soaked during 5 days at RT, then filtered at 220 nm pore size filter (Merck Millipore, Switzerland) then stored at 4°C. Cells were rinsed with warm PBS (1x) after 5 days of exposure to the perovskite solution, then fixed using increasing concentrations of ethanol for few seconds (20%, 40%, 60% and 80%). Then samples were rinsed with ddH_2O 3 times and left overnight for drying under a laminar flow then stored in a desiccator for maximum 5 days before measurements.

IR measurements using S-FTIRM

Synchrotron-based Fourier Transform Infrared Microspectroscopy (S-FTIRM) measurements were performed on dried cells. We used a Thermo Nicolet Continum IR microscope set-up[144] coupled to a Thermo Nicolet Magna 860 FTIR (Thermo Nicolet Instrument, Madison, WI). We performed sample scanning using an automated X–Y mapping stage that has a step accuracy of 1 μm. The IR beam, with an aperture of 7x7 μm^2, was positioned on a clean area of the CaF_2 window for the background collection then centered on single cells chosen randomly using a traditional optical microscope. Spectra were collected in transmission mode, at a spectral resolution of 4 cm^{-1}, and 256 to 512 scans were co-added to enhance the S/N ratio.

Data analysis

Data were analyzed using Omnic 7.4 (Thermo Fisher Scientific Inc), and Opus (Bruker). Few bad pixels were removed and replaced by the mean value of their neighbor's pixel (e.g. for odd absorbance values). The baseline was corrected using the software's algorithm. To facilitate the resolution of different overlapping spectral contributions, we also used the second derivative of the absorbance spectra to follow the changes following exposure to $MAPbI_3$ and $MASnI_3$.

4.2.2 Results and discussion

Figure 4.2 A shows the infrared absorption spectrum of a SH-SY5Y cell recorded in the photon energy range 1000 – 4000 cm^{-1} (i.e. 0.125, 0.50 eV). The main vibrational features are marked on the figure, and the spectroscopic changes are expected in the 1200 – 1800 cm^{-1} range as presented in Figure 4.2 B. Results are shown for cells exposed to 100 $\mu g/ml$ of $MAPbI_3$ (blue line) and $MASnI_3$ (red line) and for non-treated cells (black line).

The main contribution to the spectral region detailed in Figure 4.2 B arises from the absorption bands of carbonyl and imide containing compounds, although contributions from the absorption of other organic molecules are also present. The dominant contribution is usually provided by the so-called Amide I and Amide II around 1650 cm^{-1} and 1550 cm^{-1} respectively. The two bands mostly arise from the amide groups of polypeptides and are both sensitive to their secondary structure. Application to complex biological samples is challenging and limited by the compositional complexity of the samples themselves. Cells and tissues are characterized by a complex mixture of polypeptides and other organic molecules absorbing in the same spectral region. In most cases, performing a detailed analysis of secondary structure composition is unreliable in such samples because of overlapping contributions from multiple absorbing molecules. This is particularly true for the Amide II band region, where the amide contribution overlaps with the absorption of ionized carboxylate groups, which are abundant both in protein themselves and in many small metabolites.

For this reason, the Amide I band is employed more frequently than the Amide II because of its stronger molar absorbance. The Amide I itself overlaps with contributions from nucleic acid carbonyls on the higher energy side. Yet, no significant overlap from non-protein molecules is reported to date in the low energy side of the Amide I (i.e. below 1660 cm^{-1}), where the dominant contributions are provided by α-helices and β-sheets. Despite these difficulties, the Amide I band can be used to report protein conformational changes of proteins within cells or tissues. This has been especially true for some studies on neurodegenerative diseases where the formation of amyloid deposits (or misfolded polypeptides) were shown to aggregate into a β-sheet conformation,[194] and thus fall in the Amide I peak deconvolution when analyzed with S-FTIRM.[42,43] Since they are compositionally nearly pure, they can be detected from the characteristic Amide I absorption at ca. 1625-1628 cm^{-1}.[218] In Figure 4.3, we show the second derivative of the absorbance spectra to finely probe the changes following exposure to $MAPbI_3$ and $MASnI_3$. In the 1500 cm^{-1} – 1800 cm^{-1} spectral region, the thick line shows the

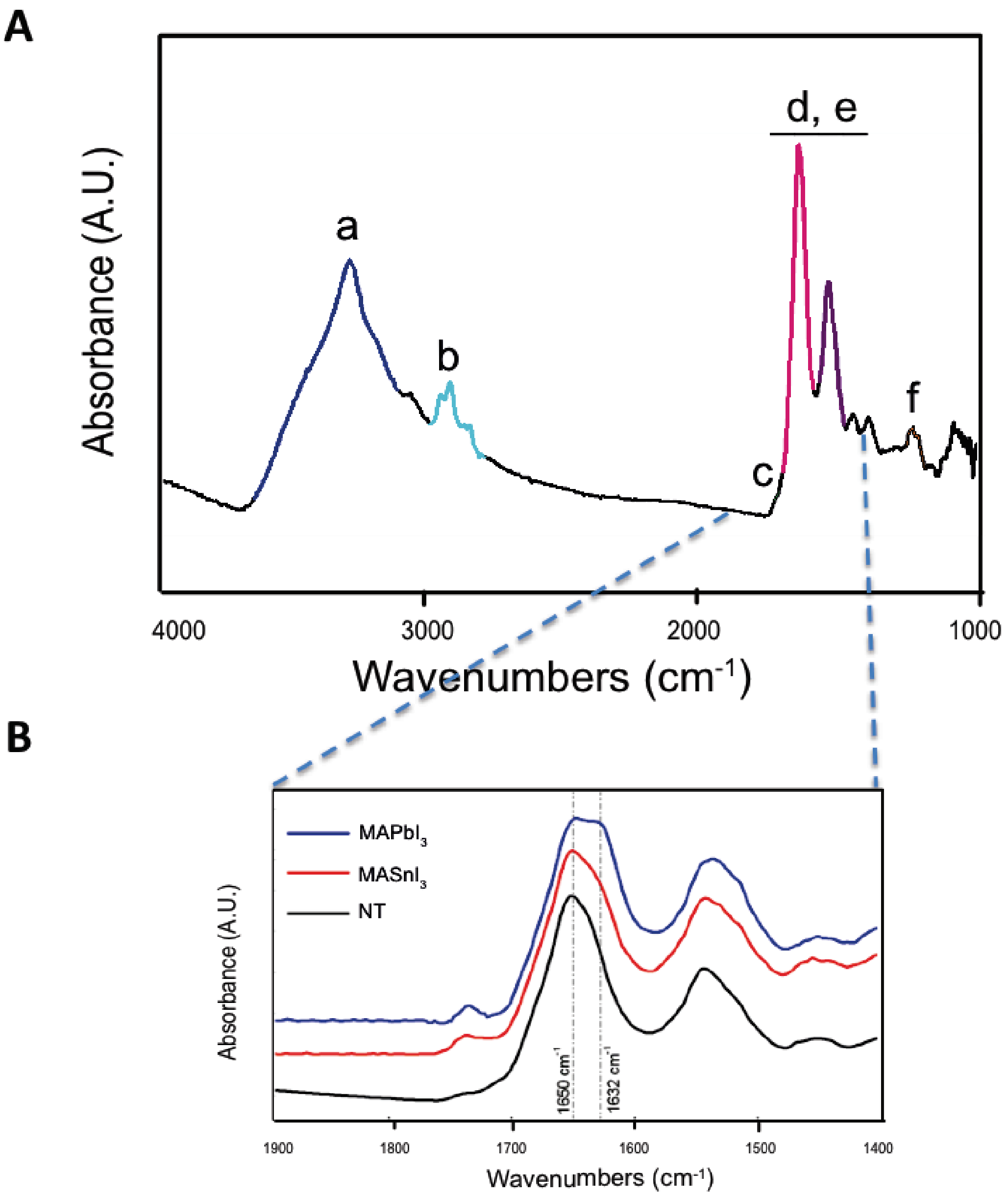

Figure 4.2 – (a) Typical spectrum of a SH-SY5Y cell with the characteristic vibrational bands (b) zoom on the absorbance in the 1350-1750 cm^{-1} range of non-treated (blue), $MAPbI_3$ (red) and $MASnI_3$ (green) treated cells using concentration of 100 $\mu g/ml$ in both cases. Cells were cultured on CaF_2 windows and IR measurements were performed 5 days post-treatment.

average trace from at least 50 spectra of individual cells. The spectra in Figure 4.3 a show the effect of exposure to $MAPbI_3$ and $MASnI_3$ on the spectra of SH-SYS5 cells. Figure 4.3 b shows the corresponding measurements performed on A549 cells. Average spectra are measured five days after treatment, and reported as their 2^{nd} derivative, showing that exposure to either metal containing agent induces major spectral changes. In treated SH-SYS5 cells, the most obvious change is observed the region of the Amide I, where two major contributions are present, at 1655 cm^{-1} and 1628 cm^{-1}. If we accept that no other contributions are present in this spectral interval except from polypeptides, the change corresponds to a marked alteration in the secondary structure of proteins within the cell. An Amide I absorption peak at 1628 cm^{-1} is characteristic for some β-sheet polypeptides. The most obvious change is the region of the Amide I, where two major contributions are observed, at 1655 cm^{-1} and 1628 cm^{-1}. If we assume that no other contributions are present in this spectra interval except from polypeptides, the change corresponds to a marked alteration in the secondary structure of proteins within the cell. A weaker contribution is also observed at 1691 cm^{-1}, which can arise from a variety of molecules, including β-sheet polypeptides, nucleic acids and small molecules, such as ketones and sphingolipids. This pattern is common to most eukaryotic cell types, and is due to the abundance of α-helical proteins absorbing around 1650 cm^{-1}. Another recurrent feature is the doublet at 1740 cm^{-1} and 1720 cm^{-1}, from ester carbonyl groups, mostly from phospholipids. A contribution to this region from the protonated form of carboxylic acids is also known. Due to the preparation protocol of the samples, involving repeated washings and fixation, it is likely that contributions from small molecules, such as metabolites and transmembrane molecules, have been removed, except for acyl lipids, which are at least partially retained by fixation protocols.

Production of uric acid, as expected from a nucleic base derivative, can be induced by lead exposure. However, its absorption falls in the 1690 cm^{-1} region and the bulk of the compound is expected to be washed away during the fixation protocol, together with other small molecule metabolites. Possible $MAPbI_3$ degradation products, including lead oxides and salts, acetonitrile and iodine anions, do not absorb in the spectral region of Amide bands. Most of them are also water soluble and removed during sample preparation. Therefore the contribution from any small molecules to absorption around 1630 cm^{-1} is ruled out. We propose that the strong band at 1628 cm^{-1} arises from extensive conformational changes in the polypeptide complement of the cells. Major changes are also seen in the Amide II region, with new lower frequency components appearing within this multiplet. Although the latter components are unresolved and this spectral region overlaps with carboxylate absorptions, the observation of parallel changes in the Amide I and Amide II regions is a necessary condition to assign the latter to polypeptides. An additional change induced by $MAPbI_3$ exposure is the relative decrease in intensity of the doublet at 1740 and 1728 cm^{-1}. Absorption from this doublet mostly arises from the headgroups of acyl lipids, mainly from intracellular membranes. The decrease of this contribution can arise from the disruption of some of the membrane systems inside the cell. The intensity of the band at 1628 cm^{-1} relative to the one at 1655 cm^{-1} is surprising, as the two bands are of comparable intensity (Figure 4.3 a, b), indicating the presence of a similar amount of polypeptides in the β-sheet and in the α-helix conformation. This corresponds to a massive change in the composition and/or the structure of the cellular proteome. These observations are consistent with the report that exposure of cells to $MAPbI_3$ induces degra-

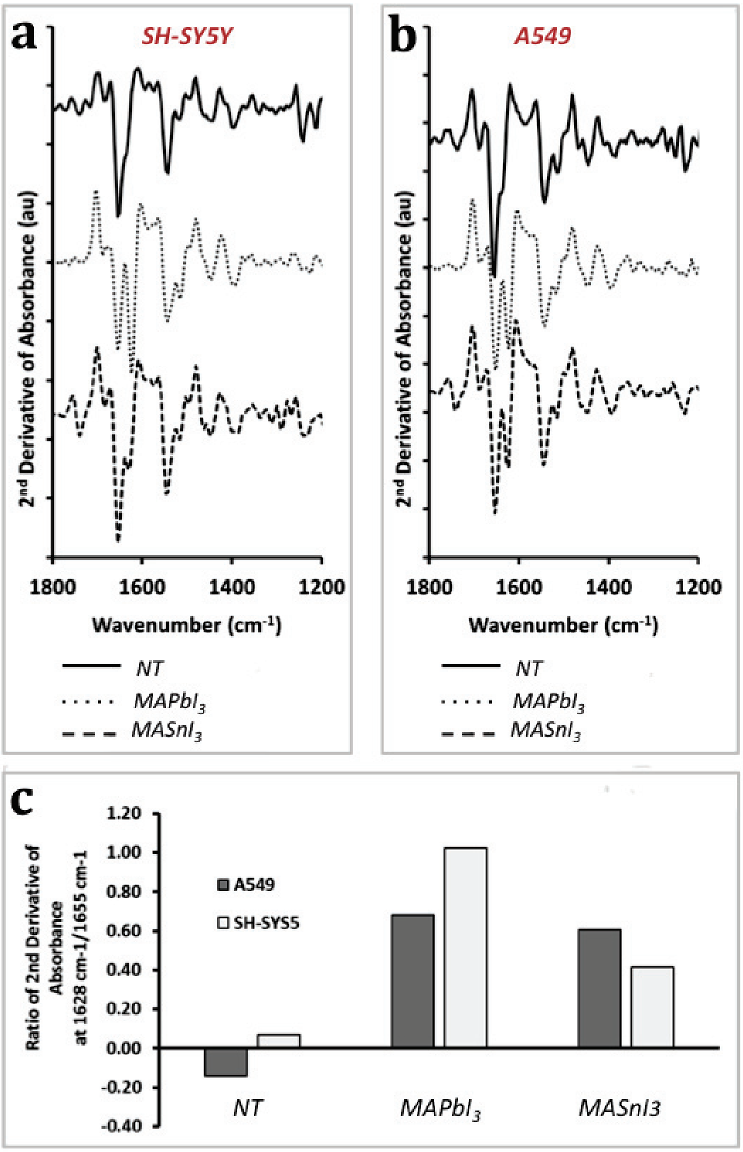

Figure 4.3 – Average 2^{nd} derivative of IR absorbance spectra in the 1200-1800 cm^{-1} range for SH-SY5Y cells exposed and non-exposed to $MAPbI_3$ and $MASnI_3$ (a), and for A549 cells, exposed and non-exposed to $MAPbI_3$ and $MASnI_3$ (b). All measurements were performed five days after exposure. (c) The ratio of 2^{nd} derivative of IR absorbance at 1628 cm^{-1} and 1656 cm^{-1} for SH-SY5Y and A549 cells five days following exposure. The small negative value of the ratio for untreated cells is due to the lack of a significant contribution from a 1628 cm^{-1} peak.

dation of the subcellular structures while triggering an apoptosis-like cell death, as reported in chapter 3 and published recently by our group.[36] Figure 4.3 c compares the ratio of the second derivative of absorption at 1655 cm^{-1} over 1628 cm^{-1} for untreated SH-SY5Y cells and for cells treated with $MAPbI_3$ or $MASnI_3$. The effect of $MAPbI_3$ on the relative structure of the proteome appears to be about four times larger. By raster-scanning single cells using S-FTIRM, IR maps of cells can be collected at various frequencies. Figure 4.4 shows IR maps of cells measured at 1652 cm^{-1} and 1628 cm^{-1}, allowing us to appreciate the distribution of the respective absorptions throughout the cell. The maps plot the value of the second derivative of absorption at the chosen wavelength (see the caption for each panel). Absorption at 1652 cm^{-1} is present in all cells, both treated and untreated. Its distribution approximately follows the topographic profile of the cell, as observed previously. Absorption at 1628 cm^{-1} has been observed only in treated cells and also tracks the profile of the cell. The resolution of the mapping measurement is close to the value allowed by diffraction, approximately $6-7$ μm for the Amide I region. The fixed and dried cells measured in these experiments are about 60 μm in size when untreated, and about $10-40$ μm when treated. As a consequence, it is difficult to resolve the distribution of IR absorption at 1628 cm^{-1} within the cell itself.

In summary, I used S-FTIRM on fixed and dried samples to investigate the biochemical and structural fingerprints of the cytotoxicity of $MAPbI_3$ and $MASnI_3$. The main changes in IR spectra following perovskites treatment were observed in the Amide I region. The effect of exposure to $MAPbI_3$ and $MASnI_3$ on A549 cells is similar to what is observed for SH-SY5 cells in the mid-IR region. Both compounds induce the formation of a strong band around 1628 cm^{-1}. The main difference between the spectroscopic response of the two cell lines is that the intensity of the band at 1628 cm^{-1} is comparable between $MAPbI_3$ treated and $MASnI_3$ treated A549 cells. These IR fingerprints of toxicity on fixed cells should be pursued at the protein level by probing the proteome profile of treated vs. untreated cells. Meanwhile, we have also measure IR absorption on living cells, to probe the real-time toxic effects of perovskites. This is reported in the following subsection.

4.3 Toxicity investigation by IR on Live cells

Cells live in a water-rich environment, and this is the major challenge for IR studies, because the vibrational frequency of O-H in water molecules overlaps with the stretching C=O from the amide bonds in proteins, which prevents access to the protein region and makes real-time imaging *in situ* of living cells difficult. Different solutions have been explored to overcome this restriction. For example, supplementing the physiological medium with D_2O, which shifts the water absorption peak away from the mid-IR range. Another option employed by Jamin et al.[112] consisted in growing cells on a barium fluoride (BaF_2) infrared window, and then apply a low-speed cytospin centrifugation. Thus cells were deprived of culture medium, and examined for 2–3 hours only. With such methods, IR measurements on living cells are possible, and images of proteins, lipids, and nucleic acids can be obtained with a spatial resolution of a few microns without labels. However, cells are not in physiological conditions, their vital processes are altered, and their viability is reduced.[118, 202] The second objective in IR studies was then the elaboration of a system to grow cells and measure their infrared absorption spectra in physiological environment. With such a device, I could run preliminary tests to assess the toxic effects of perovskites in real time.

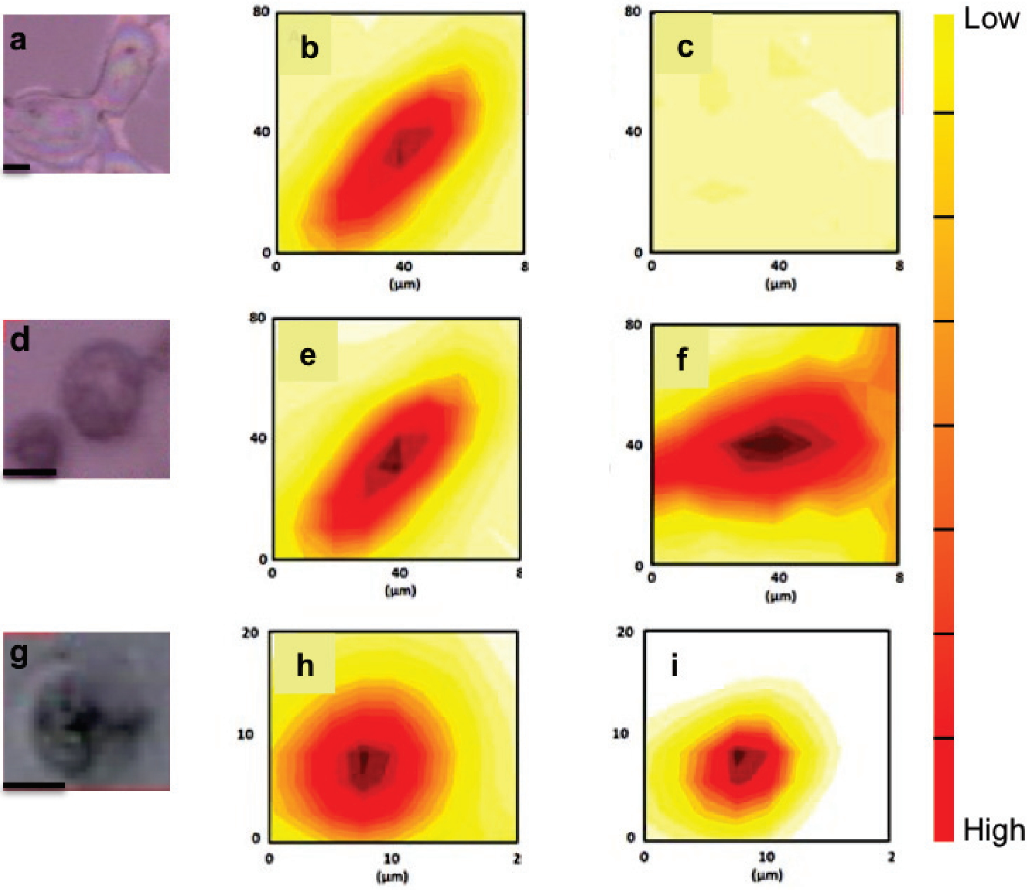

Figure 4.4 – Transmission IR absorption maps of SH-SYS5 cells. A – Bright Field (BF) micrograph of SH-SY5Y untreated cell, B- Map at 1652 cm^{-1} of an untreated cell following fixation. C – Map at 1628 cm^{-1} of the same cell as in B. D – BF micrograph of 100 $\mu g/ml$ $MAPbI_3$ treated SH-SY5Y cell, E– Map at 1652 cm^{-1} of a cell following treatment with 100 μg/ml $MAPbI_3$ and fixation. F – Map at 1628 cm^{-1} of the same treated cell as in E. G - BF micrograph of 100 $\mu g/ml$ $MASnI_3$ treated SH-SY5Y cell, H– Map at 1652 cm^{-1} of a cell following treatment with 100 μg/ml $MASnI_3$ and fixation. I – Map at 1628 cm^{-1} of the same cell as in H. Maps A to D were recorded by using a 10 x 10 μm^2 aperture and 10 μm steps. Maps E to F were recorded by using a 10 x 10 μm^2 aperture and 3 μm steps. All maps show the distribution of minus the intensity of the second derivative of absorbance at the given wavenumber value. The cells treated with $MAPbI_3$ or $MASnI_3$ show an intense absorption band at 1628 cm^{-1} with approximately the same distribution as the 1652 cm^{-1} component of the Amide I band. The 1628 cm^{-1} band is absent in the untreated cell. The scale bar in the micrographs represent 10 μm.

4.3.1 Methodology

Samples preparation

Human neuroblastoma and lung epithelial cells (respectively SH-SY5Y, and A549 cell lines) were maintained as previously described in chapter 3. For S-FTIRM live imaging experiments, cells were grown on CaF_2 optical windows, 0.5 mm thick and 13 mm in diameter, at 50% confluence. $MAPbI_3$ perovskite was used in S-FTIRM *in situ* tests for preliminary toxicity assessment, at a concentration of 100 $\mu g/ml$.

Flow cell incubator for S-FTIRM measurements

The scheme of our IR flow cell is shown in Figure 4.5. It consists of a metallic chamber where an inlet and outlet were drilled for medium exchange, and for a closed water circuit to maintain the temperature at 37°C. A CaF_2 window of 1 mm in diameter is deposited on a rubber O-ring, and covered by a top CaF_2 window in which cells are grown. A gold spacer less than 5 μm thick separates the two CaF_2 windows and assures a homogenous thermal conduction. Medium exchange is assured *via* Teflon tubing connected to a 1 μL micro syringe (Hamilton Bonaduz AG, Switzerland). Medium flow was as low as possible since it could induce relatively high hydrostatic pressure, and causing the cells to detach. The flow cell was designed to fit the shallow 1.9 and 1.0 mm working distance of the high-magnification 52 x or 74 x Schwarzschild objectives.

S-FTIRM data collection

S-FTIRM experiments were conducted at the National Synchrotron Light Source (Brookhaven National Laboratory, NYS), at beamline U10B.[16] The infrared microscope was equipped with a focal plane array (FPA) imaging detector. All spectra were collected in transmission mode every 20 minutes using OPUS (v. 6.5, Brucker, Germany), and the aperture size was 10*10 μm^2. The spectral resolution was from 8 to 32 cm^{-1}, and 256 scans were co-added in order to improve the S/N ratio. Prior to each spectrum collection, a background spectrum was carefully taken on an empty spot as close as possible to the targeted cell. Then, a linear baseline was subtracted. Experiments were done at room temperature, 3h following the extraction of cells from the incubator to avoid bubbling inside the medium exchange tubing. Bright field images were taken simultaneously to spectra collections.

4.3.2 Results

From the bright field images (Figure 4.6), I could already observe during spectral collection the same morphological effects caused by exposure to perovskites as discussed in chapter 3 . Moreover, our flow cell has the potential to maintain cell culture for several hours, without causing loss in viability, thanks to the continuous flow of culturing medium, and temperature stabilization at 37°C.

Interestingly, the collected IR transmission spectra between treated and non-treated living cells, the protein region looked similar. However, a visible change in intensity could be observed at 1041 cm^{-1} and 1128 cm^{-1} (Figure 4.7), likely due to lactates and lactic acid contribution.[52] Lactates are both waste products and active metabolites in cells, which may be oxidized as a fuel, or reconverted to pyruvate or glucose in the liver by lactate dehydrogenase isoforms and gluconeogenesis respectively.[171] When lactates are over-secreted by cancer cells, pH is slightly modified in the microenvironment, which increases tumour cell survival and proliferation, but it also stimulates angiogenesis, as lactate is consumed as a substrate.[180] Moreover, lactate accumulation in tissues has been found in many diseases including cancer

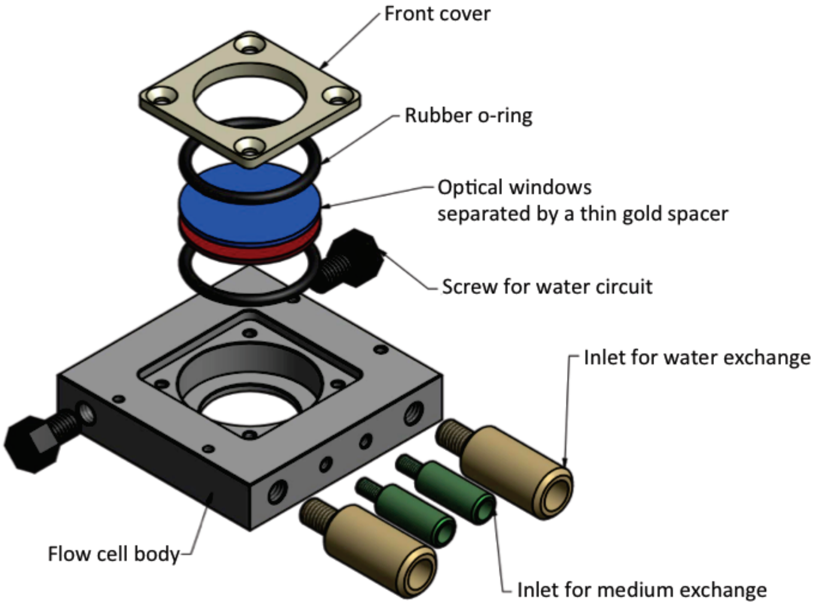

Figure 4.5 – 3D view of the S-FTIRM flow cell set-up: (a) microscope sample holder (b) gold spacer / rubber o-ring (c) rear window (CaF_2) / Cell holder (d) front cover (f) screw for water circuit at 37°C, and screw for medium exchange between the optical windows.

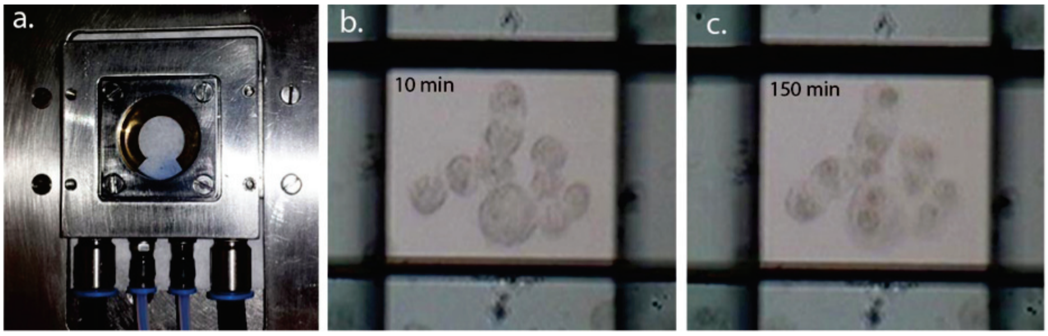

Figure 4.6 – a) image of the liquide cell designed for S-FTIRM measurements. The optical window is of 15 mm. b) A549 lung cells exposed to perovskite for 10 min and c) after 150 min. The changes on the cell membrane and nucleus densification are already visble.

and diabetes.[20] A study conducted on rat lungs after acute exposure to cadmium chloride showed a significant increase in lactate and other metabolites. These changes were correlated with a dysfunction of dehydrogenase activity and consequently leading to mitochondrial injury.[102] The differences in IR signature between fixed and dried cells are certainly due to the time-lapse in which I explored the biochemical changes: fixed cells were exposed to perovskites during 5 days, whereas living cells during less than 12 hours. In situ studies of toxicity using SR do not allow several days of time frame because of the availability of the synchrotron beam on the one hand, and because the flow cell does not represent an ideal physiological environment for the living cells on the other hand. Although temperature is maintained at 37°C, and the medium is renewed *via* the flow exchange system, cells are constantly exposed to light, the circuit of medium exchange is closed and limited in volume to the syringe capacity, and CO_2 is not maintained at 5%. For these reasons, the two methods are complementary since they do not cover the same exposure time to perovskites.

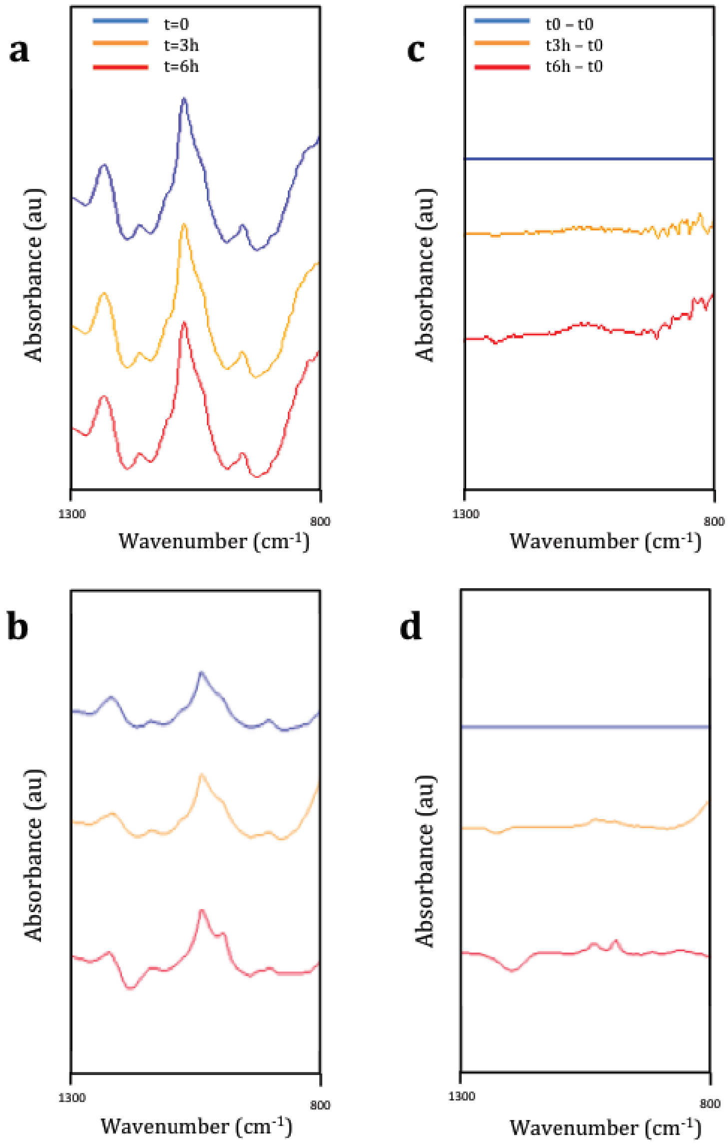

Figure 4.7 – Live IR transmission spectra of A549 cells non-exposed (a) and exposed to $MAPbI_3$ (b), 3 and 6 hours after the beginning of the measurement. The respective substraction from t0 are shown for non-exposed (c) and exposed (d) cells.

4.4 Discussion and outlooks

This study, with clear biochemical fingerprints, confirms the severe consequences of $MAPbI_3$ on human cells. I have used the common methods to prepare biological samples for S-

FTIRM to perform, for the first time, a toxicity study showing notable biochemical changes. We assume that the potential of the observed toxic effects of $MAPbI_3$ are mainly due to the release of lead after dissolution, and uptake by the cells. It has been proposed that the chemical origin of toxicity of lead ions is their capability of replacing Zn^{2+} in a native binding site in proteins, while altering the coordination geometry of the site, from tetrahedral to trigonal pyramid. Pb^{2+} is known to bind tightly to Zn^{2+} binding protein under physiologically relevant conditions, thereby disrupting their function. The change in geometry leads in turn to a destabilization of the polypeptide conformation which is normally stabilized by Zn^{2+} and to overall conformation changes.[134] This mechanism results in loss of function many proteins with a zinc finger. Overall, studies in the coordination chemistry of Pb^{2+} –bound polypeptides support the notion that binding of Zn^{2+} by Pb^{2+} can in general induce major conformational changes of polypeptide conformation. Identifying the protein or proteins that are associated to the conformational changes observed in both Figure 4.2 and Figure 4.3 is of great interest in understanding the biochemical origin of Pb^{2+} and Sn^{2+} toxicity. Therefore, a correlation can be achieved between our results together with previous reports in the literature and our own ongoing study of modification of gene expression upon exposure to $MAPbI_3$ and $MASnI_3$. Binding of lead to metallothioneins has been studied *in vitro* and proposed to occur *in vivo*.[92] Zinc finger proteins and model peptides are among the known targets of Pb^{2+} binding *in vitro* and *in vivo*.[98] Many of these proteins are transcription factors and use their Zn^{2+} binding domain for DNA binding. Disruption of their conformation results in loss of regulatory function and subsequent aberrations in cellular development. These findings are consistent with the results on cellular cycle impairment, which were recently reported from our toxicological studies.[36] In addition to IR spectroscopy, the proteome profile in both the cytosolic and vesicular fractions should be quantified. This approach is only quantitative, because it will identify the size of up- or down-regulated proteins upon perovskites exposure, which will strengthen the spectral outcomes of IR, and to validate the structural changes, circular dichroism could be applied.

5

In vivo ecotoxicity study of $MAPbI_3$ and $MASnI_3$

5.1 Introduction to the *in vivo* study

Within the field of biology, much of our knowledge relies on scientific testing using *in vivo* and *in vitro* models. In the case of disease studies, drug trials or toxicity, preliminary tests are first conducted *in vitro*, then *in vivo* by using a whole living model organism. *In vivo* testing is often employed over *in vitro* because it is better suited for observing the overall effects of an experiment on a living subject. However, each laboratory animal model has its strengths and limitations, and none is scientifically perfect, even studies on humans show unpredictable results for a large population.[110] The most used models in the laboratory are rodents. Many publications discuss the limitations of these models in terms of cost (money- and time-wise),[148,209] unpredictable outcomes in humans,[101,160] and throughput.[120] Beside these limitations, ethic regulations often represent an additional hurdle. An alternative to rodents could be the use of invertebrate small organisms widely applied in ecotoxicology. Such small organisms can be handled in laboratory by using *in vitro* techniques and can provide data for a whole animal with a metabolically active digestive, reproductive, endocrine, sensory and neuromuscular systems.[110] Moreover, trials on invertebrates are short (for example few weeks only for life span studies), not expensive and do not require ethical approval. We wanted to check how do the *in vitro* observed anomalies translate on small organisms treated by $MAPbI_3$ and $MASnI_3$ perovskites. For this purpose I have selected *Drosophila melanogaster* (the common fruit fly) and *Caenorhabditis elegans* (soil nematode) to investigate the toxic effects. In this chapter I introduce the two models and the methodology used for toxicity screening and the related results.

5.2 Ecotoxicity of MAPbI$_3$ and MASnI$_3$ on *Drosophila melanogaster*

5.2.1 Introduction to the model

Drosophila melanogaster, commonly referred to as the fruit fly is a small organism that has rapidly become a model due to the huge contributions in developmental biology studies and the field of genetics. Thomas Hunt Morgan popularized the use of *D. melanogaster* with his first studies on heredity at Columbia University in 1910.[55] The genomes of *Drosophila melanogaster* and eleven other species have been fully sequenced and annotated. Approximately 75 % of known human disease genes have a recognizable match in the fruit fly genome. In consequence, Drosophila is used in many biological studies as a gold standard to investigate the molecular mechanisms of diverse human diseases and conditions including cancer,[232] infertility,[103,125] neurodegenerative disorders,[83,185] immunity[128] and toxicity.[29,56] In addition, it is very easy to maintain flies culture in the laboratory, their food is made of an agar mixture containing mainly cornmeal and yeast. In addition, their rapid development allows a generation time of 10 days from egg to young adult at 25°C (see the life cycle in Figure 5.1). Other advantages to use Drosophila as a model include their short life span (about two months at 25°C), high fecundity (a mated female can generate an extensive progeny), adjustable life cycle by temperature and relative ease to perform genetics and cell biology experiments. Moreover, this organism has been widely studied and there is a large amount of (genetic) resources available, essentially mutants, and spatio-temporal RNAi for every gene.

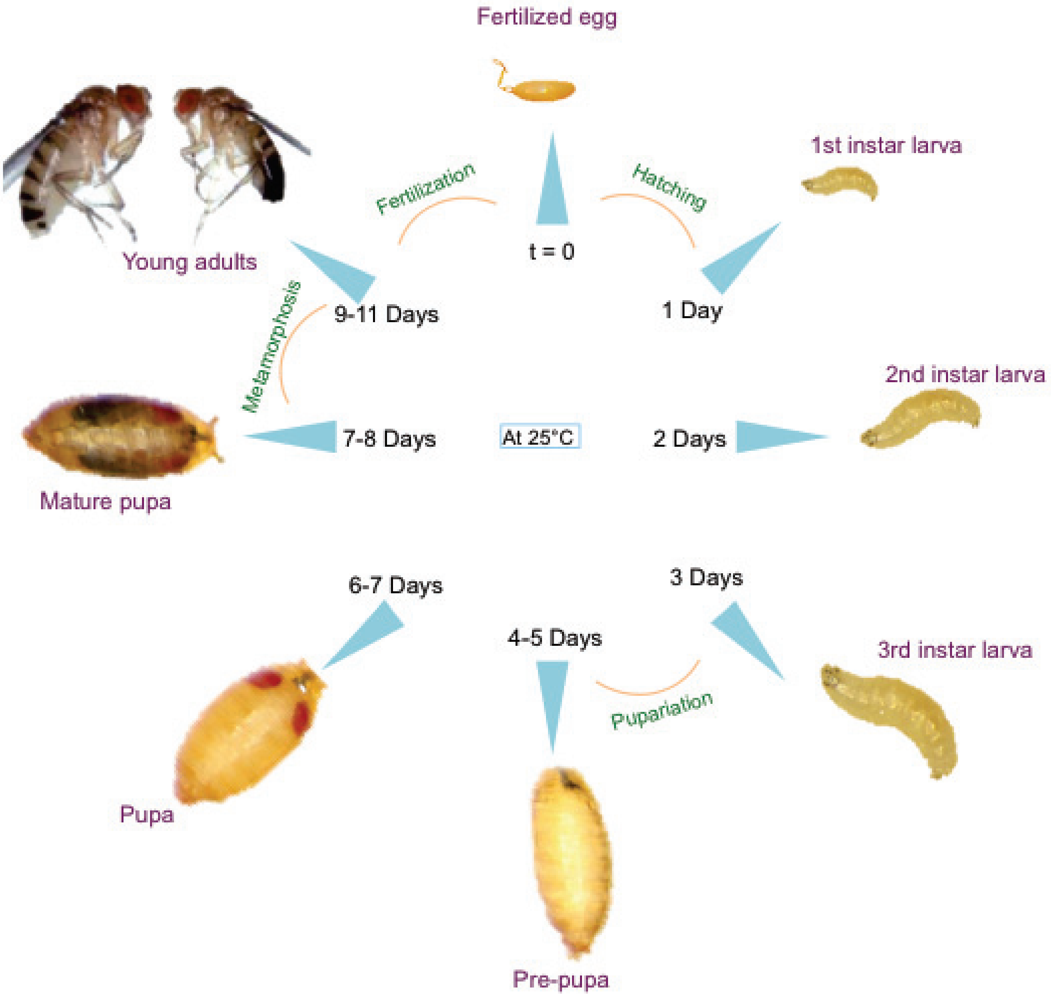

Figure 5.1 – Life cycle of the fruit fly *Drosophila melanogaster* at 25°C. The development includes 4 stages: egg, larva, pupa and adult. The transition from egg to larva is called hatching, and from larva to pupa called pupariation, Finally, the transformation from pupa to an adult insect is called metamorphosis.[131]

In this study, we used two genotypes *D. melanogaster* (Figure 5.2): Oregon-R with red eyes (Or) and white minus (w-) that has white eyes because the alleles “white” responsible for the eye pigmentation are recessive.[158] Both strains are wild types and are used commonly in research on diseases, drug development, chronic and acute stress.[39] We mixed the culturing food with the $MAPbI_3$ and $MASnI_3$ perovskites at different concentrations and investigated the life span, fertility and the life cycle of the flies. We used concentrations ranging from 50 to 1000 μg/vial administered as a single dose. In this case, flies were exposed to 10 to 200 $\mu g/ml$ of food during 2 days, at a single dose. The dry mass of an adult fruit fly is 0.25 mg (±0.05),[229] therefore these concentrations represent in total 4 mg per 100mg of body weight. This dose is below the range of previous acute and chronic toxicity studies of silver and aluminium nanoparticles on *Drosophila melanogaster*.[117,168]

Figure 5.2 – Wild type *D. melanogaster* genotypes used in our study: Or (red eyed) and w- (white eyed).

5.2.2 Materials and methods

Culturing and treatment of *D. melanogaster* strains

The wild type flies used for this study are Oregon (Or) and White – (w-) strains, obtained from the Bloomington stock center.[1,5] The fly medium recipe that we used is the following (for 1 l water): 6.2 g agar powder (ACROS N. 400400050), 58.8 g Farigel wheat (Westhove N. FMZH1), 58.8 g yeast (Springaline BA10), 100 ml grape juice, 4.9 ml propionic acid (Sigma N. P1386), 26.5 ml of methyl 4- hydroxybenzoate (VWR N. ALFAA14289.0) solution (400 g/l) in 95% ethanol and 1 l water. Fly culture was maintained at 25°C in specific culturing vials of 28.5 mm in diameter (Fischer Scientific) and capped using cotton lids. Each vial contained 5 ml of food. 20 mg of perovskite powder was first suspended in 200 μl of water, and after vortexing, the suspension was added to the preheated fly medium at a final concentration of 50, 100, 200, 500 and 1000 μg per vial with 5 ml of food, then placed at room temperature overnight (RT, O/N), and kept at 4°C. Before treatment, flies were food-deprived for one hour.

Lifespan assay

Female fruit flies represent a reference in life cycle studies because they are capable of laying hundreds of eggs allowing the population to multiply. Therefore, we isolated 30 mated adult females on CO_2 pads and placed them into vials containing regular fly medium alone or supplemented with perovskites ($MAPbI_3$ or $MASnI_3$ from 50 to 1000 μg/vial). Flies were incubated at 25 °C and the number of dead flies was counted on a daily basis until the whole population perished. Flies were transferred into new vials containing regular food every 3 days because the medium becomes sticky due to the presence of eggs on the surface. Each condition was prepared in triplicate, and the life span test was performed on both Ore and w- strains three times independently.

Fertility and life cycle study

The fruit flies were maintained at 25 °C on regular culturing media. Virgin females and males were isolated as soon as they emerged and placed inside regular vials during 2 days in regular medium or medium spiked with 50 μg of $MAPbI_3$ or $MASnI_3$ (10 $\mu g/ml$). Mating was then allowed inside home-made demography cages covered with a petri dish (60 mm in diameter) containing agar as follows: virgin females exposed to perovskites during 2 days (V2d) mated with untreated males (UM), virgin untreated females (VU) coupled with males exposed to perovskites for 2 days (M2d), and virgin untreated females with untreated males as a negative control. Eggs were collected the following day using the Jove protocol,[2] and transferred into culturing vials as follows: eggs generated by V2d + UM and VU + M2d were transferred into regular fly medium, and eggs from VU + UM placed into regular medium or medium spiked with 50 μg of $MAPbI_3$ or $MASnI_3$. The number of mature larvae together with the number of emerged young adults was counted twice per day for three weeks (Figure 5.3). This experiment was performed independently two times and in duplicate for each condition.

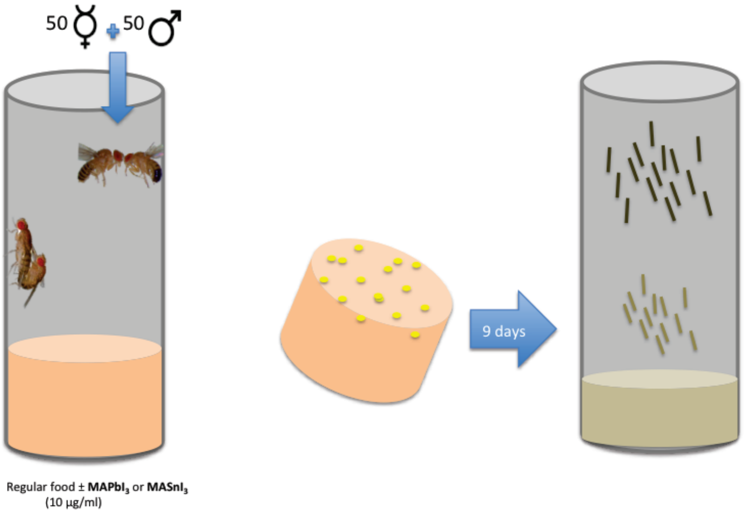

Figure 5.3 – Illustration of the fertility and development assays on *Drosophila melanogaster*.

Statistical analysis

Charts show the combination of minimum two independent repeats for life span and life cycle experiments; each condition was prepared in duplicate or triplicate. All data were cumulated by time point for each condition, and plotted as the mean standard deviation (S.D) using One-way ANOVA test followed by a Tukey-Kramer post-hoc test (non-treated vs. treated conditions). The p-value is represented as follows: *<0.05, **<0.005 and ***<0.0005.

5.2.3 Results

Effects on the lifespan

The lifespan study consisted on exposing the flies to culturing food with or without perovskites at increasing concentrations, and then we monitored the survival rate on a daily basis until the end of the life cycle and compared the different concentration of treated conditions to non-treated. The non-treated flies exhibit a standard life span curve where half of the population dies after approximately 60 days (Figure 5.4 dark blue lines). Exposure of Or flies to $MAPbI_3$ induces a decrease in their survival rate in a time- and dose-dependent manner (Figure 5.4 a). Moreover, after approximately 50 days, half of the fly populations did not survive in almost all treated conditions with concentrations from 10 to 200 $\mu g/ml$ of food. Interestingly, we observed the same effects following $MASnI_3$ exposure (Figure 5.4 b). The life span of w- strain was affected in the same trend as Or, and the time where half of the population perished remained 60 days for the negative controls and 50 days for the exposed flies (Figure 5.4 c, d). However, w- flies started to die earlier following $MASnI_3$ exposure (after 10 days) at a faster rate.

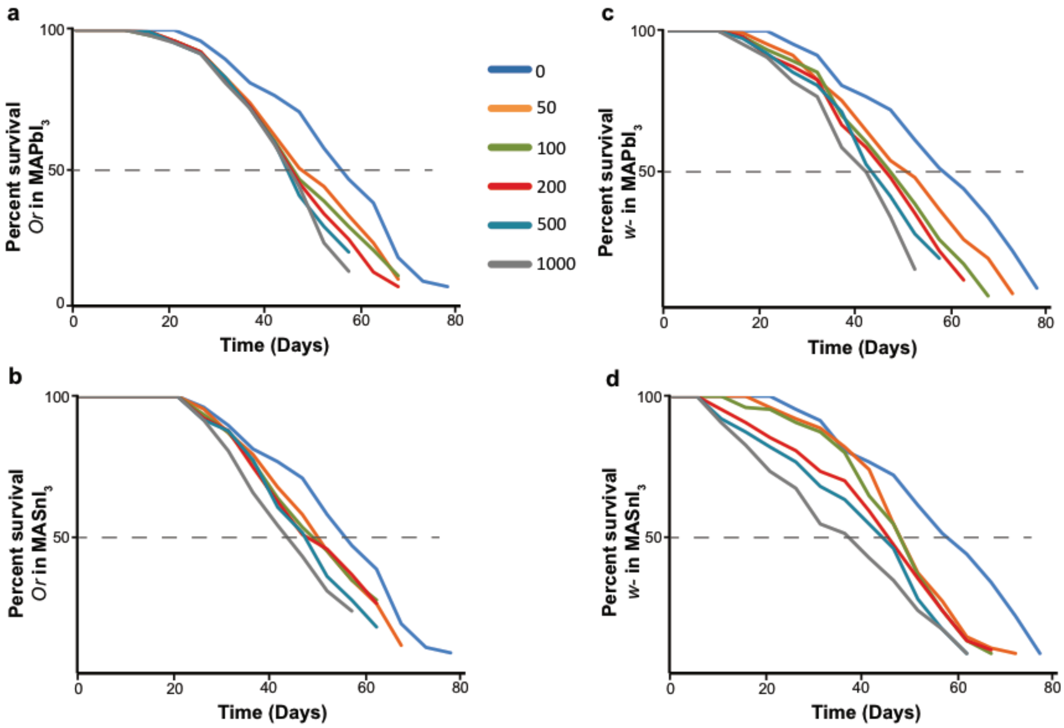

Figure 5.4 – Life span curves of treated vs. non treated flies treated with increasing doses of $MAPbI_3$ or $MASnI_3$ (0-1000 μg in 5 ml of food): Percentage of Or flies surviving the exposure of $MAPbI_3$ (a), or $MASnI_3$ (b), and the percentage of w- surviving the exposure of $MAPbI_3$ (c), or $MASnI_3$ (d).

Effects on fertility and life cycle

We next investigated how exposure of young adult flies to perovskites affects their fertility and the development of their progeny. To do so, we sorted the young adults by gender, as soon as they freshly emerged from the pupae stage. The isolated virgin females and males were immediately incubated at 25°C into different culturing environments (regular food with or without perovskites). After two days of age, we transferred them into cages for mating and collected the eggs after 24 hours. Fertilized eggs were collected then exposed to different culturing media (details in the materials and methods section). Finally, we probed the development rate by quantifying the mature pupae and the emerged young adults. This test also identifies whether the origin of toxicity is endogenous (coming from the parent male and/or female) or exogenous (due to the presence of perovskites in the food).

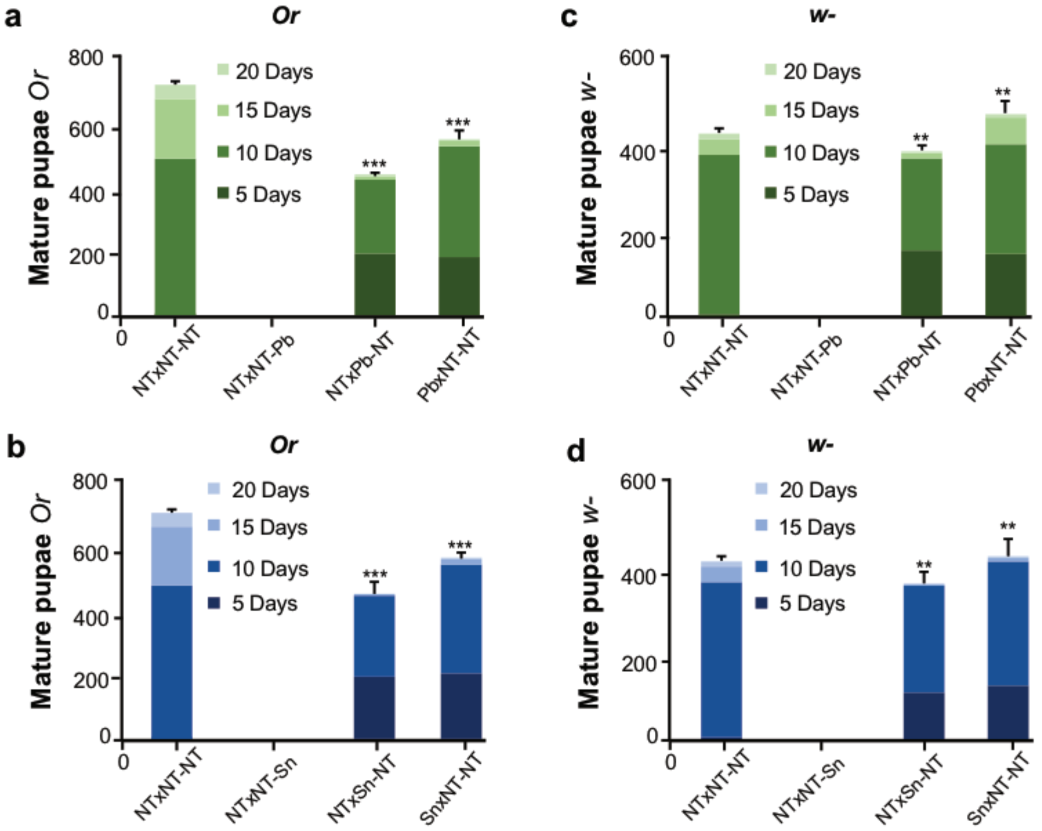

Figure 5.5 – Development test of eggs to the pupa stage generated by treated vs. non-treated flies that were exposed to 50 μg of $MAPbI_3$ (green bars) or $MASnI_3$ (blue bars). The x-axis shows the different conditions of progeny generated as follows: Male x Female – Final food; where NT is non treated, Pb refers to exposure to $MAPbI_3$ and Sn to treatment with $MASnI_3$. The number of mature Or pupae over exposure to $MAPbI_3$ (a) or $MASnI_3$ (b), and the number of mature w- pupae over exposure to $MAPbI_3$ (c) or $MASnI_3$ (d) were probed during 25 days. All histograms show an average of standard deviation (S.D.) using One-way ANOVA test followed by a Tukey-Kramer post-hoc test (non-treated vs. treated conditions), p-value<0.005.

Figure 5.5 shows the quantification of mature pupae in Or (a, b) and w- (c, d) strains that were generated by parents exposed to a single dose of 50 μg of $MAPbI_3$ (green bars) or $MASnI_3$ (blue bars). Eggs generated in regular food by non-treated flies developed normally to larvae then to pupae within 9 to 10 days (cf. "NTxNT-NT" conditions). Remarkably, eggs that were generated by non-treated parents and transferred to the perovskite-containing food were unable to develop further than the 1^{st} instar larva stage and died (cf. Figure 5.5 "NTxNT-Pb" or "NTxNT-Sn" conditions and Figure 5.6). This observation suggests that perovskites do not have a pronounced effect neither on embryonic development of *D. melanogaster* eggs nor on the hatching phase (transition from egg to larva), however they are extremely toxic to the 1^{st} instar larvae since they inhibit their development and induce their death. Regarding the progeny of Or parents that were exposed separately to perovskites (Figure 5.5 a, b), the embryonic development was heavily accelerated since mature pupae could already be observed after 5 days. In the case where the male parents were exposed ("NTxPb-NT" or "NTxSn-NT" conditions), the number of mature pupae continued to increase and stopped at 16 days for $MAPbI_3$ and at 11 days for $MASnI_3$. On the other hand, the progeny of treated females ("PbxNT-NT" or "SnxNT-NT" conditions) exhibited a similar amount of mature pupae after 10 days and very few after 15 days. We can also appreciate that $MASnI_3$ has a stronger effect on the progeny development than $MAPbI_3$.

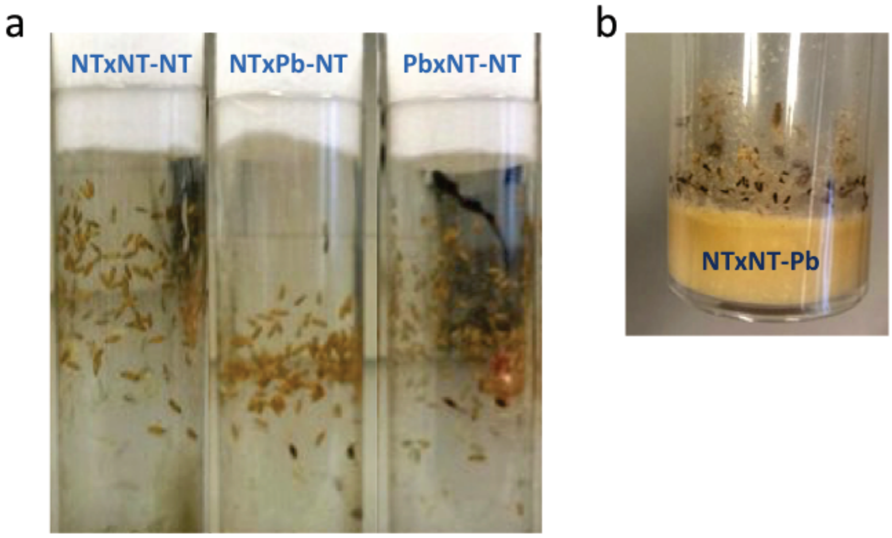

Figure 5.6 – Photographies of the progeny generated by treated or non-treated flies: 1^{st} generation of mature pupae grown on non-treated food (a) from non-treated flies (NTxNT-NT); treated male parent only (NTxPb-NT); or treated female parent only (PbxNT-NT); and progeny transferred into food containing $MAPbI_3$ (b) in which the development is altered.

Although w- strain is known to have a slower proliferation rate than Or, w- pupae also suffered a premature development when one of their parents was exposed to perovskites (Figure 5.5 c, d). As described for Or, the same trend can be observed on w-; where 1) no development could be observed when eggs generated from non-treated parents were transferred into food mixed with perovskites; 2) the total number of mature pupae between 15 and 21 days notably decreased upon treatment with perovskites; and 3) $MASnI_3$ had a higher impact on the development than $MAPbI_3$. Nevertheless, the only difference can be observed from the conditions where female progenitors were exposed to $MAPbI_3$ or $MASnI_3$. Interestingly, the total amount of mature pupae is higher than control conditions and continued to increase even at 21 days. We assume that w- females tend to lay more eggs when sensing an external stress to assure multiplication of the population. The next step of the life cycle test was to follow the development of progeny until the young adult stage. Figure 5.7 shows the quantification of emerged adults in the same conditions as for the quantification of mature pupae for Or (a, b) and w- (c, d) strains. Progeny from flies exposed to $MAPbI_3$ are presented in brown and those exposed to $MASnI_3$ in purple. We clearly see from the charts that less young adults emerge from the pupae stage when one of the parents was exposed to $MAPbI_3$ or $MASnI_3$. Once again, tin-containing perovskite impacts the life cycle more than its counterpart, and interestingly, w- strain is more sensitive to the exposure than Or. What is even more striking is that at 12 days post-fertilization, no young adult was recorded in the treated conditions (except for Or NTxSn-NT), although they showed a precocious development of mature pupae (5 days instead of 9 or 10, see Figure 5.1 and Figure 5.5).

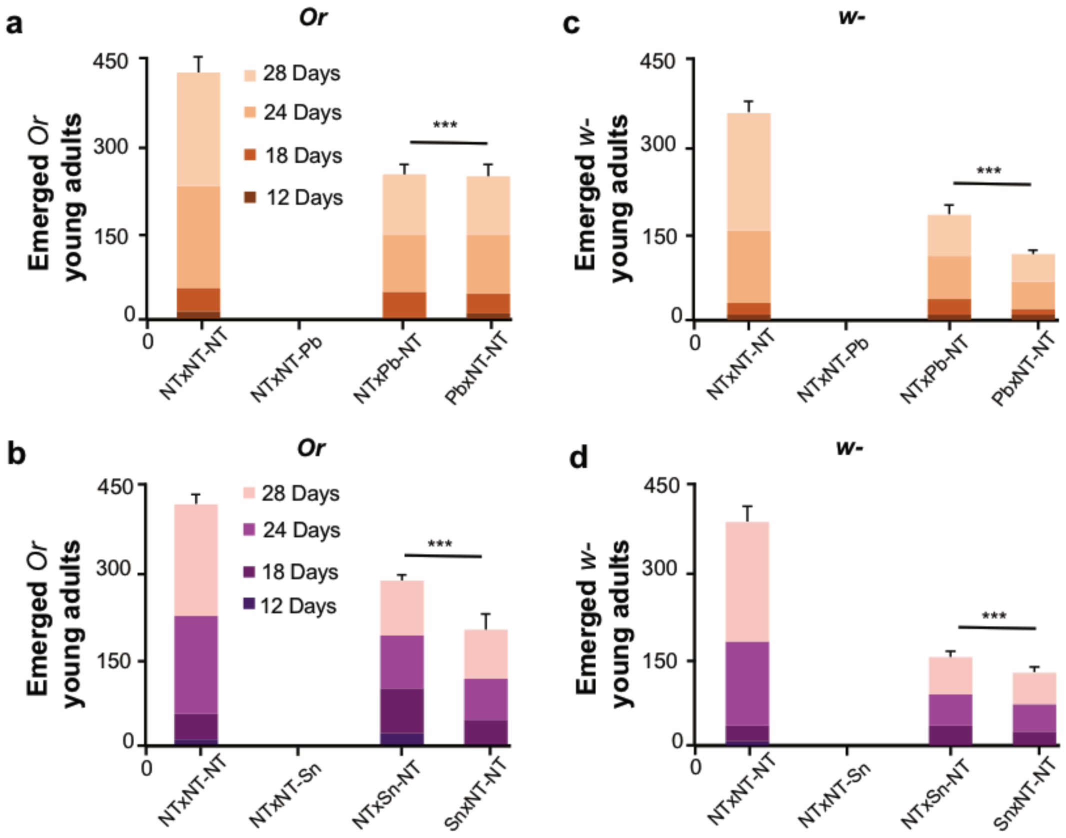

Figure 5.7 – Number of emerged young adults generated by treated vs. non-treated flies that were exposed to 50 μg of $MAPbI_3$ (brown bars) or $MASnI_3$ (purple bars). The x-axis shows the different conditions of progeny generated as follows: Male x Female – Final food; where NT is non treated, Pb refers to exposure to $MAPbI_3$ (a, c) and Sn to treatment with $MASnI_3$ (b, d). Emergence of young adults was probed during 28 days on Or strain (left panels) and w- strain (right panels). All histograms show an average of standard deviation (S.D.) using One-way ANOVA test followed by a Tukey-Kramer post-hoc test (non-treated vs. treated conditions), p-value<0.0002.

Another observation from the development/life cycle charts consists on correlating the number of mature pupae (Figure 5.1) with the total amount of emerged young adults generated by treated vs. non treated flies. This analysis shows between 50 and 60% of young adults (Or and w-) emerging from mature pupae in non-treated samples, whereas less than 50% of mature Or and w- pupae generated by $MAPbI_3$-treated flies metamorphose to young adults, and this number is even lower in the case one of the parents is exposed to $MASnI_3$: 46% in Or and 28% in w- strains. These data coherently demonstrate the adverse effects that photovoltaic perovskites cause to both the survival of adult flies and the development of *Drosophila melanogaster*. The doses administered to the selected wild type strains are based on our *in vitro* studies, and the published studies of toxicity of nanomaterials on this biological model. There is room for debate regarding all the parameters used for the *in vivo* study, and to understand more the eco-toxicity of perovskites, we investigated the response of *C. elegans*.

5.3 Ecotoxicity of $MAPbI_3$ and $MASnI_3$ on *C. elegans*

5.3.1 Introduction to the model

C. elegans is a free living, non parasitic soil nematode that can be cheaply and easily cultivated in the laboratory, where it is grown on agar plates with liquid cultures with *E. coli* as the food source. The 1 mm long organism is transparent, which facilitates organs observation and dissection, and can be housed in large numbers (10'000 worms per Petri dish). Its life span is about 3 weeks and its genome has been fully sequenced and annotated.[201] The adult body-plan is anatomically simple with 959 somatic cells and produces up to 300 eggs per adult. It reproduces within a life cycle from egg to young adult of about 3 days under optimal conditions (Figure 5.8). Another key advantage of *C. elegans* model is that feeding by RNAi facilitates gene silencing.[116] These unique properties make the worm an important model system for biological research in many fields including not only genomics, cell biology, neuroscience and aging but also toxicity.[110] Therefore we used this model to compare the dose-time response to the fruit fly's, and better understand the negative effects of perovskites. Thus we cultivated a wild type strain and used high-resolution optical microscopy to probe the changes in real-time. The major limitation of using *C. elegans* model in biology is sorting the worms by age, and regarding their fast development rate, the experimenter needs to be highly trained to sort a consequent number of worms quickly by hand for a large statistic, and isolate groups for all the test conditions without biasing the experiment. Furthermore, in our study, the continuous worm feeding as well as the high-resolution imaging implicate manual removal of the worms from the incubator to the bench at each time point, which is not applicable, and triggers undesirable temperature changes. To overcome this issue, we opted for a radically new method using a microfluidics platform combined with optical microscopy to allow sorting, continuous feeding and imaging of the worms at the same time. This novel system was developed at EPFL by our collaborators M. Cornaglia and L. Mouchiroud, who described it and tested it for a neurodegenerative disease study.[62,63]

The microfluidics device offers a fully automated and highly accurate study for time-resolved tests. It contains a matrix of microfluidic chambers (Figure 5.9) that considerably monitors the growth and development of each worm from the L1 larval stage (onset of worm larval develop-

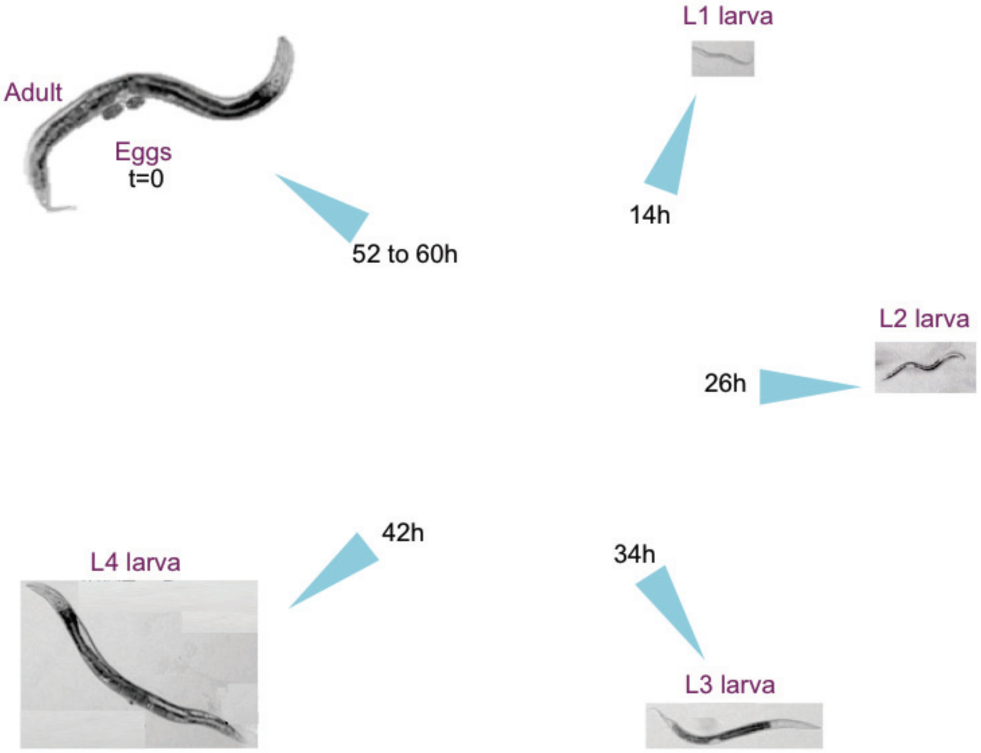

Figure 5.8 – Development phases of *Caenorhabditis elegans*: Hermaphrodite worms form eggs in their body. Once laid, the egg undergoes embryonic development during approximately 14 hours before entering the larval stage, where maturation phases of the larvae include four phases. The young adult stage is reached after 40 to 45 hours depending on the physiological conditions.

ment, upon hatching) to mature adult stage. The presence of many chambers allows following various conditions for a comparative test at the same time. It is a high throughput method. Consequently, we could easily investigate the life span, fertility, life cycle and development of the worms in real time.

5.3.2 Materials and methods

Culturing and treatment of the worm strain

Caenorhabditis elegans wild type Bristol N2 strain was cultured at 20°C on nematode growth media (NGM) agar plates seeded with the Escherichia coli strain OP50. For microfluidic experiments, the *E. coli* strain HT115 was suspended in S-medium at a concentration of $1.4 \cdot 10^9$ cells/ml. Worms were exposed to perovskite compounds from L3 stage the day of the experiment. The injected media and perovskite solutions were freshly prepared the day of the experiment as follows. $MAPbI_3$ and $MASnI_3$ were suspended in S-medium of 50 mg/ml. After filtration at 0.22 μm, this stock solution was diluted in bacteria-containing S-medium to 50, 100 and 200 $\mu g/ml$.

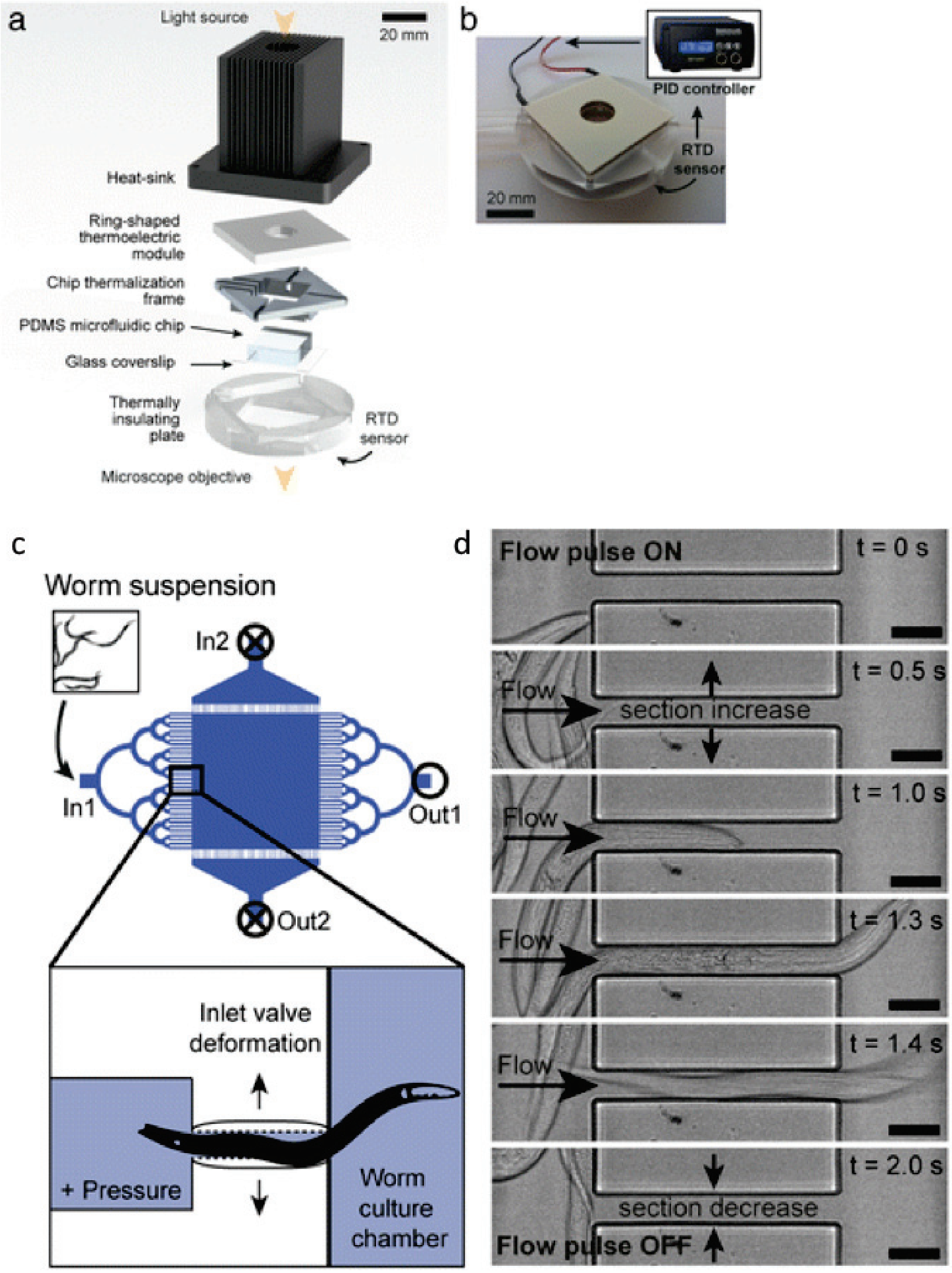

Figure 5.9 – Schematic representation of the main constitutive components of the microfluidic platform (a). Photograph of the device, with schematic picture of the closed-loop temperature control system(b). Schematic representation of the worm loading process(c). A pressure pulse triggers the fast deformation of the PDMS valving channels and allows the injection of worms of desired size into the culture chamber. Time-lapse pictures of a valving channel, as obtained during the injection of L3 worm in the chip(d). Scale bars = 10μm (with permission)[62]

Microfluidics experiments

The microfluidics device fabricated and tested by Cornaglia et al.[62] contains 8 separated channels and allows for testing 8 biological conditions during one experiment. Each channel is subdivided into 6 connected chambers offering the possibility for biological replicates. The whole setup was placed within an inverted microscope (Axio Observer, Zeiss) equipped with two illumination systems: (i) a precisExcite High-Power LED illumination system (Visitron, Puchheim, Germany) for brightfield imaging. The microscope had a motorized xy-stage and the automated imaging process was controlled using VisiView Premier Image acquisition software (Visitron, Puchheim, Germany). Images were acquired every 20 minutes during one week through a Hamamatsu Orca-ER CCD camera (Hamamatsu, Solothurn, Switzerland).

Data analysis and statistics

The recorded images allowed for survival studies, growth measurements, and fertility assessment. Image processing was performed using Fiji software[186] (version 2.0.0-rc-15/1.49k). For Survival, we plotted the time point where we observed a dead worm in each condition. Worm areas were measured by processing time-lapse brightfield pictures as follows; Each frame was first converted to a binary image by applying a threshold to the full stack of time-lapse images and transforming it into a set of binary masks. Each stack of masks was then analysed using the "particle analysis" Fiji plugin, which allows directly extracting area values for each picture in the stack. For fertility assessment, we tracked the sequence where the first egg was laid, and then we probed the time point where the first larva emerged. The experiment was repeated 3 times independently using new batches of media, perovskites and by inverting the position of the conditions in the device channels. We analysed each dataset alone by averaging the sextuplicate of each condition and measuring the standard deviation (S.D.) using One-way ANOVA test followed by a Tukey-Kramer post-hoc test (non-treated vs. treated conditions).

5.3.3 Results

In this section, we will present the toxicity data we obtained from real-time imaging (Figure 5.10), by combining 3 independent repeats performed on *C. elegans* by continuous injection of S-medium containing *E. coli* with or without perovskites during one week.

Effects on the worms' survival

The survival rate of treated worms was normalized to controls and plotted as a function of time (Figure 5.11) for samples containing 50, 100 and 200 $\mu g/ml$ of $MAPbI_3$ (top panels) or $MASnI_3$ (bottom panels). Non-treated worms (blue line) exhibited a survival rate of 100 % then started to decay after 6 days. When worms were exposed to $MAPbI_3$, the population began to die after 60 hours from the beginning of the experiment. This trend was more pronounced with higher doses (green and red lines), especially at the highest dose where no living worm could be observed after 5 days of exposure. $MASnI_3$ started interrupting the

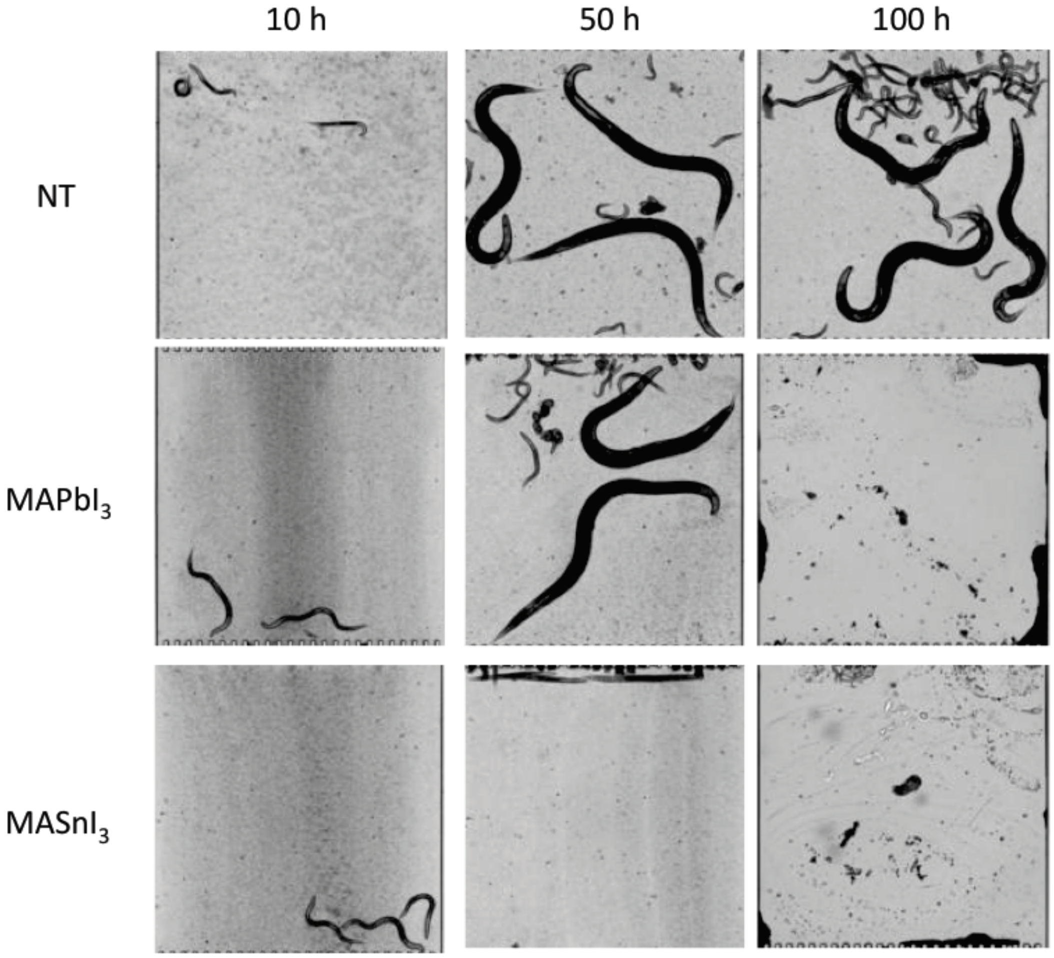

Figure 5.10 – Bright field images of *C. elegans* cultured inside microfluidic chambers at 20°C, and fed by continuous injection of S-medium spiked with bacteria (top panels, NT for non-treated), and $MAPbI_3$ at 100 $\mu g/ml$ (medium panels), or $MASnI_3$ at 100 $\mu g/ml$ (lower panels), during 10, 50 and 100 hours. The videos can be found at: http://go.epfl.ch/Worms_NT for non treated worms, http://go.epfl.ch/Worms_L100 for worms exposed to $MAPbI_3$ at 100 $\mu g/ml$, and http://go.epfl.ch/Worms_Sn100 for worms exposed to $MASnI_3$ at 100 $\mu g/ml$.

worms' survival as early as 20 hours, also in a time and dose-dependent fashion. At 200 $\mu g/ml$, the population suffered extensively the exposure and perished after 60 hours.

Effects on the worms' growth size

The body area of living worms was measured using a logarithm and the values are reported in Figure 5.12. The blue-lined curves show the increasing body area of non-treated nematodes. Due to their natural sinusoidal movement allowed by muscular contraction, and the lack of space inside the microfluidic chambers, the body size shrinks after 70 hours. After treatment with $MAPbI_3$ at 50 $\mu g/ml$ (orange line), the worms' body size reaches a plateau at the same time point as control, however it has a smaller area. This observation is even more striking with the curve profile of worms exposed to 100 $\mu g/ml$ (green line) and to 200 $\mu g/ml$ (red line)

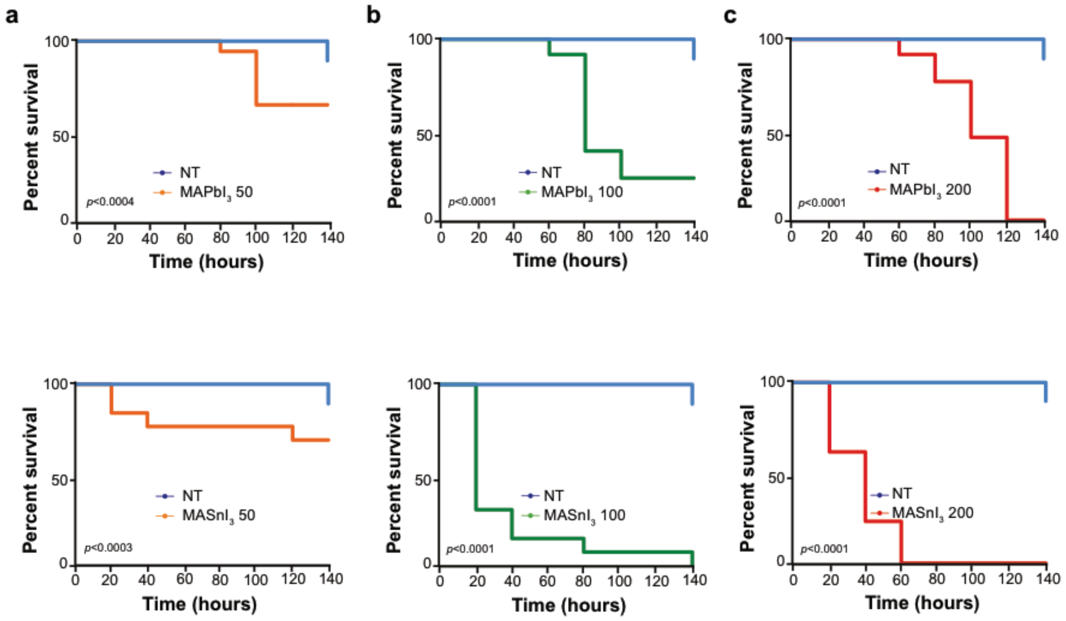

Figure 5.11 – Survival rate of treated vs. non treated worms treated with $MAPbI_3$ (top panels) or $MASnI_3$ (bottom panels) at 50 $\mu g/ml$ (a), 100 $\mu g/ml$ (b) and 200 $\mu g/ml$ (c). All curves show an average of standard deviation (S.D.) using One-way ANOVA test followed by a Tukey-Kramer post-hoc test (non-treated vs. treated conditions), p-value (<0.0005) is indicated on each panel.

of $MAPbI_3$.

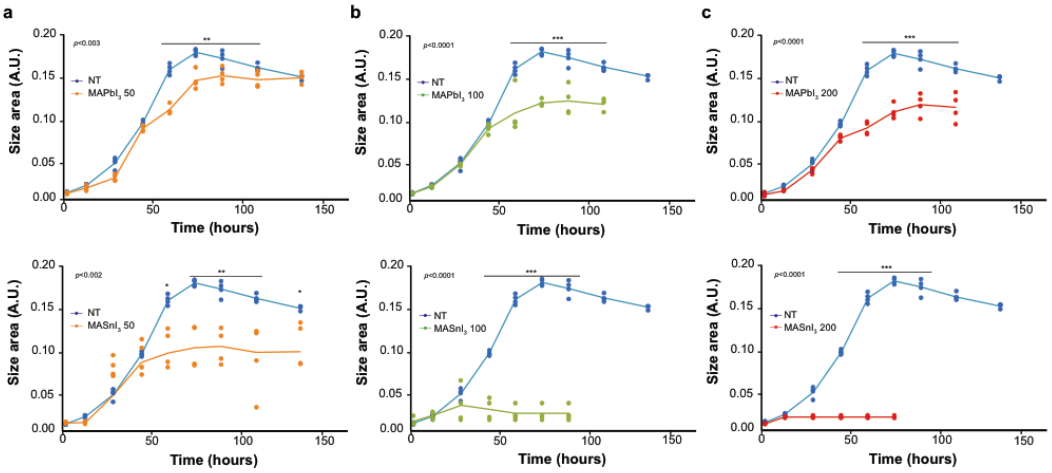

Figure 5.12 – Development curve of *C. elegans* from the larval stage to adults over $MAPbI_3$ (top panels) or $MASnI_3$ (bottom panels) exposure at 50 $\mu g/ml$ (a), 100 $\mu g/ml$ (b) and 200 $\mu g/ml$ (c). All curves show an average of standard deviation (S.D.) using One-way ANOVA test followed by a Tukey-Kramer post-hoc test (non-treated vs. treated conditions), p-value (<0.003) is indicated on each panel.

On the other hand, exposure of nematodes to $MASnI_3$ resulted in a much stunning body size freezing (Figure 5.12 bottom panels). In addition, the area values reached a plateau earlier than non-treated samples, and this effect was dose-dependent. From these observations we assumed that perovskites prevent the larvae to reach the young adult stage. Therefore, we sought to verify if the decrease in the worms' size is due to an affected development by tracking the young adults and quantifying the time-lapse when they developed.

Effects on the development of worms

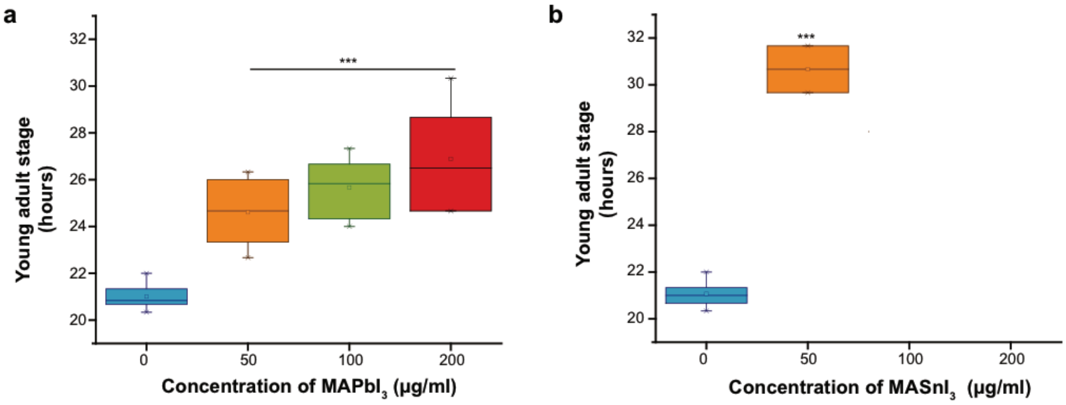

Figure 5.13 – Young adult stage reached by C elegans after the 3^{rd} larval stage, when exposed or not to $MAPbI_3$ (a) or $MASnI_3$ (b) at increasing concentrations: 50 (orange), 100 (green), and 200 $\mu g/ml$ (red). All plots show an average of standard deviation (S.D.) using One-way ANOVA test followed by a Tukey-Kramer post-hoc test (non-treated vs. treated conditions), p-value<0.002.

The first young adult observed in control samples was between 20 and 22 hours from the L3 stage(Figure 5.13). Injection of $MAPbI_3$ delayed the developmental process by 3 hours at the lowest concentration and by 5.5 hours at the highest one. Treatment with $MASnI_3$ induced an even worse delay in development already at 50 $\mu g/ml$, where the majority of larvae became adults after 30 hours. For higher concentrations, as observed in the previous parts (5.3.3 Effects on the worms' survival and 5.3.3 Effects on the worms' growth size), most of nematodes either perished or remained small, which explains the absence of young adult "phenotype".

Effects on fertility

The next live-imaging analysis concerned the extraction of the time point where the first egg was observed. This was acquired for the non-treated nematodes before 23 hours after the 3^{rd} larval stage (Figure 5.14 a, b. Blue boxes). As for the worms exposed to $MAPbI_3$, the first egg was observed after 23 hours at the lowest dose, and after 26 hours at the highest one (Figure 5.14 a, orange, green and red boxes). Clearly, there is a shift in the worms' fertility over exposure to perovskites, especially the tin-based one (Figure 5.14 b.), where we can observe a more marked delay for a concentration as low as 50 $\mu g/ml$. The first generation of eggs from the non-treated worms progressed to the larval stage for the first time before 36 hours (Figure 5.14 c, d. Blue boxes) and continued to proliferate until the end of the experiment (140 hours), where space in the chambers represented a limitation to continue the study. In parallel, eggs generated by treated nematodes developed to larvae much later for $MAPbI_3$

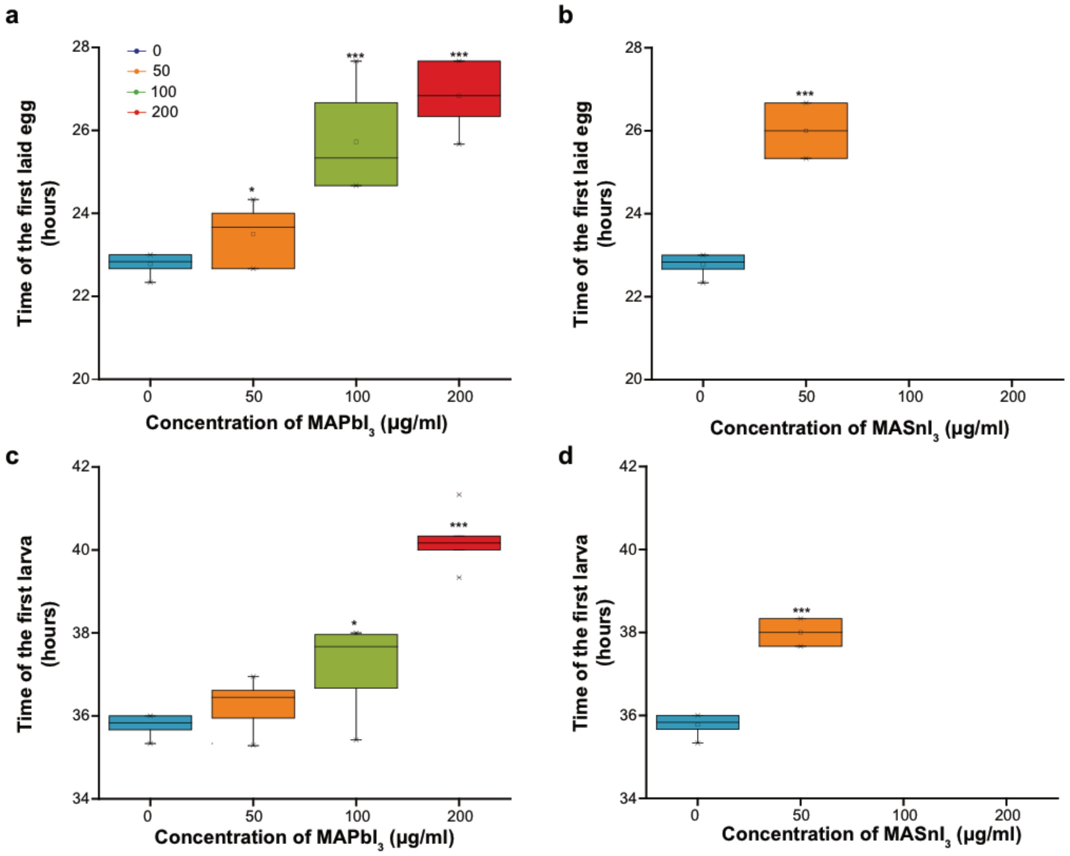

Figure 5.14 – Fertility investigation of *C. elegans* over $MAPbI_3$ (left panels) or $MASnI_3$ (right panels) exposure at increasing concentrations: 50 (orange), 100 (green), and 200 $\mu g/ml$ (red). The time point where the first egg was observed in each of the six chambers in all channels (or conditions) was monitored after the 3^{rd} larval stage and extracted using live-imaging then plotted in the top panels (a, b); and time point of the first observed larva in all chambers of each condition is plotted in the bottom panels (c, d). All plots show an average of standard deviation (S.D.) using One-way ANOVA test followed by a Tukey-Kramer post-hoc test (non-treated vs. treated conditions), p-value (<0.003) is indicated on each panel.

(between 36 and 42 hours). Additionally, the delay was even more pronounced in the case of exposure to $MASnI_3$ (around 38 hours at 50 $\mu g/ml$). Finally, the absence of progeny at 100 and 200 $\mu g/ml$ of perovskites confirms the retard in development.

In summary, the marked changes observed in *C. elegans*' viability, growth, development and fertility; reinforce the results obtained on *D. melanogaster*, and clearly demonstrate the toxic impact of photovoltaic perovskites on the environment. Furthermore, the microfluidic device used in our study simplified the screening of worms and allowed for analysing many parameters including development, lifespan and fertility in a single assay. The device is revolutionizing the field of toxicology when using *C. elegans* as a model, and could be employed in other disciplines such as neurodegeneration, immunology and pharmacology.

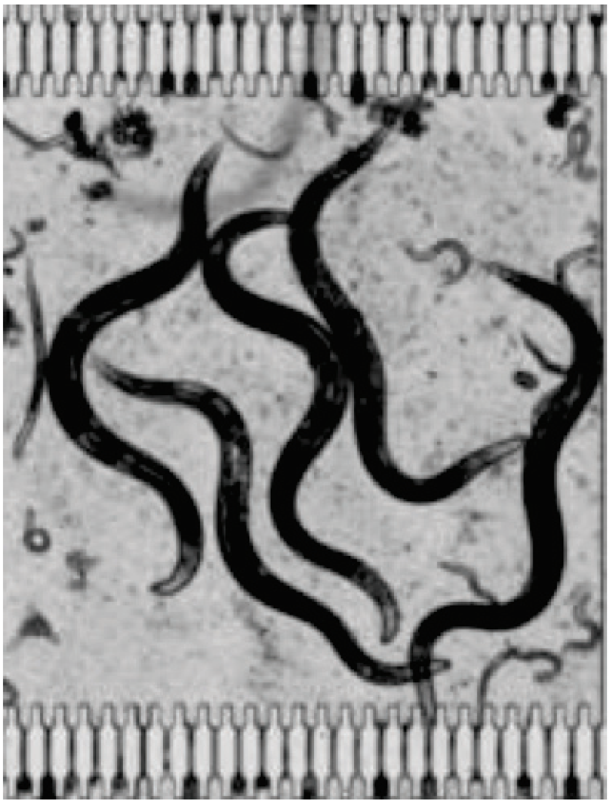

Figure 5.15 – Photography of a microfluidic chamber 4 days after the beginning of the toxicity test on C. elegans. Lack of space is the main limitation in the current state of our microfluidic device.

5.4 Conclusions and outlooks of the *in vivo* study

The *in vivo* experimentation presented in this chapter strengthens the *in vitro* outcomes presented in chapter 3, and validates toxic profile of perovskites, which will potentially constitute the next generation of solar panels that will cover our buildings. The eco-toxic effects observed in our study demonstrate the hazards on small model organisms (fruit fly and nematode), and are translated in a decrease of viability, a retard in growth and development, as well as in an altered fertility. These effects may be due in both models by an induced mitochondrial stress, as predicted by the RNA-seq data in chapter III. We believe a homolog of the transcription factor p53 in *D. melanogaster* (dp53)[115] and in *C. elegans* (CEP-1)[105,189] may be at the origin of the mitochondrial stress, which, together with DNA damage, could be responsible of the adverse effects of perovskites observed on the whole organisms. Mitochondrial stress and DNA damage may target in both models the hormone ecdysone, which directs progression through larval stages.[21,175] Moreover, in embryonic development, such a stress could alter oogenesis as shown by a recent study on *D. melanogaster* treated with magnetite nanoparticles, and metal traces were found along the anterior–posterior axis of the fertilized eggs.[54] Additionally, the molecular signaling pathway of the dorso-ventral axis formation was found to be affected by perovskite exposure of human cells (Appendix E). On *C. elegans*, strong correlation of mitochondrial or DNA damage and cell cycle or apoptosis have been made to evidence developmental impacts and even a shortened life span.[199] These publications may hold an explanation of our results, and encourage our research to assess mitochondrial imbalance as well as metal traces in our *in vivo* models. Considering the genome conservation between humans and *D. melanogaster* or *C. elegans*,[39] and the analysis of the genome expression profile obtained from human cells using RNA-seq (Chapter 3), the data presented in this chapter could predict the potential hazards of the photovoltaic perovskites on humans. As an outlook of this *in vivo* study, our protocols must obviously be improved for a more accurate and predictable outcome. There is room for debate regarding dose, time lapse and pathway of exposure on each organism. Nevertheless, the adverse effects observed in the laboratory are indisputable, and they can be even pursued to verify whether generations n2 and n3 still suffer the exposure of their grand-parents, and determine when the observed toxic effects stop inter-generation transmission. For *C. elegans*, because of a lack of space after one week(Figure 5.15), worms should be transferred into petri dishes and evaluation of toxicity should be continued without adding extra perovskites.

Conclusion & Outlook

5.5 Summary of the dissertation

The broad context of my PhD program reported in this dissertation is the toxicity study of a novel class of materials. The methylammonium lead iodide ($CH_3NH_3PbI_3$, or $MAPbI_3$) compound is the biggest surprise in the last 4 years to come out in the field of photovoltaics. With a relatively simple architecture, devices based on this material show an amazing 21 % efficiency in converting light into electricity. The biggest hurdle to overcome in terms of its large-scale application is its lead content. It is known that in contact with the human body, lead represents a severe danger. I addressed this issue with detailed *in vivo* and *in vitro* studies, and documented that the material is heavily toxic. Some researchers have high hopes of replacing lead with other elements and maintaining a comparable efficiency. The most discussed candidate is tin, and the $CH_3NH_3SnI_3$ perovskite ($MASnI_3$) is considered to be non-toxic. I focused on verifying this material, as well and its toxicity is comparable or worse to the lead-containing mother compound. The physical appearance of the two compounds is shown in Figure 5.16. I have characterized the materials, and the initial crystalline perovskite dissolves entirely in water, while in physiological media a precipitate forms. Iodine and the metal contained in the perovskite were detected in the precipitate as well as in the filtered solution. For this reason, the shape and size of the photovoltaic perovskites are not critical in toxicity studies. The filtered solution of the perovskites was the main subject of our toxicity evaluation because when the material is in contact with body fluids or released into the environment, it is likely to degrade because of humidity, and the soluble part may propagate rapidly.

Figure 5.16 – Characteristic image of the two photovoltaic perovskites used in the present studies.

In our *in vitro* toxicity study, the response is not only dose- and time-dependent but also cell-type dependent. Neuronal human cells (SH-SY5Y) suffered an apoptosis-like cell death in the presence of the perovskites (see illustrative Figure 5.17). Apoptosis occurs 24 hours following perovskites exposure via the intrinsic-mitochondrial pathway through the activation of caspase 9.

Regarding the human epithelial lung cell line A549, the effect was different, not any of the

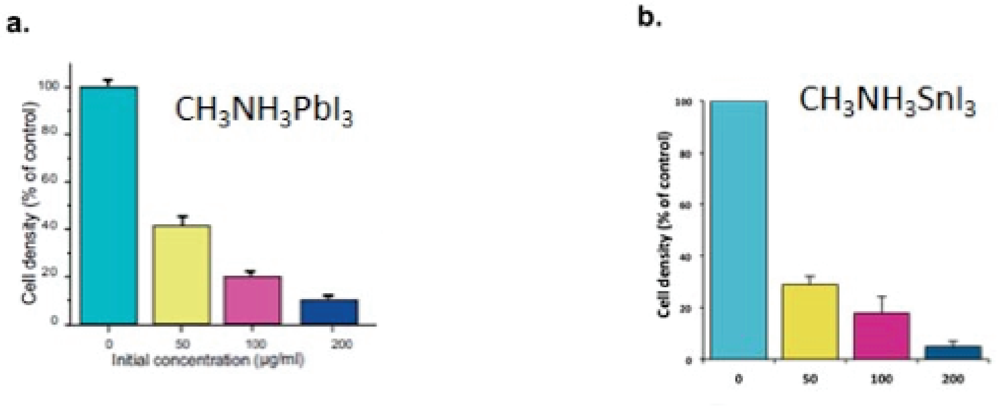

Figure 5.17 – The density of live SH-SY5Y cells exposed to $MAPbI_3$ or $MASnI_3$ decreases significantly with increasing concentrations.

caspases were not activated, however, the morphology was affected since the cells became giant and polynucleated (Figure 5.18). Further analysis showed that the mitochondria were heavily damaged, although their activity drastically increased compared to the untreated cells. While the cell cycle phases were not altered, the kinetics of cell division into daughter cells were slowed down. Detailed investigations of the genome profile by RNA-sequencing suggested many differences in gene expression levels. Some pathways that are critical to basic cellular functions were heavily affected by $MAPbI_3$ exposure (regulation of the metabolism, cell division, cell signaling etc.). These data are clearly in line with the results obtained from *in vitro* manipulations. For a better comprehension, I used a method which is very sensitive to biochemical and structural changes: S-FTIRM. This was the first time this method was used to evaluate toxicity. One reason for this is the availability of synchrotron radiation in the mid-IR range. Few laboratories are equipped with synchrotrons worldwide, which means there is little accessibility to the beamlines. Another problem with this technique is water absorption. As discussed in Chapter 4, the water signature overlaps with biological matter in IR spectra.

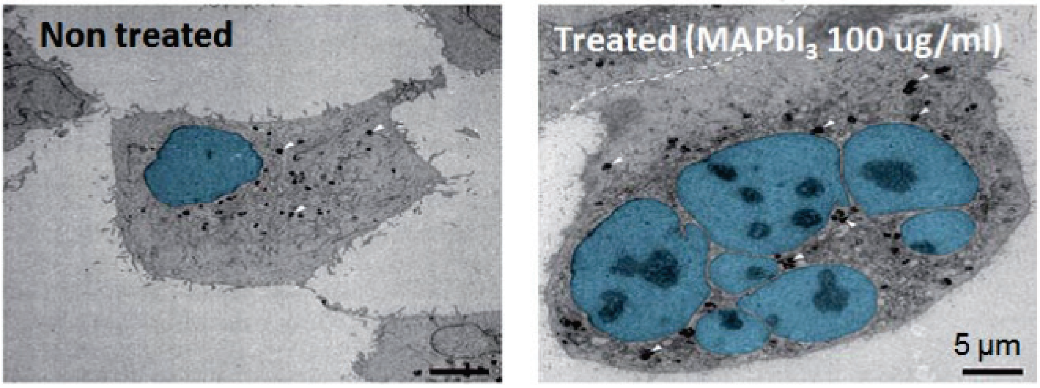

Figure 5.18 – Electron microscopy images of human lung cells (A549) before and after exposure.

That is why biological samples have to be fixed and dried before IR measurements.

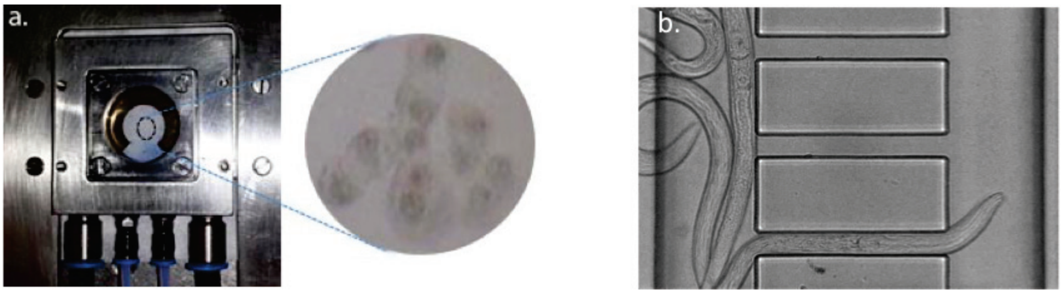

Figure 5.19 – Microfluidic chambers to conduct toxicity tests. a. Image of a liquid cell for infrared investigation of the toxicity effect of the perovskites on living cells. b. Microfluidic platform to assess toxicity in real-time on *C. elegans*.

I also developed an interesting platform to conduct S-FTIRM measurements on living cells (Figure 5.19 a.) and shift the water signal from the biological one. Our approach consisted in combining a chamber for cellular growth with an inlet and an outlet to allow fluid exchange, as well as a heating stage for long experiments. I studied the effects of $MAPbI_3$ in real-time using live S-FTIRM, and I observed specific changes in the resulting IR spectra. Since the cells grow in between two optical windows, the focus on the cell layer was difficult, therefore the use of a big aperture (20 μm x 20 μm) was necessary. This kind of aperture can also be used in standard FTIR microspectroscopes (with a thermal source instead of a synchrotron), because at an aperture of 20 μm^2, the S/N is comparable using both sources.[143] This makes the application of IR to real-time toxicity studies more accessible in terms of cost and availability. A second novelty I introduced into my investigations is the use of a microfluidic platform for in vivo toxicity studies on nematodes (*Caenorhabditis elegans*) (see Figure 5.19.b.). The multichannel configuration of the device combined with a CCD camera for real-time imaging enabled a high throughput analysis not only of the perovskite but also of other nanoparticles on the nematodes. Aside from nematodes, I also designed a detailed protocol to study the effects of perovskites on fruit flies (*Drosophila melanogaster*). These two model organisms are the gold standards for in vivo eco-toxicological tests. I have found that the life span and development of larvae were reduced by perovskite exposure. Moreover, the fertility of the organisms was drastically affected. This eco-toxicity study was set as a starting program for the *in vivo* toxicity. In summary, both the *in vitro* and *in vivo* studies I conducted showed that the current photovoltaic perovskites are acutely and chronically toxic compounds, even at low concentrations. Our studies also showed that the ad hoc idea to replace Pb with Sn is not a viable option, since$MASnI_3$ produces the same effects as the parent compound. Therefore, replacing both $MAPbI_3$ and $MASnI_3$ with less toxic compounds, or adding a hydrophobic encapsulation that still maintains the high energy efficiency, underlines the importance of more chemical engineering of new photovoltaic materials, which could still preserve the high conversion efficiency. Today, solar panels containing cesium, gallium, indium and arsenide can be found easily on the market, and the problem of toxicity cannot be addressed in the same manner because these compounds are more stable in humid conditions than perovskites, nevertheless we should have a critical view on them, as well, especially for recycling approaches. On the other hand, the development of new compounds for many applications, including photovoltaics, is progressing rapidly. Therefore, the community requires straightforward and reliable methods to assess their toxicity in a rapid and significant manner. Some conventional methods could be used (such as flow cytometry or fluorescence microscopy), but often trained scientists are required to perform the assays. We also suggest the use of innovative methods like IR spectroscopy or organ-on-a-chip to rapidly screen the toxicity of novel materials.

5.6 Future development

Future studies should address the details of the toxicity mechanism of photovoltaic perovskites, since there is no doubt that these materials represent a danger to public health. For the *in vitro* study, a detailed comprehension of the cellular uptake is very important. For this first study, I investigated the clathrin-dynamin pathway, and so a next step and significant follow-up would be to study the caveolae-dependent pathway. Furthermore, revealing subsequent signaling pathways could indicate more about the uptake dynamics[38, 46, 49, 70, 122, 135] . One of the main hallmarks of toxicity could be caused by an induced oxidative stress. Evaluation of the latter can be assessed in vitro using either label-based trials (such as fluorescent kits against free radicals or mitochondrial proteins), or label free assays (e.g. Electron spin resonance or IR spectroscopy). We have noticed that the induced phenotypical changes in A549 cells upon perovskites exposure (i.e. giant size and polynucleation) are comparable to the typical standard morphology of senescent cells. Verifying a potential correlation between senescence and perovskite exposure, at the molecular signaling level, would be extremely important. Today, detection kits can be found on the market that reveal the activation of the signaling cascade of senescence in vitro. Furthermore, Doxorubucin (DXB, a therapeutic drug in cancer) could be used as a positive control, because DXB induces senescence in mammalian cells. Although genome profiling indicated several signaling pathways that were affected by $MAPbI_3$ exposure, tests should also be done following $MASnI_3$ exposure, and the results should be validated at the RNA level (using RT-PCR) and at the protein level by immunoblotting the up- and down-regulated proteins. We are aware that tests on primary cells from human lungs would be more relevant for all these assays as compared to cell lines. These can be obtained from hospitals via biopsy. Finally, recent advances in bioengineering make it possible to reconstitute organs on a chip. For example, Donald Ingber and colleagues have published remarkable papers on the development of devices that emulate the biology of human tissues, organs and circulation in vitro.[23, 35, 77, 109, 138] Lung-on-a-chip was hence modeled in vitro to test the efficacy and toxicity of drugs and chemicals (Figure 5.20). The 3D Co-culture of various cell types constitutes both the mucociliary bronchiolar epithelium on the upper air-liquid layer, and the underlying microvascular endothelium, which is exposed to fluid flow. The device is also able to stretch, in order to mimic tissue extension during respiration. This important development could be considered as a follow up in the toxicity assessment of photovoltaic perovskites, and extended to other nanomaterials.

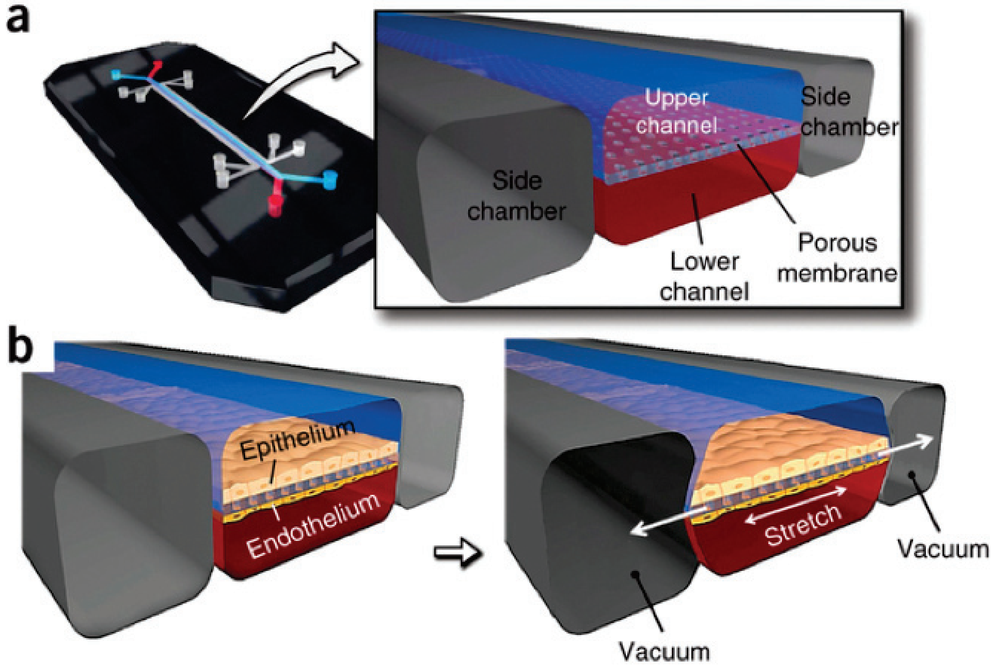

Figure 5.20 – The human lung-on-a-chip microsystem is constructed in a multilayered microfluidic device comprising the upper (blue) and lower (red) cell culture microchannels with a microfabricated porous elastic membrane sandwiched in-between. The microdevice is also equipped with two full-height, hollow microchambers alongside the cell culture channels. (b) Physiological breathing motions in the living human lung are reproduced by applying a vacuum to the side chambers. This action causes the lateral elongation of the intervening elastic membrane, which induces mechanical stretching of the adherent tissue layers in the central channels.[109] (With permission)

Also, IR microspectroscopy can be considered as a reinforcement of the toxicity study. Our data on living and fixed cells are promising, and we are aiming to measure IR absorption of tissue co-cultures (mainly macrophages, fibroblasts and epithelial lung cells) for both compounds. The in vivo tests on *Drosophila melanogaster* could be pursued by observing the treated and non-treated flies at the organ level. Routine procedures to section the flies' brain and gut could be used, then followed by fluorescence staining of stress markers such as inflammation, apoptosis, heat shock proteins etc. *Caenorhabditis elegans* presents a greater advantage than *D. melanogaster* in genetics because of the possibility to make mutants easily via siRNA feeding. With the perspective of understanding the toxic effects of $MAPbI_3$ and $MASnI_3$, transfecting worms with GFP-tagged markers would shed light on the pathways involved in the worms' toxicity response. For example, observing p53-GFP worms upon perovskites exposure could reveal a potential mitochondrial stress.[208] This leaves ample room, of course, for more eco-toxicity tests on small organisms such as zebrafish (Danio rerio) or plants (Arabidopsis thaliana…). Ultimately, however, the most important development in photovoltaic devices should replace perovskites with less toxic compounds or involve a hydrophobic encapsulation that would still maintain the high-energy efficiency.

Appendix A

History of asbestos

Asbestos was first used for thermal and fire isolation mainly: Finnish strengthened their cooking pots by using the ceramic form of asbestos (or anthophyllite), then ancient Greeks described it as the “unquenchable” before modern Greeks entitled it “Amiantos” (meaning “pure”). Few hundred years later, Persians used it in napkins then clothes; where they cleaned the fabrics by throwing them into fire. Some archeologists believe that ancients made grave-clothes of asbestos, wherein they incinerated the bodies of their kings, in order to preserve only their ashes, and prevent them from being mixed with those of the combustible materials commonly used in funeral rituals.[68] In the 17^{th} century, asbestos was considered as the “magic mineral”,[184,212] it was also used in lamps or candlewicks or even prescribed for diseases of the skin. Extensive mining began at the end of the 19^{th} century in Canada with the industrial revolution. New properties of the mineral were exploited and patents started to be established. Mining of asbestos continued worldwide and production of derived-products included fire retardant coatings, concrete, bricks, pipes and fireplace cement, heat, fire, and acid resistant gaskets, pipe and ceiling insulation, fireproof drywall, flooring, roofing, lawn furniture, and drywall joint compound. Asbestos was even incorporated in rice manufacturing in Japan. The very first observation of toxicity was found in a letter addressed by Pliny the Younger (61-113 AD)[86] and the second one appeared in 16^{th} century but fell into oblivion again until 1898 in a letter of Lucy Deane, one of the first Women Inspectors of Factories in the UK. In 1899, Dr. Montague Murray reported death related to asbestos chronic exposure via inhalation.[184,211] All types of asbestos fibers are toxic to humans and animals, and a consequent exposure results in asbestosis or mesothelioma (the most common diseases). Litigation regarding asbestos is one of the heaviest cases in legal history in terms of duration, claim size, and scope: on the one hand, the use of asbestos was extremely widespread across many applications; industries; sectors and countries. On the other hand, the knowledge of toxicity was not solicited although suspected long time ago. Since there is no safe level of asbestos exposure for any type of asbestos fiber,[95,195,217] its use is strictly banned in many countries from 2011.

Appendix B

Composition of the cell culture media

We used DMEM and DMEM:F12 to maintain A549 and SH-SY5Y cell lines, respectively. In order to evaluate the perovskite precipitate composition, once formed after contact with cell culture media, knowing the complete formulation of the latter is crucial to interpret the analytical chemistry results.The following information was taken from the provider's website.

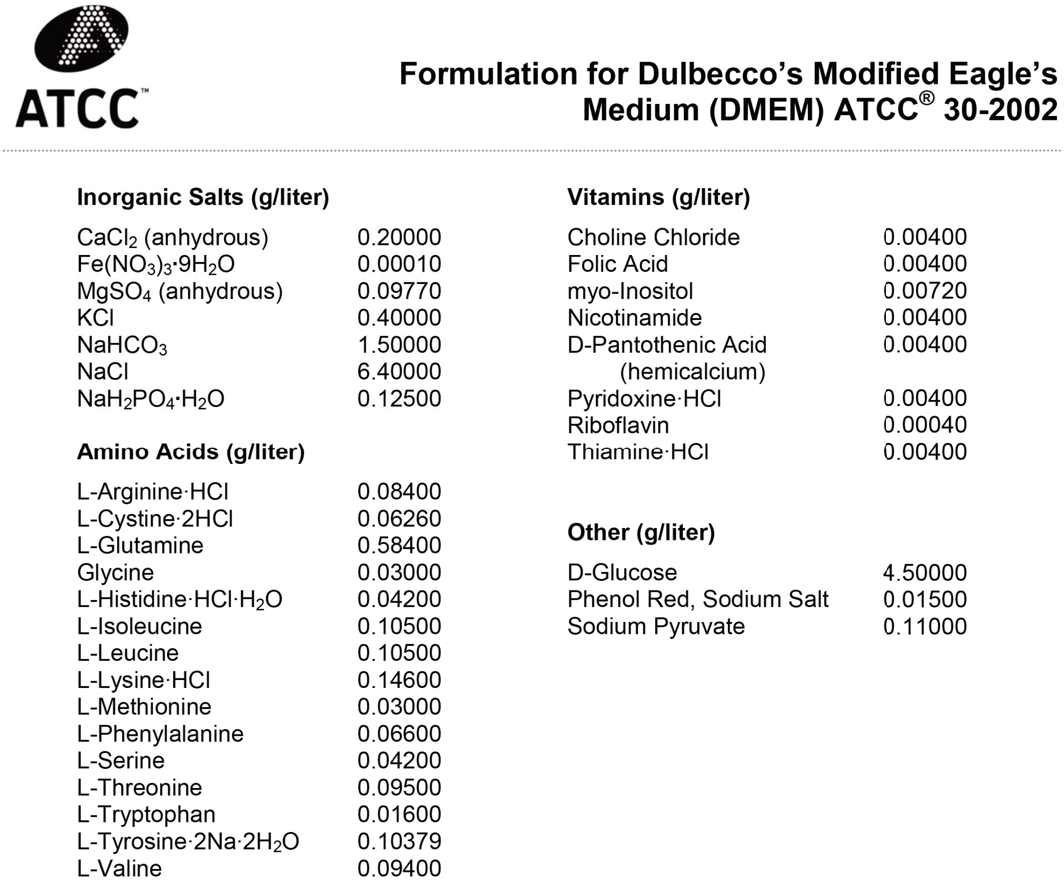

Formulation for Dulbecco's Modified Eagle's Medium (DMEM) ATCC® 30-2002

Inorganic Salts (g/liter)	
$CaCl_2$ (anhydrous)	0.20000
$Fe(NO_3)_3{\cdot}9H_2O$	0.00010
$MgSO_4$ (anhydrous)	0.09770
KCl	0.40000
$NaHCO_3$	1.50000
NaCl	6.40000
$NaH_2PO_4{\cdot}H_2O$	0.12500

Amino Acids (g/liter)	
L-Arginine·HCl	0.08400
L-Cystine·2HCl	0.06260
L-Glutamine	0.58400
Glycine	0.03000
L-Histidine·HCl·H_2O	0.04200
L-Isoleucine	0.10500
L-Leucine	0.10500
L-Lysine·HCl	0.14600
L-Methionine	0.03000
L-Phenylalanine	0.06600
L-Serine	0.04200
L-Threonine	0.09500
L-Tryptophan	0.01600
L-Tyrosine·2Na·$2H_2O$	0.10379
L-Valine	0.09400

Vitamins (g/liter)	
Choline Chloride	0.00400
Folic Acid	0.00400
myo-Inositol	0.00720
Nicotinamide	0.00400
D-Pantothenic Acid (hemicalcium)	0.00400
Pyridoxine·HCl	0.00400
Riboflavin	0.00040
Thiamine·HCl	0.00400

Other (g/liter)	
D-Glucose	4.50000
Phenol Red, Sodium Salt	0.01500
Sodium Pyruvate	0.11000

ATCC™

Formulation for DMEM:F-12 Medium
ATCC® 30-2006

Inorganic Salts (g/liter)

$CaCl_2$ (anhydrous)	0.11665
$CuSO_4$ (anhydrous)	0.0000008
$Fe(NO_3)_3 \cdot 9H_2O$	0.00005
$FeSO_4 \cdot 7H_2O$	0.000417
$MgSO_4$ (anhydrous)	0.08495
KCl	0.3118
$NaHCO_3$	1.20000
NaCl	7.00000
Na_2HPO_4 (anhydrous)	0.07100
$NaH_2PO_4 \cdot H_2O$	0.06250
$ZnSO_4 \cdot 7H_2O$	0.000432

Amino Acids (g/liter)

L-Alanine	0.00445
L-Arginine·HCl	0.14750
L-Asparagine·H_2O	0.00750
L-Aspartic Acid	0.00665
L-Cysteine·HCl·H_2O	0.01756
L-Cystine·2HCl	0.03129
L-Glutamic Acid	0.00735
L-Glutamine	0.36510
Glycine	0.01875
L-Histidine·HCl·H_2O	0.03148
L-Isoleucine	0.05437
L-Leucine	0.05895
L-Lysine·HCl	0.09135
L-Methionine	0.01724
L-Phenylalanine	0.03548
L-Proline	0.01725
L-Serine	0.02625
L-Threonine	0.05355
L-Tryptophan	0.00902
L-Tyrosine·2Na·$2H_2O$	0.05582
L-Valine	0.05285

Vitamins (g/liter)

D-Biotin	0.00000365
Choline Chloride	0.00898
Folic Acid	0.00265
myo-Inositol	0.01261
Niacinamide	0.00202
D-Pantothenic Acid (hemicalcium)	0.00224
Pyridoxine·HCl	0.00203
Riboflavin	0.00022
Thiamine·HCl	0.00217
Vitamin B-12	0.00068

Other (g/liter)

D-Glucose	3.15100
HEPES	3.57480
Hypoxanthine	0.00239
Linoleic Acid	0.000044
Phenol Red, Sodium Salt	0.00810
Putrescine·2HCl	0.00008
Pyruvic Acid·Na	0.05500
DL-Thioctic Acid	0.000105
Thymidine	0.000365

Appendix C

Count of viable cell using a Neubauer chamber

The number of viable cells was counted using a haemocytometer (or a Neubauer chamber, Figure C1 a) and bright field microscopy. Viable cells are easily distinguished from nonviable ones, where the former present clear cytoplasm and dead cells are darker. For the counting, only clear cells were considered as follows: A glass cover was centred on top of the counting chamber, and 10 μl of a homogenous cell suspension was injected uniformly in between using a pipet. The cell suspension diffuses by capillarity. (Figure C1 b).

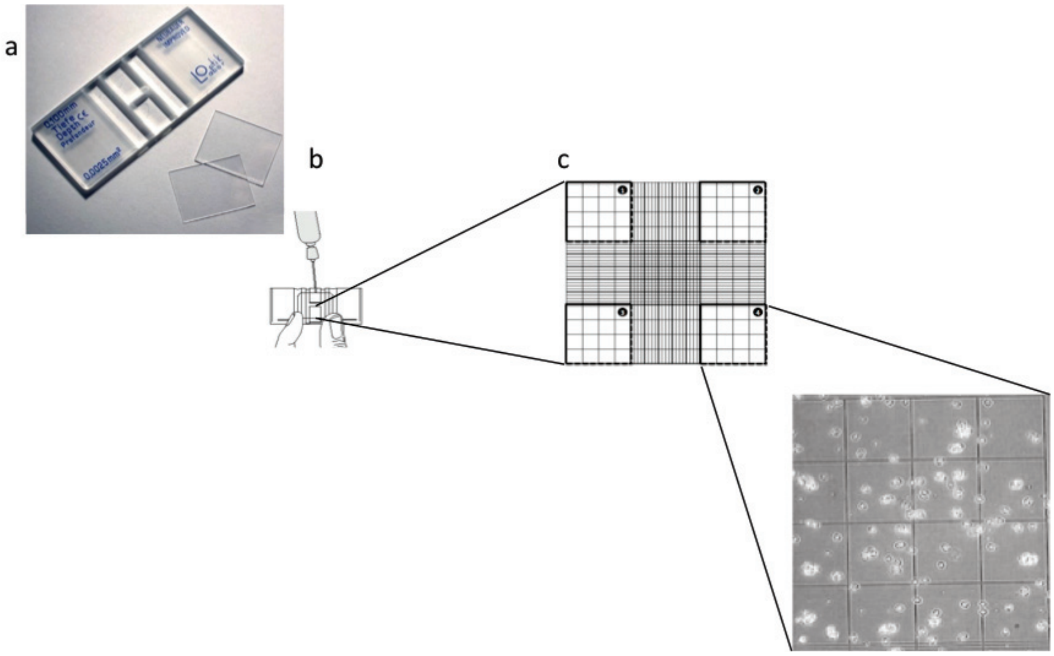

Figure C1 – Cell counting using a haemocytometer. Picture of the improved Neubauer haemocytometer (a), injection of cell suspension in between the glass cover and the Neubauer chamber (b), Appearance of the haemocytometer grids under microscope (c). Cells within the large square and those crossing the edge on two out of the four sides are counted (c). Source: Google image gallery.

The haemocytometer grid (Figure C1 c) was observed under a microscope and using a hand tally counter, the number of viable cells was counted in the four primary corner squares. The number of cells in one primary corner square is equivalent to the number of cells $\cdot\ 10^4/mL$.

$$\text{The cell concentration per mL} = \frac{\text{The total count in 4 large squares}\cdot 10^4}{4}\cdot \text{dilution factor} \tag{C1}$$

The dilution factor is 2 if trypan blue is used at 1:1 dilution. The conversion factor to convert $10^4\ mL$ to 1ml.

Dye exclusion method using flow cytometry

The cell membrane integrity was assessed using Sytox green and flow cytometry. The latter generated two dimensional plots displaying the side scattering of cells vs. their forward scattering (SSCA vs. FSCA). The population of interest was gated in non-treated cells, and the pattern was conserved for the other conditions of cells exposed to $MAPbI_3$. (Figure C2 upper panels). From the gating, histograms of fluorescence are extracted (Figure C2 lower panels). The percentage of fluorescence of sytox green can then be quantified. The highest peak corresponds to the autofluorescence of cells.

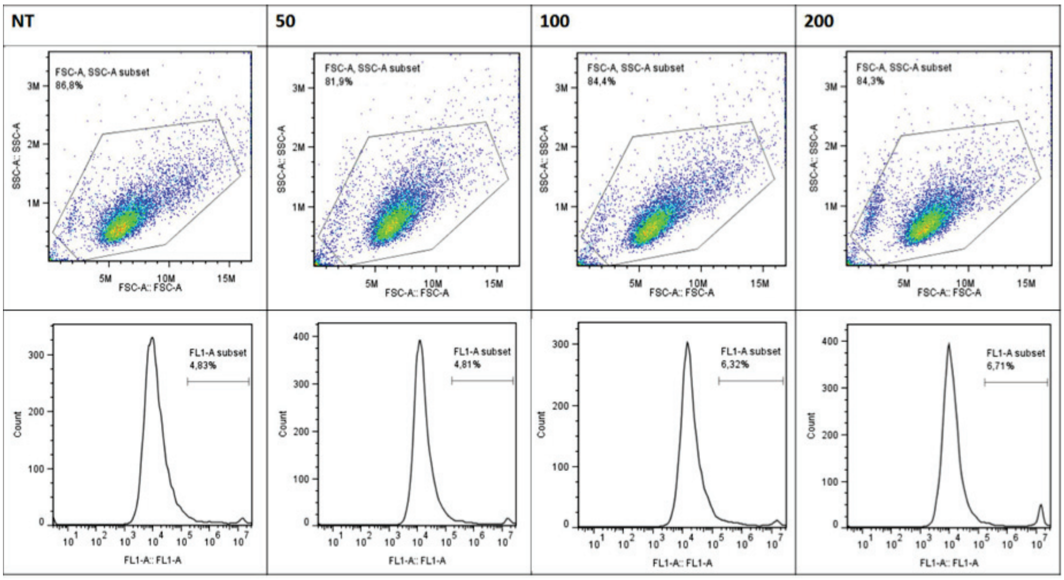

Figure C2 – Flow cytometry plots of membrane integrity assessed by exclusion of Sytox Green performed on A549 cells. Dot plots of SSCA vs. FSCA with a gate on the population of interest (upper panels), and Sytox Green fluorescence histograms (lower panels) of A549 cells for the following concentrations of $MAPbI_3$: non-treated (NT), exposed to 50 μg/ml (50), 100 μg/ml (100) and 200 μg/ml (200).

Transfection with siRNA protocol

A549 cells were transfected with siRNA for gene silencing of clathrin and dynamin. The reagents were purchased from Life technologies and the related protocol was applied for a volume corresponding to 6 well plates.

Protocol Pub. No. MAN0007825 Rev.1.0

Lipofectamine® RNAiMAX Reagent

Package Contents

Catalog Number	Size
13778-100	0.1 mL
13778-030	0.3 mL
13778-075	0.75 mL
13778-150	1.5 mL
13778-500	15 mL

Storage Conditions

Store at 4°C (do not freeze).

Required Materials

- siRNA or miRNA (10 µM stock)
- Opti-MEM® Reduced Serum Medium
- Eppendorf tubes

Timing

Preparation: 10 minutes
Incubation: 5 minutes
Final Incubation: 1-3 days

Selection Guide

Lipofectamine® Reagents

Go online to view related products.

Product Description

- Lipofectamine® RNAiMAX Transfection Reagent is a proprietary formulation for transfecting small RNAs (e.g., siRNA, Silencer® Select siRNA, Stealth® RNAi, mirVana™ miRNA mimics and inhibitors) into a wide range of eukaryotic cells.

Important Guidelines

- RNA-Lipofectamine® RNAiMAX complexes must be made in serum-free medium such as Opti-MEM® Reduced Serum Medium and can be added directly to cells in culture medium, in the presence or absence of serum/antibiotic.
- It is not necessary to remove complexes or change/add medium after transfection.
- Use 10 nM RNAi duplex as a starting point. BLOCK-iT™ Alexa Fluor® Red Fluorescent Oligo (Cat. no. 14750100) can be used to determine transfection efficiency.

Online Resources

Visit our product page for additional information and protocols. For support, visit www.lifetechnologies.com/support.

Protocol Outline

A. Plate cells so they will be 60-80% confluent at the time of transfection.
B. Prepare RNA-lipid complexes.
C. Add RNA-lipid complexes to cells.

Lipofectamine® RNAiMAX Transfection Protocol

ℹ See page 2 to view a typical RNAiMAX transfection procedure.

Transfection Amounts

	96-well	24-well	6-well
Final siRNA used per well	1 pmol	5 pmol	25 pmol
Final Lipofectamine® RNAiMAXused per well	0.3 µL	1.5 µL	7.5 µL

Reverse Transfection of RNAi

Reverse transfection is faster to perform than forward transfection and is the method of choice for high-throughput transfection. Perform reverse transfection by preparing complexes inside the wells, and then adding cells and medium. Because the cells and siRNA-lipid complexes are prepared on the same day, we recommended using 2.5× more cells than for a regular transfection method.

ℹ Scaling Up or Down Transfections

ℹ Limited Product Warranty and Disclaimer Details

Typical RNAiMAX Transfection Procedure

Transfect cells according to the following table. The transfection is designed for one RNA amount combined with one amount of Lipofectamine® RNAiMAX. **The prepared mix is enough to have triplicates (96-well), duplicates (24-well), and single well (6-well) transfections, and account for pipetting variations.** For additional information on scaling your transfection reaction, see page 1.

Timeline		Steps	Procedure Details			
			Component	96-well	24-well	6-well
Day 0	1	**Seed cells to be 60-80% confluent at transfection**	Adherent cells	1–4 × 10⁴	0.5–2 × 10⁵	0.25–1 × 10⁶
Day 1	2	**Dilute Lipofectamine® RNAiMAX Reagent in Opti-MEM® Medium**	Opti-MEM® Medium	25 µL	50 µL	150 µL
			Lipofectamine® RNAiMAX Reagent	1.5 µL	3 µL	9 µL
	3	**Dilute siRNA in Opti-MEM® Medium**	Opti-MEM® Medium	25 µL	50 µL	150 µL
			siRNA (10 µM)	0.5 µL (5 pmol)	1 µL (10 pmol)	3 µL (30 pmol)
	4	**Add diluted siRNA to diluted Lipofectamine® RNAiMAX Reagent (1:1 ratio)**	Diluted siRNA	25 µL	50 µL	150 µL
			Diluted Lipofectamine® RNAiMAX Reagent	25 µL	50 µL	150 µL
	5	**Incubate**	Incubate for 5 minutes at room temperature.			
			Component	96-well	24-well	6-well
	6	**Add siRNA-lipid complex to cells**	siRNA-lipid complex per well	10 µL	50 µL	250 µL
			Final siRNA used per well	1 pmol	5 pmol	25 pmol
			Final Lipofectamine® RNAiMAX used per well	0.3 µL	1.5 µL	7.5 µL
Day 2–4	7	**Visualize/analyze transfected cells**	Incubate cells for 1–3 days at 37°C. Then, analyze transfected cells.			

Protocols used for molecular biology

Cell lysis

Preparation of the lysing buffer:

- 0.25 g Tris
- 0.35 g NaCl
- 11.75 mg EDTA
- 100 μ NP-40
- 100 μ Triton X-100
- 40 ml ddH_2O

Alicots of 1 ml and add :

- 10 μl PI (protease inhibitor, 1:100)
- 1 μl PMSF (1:1000)
- 10 μl Phosphatase inhibitor

On ice / 4°C,
Harvest cells, Wash 1x with cold PBS, Resuspend in 500 μl Lysis buffer. Incubate on ice for 20 minutes (if cells clumped into a snot, vortex 5-6 times, and put 5 extra minutes of incubation on a rotation shaker). Scrape each well and transfer to labelled 1 ml tubes. Centrifuge 20 minutes at 14’000 rpm, 4°C, then transfer supernatant, which contains the cytosolic soluble fraction.
At room temperature,
Resuspend pellet in the same amount of lysis buffer (200 μl) + 5% SDS 20% (50 μl). Sonicate (3s interval for 15 seconds, 60% amplitude). This part contains the vesicular content which is detergent-insoluble.

Quantification of proteins by BCA

We quantified proteins using Pierce BCA (Pierce BCA kit + BSA 1 $\mu g / \mu l$ stock + ELISA plate) as follows:
In a 96 well plate: pipet into the 3 first lines (ABC) a triplicate of BSA -> 1 $\mu g / \mu l$ BSA stock, then duplicate the sample in the following lines (DE).
Prepare a mixture of 1:50 Reagents B:A from the kit (200 μl x number of wells = V_{tot}). . Add 200 μl of the mixture B:A in each well of the 96 well-plate, and protect from light and evaporation. . Incubate 30 minutes at 37°C, then read absorbance at 562 nm on spectrophotometer .
- Calculate the concentration and prepare the sample for migration.
- Vortex, quick spin - Boil samples for 10 minutes. - Use directly for migration on the gels according to calculated volumes. (60 μl maximum, and 20 μg minimum per well)

Electrophoresis

The gels for electrophoresis should be prepared in advance according to the size of proteins of interest (Table 5.1).

Protein size (kDa)	Gel percentage (%)
4-40	20
12-45	15
10-70	12.5
15-100	10
25-200	8

Table 5.1 – Electrophoresis gel percentage according to the size of protein of interest.

Western blotting

After gel migration, Blot should be transferred semi-dry:

Cut 6 filter papers and 1 nitrocellulose membrane to cover all gels, and prepare a tray with Transfer buffer. Uncast the gel and cut out the upper part of wells.

On the Transblot machine drawer, place the first stack soaked filter papers, place the membrane, place the gel, and finally, place the other stack of soaked filter papers. Eliminate bubbles between each step. Wet the machine plate with Transfer buffer, then launch the transfer at 13V for 90 minutes.

After transfer, block the proteins using 1:3 of Licor blocking buffer diluted in PBS, then wash with PBS/Tween (100 ml in 900 ml + 1ml tween) We immunoblotted using primary antibodies (1:1000), and secondary at (1:2000) diluted in the blocking buffer as follows:

- To prepare the TBS/Tween: 10 ml Tris/HCl pH 7.5 30 ml NaCl 5M Fill until 1 L with mQ H_2O 500 μl Tween 20 Stir using a magnetic bar.
- Cut the membrane according to the gel: Harvest it and place it in cuves containing TBS/Tween for 10' under agitation. Repeat the washing step.
- Prepare the 5% blotto by mixing 2.5 g of milk powder and 50 ml TBS/Tween. Prepare blotto 3% by mixing 3 g of milk powder 100 ml TBS/Tween
- Place the membrane in 25 ml of the 5% blotto for 1 hr, then prepare primary antibodies in 3% blotto.
- Discard the 5% blotto, Add 10 ml of the 3% blotto containing the Ab - Cover the box, place it O/N in the cold room under agitation (50 rpm)
- When primary incubation is over: . Wash membrane 3x 10 minutes with PBS/Tween . Prepare secondary Ab diluted in blocking buffer . Incubate 1hr at RT on shaker . Wash membrane 3x 10 minutes with PBS/Tween
- Revelation: We used LICOR system to scan the membranes.

Genome profiling methods for analysis

Details on the quality control tests

The total RNA from A549 cells (exposed or non-exposed to perovskites), was encoded by Sanger, Illumina 1.9 at GTF Lausanne. As mentioned in chapter 3, a quality score boxplot was drawn for each sample. The higher the score the better the base call. The background of the graph divides the y axis into very good quality calls (green), calls of reasonable quality (orange), and calls of poor quality (red) (Figure C3).

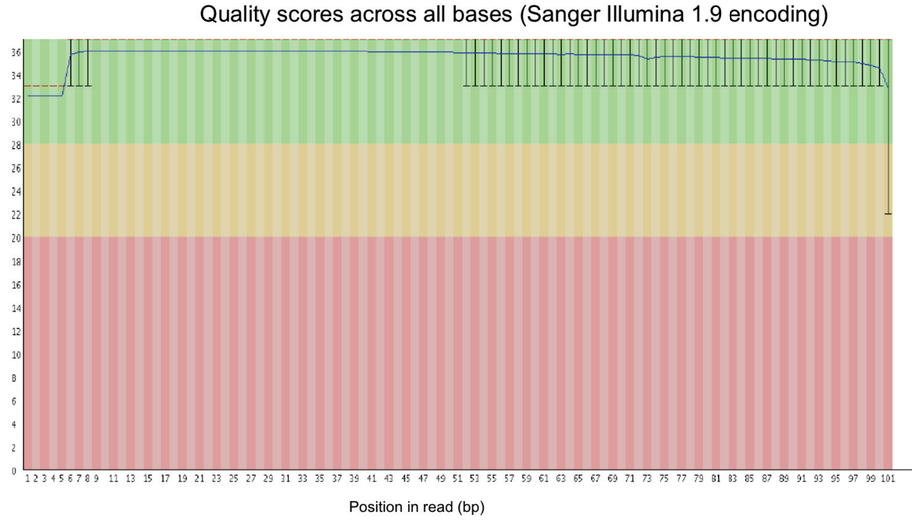

Figure C3 – Quality score across all bases within the same RNA sample.

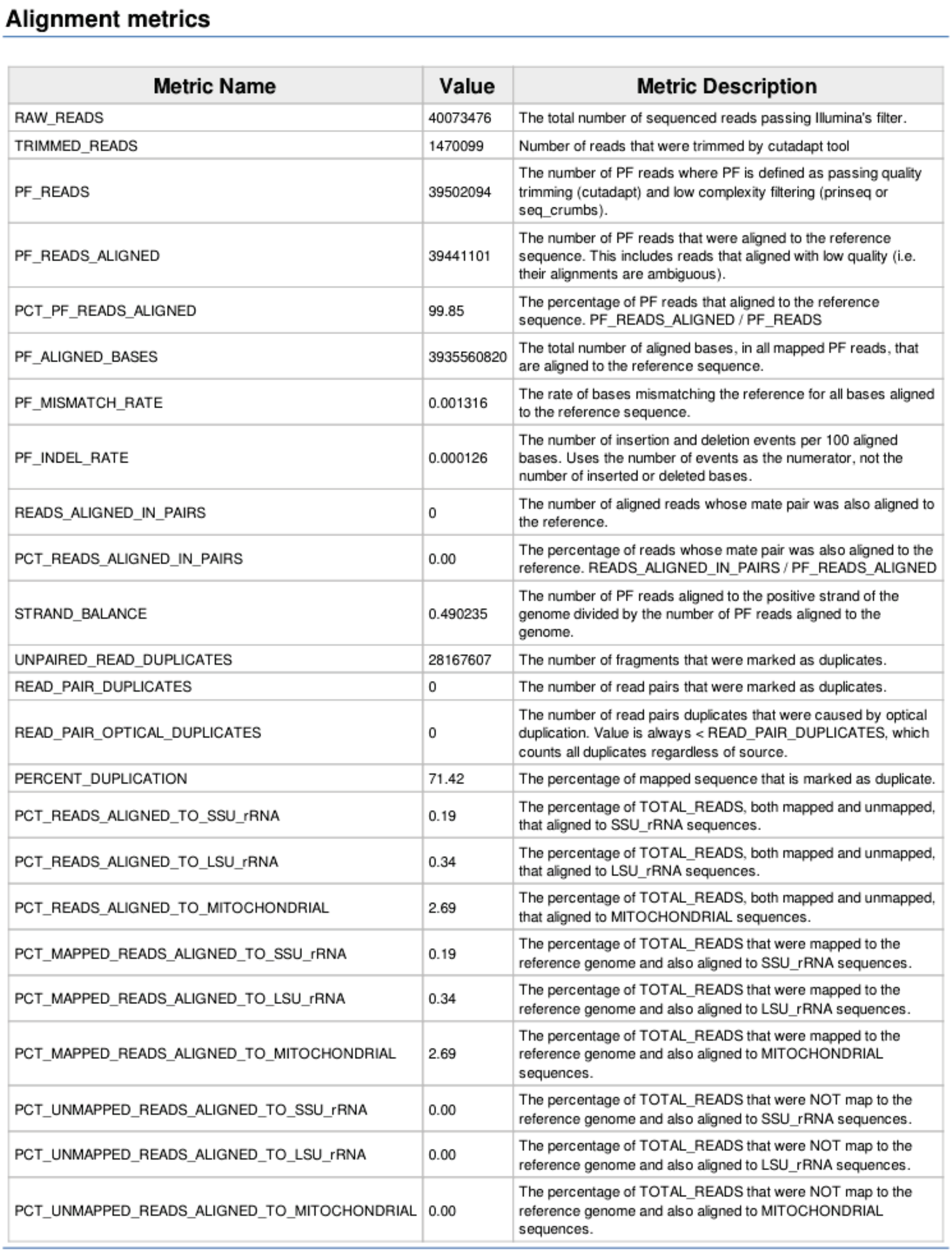

Alignment metrics

Metric Name	Value	Metric Description
RAW_READS	40073476	The total number of sequenced reads passing Illumina's filter.
TRIMMED_READS	1470099	Number of reads that were trimmed by cutadapt tool
PF_READS	39502094	The number of PF reads where PF is defined as passing quality trimming (cutadapt) and low complexity filtering (prinseq or seq_crumbs).
PF_READS_ALIGNED	39441101	The number of PF reads that were aligned to the reference sequence. This includes reads that aligned with low quality (i.e. their alignments are ambiguous).
PCT_PF_READS_ALIGNED	99.85	The percentage of PF reads that aligned to the reference sequence. PF_READS_ALIGNED / PF_READS
PF_ALIGNED_BASES	3935560820	The total number of aligned bases, in all mapped PF reads, that are aligned to the reference sequence.
PF_MISMATCH_RATE	0.001316	The rate of bases mismatching the reference for all bases aligned to the reference sequence.
PF_INDEL_RATE	0.000126	The number of insertion and deletion events per 100 aligned bases. Uses the number of events as the numerator, not the number of inserted or deleted bases.
READS_ALIGNED_IN_PAIRS	0	The number of aligned reads whose mate pair was also aligned to the reference.
PCT_READS_ALIGNED_IN_PAIRS	0.00	The percentage of reads whose mate pair was also aligned to the reference. READS_ALIGNED_IN_PAIRS / PF_READS_ALIGNED
STRAND_BALANCE	0.490235	The number of PF reads aligned to the positive strand of the genome divided by the number of PF reads aligned to the genome.
UNPAIRED_READ_DUPLICATES	28167607	The number of fragments that were marked as duplicates.
READ_PAIR_DUPLICATES	0	The number of read pairs that were marked as duplicates.
READ_PAIR_OPTICAL_DUPLICATES	0	The number of read pairs duplicates that were caused by optical duplication. Value is always < READ_PAIR_DUPLICATES, which counts all duplicates regardless of source.
PERCENT_DUPLICATION	71.42	The percentage of mapped sequence that is marked as duplicate.
PCT_READS_ALIGNED_TO_SSU_rRNA	0.19	The percentage of TOTAL_READS, both mapped and unmapped, that aligned to SSU_rRNA sequences.
PCT_READS_ALIGNED_TO_LSU_rRNA	0.34	The percentage of TOTAL_READS, both mapped and unmapped, that aligned to LSU_rRNA sequences.
PCT_READS_ALIGNED_TO_MITOCHONDRIAL	2.69	The percentage of TOTAL_READS, both mapped and unmapped, that aligned to MITOCHONDRIAL sequences.
PCT_MAPPED_READS_ALIGNED_TO_SSU_rRNA	0.19	The percentage of TOTAL_READS that were mapped to the reference genome and also aligned to SSU_rRNA sequences.
PCT_MAPPED_READS_ALIGNED_TO_LSU_rRNA	0.34	The percentage of TOTAL_READS that were mapped to the reference genome and also aligned to LSU_rRNA sequences.
PCT_MAPPED_READS_ALIGNED_TO_MITOCHONDRIAL	2.69	The percentage of TOTAL_READS that were mapped to the reference genome and also aligned to MITOCHONDRIAL sequences.
PCT_UNMAPPED_READS_ALIGNED_TO_SSU_rRNA	0.00	The percentage of TOTAL_READS that were NOT map to the reference genome and also aligned to SSU_rRNA sequences.
PCT_UNMAPPED_READS_ALIGNED_TO_LSU_rRNA	0.00	The percentage of TOTAL_READS that were NOT map to the reference genome and also aligned to LSU_rRNA sequences.
PCT_UNMAPPED_READS_ALIGNED_TO_MITOCHONDRIAL	0.00	The percentage of TOTAL_READS that were NOT map to the reference genome and also aligned to MITOCHONDRIAL sequences.

All-expressed genes

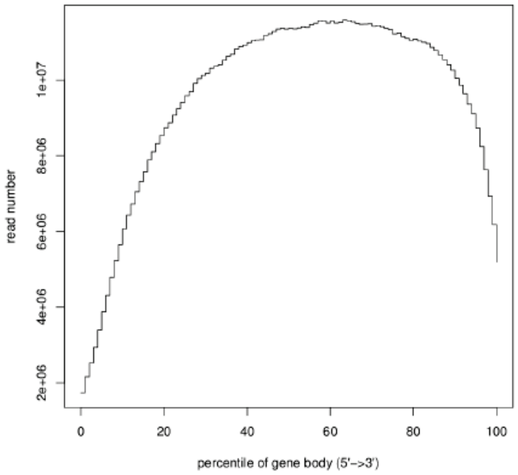

rRNA-expressed genes

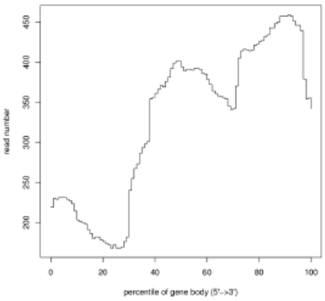

mitochondria-expressed genes

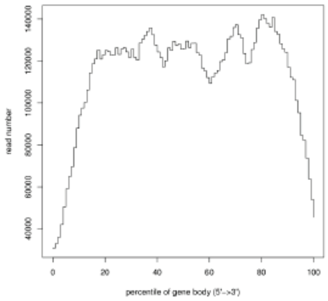

protein-coding-expressed genes

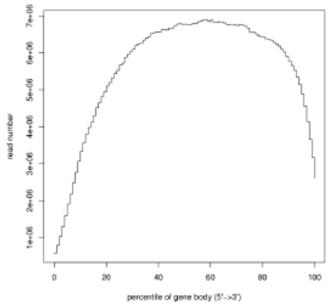

This module is used to check if reads coverage is uniform and if there is any 5'/3' bias. This module scales transcripts to 100 nt and calculates the number of reads covering each nucleotide position. Finally, it generates a plot illustrating the coverage profile along the gene body.

When genome features are overlapped, they are prioritize as: CDS exons > UTR exons > Introns > Intergenic regions. Tags: reads spliced once will be counted as 2 tags, reads spliced twice will be counted as 3 tags, etc.

Details on the bioinformatics tools to analyze the genome profile

SPIA combines: the over-representation of DE genes in a given pathway and the perturbation of that pathway. These two aspects are captured by two independent probability values: PNDE (Number of DE genes) and PPERT (amount of perturbation measured in each pathway). PNDE is the probability of observing the given number of DE genes or higher. PPERT assesses the significance of the observed total pathway perturbation as p-value calculated in a bootstrapping process. We use the parameter number of bootstrap iterations=2000. PPERT will become significant only if the observed fold change in the considered pathway nodes yields a significant

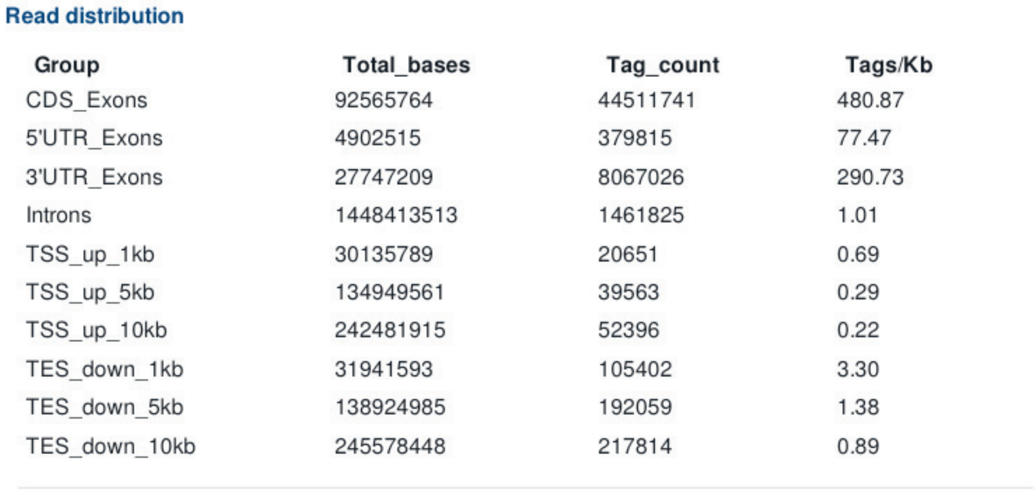

Read distribution

Group	Total_bases	Tag_count	Tags/Kb
CDS_Exons	92565764	44511741	480.87
5'UTR_Exons	4902515	379815	77.47
3'UTR_Exons	27747209	8067026	290.73
Introns	1448413513	1461825	1.01
TSS_up_1kb	30135789	20651	0.69
TSS_up_5kb	134949561	39563	0.29
TSS_up_10kb	242481915	52396	0.22
TES_down_1kb	31941593	105402	3.30
TES_down_5kb	138924985	192059	1.38
TES_down_10kb	245578448	217814	0.89

different impact compared compared with what is observed on the same pathway when the same number of fake DE genes is thrown in random loactions throughout the same pathway. The two types of evidence, PNDE and PPERT, are finally combined by the Fisherf method into one global probability value, PG, that is used to rank the pathways and test the hypothesis that the pathway is significantly perturbed in the condition under the study (low P-value). The SPIA two-way evidence plot show the pathways that meet the criterion (PNDE< α) and (PPERT < α). We fixe α=0.05 (red dot line-log(0.05) 3). Pathways above the oblique red line are significant at 5% after Bonferroni correction, while those above the oblique blue line are significant at 5% after FDR correction. After GAGE and SPIA, we use Pathview to map our data onto pathway graphs and visualize very intuitive, informative and well annotated pathways.

Other affected networks

In this part, I present some of the affected signaling pathways in A549 cells exposed to $MAPbI_3$. These pathways were common in GAGE and SPIA methods, for a fold change > 2, and significant with a p-value < 0.05. On each figure, the over-expressed genes are displayed in red and the under-expressed ones in green

Among these pathways, we can find the calcium signaling cascade, where Pb^{2+} and Sn^{2+} ions are strong competitors to Ca. We can also find an altered regulation of the programmed cell death (apoptosis and autophagy), which is in accordance with our findings on caspases cascade inactivation when A549 cells were exposed to perovskites.

Appendix C

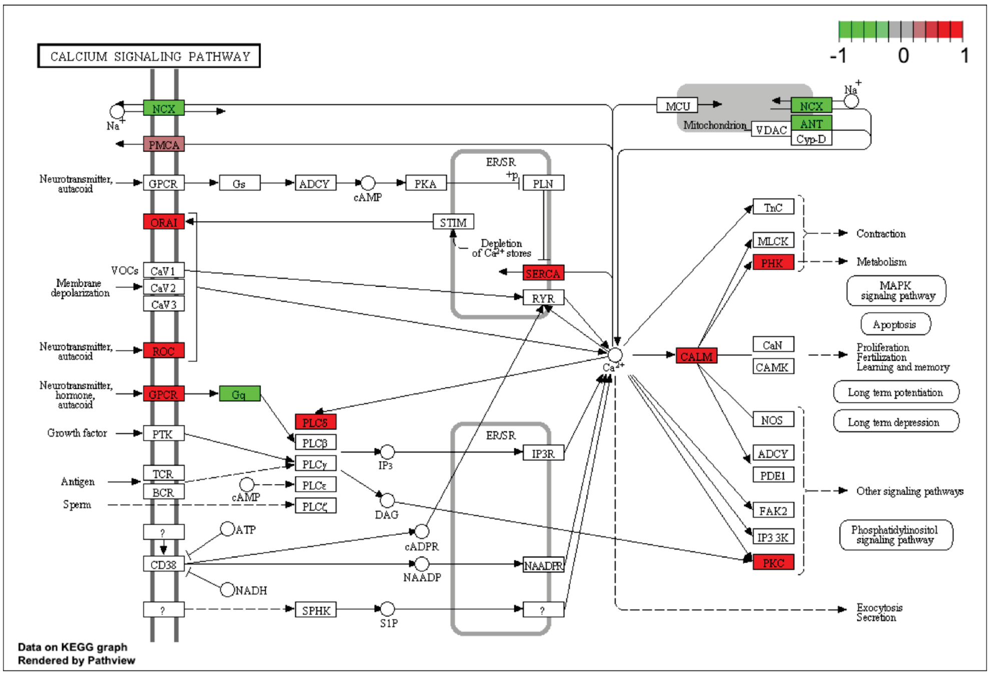
CALCIUM SIGNALING PATHWAY
-1
0
1
NCX
Na+
PMCA
Neurotransmitter, autacoid
GPCR
Gs
ADCY
cAMP
PKA
ER/SR
+p
PLN
ORAI
STIM
Depletion of Ca2+ stores
VOCs
CaV1
Membrane depolarization
CaV2
CaV3
SERCA
RYR
Neurotransmitter, autacoid
ROC
Neurotransmitter, hormone, autacoid
GPCR
Gq
PLCδ
Growth factor
PTK
PLCβ
PLCγ
IP3
ER/SR
IP3R
Antigen
TCR
BCR
PLCε
Sperm
PLCζ
DAG
?
ATP
cADPR
CD38
NAADP
NAADPR
NADH
?
SPHK
S1P
?
MCU
Mitochondrion
VDAC
NCX
ANT
Cyp-D
Na+
TnC
MLCK
PHK
Contraction
Metabolism
MAPK signaling pathway
Apoptosis
Ca2+
CALM
CaN
CAMK
Proliferation
Fertilization
Learning and memory
Long term potentiation
Long term depression
NOS
ADCY
PDE1
Other signaling pathways
FAK2
IP3 3K
Phosphatidylinositol signaling pathway
PKC
Exocytosis
Secretion
Data on KEGG graph
Rendered by Pathview

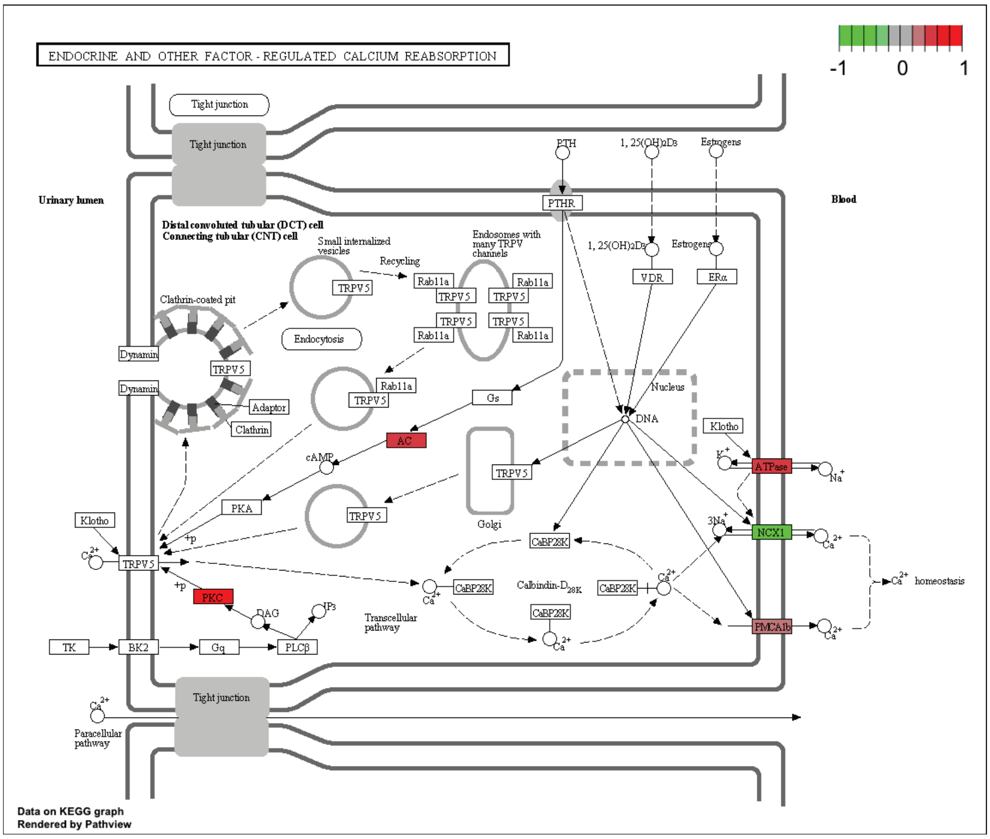
ENDOCRINE AND OTHER FACTOR-REGULATED CALCIUM REABSORPTION
-1
0
1
Tight junction
Tight junction
Urinary lumen
Blood
PTH
1, 25(OH)2D3
Estrogens
PTHR
Distal convoluted tubular (DCT) cell
Connecting tubular (CNT) cell
Small internalized vesicles
Endosomes with many TRPV channels
1, 25(OH)2D3
Estrogens
Recycling
TRPV5
Rab11a
TRPV5
Rab11a
TRPV5
TRPV5
TRPV5
Rab11a
Rab11a
VDR
ERα
Clathrin-coated pit
Endocytosis
Dynamin
TRPV5
Dynamin
Adaptor
Clathrin
Rab11a
TRPV5
Gs
Nucleus
DNA
Klotho
AC
K+
ATPase
Na+
cAMP
TRPV5
Golgi
PKA
TRPV5
3Na+
NCX1
Ca2+
Klotho
+p
Ca2+
homeostasis
Ca2+
TRPV5
CaBP28K
Ca2+
CaBP28K
Calbindin-D28K
CaBP28K
Ca2+
+p
PKC
DAG
IP3
Transcellular pathway
CaBP28K
PMCA1b
Ca2+
Ca2+
TK
BK2
Gq
PLCβ
Tight junction
Ca2+
Paracellular pathway
Data on KEGG graph
Rendered by Pathview

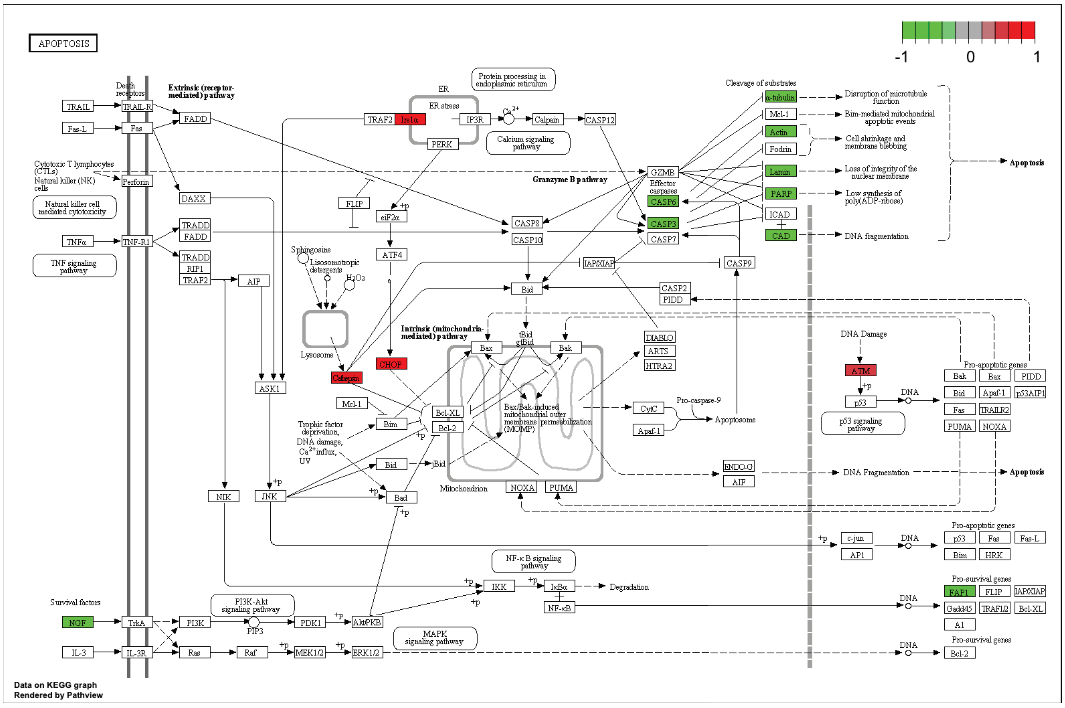
APOPTOSIS
-1
0
1
Death receptors
Extrinsic (receptor-mediated) pathway
TRAIL
TRAIL-R
Fas-L
Fas
FADD
Cytotoxic T lymphocytes (CTLs)
Natural killer (NK) cells
Perforin
Natural killer cell mediated cytotoxicity
DAXX
TRADD
FADD
TNFα
TNF-R1
TNF signaling pathway
TRADD
RIP1
TRAF2
AIP
ASK1
NIK
JNK
Protein processing in endoplasmic reticulum
ER
ER stress
TRAF2
Ire1α
IP3R
Ca^{2+}
Calpain
CASP12
PERK
Calcium signaling pathway
FLIP
eIF2α
ATF4
CHOP
Sphingosine
Lisosomotropic detergents
H_2O_2
Lysosome
Cathepsin
Granzyme B pathway
GZMB
Effector caspases
CASP6
CASP3
CASP7
CASP8
CASP10
IAP/XIAP
CASP9
Bid
CASP2
PIDD
Intrinsic (mitochondria-mediated) pathway
tBid
Bax
Bak
DIABLO
ARTS
HTRA2
Mcl-1
Bim
Bcl-XL
Bcl-2
Trophic factor deprivation, DNA damage, Ca^{2+} influx, UV
Bid
jBid
Bad
Bax/Bak-induced mitochondrial outer membrane permeabilization (MOMP)
Mitochondrion
NOXA
PUMA
CytC
Apaf-1
Pro-caspase-9
Apoptosome
ENDO-G
AIF
Cleavage of substrates
α-tubulin
Mcl-1
Actin
Fodrin
Lamin
PARP
ICAD
CAD
Disruption of microtubule function
Bim-mediated mitochondrial apoptotic events
Cell shrinkage and membrane blebbing
Loss of integrity of the nuclear membrane
Low synthesis of poly(ADP-ribose)
DNA fragmentation
Apoptosis
DNA Damage
ATM
p53
p53 signaling pathway
DNA
Pro-apoptotic genes
Bak
Bax
PIDD
Bid
Apaf-1
p53AIP1
Fas
TRAIL-R2
PUMA
NOXA
DNA Fragmentation
Apoptosis
c-jun
AP1
Pro-apoptotic genes
p53
Fas
Fas-L
Bim
HRK
NF-κB signaling pathway
IKK
IκBα
NF-κB
Degradation
Pro-survival genes
FAP1
FLIP
IAP/XIAP
Gadd45
TRAF1/2
Bcl-XL
A1
Pro-survival genes
Bcl-2
Survival factors
NGF
TrkA
PI3K
PIP3
PI3K-Akt signaling pathway
PDK1
Akt/PKB
IL-3
IL-3R
Ras
Raf
MEK1/2
ERK1/2
MAPK signaling pathway
+p
Data on KEGG graph
Rendered by Pathview

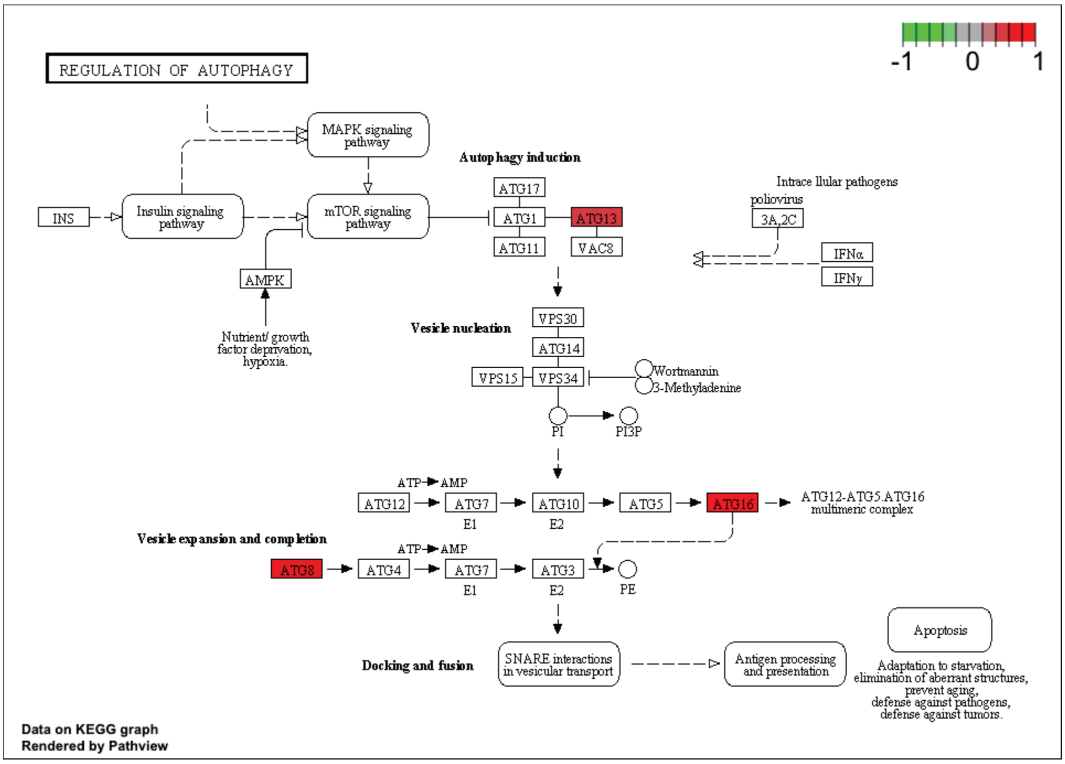
REGULATION OF AUTOPHAGY
-1
0
1
MAPK signaling pathway
INS
Insulin signaling pathway
mTOR signaling pathway
AMPK
Nutrient/ growth factor deprivation, hypoxia.
Autophagy induction
ATG17
ATG1
ATG13
ATG11
VAC8
Intracellular pathogens
poliovirus
3A,2C
IFNα
IFNγ
Vesicle nucleation
VPS30
ATG14
VPS15
VPS34
Wortmannin
3-Methyladenine
PI
PI3P
ATP
AMP
ATG12
ATG7
E1
ATG10
E2
ATG5
ATG16
ATG12-ATG5.ATG16 multimeric complex
Vesicle expansion and completion
ATP
AMP
ATG8
ATG4
ATG7
E1
ATG3
E2
PE
Docking and fusion
SNARE interactions in vesicular transport
Antigen processing and presentation
Apoptosis
Adaptation to starvation, elimination of aberrant structures, prevent aging, defense against pathogens, defense against tumors.
Data on KEGG graph
Rendered by Pathview

Appendix C

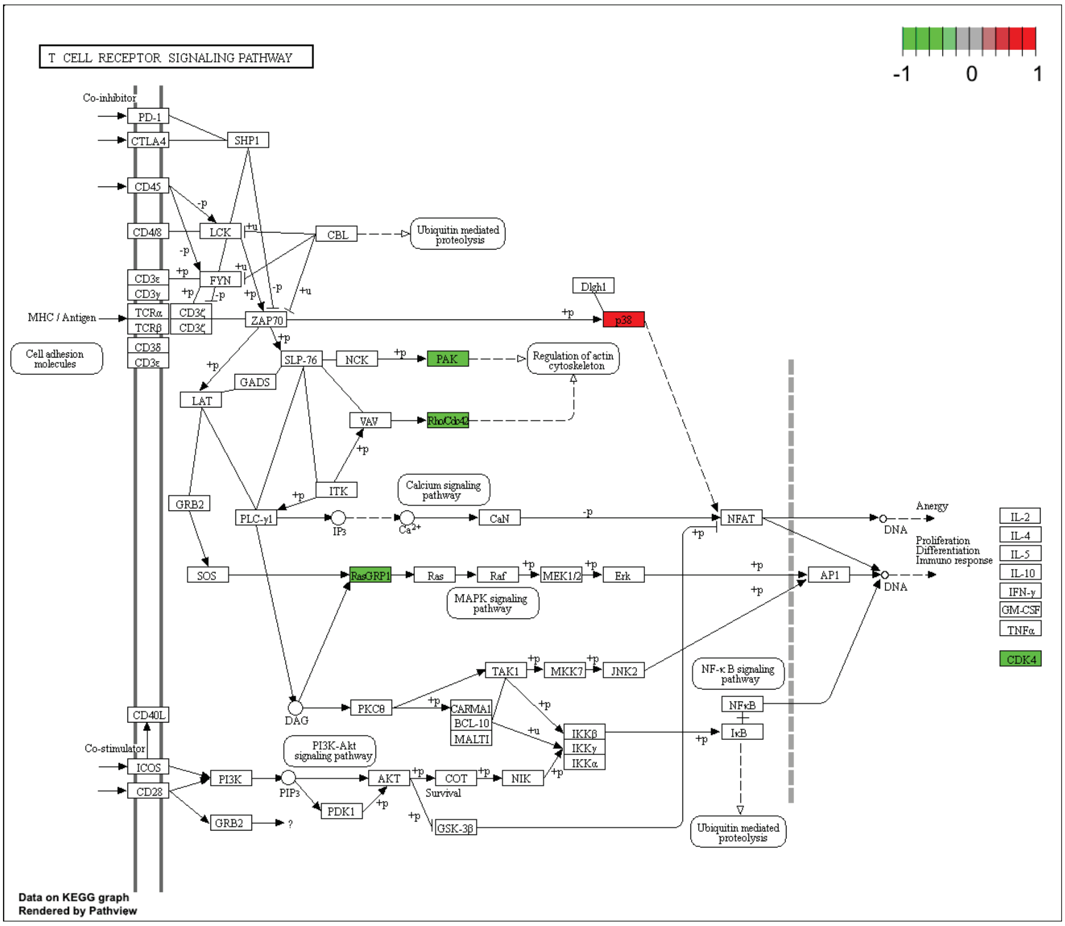
T CELL RECEPTOR SIGNALING PATHWAY
-1
0
1
Co-inhibitor
PD-1
CTLA4
SHP1
CD45
-p
CD4/8
LCK
+u
CBL
Ubiquitin mediated proteolysis
-p
+p
CD3ε
FYN
+u
CD3γ
+p
-p
+p
-p
+u
Dlgh1
MHC / Antigen
TCRα
CD3ζ
TCRβ
CD3ζ
ZAP70
+p
p38
CD3δ
CD3ε
Cell adhesion molecules
+p
SLP-76
NCK
+p
PAK
Regulation of actin cytoskeleton
+p
GADS
LAT
VAV
RhoCdc42
+p
GRB2
ITK
Calcium signaling pathway
+p
PLC-γ1
IP3
Ca2+
CaN
-p
NFAT
+p
Anergy
DNA
Proliferation
Differentiation
Immuno response
IL-2
IL-4
IL-5
IL-10
IFN-γ
GM-CSF
TNFα
CDK4
SOS
RasGRP1
Ras
Raf
+p
MEK1/2
+p
Erk
+p
+p
AP1
DNA
MAPK signaling pathway
+p
+p
TAK1
MKK7
JNK2
NF-κB signaling pathway
DAG
PKCθ
+p
CARMA1
BCL-10
MALT1
+p
+u
NFκB
IKKβ
IKKγ
IKKα
IκB
+p
CD40L
Co-stimulator
ICOS
CD28
PI3K
PIP3
PI3K-Akt signaling pathway
AKT
+p
COT
+p
NIK
+p
Survival
PDK1
+p
+p
GRB2
?
GSK-3β
Ubiquitin mediated proteolysis
Data on KEGG graph
Rendered by Pathview

Appendix D

Appendix D

Proteome profiling of A549 cells exposed to perovskites

To test whether changes in Amide I absorption are accompanied by corresponding changes in cellular protein expression we ran gel electrophoresis measurements on fractions extracted from untreated and treated cells.

Cells were lysed as previously described in the molecular biology protocols (5.6 Cell Lysis). After centrifugation, the pellet (insoluble fraction containing the vesicles), and the supernatant (soluble fraction containing the cytoplasmic proteins) were conserved for subsequent analysis. The pellet was sonicated as follows, in order to quantify vesicular proteins.

1. Pellets were washed once with 200 μ of lysis buffer.
2. To each tube containing pellet, 100 μ of Lysis buffer + 5% SDS was added and briefly sonicated at 60% amplitude, 3 sec on/ 3 sec off, 18 sec total time.
3. Proteins were heated for up to 5 minutes, then quantified using BCA kit. Concentration of each tube 1.2-1.7 $\mu g/ml$
4. Proteins were loaded on the gels together with a protein marker as a reference (Stacking gel at 4%, and resolving gel at 12%), and electrophoresis run during 30-50 minutes at 220 V.
5. The gel cassette is disassembled and the gel placed in a box and covered with bidistilled water, then heated in the microwave oven for 30 sec. Heating should be stopped before boiling occurs. The box with the gel is then placed on a shaker for 3-5 minutes. and this washing step is repeated twice with fresh water.
6. Coomassie staining solution is added to cover the gel in the box, then heated in the microwave for 10 sec. without boiling. The box with the gel is then placed on a shaker for 15-30 minutes for complete staining. Already after 1 minute, protein bands can be observed.
7. The staining solution is poured off and 50-100 ml bidistilled water is added in order to further unstain the light blue background of the gel on a shaker. The water can be replaced by fresh water for further unstaining if needed.
8. The gel can be scanned, photographed or dried for long-term storage.

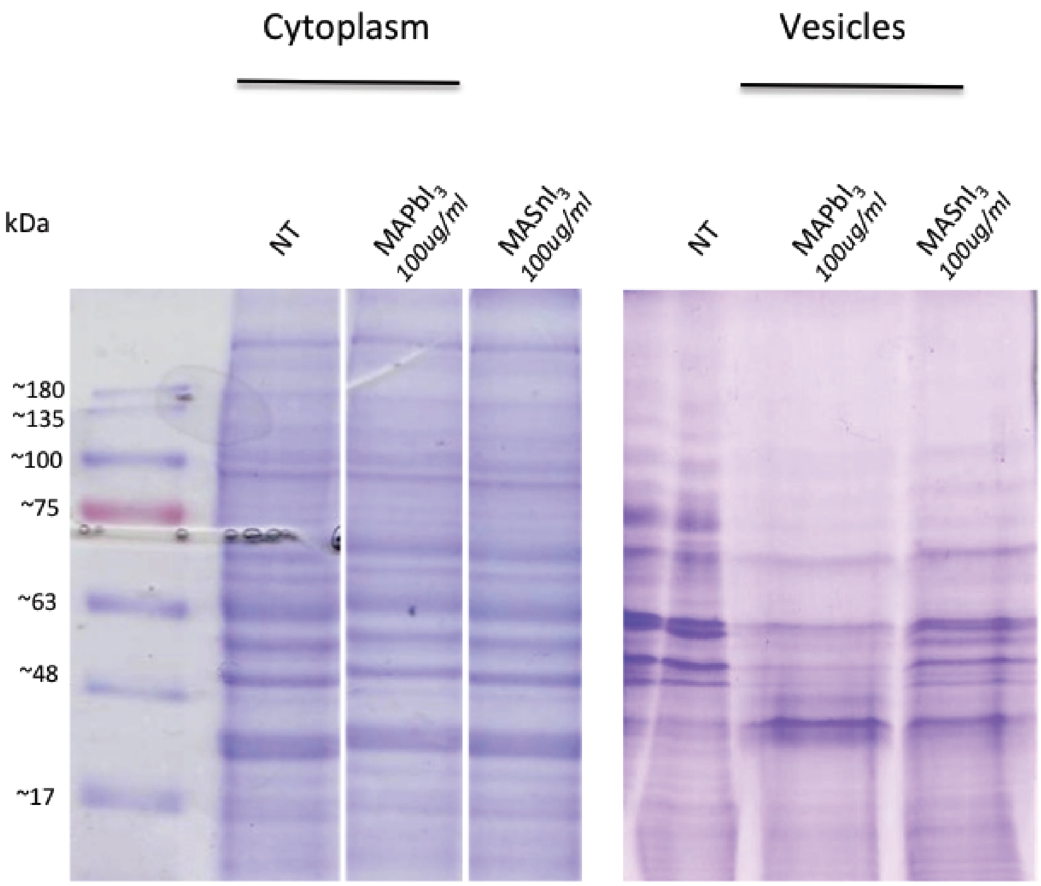

Figure D1 – SDS gels with Coomassie blue staining of A549 lysates from the soluble fraction of the cell composed of the cytoplasmic content (left), and the insoluble fraction composed of vesicles and other internal compartments.

Figure D1 shows a preliminary SDS-PAGE tracks from the cytoplasmic and microsomal fractions of cells that were untreated or treated with 100 μg/ml of $MAPbI_3$ or $MASnI_3$. It is apparent that the proteome of the cytoplasmic fraction is barely affected by exposure to $MAPbI_3$ or $MASnI_3$. In contrast, major differences are observed in the microsomal fractions of treated cells. The most striking difference is observed following treatment with $MAPbI_3$, which reduces expression of several proteins in the 48 – 100 kDa range while increasing expression of at least one protein of approximately 32 kDa mass. Similar changes are also induced by exposure to $MASnI_3$, although the effect is much reduced for a comparable dose and exposure time.

Appendix E

Molecular signaling pathway affected by perovskite exposure

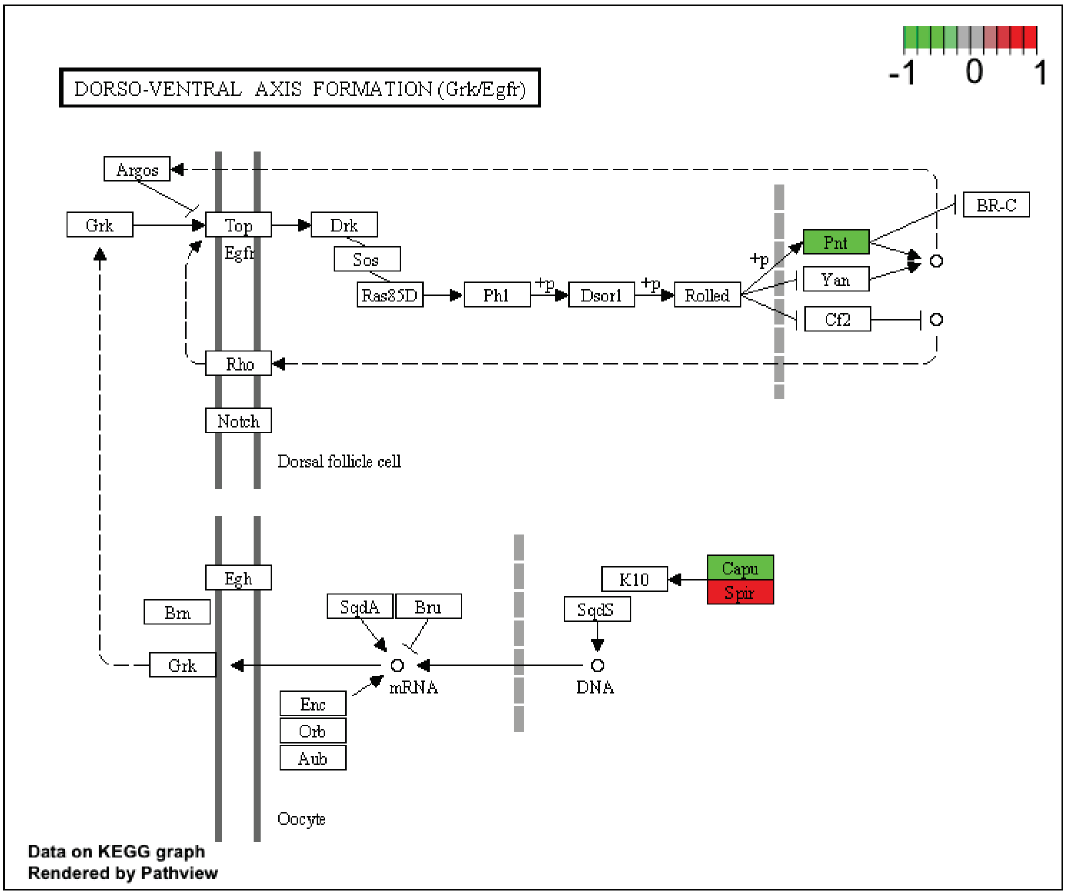

Figure D1 – The molecular signaling pathway of the dorso-ventral axis formation affected by perovskite exposure of A549 cells.

Bibliography

[1] \#3605 w[1118]. Url: http://flystocks.bio.indiana.edu/Reports/3605.html.

[2] Drosophila melanogaster Embryo and Larva Harvesting and Preparation | Protocol, Url: http://www.jove.com.

[3] Efficiency chart of photovoltaic novel materials - Url: http://www.nrel.gov/ ncpv/images/-efficiency_chart.jpg).

[4] Eur-lex - 32009l0028 - en - eur-lex - url: http://eur-lex.europa.eu/legal-content/en/all/?uri=celex%3a32009l0028.

[5] FlyBase Stock Center Stock Record. Url: http://flybase.org/reports/FBst0000005.html.

[6] Information Bureau - Url: http://pib.nic.in/newsite/erelease.aspx?relid=146680.

[7] Lausanne Genomic Technologies Facility -.

[8] Lead iodide (PbI2) (cas 10101-63-0) msds - http://www.guidechem.com/msds/10101-63-0.html.

[9] Live cell imaging of cell cycle and division—premo fucci cell cycle sensor | thermo fisher scientific.

[10] Nanomaterials - ECHA - Url: http://echa.europa.eu/en/regulations/nanomaterials.

[11] Rain on Methylammonium Lead Iodide Based Perovskites: Possible Environmental Effects of Perovskite Solar Cells - The Journal of Physical Chemistry Letters ACS Publications.

[12] Rneasy mini handbook - en - qiagen - url: https://www.qiagen.com/ch/resources/resourcedetail?id=14e7cf6e-521a-4cf7-8cbc-bf9f6fa33e24&lang=en.

[13] Science's Top 10 Breakthroughs of 2013 | Science | AAAS - Url: http://www.sciencemag.org/news/2013/12/sciences-top-10-breakthroughs-2013.

[14] This Day in Quotes: "Too cheap to meter" – the infamous nuclear power misquote... - Url: http://www.thisdayinquotes.com/2009/09/too-cheap-to-meter-nuclear-quote-debate.html.

[15] TiO2 Photocatalysis: Uses of Titanium Dioxide- Learn Chemistry - Url: http://www.rsc.org/learn-chemistry/resource/res00001268/tio2-photocatalysis-uses-of-titanium-dioxide?cmpid=CMP00002618.

[16] U10b nsls beamline description, url: https://pubweb.bnl.gov/˜carr/u10b.html.

[17] World Energy Statistics 2015 - http://www.iea.org/publications/freepublications/ publication/KeyWorld_Statistics_2015.pdf.

[18] The Cdt1 protein is required to license DNA for replication in fission yeast. 404(6778):625–628, 2000.

[19] A.-L. a L Mahul-Mellier, F. Vercruysse, B. Maco, N. Ait-Bouziad, M. De Roo, D. Muller, and H. A. Lashuel. Fibril growth and seeding capacity play key roles in alpha-synuclein-mediated apoptotic cell death. *Cell Death and Differentiation*, 22(12):1–16, 2015.

[20] M. Adeva-Andany, M. López-Ojén, R. Funcasta-Calderón, E. Ameneiros-Rodríguez, C. Donapetry-García, M. Vila-Altesor, and J. Rodríguez-Seijas. Comprehensive review on lactate metabolism in human health. *Mitochondrion*, 17:76–100, 2014.

[21] J M Ahn, H J Eom, X Yang, J N Meyer, and J Choi. Comparative toxicity of silver nanoparticles on oxidative stress and DNA damage in the nematode, Caenorhabditis elegans. *Chemosphere*, 108:343–352, 2014.

[22] Bruce Alberts et al. *2014 ASCB/IFCB Meeting abstracts*, volume 25. Garland Science, 4th edition, 2014.

[23] Natalie Alépée, Anthony Bahinski, Mardas Daneshian, Bart De Wever, Ellen Fritsche, and et al. State-of-the-art of 3D cultures (organs-on-a-chip) in safety testing and pathophysiology. *Altex*, 31(4):441–477, 2014.

[24] Jihyun An, Richard P. Fiorella, Steven J. Geib, and Nathaniel L. Rosi. Synthesis, structure, assembly, and modulation of the co2 adsorption properties of a zinc-adeninate macrocycle. *Journal of the American Chemical Society*, 131(24):8401–8403, 2009.

[25] Simon Anders, Paul Theodor Pyl, and Wolfgang Huber. HTSeq-A Python framework to work with high-throughput sequencing data. *Bioinformatics*, 31(2):166–169, 2015.

[26] Richard G W Anderson. The Caveolae Membrane System. 67(1):199–225.

[27] G E Andersson, Olof Karlberg, Björn Canbäck, and Charles G Kurland. On the origin of mitochondria: a genomics perspective. 358(1429):165–179.

[28] Anon. Lead poisoning. *Field and Game News*, August(1):24–25, 1986.

[29] Maria Augustyniak, Marcin Gladysz, and Marta Dziewięcka. The Comet assay in insects–Status, prospects and benefits for science. 767:67–76, 2016.

[30] Tarek Baati, Patricia Horcajada, Olivier David, Ruxandra Gref, Patrick Couvreur, and Christian Serre. Quantification of tetramethyl-terephthalic acid in rat liver, spleen and urine matrices by liquid-liquid phase extraction and hplc-photodiode array detection. *Journal of Pharmaceutical and Biomedical Analysis*, 67-68:98–103, 2012.

[31] Tarek Baati, Leila Njim, Fadoua Neffati, Abdelhamid Kerkeni, Muriel Bouttemi, Ruxandra Gref, Mohamed Fadhel Najjar, Abdelfateh Zakhama, Patrick Couvreur, Christian Serre, and Patricia Horcajada. In depth analysis of the in vivo toxicity of nanoparticles of porous iron(iii) metal-organic frameworks. *Chemical Science*, 4(4):1597–1607, 2013.

[32] Aslihan Babayigit, Dinh Duy Thanh, Anitha Ethirajan, Jean Manca, Marc Muller, Hans-Gerd Boyen, and Bert Conings. Assessing the toxicity of pb- and sn-based perovskite solar cells in model organism danio rerio. *Scientific Reports*, 6:18721, jan 2016.

[33] J M Barnes and H B Stoner. The toxicology of tin compounds. *Pharmacological Reviews*, 11(2):211–231, jun 1959.

[34] G.M.J. Beaudoin III, Dipika S. Seung-Hye L, Yu-Gie Ng. Yang Y, and Arikkath J. Reichardt L.F. Culturing pyramidal neurons from the early postnatal mouse hippocampus and cortex. *Nature Protocols.*, 7(9):1741–1754., 2012.

[35] Kambez H Benam, Remi Villenave, Carolina Lucchesi, Antonio Varone, Cedric Hubeau, Hyun-Hee Lee, Stephen E Alves, Michael Salmon, Thomas C Ferrante, James C Weaver, Anthony Bahinski, Geraldine A Hamilton, and Donald E Ingber. SL Small airway-on-a-chip enables analysis of human lung inflammation and drug responses in vitro. *Nat Meth*, 13(2):151–157, 2016.

[36] Ines Ryma Benmessaoud, Anne-Laure Mahul-Mellier, Endre Horvath, Bohumil Maco, Massimo Spina, Hilal Lashuel, and Laszlo Forro. Health hazard of the Methylammonium Lead Iodide based Perovskites: cytotoxicity studies. *Toxicol. Res.*, 5(2):In press, 2015.

[37] Gary F Bennett. *Sittig's Handbook of Toxic and Hazardous Chemicals and Carcinogens, 4th Edition*, volume 94. William Andrew, 2002.

[38] Sayak Bhattacharya, Kevin E. McElhanon, Liubov V. Gushchina, and Noah Weisleder. Role of phosphatidylinositol-4,5-bisphosphate 3-kinase signaling in vesicular trafficking. *Life Sciences*, 167:39–45, 2016.

[39] E Bier. Drosophila, the golden bug, emerges as a tool for human genetics. *Nat Rev Genet*, 6(1):9–23, 2005.

[40] Steve Blunden and Tony Wallace. Tin in canned food: A review and understanding of occurrence and effect. *Food and Chemical Toxicology*, 41(12):1651–1662, 2003.

[41] Jasmina Bogojeska, Adrian Alexa, André Altmann, Thomas Lengauer, and Jörg Rahnenführer. Rtreemix: An R package for estimating evolutionary pathways and genetic progression scores. *Bioinformatics*, 24(20):2391–2392, 2008.

[42] Markus Bonda. Characterisation of Living Matter Using Advanced Spectroscopy Techniques. 2011.

[43] Markus Bonda, Valérie Perrin, Bertrand Vileno, Heike Runne, Ariane Kretlow, Laszlo Forro, Ruth Luthi-Carter, Lisa M. Miller, and Sylvia Jeney. Synchrotron infrared microspectroscopy detecting the evolution of Huntington's disease neuropathology and suggesting unique correlates of dysfunction in white versus gray brain matter. *Analytical Chemistry*, 83(20):7712–7720, 2011.

[44] Peter J. Boogaard, Michel Boisset, Steve Blunden, Scot Davies, Teng Jin Ong, and Jean Pierre Taverne. Comparative assessment of gastrointestinal irritant potency in man of tin(II) chloride and tin migrated from packaging. *Food and Chemical Toxicology*, 41(12):1663–1670, 2003.

[45] Paul J a Borm and Wolfgang Kreyling. Toxicological hazards of inhaled nanoparticles–potential implications for drug delivery. *Journal of nanoscience and nanotechnology*, 4(5):521–531, 2004.

[46] Emmanuel Boucrot, Antonio P A Ferreira, Leonardo Almeida-Souza, Sylvain Debard, Yvonne Vallis, Gillian Howard, Laetitia Bertot, Nathalie Sauvonnet, and Harvey T McMahon. Endophilin marks and controls a clathrin-independent endocytic pathway. 517(7535):460–465, 2015.

[47] Brian Martin. Opposing nuclear power: past and present. Vol. 26, N:43–47, 2007.

[48] L. A. Burns, E. E. Sikorski, J. J. Saady, and A. E. Munson. Evidence for arsenic as the immunosuppressive component of gallium arsenide. *Toxicology and Applied Pharmacology*, 110(1):157–169, 1991.

[49] Chantel M Cadwell, Wenji Su, and Andrew P Kowalczyk. Cadherin tales: Regulation of cadherin function by endocytic membrane trafficking. 2016.

[50] W Z Cande, E Lazarides, and J R McIntosh. A comparison of the distribution of actin and tubulin in the mammalian mitotic spindle as seen by indirect immunofluorescence. 72(3):552–567, 1977.

[51] Jeffrey W Card, Darryl C Zeldin, James C Bonner, and Earle R Nestmann. Pulmonary applications and toxicity of engineered nanoparticles. *American journal of physiology. Lung cellular and molecular physiology*, 295(3):L400–11, 2008.

[52] G. Cassanas, M. Morssli, E. Fabrègue, and L. Bardet. Vibrational spectra of lactic acid and lactates. *Journal of Raman Spectroscopy*, 22(7):409–413, 1991.

[53] David C. Chan. Mitochondria: Dynamic Organelles in Disease, Aging, and Development. *Cell*, 125(7):1241–1252, 2006.

[54] Hanqing Chen, Bing Wang, Weiyue Feng, Wei Du, Hong Ouyang, Zhifang Chai, and Xiaolin Bi. Oral magnetite nanoparticles disturb the development of Drosophila melanogaster from oogenesis to adult emergence. *Nanotoxicology*, 5390(August):1–11, 2014.

[55] Chial, Heidi, Drovdlic, Carrie, Koopman, Maggie, Nelson, Sarah C., Spivey, Angela, and Smith, Robin. *Introduction to Essentials of Genetics.* Nature sci edition.

[56] Mariana Carmen Chifiriuc, Attila Cristian Ratiu, Marcela Popa, and Alexandru Al Ecovoiu. Drosophotoxicology: An emerging research area for assessing nanoparticles interaction with living organisms. *International Journal of Molecular Sciences*, 17(2):36, 2016.

[57] Leo Y T Chou, Kevin Ming, and Warren C W Chan. Strategies for the intracellular delivery of nanoparticles. *Chemical Society reviews*, 40(1):233–245, 2011.

[58] Nicole Cloonan, Alistair R R Forrest, Gabriel Kolle, Brooke B a Gardiner, Geoffrey J Faulkner, Mellissa K Brown, Darrin F Taylor, Anita L Steptoe, Shivangi Wani, Graeme Bethel, Alan J Robertson, Andrew C Perkins, Stephen J Bruce, Clarence C Lee, Swati S Ranade, Heather E Peckham, Jonathan M Manning, Kevin J McKernan, and Sean M Grimmond. Stem cell transcriptome profiling via massive-scale mRNA sequencing. *Nature methods*, 5(7):613–9, 2008.

[59] Constante Ceccarini and Harry Eagle. {pH} as a determinant of cellular growth and contact inhibition. 68(1):229–233, 1971.

[60] Geoffrey M Cooper. *The Cell.* Sinauer Associates, 2nd edition, 2000.

[61] COP21. United nations conference on climate change - Url: http://www.cop21.gouv.fr/. 2015.

[62] Matteo Cornaglia, Gopalan Krishnamani, Laurent Mouchiroud, Vincenzo Sorrentino, Thomas Lehnert, Johan Auwerx, and Martin A. M. Gijs. Automated longitudinal monitoring of in vivo protein aggregation in neurodegenerative disease C. elegans models. *Molecular Neurodegeneration*, 11(1):17, 2016.

[63] Matteo Cornaglia, Laurent Mouchiroud, Alexis Marette, Shreya Narasimhan, Thomas Lehnert, Virginija Jovaisaite, Johan Auwerx, and Martin A M Gijs. An automated microfluidic platform for C. elegans embryo arraying, phenotyping, and long-term live imaging. 5:10192, 2015.

[64] A.J. Crimmins, J.L. Balbus, Gamble, C.B. Beard, J.E. Bell, and et al. Usgcrp, 2016: The impacts of climate change on human health in the united states: A scientific assessment. pages 1–312, 2016.

[65] Thomas P Moyer Ph D. Toxic Metals. (3):1189–1205.

[66] Maria Davoren, Eva Herzog, Alan Casey, Benjamin Cottineau, Gordon Chambers, Hugh J. Byrne, and Fiona M. Lyng. In vitro toxicity evaluation of single walled carbon nanotubes on human A549 lung cells. *Toxicology in Vitro*, 21(3):438–448, 2007.

[67] Florencia di Pietro, Arnaud Echard, and Xavier Morin. Regulation of mitotic spindle orientation: an integrated view. *EMBO reports*, 17(8):1106–1130, 2016.

[68] Y Dilek, S Newcomb, and G S A Meeting. *Ophiolite Concept and the Evolution of Geological Thought.* Geological Society of America, 2003.

[69] Alexander Dobin, Carrie A Davis, Felix Schlesinger, Jorg Drenkow, Chris Zaleski, Sonali Jha, Philippe Batut, Mark Chaisson, and Thomas R Gingeras. Star: ultrafast universal rna-seq aligner. 29(1):15–21, 2013.

[70] Gary J. Doherty and Richard Lundmark. GRAF1-dependent endocytosis: Figure 1. *Biochemical Society Transactions*, 37(5):1061–1065, 2009.

[71] P Dumas and L Miller. Biological and Biomedical Applications of Synchrotron Infrared Microspectroscopy. 29(2):201–218, 2003.

[72] W D Duncan and Gwyn P Williams. Infrared synchrotron radiation from electron storage rings. 22(18):2914–2923.

[73] Rosemary Dunford, Angela Salinaro, Lezhen Cai, Nick Serpone, Satoshi Horikoshi, Hisao Hidaka, and John Knowland. Chemical oxidation and DNA damage catalysed by inorganic sunscreen ingredients. *FEBS Letters*, 418(1-2):87–90, 1997.

[74] Commonwealth Edison. Costs of Nuclear Power Plants — What Went Wrong ? - http://www.phyast.pitt.edu/~blc/book/chapter9.html. pages 1–10, 2014.

[75] Figures Edition. Global Cancer - Url: http://gco.iarc.fr/. (800), 2012.

[76] EEA - European Environmental Agency. Assessment of global megatrends - an update. Global megatrend 1: Diverging global population trends - http://www.eea.europa.eu/publications/global-megatrend-update-1-diverging. 2014.

[77] E W Esch, A Bahinski, and D Huh. Organs-on-chips at the frontiers of drug discovery. 14(4):248–260, 2015.

[78] Ting-Jun Fan, Li-Hui Han, Ri-Shan Cong, and Jin Liang. Caspase Family Proteases and Apoptosis. 37(11):719–727, 2005.

[79] Julie Fisher and John Arnold. *{BIOS} Instant Notes in Chemistry for Biologists*. Garland Science, 2003.

[80] Gagan Flora, Deepesh Gupta, and Archana Tiwari. Toxicity of lead: a review with recent updates. *Interdisciplinary Toxicology*, 5(2):47–58, 2012.

[81] S.J.S. Flora, S.N. Dube, R. Vijayaraghavan, and S.C. Pant. Changes in certain hematological and physiological variables following single gallium arsenide exposure in rats. *Biological Trace Element Research*, 58(3):197–208, 1997.

[82] Swaran J S Flora, Pradeep Kumar, Gurusamy M. Kannan, and Ganga P. Rai. Acute oral gallium arsenide exposure and changes in certain hematological, hepatic, renal and immunological indices at different time intervals in male wistar rats. *Toxicology Letters*, 94(2):103–113, 1998.

[83] Zachary Freyberg, Mark S Sonders, Jenny I Aguilar, Takato Hiranita, Caline S Karam, Jorge Flores, Andrea B Pizzo, Yuchao Zhang, Zachary J Farino, Audrey Chen, Ciara A Martin, Theresa A Kopajtic, Hao Fei, Gang Hu, Yi-Ying Lin, Eugene V Mosharov, Brian D McCabe, Robin Freyberg, Kandatege Wimalasena, Ling-Wei Hsin, Dalibor Sames, David E Krantz, Jonathan L Katz, David Sulzer, and Jonathan A Javitch. Mechanisms of amphetamine action illuminated through optical monitoring of dopamine synaptic vesicles in Drosophila brain. *Nature communications*, 7:10652, 2016.

[84] Lorenzo Galluzzi, Gerald M Cohen, S A Aaronson, György Hajnóczky, John M Abrams, Junying Yuan, Emad S Alnemri, David W Andrews, Eric H Baehrecke, Mikhail V Blagosklonny, N G Bazan, Dale E Bredesen, J A Cidlowski, K Blomgren, A Ciechanover, Wafik S El-Deiry, C Borner, Richard A Flavell, Simone Fulda, C Brenner, Douglas R Green, M Castedo, Hidenori Ichijo, Marja Jäättelä, A Kimchi, Daniel J Klionsky, V De Laurenzi, R A Knight, R De Maria, Sally Kornbluth, M Deshmukh, B D Dynlacht, Beth Levine, S A Lipton, Frank Madeo, Seamus J Martin, Gerry Melino, C Garrido, Ute M Moll, P Golstein, M-L Gougeon, Donald W Nicholson, Marcus E Peter, H Gronemeyer, Jochen H M Prehn, G A Rabinovich, J M

Hardwick, Hans-Uwe Simon, M O Hengartner, Jürg Tschopp, Peter Vandenabeele, Karen H Vousden, O Kepp, Boris Zhivotovsky, Guido Kroemer, S Kumar, E Lugli, W Malomi, J-C W Marine, J P Medema, P Mehlen, E Morselli, S Nagata, P Nicotera, G Nuñez, M Oren, J Penninger, S Pervaiz, M Piacentini, H Puthalakath, R Rizzuto, C M P Rodrigues, D C Rubinsztein, T Rudel, L Scorrano, H Steller, Y Tsujimoto, I Vitale, and R J Youle. Guidelines for the use and interpretation of assays for monitoring cell death in higher eukaryotes. *Cell death and differentiation*, 16(8):1093–107, 2009.

[85] Lorenzo Galluzzi, Oliver Kepp, Christina Trojel-Hansen, and Guido Kroemer. Mitochondrial control of cellular life, stress, and death. 111(9):1198–1207, 2012.

[86] L. Garfinkel. Asbestos: Historical Perspective. *CA: A Cancer Journal for Clinicians*, 34(1):44–47, 1984.

[87] Peter Gehr, Marianne Bachofen, and Ewald R. Weibel. The normal human lung: ultrastructure and morphometric estimation of diffusion capacity. *Respiration Physiology*, 32(2):121–140, 1978.

[88] Marianne Geiser and Wolfgang G Kreyling. Deposition and biokinetics of inhaled nanoparticles. *Particle and Fibre Toxicology*, 7(i):2, 2010.

[89] Mohammad Ali Ghaffari and Behrooz Motlagh. In vitro effect of lead, silver, tin, mercury, indium and bismuth on human sperm creatine kinase activity: A presumable mechanism for men infertility. *Iranian Biomedical Journal*, 15(1-2):38–42, 2011.

[90] Bruce Gillis, Zarema Arbieva, and Igor Gavin. Analysis of lead toxicity in human cells. *BMC Genomics*, 13(1):344, 2012.

[91] Peter L. Goering, Robert R. Maronpot, and Bruce A. Fowler. Effect of intratracheal gallium arsenide administration on delta-aminolevulinic acid dehydratase in rats: Relationship to urinary excretion of aminolevulinic acid. *Toxicology and Applied Pharmacology*, 92(2):179–193, 1988.

[92] Harvey C. Gonick. Lead-binding proteins: A review. *Journal of Toxicology*, 2011:686050, 2011.

[93] Martin A Green. *the Future of Thin Film Solar Cells*. Tsinghua University Press, 2006.

[94] Martin A Green, Anita Ho-Baillie, and Henry J Snaith. The emergence of perovskite solar cells. *Nature Photonics*, 8(7):506–514, 2014.

[95] Morris Greenberg and T. a. Lloyd Davies. Mesothelioma Register 1967-68. *British journal of industrial medicine*, 31(2):91–104, 1974.

[96] I Guest and D R Varma. Developmental toxicity of methylamines in mice. *Journal of Toxicology & Environmental Health*, 32(3):319–330, 1991.

[97] Severin N. Habisreutinger, Tomas Leijtens, Giles E. Eperon, Samuel D. Stranks, Robin J. Nicholas, and Henry J. Snaith. Carbon nanotube/polymer composites as a highly stable hole collection layer in perovskite solar cells. *Nano Letters*, 14(10):5561–5568, 2014.

[98] J S Hanas, J S Rodgers, J A Bantle, and Y G Cheng. Lead inhibition of {DNA}-binding mechanism of Cys(2)His(2) zinc finger proteins. 56(5):982–988, 1999.

[99] Tian Hang, Wen Zhang, Heng-Yun Ye, and Ren-Gen Xiong. Metal-organic complex ferroelectrics. *Chemical Society reviews*, 40(7):3577–98, 2011.

[100] Feng Hao, Constantinos C. Stoumpos, Duyen Hanh Cao, Robert P. H. Chang, and Mercouri G. Kanatzidis. Lead-free solid-state organic–inorganic halide perovskite solar cells. *Nature Photonics*, 8(6):489–494, 2014.

[101] Thomas Hartung, Michael Balls, Claudia Bardouille, Olivier Blanck, Sandra Coecke, Gerhard Gstraunthaler, David Lewis, and ECVAM Good Cell Culture Practice Task Force. Good Cell Culture Practice. {ECVAM} Good Cell Culture Practice Task Force Report 1. 30(4):407–414, 2002.

[102] J A Hayes, G L Snider, and K C Palmer. The evolution of biochemical damage in the rat lung after acute cadmium exposure. *The American review of respiratory disease*, 113(2):121–130, 1976.

[103] Tom Hill, Christian Schlötterer, and Andrea J. Betancourt. Hybrid Dysgenesis in Drosophila simulans Associated with a Rapid Invasion of the P-Element. *PLoS Genetics*, 12(3):e1005920, 2016.

[104] J T Hodgson and a Darnton. The quantitative risks of mesothelioma and lung cancer in relation to asbestos exposure. *The Annals of occupational hygiene*, 44(8):565–601, 2000.

[105] Sandy Hoffman, Daniel Martin, Alicia Meléndez, and Jill Bargonetti. *C. elegans {CEP}-1/p53 and {BEC}-1 Are Involved in {DNA} Repair*, volume 9. 2014.

[106] Patricia Horcajada, Tamim Chalati, Christian Serre, Brigitte Gillet, Catherine Sebrie, Tarek Baati, Jarrod F Eubank, Daniela Heurtaux, Pascal Clayette, Christine Kreuz, Jong-San Chang, Young Kyu Hwang, Veronique Marsaud, Phuong-Nhi Bories, Luc Cynober, Sophie Gil, Gerard Ferey, Patrick Couvreur, and Ruxandra Gref. Porous metal-organic-framework nanoscale carriers as a potential platform for drug delivery and imaging. *Nature Materials*, 9(2):172–178, 2010.

[107] Patricia Horcajada, Ruxandra Gref, Tarek Baati, Phoebe K. Allan, Guillaume Maurin, Patrick Couvreur, Gérard Férey, Russell E. Morris, and Christian Serre. Metal-organic frameworks in biomedicine. *Chemical Reviews*, 112(2):1232–1268, 2012.

[108] Yu Fen Huang, Haipeng Liu, Xiangling Xiong, Yan Chen, and Weihong Tan. Nanoparticle-mediated IgE-receptor aggregation and signaling in RBL mast cells. *Journal of the American Chemical Society*, 131(47):17328–17334, 2009.

[109] Dongeun Huh, Hyun Jung Kim, Jacob P Fraser, Daniel E Shea, Mohammed Khan, Anthony Bahinski, Geraldine a Hamilton, and Donald E Ingber. Microfabrication of human organs-on-chips. *Nature protocols*, 8(11):2135–57, 2013.

[110] Piper Reid Hunt. The C. elegans model in toxicity testing. pages n/a—-n/a.

[111] Chris Isidore. Dunkin' Donuts to remove titanium dioxide from donuts. 2015.

[112] Nadge Jamin, Paul Dumas, Janine Moncuit, Wolf-Herman Fridman, Jean-Luc Teillaud, G Lawrence Carr, and Gwyn P Williams. Highly resolved chemical imaging of living cells by using synchrotron infrared microspectrometry. *Applied Biological Sciences*, 95(9):4837–4840, 1998.

[113] Guang-yu Jiang, Shu-jiao Wei, Xiao-ping Li, Li-heng Wang, Zhi-dan Mai, and Xian-min Ge. [{{Pathological}} observation of lung injury in experimental animals induced by non-ferrous metal (tin) dusts]. 30(8):561–566, 2012.

[114] Wen Jiang, Betty Y S Kim, James T Rutka, and Warren C W Chan. Nanoparticle-mediated cellular response is size-dependent. *Nature nanotechnology*, 3(3):145–50, 2008.

[115] S Jin, S Martinek, W S Joo, J R Wortman, N Mirkovic, a Sali, M D Yandell, N P Pavletich, M W Young, and a J Levine. Identification and characterization of a p53 homologue in Drosophila melanogaster. *Proceedings of the National Academy of Sciences of the United States of America*, 97(13):7301–7306, 2000.

[116] R S Kamath, M Martinez-Campos, P Zipperlen, A G Fraser, and J Ahringer. Effectiveness of specific RNA-mediated interference through ingested double-stranded RNA in Caenorhabditis elegans. *Genome biology*, 2(1):RESEARCH0002, 2001.

[117] Ewelina Kijak, Ezio Rosato, Katarzyna Knapczyk, and Elżbieta Pyza. Drosophila melanogaster as a model system of aluminum toxicity and aging. 21(2):189–202, 2014.

[118] Chinpal Kim, Sara Layman, Dorothy M Morré, and D James Morré. Structural Changes Revealed by Fourier Transform Infrared and Circular Dichroism Spectroscopic Analyses Underlie {tNOX} Periodic Oscillations. 3(3):391–413, 2006.

[119] Min-Sik Kim, Sneha Pinto, Derese Getnet, Raja Nirujogi, Srikanth Manda, and et al. A draft map of the human proteome. *Nature*, 509(7502):575–581, 2014.

[120] Andrew W Knight, Stephen Little, Keith Houck, David Dix, Richard Judson, Ann Richard, Nancy McCarroll, Gregory Akerman, Chihae Yang, Louise Birrell, and Richard M Walmsley. Evaluation of high-throughput genotoxicity assays used in profiling the {US} {EPA} {ToxCast} chemicals. 55(2):188–199, 2009.

[121] Akihiro Kojima, Kenjiro Teshima, Yasuo Shirai, and Tsutomu Miyasaka. Organometal halide perovskites as visible-light sensitizers for photovoltaic cells. *Journal of the American Chemical Society*, 131(17):6050–6051, 2009.

[122] Sudha Kumari and Satyajit Mayor. ARF1 is directly involved in dynamin-independent endocytosis. *Nature Cell Biology*, 10(1):30–41, 2008.

[123] Mohamedally Kurmoo. Magnetic metal–organic frameworks. *Chemical Society Reviews*, 38(5):1353, 2009.

[124] Petri Kursula and Viivi Majava. A structural insight into lead neurotoxicity and calmodulin activation by heavy metals. *Acta Crystallographica Section F: Structural Biology and Crystallization Communications*, 63(8):653–656, 2007.

[125] Barbara Laurinyecz, Mária Péter, Viktor Vedelek, Attila L Kovács, Gábor Juhász, Péter Maróy, László Vígh, Gábor Balogh, and Rita Sinka. Reduced expression of CDP-DAG synthase changes lipid composition and leads to male sterility in Drosophila. *Open biology*, 6(1):50169, 2016.

[126] M M Teuscher Lee J Miyasaka, T Murakami, TN Snaith, HJ. Efficient Hybrid Solar Cells Based on Meso-Superstructured Organometal Halide Perovskites. *Science*, 338(6107):647, 2012.

[127] Irina Lehmann, Ulrich Sack, and Jörg Lehmann. Metal ions affecting the immune system. *Metal ions in life sciences*, 8:157–85, 2011.

[128] Bruno Lemaitre and Irene Miguel-Aliaga. The digestive tract of Drosophila melanogaster. 47:377–404, 2013.

[129] Bo Li and Colin N Dewey. {RSEM}: accurate transcript quantification from {RNA}-Seq data with or without a reference genome. 12:323, 2011.

[130] H Li, M Eddaoudi, M O'Keeffe, and O M Yaghi. Design and synthesis of an exceptionally stable and highly porous metal-organic framework. *Nature*, 402(November):276–279, 1999.

[131] Jingyi Jessica Li, Haiyan Huang, Peter J Bickel, and Steven E Brenner. Comparison of D. melanogaster and C. elegans developmental stages, tissues, and cells by {modENCODE} {RNA}-seq data. 24(7):1086–1101, 2014.

[132] Chi-Hung Liu, Chu-Yun Huang, and Chin-Chang Huang. Occupational Neurotoxic Diseases in Taiwan. *Safety and Health at Work*, 3(4):257–267, 2012.

[133] Hearst Magazines. *Popular Mechanics, 1952.* Hearst Magazines, 1952.

[134] John S. Magyar, Tsu Chien Weng, Charlotte M. Stern, David F. Dye, Brian W. Rous, John C. Payne, Brian M. Bridgewater, Ana Mijovilovich, Gerard Parkin, Jeffrey M. Zaleski, James E. Penner-Hahn, and Hilary Arnold Godwin. Reexamination of lead(II) coordination preferences in sulfur-rich sites: Implications for a critical mechanism of lead poisoning. *Journal of the American Chemical Society*, 127(26):9495–9505, 2005.

[135] N. Marina-Garcia, L. Franchi, Y.-G. Kim, Y. Hu, D. E. Smith, G.-J. Boons, and G. Nunez. Clathrin- and Dynamin-Dependent Endocytic Pathway Regulates Muramyl Dipeptide Internalization and NOD2 Activation. *The Journal of Immunology*, 182(7):4321–4327, 2009.

[136] Marcel Martin. Cutadapt removes adapter sequences from high-throughput sequencing reads. 17(1):pp. 10—-12, 2011.

[137] Michael C Martin, Nelly M Tsvetkova, John H Crowe, and Wayne R McKinney. Negligible Sample Heating from Synchrotron Infrared Beam. 55(2):111–113, 2001.

[138] U Marx, T B Andersson, A Bahinski, M Beilmann, S Beken, F R Cassee, M Cirit, M Daneshian, S Fitzpatrick, O Frey, C Gaertner, C Giese, L Griffith, T Hartung, M B Heringa, J Hoeng, Jong De, H Kojima, J Kuehnl, M Leist, A Luch, I Maschmeyer, D Sakharov, A.J.A.M. Sips, T Steger-Hartmann, D A Tagle, A Tonevitsky, T Tralau, S Tsyb, De Stolpe Van, R Vandebriel, P Vulto, J Wang, J Wiest, M Rodenburg, and A Roth. Biology-inspired microphysiological system approaches to solve the prediction dilemma of substance testing. 33(3):272–321, 2016.

[139] Pieta K Mattila and Pekka Lappalainen. Filopodia: molecular architecture and cellular functions. *Nature Reviews: Molecular Cell Biology*, 9(6):446–454, 2008.

[140] Andrew Maynard. Dunkin' Donuts ditches titanium dioxide – but is it actually harmful?

[141] Heidi M. McBride, Margaret Neuspiel, and Sylwia Wasiak. Mitochondria: More Than Just a Powerhouse. *Current Biology*, 16(14):R551—-R560, 2006.

[142] Alistair C. McKinlay, Russell E. Morris, Patricia Horcajada, Gérard Férey, Ruxandra Gref, Patrick Couvreur, and Christian Serre. BioMOFs: Metal-organic frameworks for biological and medical applications. *Angewandte Chemie - International Edition*, 49(36):6260–6266, 2010.

[143] Lisa M. Miller and Paul Dumas. Chemical imaging of biological tissue with synchrotron infrared light. *Biochimica et Biophysica Acta - Biomembranes*, 1758(7):846–857, 2006.

[144] Lisa M Miller and Randy J Smith. Synchrotrons versus globars, point-detectors versus focal plane arrays: Selecting the best source and detector for specific infrared microspectroscopy and imaging applications. 38(1):237–240, 2005.

[145] Brooke T Mossman and Andrew Churg. Mechanisms in the patheogenesis of asbestosis and silicosis. *Am J Rep*, 157:1666–1689, 1998.

[146] Seyed Ali Mousavi, Lene Malerød, Trond Berg, and Rune Kjeken. Clathrin-dependent endocytosis. 377(Pt 1):1–16, 2004.

[147] Ugrappa Nagalakshmi, Zhong Wang, Karl Waern, Chong Shou, Debasish Raha, Mark Gerstein, and Michael Snyder. The transcriptional landscape of the yeast genome defined by RNA sequencing. *Science (New York, N.Y.)*, 320(5881):1344–9, 2008.

[148] Richard Nass and Iqbal Hamza. The nematode C. elegans as an animal model to explore toxicology in vivo: solid and axenic growth culture conditions and compound exposure parameters. In *Current protocols in toxicology / editorial board, Mahin D. Maines (editor-in-chief) ... [et al.]*, volume Chapter 1, page Unit1.9. John Wiley & Sons, Inc., 2007.

[149] National Institute for Occupational Safety and Health. Occupational exposure to titanium dioxide. 63(63):1–140, 2011.

[150] NIOSH. The National Institute for Occupational Safety and Health - http://www.cdc.gov/niosh/about.html. 2013.

[151] H Nishitani, Z Lygerou, and T Nishimoto. Proteolysis of DNA replication licensing factor Cdt1 in S-phase is performed independently of Geminin through its N-terminal region. 279(29):30807–30816, 2004.

[152] National Toxicology Program NTP. NTP Toxicology and Carcinogenesis Studies of Methyleugenol (CAS No. 93-15-2). *Natl. Toxicol. Prog. Tech. Rep. Ser*, 491(F344/N Rats and B6C3F1 Mice (Gavage Studies)):1–412, 2000.

[153] Center for Food Safety Nutrition and Applied. *FDA Authority Over Cosmetics: How Cosmetics Are Not FDA-Approved, but Are FDA-Regulated.*

[154] G Oberdörster, Z Sharp, V Atudorei, A Elder, R Gelein, W Kreyling, and C Cox. Translocation of Inhaled Ultrafine Particles to the Brain. *Inhalation Toxicology*, 16(6-7):437–445, 2004.

[155] Gunter Oberdorster, Juraj Ferin, Robert Gelein, Sidney C Soderholm, and Jacob Finkelstein. Role of the Alveolar Macrophage in Lung In jury : Studies with Ultrafine Particles. *Environ. Health Perspect.*, 97:193–199, 1992.

[156] Günter Oberdörster, Eva Oberdörster, and Jan Oberdörster. Nanotoxicology: An emerging discipline evolving from studies of ultrafine particles. *Environmental Health Perspectives*, 113(7):823–839, 2005.

[157] Office of the Commissioner. Search for FDA Guidance Documents - Considering Whether an FDA-Regulated Product Involves the Application of Nanotechnology.

[158] Genetics of the white Locus. Url: http://www.indiana.edu/%7b %7doso/lessons/white.htm.

[159] Shiro Ohyama, Noburu Ishinishi, Akira Hisanaga, and Akiyo Yamamoto. Comparative chronic toxicity, including tumorigenicity, of gallium arsenide and arsenic trioxide intratracheally instilled into hamsters. 2(4):333–337, 1988.

[160] H Olson, G Betton, D Robinson, K Thomas, A Monro, G Kolaja, P Lilly, J Sanders, G Sipes, W Bracken, M Dorato, K Van Deun, P Smith, B Berger, and A Heller. Concordance of the toxicity of pharmaceuticals in humans and in animals. 32(1):56–67, 2000.

[161] M Omura. Testicular Toxicity of Gallium Arsenide, Indium Arsenide, and Arsenic Oxide in Rats by Repetitive Intratracheal Instillation. *Fundamental and Applied Toxicology*, 32(1):72–78, 1996.

[162] M Omura, M Hirata, A Tanaka, M Zhao, Y Makita, N Inoue, K Gotoh, and N Ishinishi. Testicular toxicity evaluationof arsenic-conatining binary compound semiconductors, gallium arsenide and indium arsenide, in hamsters. *Toxicol Lett*, 89(2):123–129, 1996.

[163] M Omura, A Tanaka, M Zhao, M Hirata, Y Makita, N Inoue, and K Gotoh. Toxic effects of gallium arsenide on sperm in rats by repeated intratracheal instillations. *Sangyo eiseigaku zasshi = Journal of occupational health*, 37(3):165–6, 1995.

[164] M. Omura, K. Yamazaki, A. Tanaka, M. Hirata, Y. Makita, and N. Inoue. Changes in the testicular damage caused by indium arsenide and indium phosphide in hamsters during two years after intratracheal instillations. *Journal of Occupational Health*, 42(4):196–204, 2000.

[165] E. M. Ophus, L. Rode, B. Gylseth, D. G. Nicholson, and K. Saeed. Analysis of titanium pigments in human lung tissue. *Scandinavian Journal of Work, Environment and Health*, 5(3):290–296, 1979.

[166] Brian O'Regan and Michael Gratzel. A low-cost,high-efficiency solar cell based on dye-sensitized colloidal TiO2 films. *Nature*, 353(24 OCTOBER 1991):737–740, 1991.

[167] L. Ouyang, Z. Shi, S. Zhao, F. T. Wang, T. T. Zhou, B. Liu, and J. K. Bao. Programmed cell death pathways in cancer: A review of apoptosis, autophagy and programmed necrosis. *Cell Proliferation*, 45(6):487–498, 2012.

[168] Ales Panacek, Robert Prucek, Dana Safarova, Milan Dittrich, Jana Richtrova, Katerina Benickova, Radek Zboril, and Libor Kvitek. Acute and chronic toxicity effects of silver nanoparticles (NPs) on Drosophila melanogaster. *Environmental Science & Technology*, 45(11):4974–4979, 2011.

[169] Margot G. Paulick and Carolyn R. Bertozzi. The glycosylphosphatidylinositol anchor: A complex membrane-anchoring structure for proteins. *Biochemistry*, 47(27):6991–7000, 2008.

[170] Lucas Pelkmans. Secrets of caveolae- and lipid raft-mediated endocytosis revealed by mammalian viruses. 1746(3):295–304, 2005.

[171] Andrew Philp, Adam L Macdonald, and Peter W Watt. Lactate – a signal coordinating cell and systemic function. *Journal of Experimental Biology*, 208(24):4561–4575, 2005.

[172] A. Poglitsch and D. Weber. Dynamic disorder in methylammoniumtrihalogenoplumbates (II) observed by millimeter-wave spectroscopy. *The Journal of Chemical Physics*, 87(11):6373, 1987.

[173] J R Pollack, C M Perou, A A Alizadeh, M B Eisen, A Pergamenschikov, C F Williams, S S Jeffrey, D Botstein, and P O Brown. Genome-wide analysis of DNA copy-number changes using cDNA microarrays. *Nature Genetics*, 23(1):41–46, 1999.

[174] Liam Portt, Grant Norman, Caitlin Clapp, Matthew Greenwood, and Michael T. Greenwood. Anti-apoptosis and cell survival: A review. *Biochimica et Biophysica Acta - Molecular Cell Research*, 1813(1):238–259, 2011.

[175] Ryan Posgai, Caitlin B. Cipolla-McCulloch, Kyle R. Murphy, Saber M. Hussain, John J. Rowe, and Mark G. Nielsen. Differential toxicity of silver and titanium dioxide nanoparticles on Drosophila melanogaster development, reproductive effort, and viability: Size, coatings and antioxidants matter. *Chemosphere*, 85(1):34–42, 2011.

[176] PrChemOnline.com. *Tin iodide safety data sheet - Url: http://www.prochemonline.com/upload/MSDS/3661.Tin(IV)Iodide.pdf.*

[177] G. Puccetti, F. Lahjomri, and R. M. Leblanc. Pulsed photoacoustic spectroscopy applied to the diffusion of sunscreen chromophores in human skin: The weakly absorbent regime. *Journal of Photochemistry and Photobiology B: Biology*, 39(2):110–120, 1997.

[178] Fei Ren, Baochun Yang, Jing Cai, Yaodong Jiang, Jun Xu, and Shan Wang. Toxic effect of zinc nanoscale metal-organic frameworks on rat pheochromocytoma (PC12) cells in vitro. *Journal of Hazardous Materials*, 271:283–291, 2014.

[179] Terry L Riss, Richard A Moravec, Andrew L Niles, Sarah Duellman, Hélène A Benink, Tracy J Worzella, and Lisa Minor. Cell Viability Assays. 2004.

[180] Susana Romero-Garcia, Mar??a Maximina B Moreno-Altamirano, Heriberto Prado-Garcia, and Francisco Javier S??nchez-Garc??a. Lactate contribution to the tumor microenvironment: Mechanisms, effects on immune cells and therapeutic relevance. *Frontiers in Immunology*, 7(FEB), 2016.

[181] Peter Roose, Michael G Turcotte, and John W Mitchell. Methylamines. isbn: 978-0-471-23896-6. In *Kirk-Othmer Encyclopedia of Chemical Technology*. John Wiley & Sons, Inc., 2000.

[182] W. Rüdig. *Anti-nuclear movements: a world survey of opposition to nuclear energy*. {Longman Current Affairs}, isbn :978-0-582-90269-5, 1990.

[183] Asako Sakaue-Sawano, Hiroshi Kurokawa, Toshifumi Morimura, Aki Hanyu, Hiroshi Hama, Hatsuki Osawa, Saori Kashiwagi, Kiyoko Fukami, Takaki Miyata, Hiroyuki Miyoshi, Takeshi Imamura, Masaharu Ogawa, Hisao Masai, and Atsushi Miyawaki. Visualizing spatiotemporal dynamics of multicellular cell-cycle progression. 132(3):487–498.

[184] P Sandin. *The precautionary principle in the 20th century: Late lessons from early warnings*, volume 7. Routledge, 2004.

[185] Ismael Santa-Maria, Maria E. Alaniz, Neil Renwick, Carolina Cela, Tudor A. Fulga, David Van Vactor, Thomas Tuschl, Lorraine N. Clark, Michael L. Shelanski, Brian D. McCabe, and John F. Crary. Dysregulation of microRNA-219 promotes neurodegeneration through post-transcriptional regulation of tau. *Journal of Clinical Investigation*, 125(2):681–686, 2015.

[186] Johannes Schindelin, Ignacio Arganda-Carreras, Erwin Frise, Verena Kaynig, Mark Longair, Tobias Pietzsch, Stephan Preibisch, Curtis Rueden, Stephan Saalfeld, Benjamin Schmid, Jean-Yves Tinevez, Daniel James White, Volker Hartenstein, Kevin Eliceiri, Pavel Tomancak, and Albert Cardona. Fiji: an open-source platform for biological-image analysis. *Nature Methods*, 9(7):676–682, 2012.

[187] S L Schmid. Clathrin-coated vesicle formation and protein sorting: an integrated process. 66:511–548.

[188] Gerd Schmitz and G Müller. Structure and function of lamellar bodies, lipid-protein complexes involved in storage and secretion of cellular lipids. *Journal of lipid research*, 32(10):1539–70, 1991.

[189] B Schumacher, K Hofmann, S Boulton, and a Gartner. The C. elegans homolog of the p53 tumor suppressor is required for DNA damage-induced apoptosis. *Current biology : CB*, 11(21):1722–1727, 2001.

[190] Björn Schwanhäusser, Dorothea Busse, Na Li, Gunnar Dittmar, Johannes Schuchhardt, Jana Wolf, Wei Chen, and Matthias Selbach. Global quantification of mammalian gene expression control. 473(7347):337–342, 2011.

[191] Js Seo, D Whang, H Lee, Si Jun, J Oh, Yj Jeon, and K Kim. A homochiral metal-organic porous material for enantioselective separation and catalysis. *Nature*, 404(April):982–986, 2000.

[192] E. E. Sikorski, L. A. Burns, K. L. McCoy, M. Stern, and A. E. Munson. Suppression of splenic accessory cell function in mice exposed to gallium arsenide. *Toxicology and Applied Pharmacology*, 110(1):143–156, 1991.

[193] E. E. Sikorski, L. A. Burns, M. L. Stern, M. I. Luster, and A. E. Munson. Splenic cell targets in gallium arsenide-induced suppression of the primary antibody response. *Toxicology and Applied Pharmacology*, 110(1):129–142, 1991.

[194] L K Simmons, P C May, K J Tomaselli, R E Rydel, K S Fuson, E F Brigham, S Wright, I Lieberburg, G W Becker, and D N Brems. Secondary structure of amyloid beta peptide correlates with neurotoxic activity in vitro. 45(3):373–379, 1994.

[195] E Skammeritz, L H Omland, J P Johansen, and Ø Omland. Asbestos Exposure and an Occupational Clinic. 2(4):224–236, 2011.

[196] Stefaan J H Soenen, Nele Nuytten, Simon F De Meyer, Stefaan C De Smedt, and Marcel De Cuyper. High intracellular iron oxide nanoparticle concentrations affect cellular cytoskeleton and focal adhesion kinase-mediated signaling. 6(7):832–842, 2010.

[197] SolarCellCentral. Solar Markets Around The World - http://solarcellcentral.com/markets_page.html. 2016.

[198] Jeanne Mager Stellman and International Labour Office. Encyclopaedia of occupational health and safety. 31(1):141, 1998.

[199] L Stergiou and M O Hengartner. Death and more: DNA damage response pathways in the nematode C. elegans. *Cell death and differentiation*, 11(1):21–28, 2004.

[200] B Stuart and D J Ando. *Biological applications of infrared spectroscopy*. John Wiley & Sons, 1997.

[201] J E Sulston and S Brenner. The {DNA} of {CAENORHABDITIS} {ELEGANS}. 77(1):95–104, 1974.

[202] H Takeda, Y Nio, H Omori, K Uegaki, N Hirahara, S Sasaki, K Tamura, and H Ohtani. Mechanisms of cytotoxic effects of heavy water (deuterium oxide: D2O) on cancer cells. 9(8):715–725.

[203] M H Tan, C A Commens, L Burnett, and P J Snitch. A pilot study on the percutaneous absorption of microfine titanium dioxide from sunscreens. *The Australasian journal of dermatology*, 37(4):185–7, 1996.

[204] Akiyo Tanaka, Akira Hisanaga, Miyuki Hirata, and Noburu Ishinishi. Comparative study on the tumorigenicity in mice of gallium arsenide, gallium phosphide and gallium oxide following subcutaneous and intraperitoneal injections. 4(3):231–237, 1990.

[205] Akiyo Tanaka, Akira Hisanaga, Miyuki Hirata, Minoru Omura, Naohide Inoue, and Noburu Ishinishi. Pulmonary toxicity of indium arsenide and arsenic selenide following repeated intratracheal instillations to the lungs of hamsters. *Applied Organometallic Chemistry*, 8(3):265–271, 1994.

[206] Steven W Taylor, Eoin Fahy, Bing Zhang, Gary M Glenn, Dale E Warnock, Sandra Wiley, Anne N Murphy, Sara P Gaucher, Roderick A Capaldi, Bradford W Gibson, and Soumitra S Ghosh. Characterization of the human heart mitochondrial proteome. *Nature biotechnology*, 21(3):281–286, 2003.

[207] Thommey P. Thomas, Rameshwer Shukla, Alina Kotlyar, Bradley Liang, Jing Yong Ye, Theodore B. Norris, and James R. Baker. Dendrimer-epidermal growth factor conjugate displays superagonist activity. *Biomacromolecules*, 9(2):603–609, 2008.

[208] Alessandro Torgovnick, Alfonso Schiavi, Roberto Testi, and Natascia Ventura. A role for p53 in mitochondrial stress response control of longevity in C. elegans. *Experimental Gerontology*, 45(7-8):550–557, 2010.

[209] Tewes Tralau, Christian Riebeling, Ralph Pirow, Michael Oelgeschläger, Andrea Seiler, Manfred Liebsch, and Andreas Luch. Wind of change challenges toxicological regulators. 120(11):1489–1494.

[210] Benedicte Trouiller, Ramune Reliene, Aya Westbrook, Parrisa Solaimani, and Robert H. Schiestl. Titanium dioxide nanoparticles induce DNA damage and genetic instability in vivo in mice. *Cancer Research*, 69(22):8784–8789, 2009.

[211] G Tweedale and P Hansen. Protecting the workers: the medical board and the asbestos industry, 1930s-1960s. *Medical history*, 42(4):439–57, 1998.

[212] Tweedale G. *Magic Mineral to Killer Dust, Med Hist. 1998 ; 42(4): 439–457.*

[213] Unfccc.com. India and France Launch International Solar Energy Alliance at COP21.

[214] United Nations Secretariat. World Population Prospects. 2012.

[215] U.S. Environmental Protection Agency. Inventory of U.S. Greenhouse Gas: 1990-2014. 2016.

[216] US EPA. How to Access the TSCA Inventory - https://www.epa.gov/tsca-inventory/how-access-tsca-inventory.

[217] US OSHA. Safety and Health Topics - Benzene, 2014.

[218] B Vileno, S Jeney, A Sienkiewicz, P R Marcoux, L M Miller, and L Forró. Evidence of lipid peroxidation and protein phosphorylation in cells upon oxidative stress photo-generated by fullerols. 152(1):164–169, 2010.

[219] Cheng Wang, Teng Zhang, and Wenbin Lin. Rational synthesis of noncentrosymmetric metal-organic frameworks for second-order nonlinear optics. *Chemical Reviews*, 112(2):1084–1104, 2012.

[220] Zhong Wang, Mark Gerstein, and Michael Snyder. RNA-Seq: a revolutionary tool for transcriptomics. *Nature reviews. Genetics*, 10(1):57–63, 2009.

[221] D R Webb, I G Sipes, and D E Carter. In Vitro Solubility and in Viva Toxicity of Gallium Arsenide ',*. *In Vitro*, 76(1):96–104, 1984.

[222] D. R. Webb, S. E. Wilson, and D. E. Carter. Comparative pulmonary toxicity of gallium arsenide, gallium(III) oxide, or arsenic(III) oxide intratracheally instilled into rats. *Toxicology and Applied Pharmacology*, 82(3):405–416, 1986.

[223] D.R. WEBB, S.E. WILSON, and D.E. CARTER. Pulmonary Clearance and Toxicity of Respirable Gallium Arsenide Particulates Intratracheally Instilled Into Rats. *American Industrial Hygiene Association Journal*, 48(7):660–667, 1987.

[224] Dieter Weber. CH3NH3PbX3, ein Pb(II)-System mit kubischer Perowskitstruktur. *Zeitschrift fur Naturforschung - Section B Journal of Chemical Sciences*, 33(12):1443–1445, 1978.

[225] D L Wetzel and S M LeVine. Imaging molecular chemistry with infrared microscopy. 285(5431):1224–1225, 1999.

[226] Lyle Wiemerslage and Daewoo Lee. Quantification of mitochondrial morphology in neurites of dopaminergic neurons using multiple parameters. 262:56–65.

[227] IARC working group. *IARC Monographs on the evaluation of carcinogenic risks to humans.* 2007.

[228] World Nuclear Organisation. The Nuclear Renaissance - http://www.world-nuclear.org/information-library/current-and-future-generation/the-nuclear-renaissance.aspx. 2012.

[229] Wade B Worthen. Latitudinal Variation in Developmental Time and Mass in Drosophila melanogaster. 50(6):2523, 1996.

[230] Jianhong Wu, Wei Liu, Chenbing Xue, Shunchang Zhou, Fengli Lan, Lei Bi, Huibi Xu, Xiangliang Yang, and Fan Dian Zeng. Toxicity and penetration of TiO2 nanoparticles in hairless mice and porcine skin after subchronic dermal exposure. *Toxicology Letters*, 191(1):1–8, 2009.

[231] Shengchang Xiang, Yabing He, Zhangjing Zhang, Hui Wu, Wei Zhou, Rajamani Krishna, and Banglin Chen. Microporous metal-organic framework with potential for carbon dioxide capture at ambient conditions. *Nature Communications*, 3:954, 2012.

[232] Amarish Kumar Yadav, Saripella Srikrishna, and Subash Chandra Gupta. Cancer Drug Development Using Drosophila as an in vivo Tool: From Bedside to Bench and Back. 37(9):789–806, 2016.

[233] O. M. Yaghi, Guangming Li, and Hailian Li. Selective binding and removal of guests in a microporous metal–organic framework. *Nature*, 378(6558):703–706, 1995.

[234] Woon Seok Yang, Jun Hong Noh, Nam Joong Jeon, Young Chan Kim, Seungchan Ryu, Jangwon Seo, and Sang Il Seok. High-performance photovoltaic perovskite layers fabricated through intramolecular exchange. *Science*, 348(May):science.aaa9272–, 2015.

[235] Amir S Yazdi, Greta Guarda, Nicolas Riteau, Stefan K Drexler, Aubry Tardivel, Isabelle Couillin, and Jürg Tschopp. Nanoparticles activate the NLR pyrin domain containing 3 (Nlrp3) inflammasome and cause pulmonary inflammation through release of IL-1a and IL-1b. *Proceedings of the National Academy of Sciences of the United States of America*, 107(45):19449–19454, 2010.

[236] A. Yella, H.-W. Lee, H. N. Tsao, C. Yi, A. K. Chandiran, M. K. Nazeeruddin, E. W.-G. Diau, C.-Y. Yeh, S. M. Zakeeruddin, and M. Gratzel. Porphyrin-Sensitized Solar Cells with Cobalt (II/III)-Based Redox Electrolyte Exceed 12 Percent Efficiency. *Science*, 334(6056):629–634, 2011.

[237] Rudolfs K Zalups and D James Koropatnick. *Molecular Biology and Toxicology of Metals*. CRC Press.

[238] Yanglong Zhu, John W. Eaton, and Chi Li. Titanium Dioxide (TiO2) Nanoparticles Preferentially Induce Cell Death in Transformed Cells in a Bak/Bax-Independent Fashion. *PLoS ONE*, 7(11), 2012.

[239] Arthur Zimmerman. *Mitosis/Cytokinesis.* Academic Press, 2012.

List of Figures

List of Tables

Acknowledgements

The path towards this thesis has been circuitous given its interdisciplinary nature. Its completion is thanks to many people who supported me and stuck with me along the way.

Professor László Forró, you gave me the golden opportunity to join your team and manage many projects from physics to biology. Although sometimes we had different opinions, you have always provided me with coaching and valuable discussions in the form of regular meetings, almost on a daily basis, and throughout my entire PhD training. I admire your curiosity in different disciplines, and respect your broad knowledge. Your trust, teachings and support were key to the maturity of both my scientific and personal profile. Au départ, mon objectif était de faire mon doctorat avec toi, et je repars avec beaucoup plus que cela, donc un merci n'est pas assez pour exprimer ma reconnaissance envers toi.

Professor Hilal Lashuel, I would like to express my special appreciation and gratitude to you for your perfect mentoring and advisorship. You gave me valuable advices both personally and scientifically and you volunteered your time and energy to train me as a young scientist and critical thinker. You offered me access to your lab, considered me as a team member and provided me intellectual guidance, and technical support. I owe you the success of this thesis, thank you very much Hilal.

I would like to warmly acknowledge Prof. Matteo dal Peraro, Prof. Aleksandra Radenovic, Dr. Beat Schmid and Dr. Anthony Bahinski, who accepted to be part of my jury committee to peer-review and evaluate my scientific work, and also who helped me to improve the manuscript with their constructive remarks.

My deepest acknowledgements go to all the scientists, mainly post-docs, who taught me the fundamentals in designing experiments and data analysis, I would like to start with researchers from the groups I'm affiliated in:
Many thanks to Dr. Endre Horvath our chemist who, among other skills, synthesizes perovskites, and Dr. Massimo Spina "le docteur à cinq-pattes". Your tremendous help and valuable advices were essential in this thesis because without a good understanding of the physico-chemical characteristics of the material, toxicity studies are not significant. Thank you very much!
I am most indebted to Dr. Anne-Laure Mahul, a very good biologist who not only helped me address many research questions, but also was the catalyzer in publishing our first paper on toxicity. Even more than that, you offered me confidence in cell biology, in designing and planning my experiments but also how to present our data, and communicate my ideas clearly. I could really count on you at any time.
Many thanks to Dr. Bohumil Maco, a great microscopist who spent a lot of time and energy on electron microscopy to help me elucidating the phenotypical toxicity on human lung cells.

I was very fortunate to do my PhD training at EPFL, where I could work in close collaboration with brilliant professors and researchers to push the work as far as possible. I am very grateful to Prof. Gisou Van der Goot, Dr. Oksana Sergeeva, Prof. Johan Auwerx, Dr. Laurent Mouchiroud, Prof. Martin Gijs, Dr. Matteo Cornaglia, Prof. Bart Deplancke, Dr. Maroun Bou Sleiman, Roel Bevers, and Michaël Frochaux. Moreover, I would like to address my special thanks to the highly-qualified scientists working at various platforms (Flow cytometry, microscopy, bioinformatics, CMI…) for their trainings, availability and tremendous help for trouble-shooting.

Many scientists outside EPFL contributed significantly to the success of this thesis: I would like to express my acknowledgements to Prof. Beat Schwaller and Valérie Salicio (University of medicine in Fribourg) for their time and guidance at the beginning of my PhD thesis, and also to Dr. Philippe Lerch (at the Swiss Light Source, PSI) for his kindness, availability and teachings on IR spectroscopy, before the beamline shut down.

To continue the project on IR spectroscopy, I could count at anytime on Dr. Bertrand Vileno, a former group member and devoted scientist that became a very good friend. I enjoyed very much working, travelling and spending sleepless nights in the lab with you Bert, you really made the beamtimes enjoyable and BNL food taste great. Tu as bossé sur mon projet comme si c'était ta propre thèse, quittant ton boulot et ta famille. J'en profite pour dédier ces quelques lignes à Manue, Juliette et Léo, vous êtes les meilleurs!

I could also trust on Dr. Luca Quaroni, a brilliant spectroscopist and biochemist who welcomed me in Krakow and made a tremendous effort in advancing the project. Thanks a lot Luca.

I would like to acknowledge all the beamline scientists in the US. Dr. Lisa Miller, Dr. Randy Smith, Paul Gelfand, and in Paris Dr. Paul Dumas, Dr. Ferenc Borondics and Dr. Christophe Sandt who contributed to the success of our beamtimes.

During my undergraduate studies, I had the chance to have many gifted professors and mentors to whom I owe my passion for interdisciplinary science. I would like to thank particularly Prof. Philippe Berta, Dr. Pierre Parot, Prof. Giovanni Dietler, Dr. Sandor Kasas, and Dr. Sylvia Jeney, you introduced me to one another, and this is how I landed in László's group.

A positive and inspiring atmosphere in the lab is key to stimulating the efficiency in the group. I would like to thank all people that I met during my thesis, that became very good friends mainly: Prof. Davor Pavuna for the joy and "Agape" you carry and spread all the time.

Current and previous NN members not only for the valuable scientific discussions and interactions we had but also for the extra-professional activities, easy drinks, and trips we organized, which set a great atmosphere, we are like a big family. Thanks to Maryam, Lydia, Mass, Edo, Endre, Xavier, Pavao, Andrea, Luka, Syavoch, Flavius ;), Axel, Gaëtan, Bibe, the two Peters, Sergiy, Arnaud, Konstantin, Lin, Alla and Anastasia, and of course all your partners for joining

the happy hours in and outside the lab.
I am very grateful to the LMNN members for their tremendous support, guidance and high professionalism. We discussed very often ideas, you've all helped me troubleshoot many issues during my stay in SV, and also provided me with tips to be more efficient in many aspects. Special thanks to Nadine, Sophie, Anass, John, Bilal, JC, Mahmood, Layane, Niran, Joan, Abid, Ritwick, Céline, Juan and Filip.

I would also like to acknowledge Nathalie Jordan and Liliane Glauser, great lab technicians who have answers to many life-science questions, your help and efforts in making things hold together deserve more than words to thank you.
I also benefited from the meticulous work and sympathy of Primo Locatelli, Guillaume Camarda and Gilles Grandjean. Thank you very much.
I am very grateful to the amazing secretaries I shared stress and laughs with, Evelyn, Nicole, Rachel, Marie, Dorothée and Caroline, I enjoyed your effectiveness and accuracy, sometimes just some words from you or going for a coffee was enough to raise my motivation and mood.
I am especially thankful to other administrative assistants with whom I closely worked with to respect the deadlines of my doctoral studies: Sonja and Sandra, you were the sunshine when I was hopeless, thank you so much for the positive energy you transferred to me, and also the rich discussions we had, I hope we keep in touch.
I warmly thank all the persons, that I did not cite, that were involved directly or indirectly in this work.

I am very lucky to have a golden family that supports me no matter what.
Maman, Papa, en plus de me donner une éducation qui me permet de passer partout où je vais, vous me donnez une force inépuisable, vous avez le sens du sacrifice que j'ai rarement vu ailleurs. Vous m'avez accompagnée tout le long de cette thèse (et avant et sans doute après), en restant à la fois discrets et fortement presents quand j'en avais besoin. Vous êtes l'éternelle source d'amour et d'inspiration à mes yeux.

Mon frère Mamiche et mes soeurs Yaz, Saly et Ismou, votre bienveillance est hors paire, on fait vraiment une belle brochette quand on se retrouve, vous êtes clairement le moteur de ma réussite, je suis heureuse de voir notre famille s'agrandir avec Geo, Kaïs, Kenzi et Laura.

Sami, en plus d'être mon collègue et mon meilleur ami, t'es mon “soul-mate”, c'est pour cela que je te réserve cette place dans mes remerciements. Tu ne m'as jamais laissée tomber et tu m'as toujours sauvée dans mes détresses. J'étais particulièrement pénible avec toi durant ces 5 dernières années, surtout à des moments où c'était noir pour nous deux, et tu me l'as toujours rendu en bien. De plus, tu as toujours sû garder mes pieds sur Terre, en faisant attention à mon équilibre, tu as changé ma vie.

Lausanne, February 18th2017 I. B.

Curriculum Vitae

Ines Benmessaoud

Algerian and French citizen.
Born on April 13th, 1988.
Contact: Avenue de Beaulieu 39
1004 Lausanne
ines.benmess@gmail.com

Education

Ph.D., Biotechnology and Bioengineering, 2016.

Swiss Federal Institute of Technology, EPFL

MSc in Biotechnology and Bioengineering (with merits), 2011

Ecole des Mines d'Alès, Université de Nîmes, Université de Montpellier. (France)

BSc in Biology and Environmental sciences, 2009

Université de Nîmes, Ecole des Mines d'Alès (France)

Research

From 2012 to 2016

Doctoral research in evaluating the toxicity of engineered materials used for energy and medical applications. EPFL, Switzerland.

My responsibilities included the full chemical characterization of organometallic compounds, and I designed the toxicity studies *in vitro* and *in vivo* using biological models. I managed collaborations between 13 laboratories. I took the lead of all the multidisciplinary sub-projects, and my data got published in peer-reviewed papers. I was in charge of teaching bachelor and master students, I attended international conferences and I participated in writing proposals.

2011

Master thesis in characterizing the stiffness tomography of cells by Atomic Force Microscopy (AFM). EPFL, Switzerland.

I validated an analysis software developed in the lab by doing *in vitro* experimentation using AFM. The results got published in a peer-reviewed journal article.

2010

Master project in extracting the biophysical properties of protein-protein interaction by AFM. CEA Marcoule, France.

I was in charge of quantifying the energy landscape of Botulinum neurotoxin with different antibodies using AFM. This bio-physico-chemical characterization was essential for therapeutic applications.

2009

Bachelor internship in characterizing Roman statues found in Rhône river.
CNRS Nîmes and Musée de l'Arles et de la Provence antiques, France.
My duties included Strontium-Rubidium dating (87Rb-87Sr,86Sr) of Roman statues using mass spectroscopy.

Publications

I.R. Benmessaoud, *et. al.*
In vivo toxicity study of the photovoltaic perovskites in *Drosophila melanogaster*. In preparation.

I.R. Benmessaoud, *et. al.*
Microfluidic approach to *In vivo* toxicity study of the photovoltaic perovskites on *Caenorhabditis elegans*. In preparation.

I.R. Benmessaoud, *et. al.*
Comparative toxicity assessment *in vitro* of lead versus tin photovoltaic perovskites. In preparation.

I.R. Benmessaoud, *et. al.*
Infrared spectral fingerprints of the toxicity effects of photovoltaic perovskites. Anal. Chem., in preparation.

I.R. Benmessaoud, *et. al.*
Consequences of exposure to photovoltaic perovskites on the gene expression of epithelial cells. In preparation.

I.R. Benmessaoud, A-L. Mahul Mellier, E. Horvath, B. Maco, M. Spina, H. A. Lashuel, and L. Forro.
Health hazards of halide perovskites: cytotoxicity studies, Tox. Res. RSC, 2015.

C. Roduit · G. Longo, **I.R. Benmessaoud**, A Volterra · B Saha · G Dietler · S Kasas.
Stiffness tomography exploration of living and fixed macrophages. J Mol Recognit, 2012.

Conferences

Posters:

Spectroscopic approaches to probe toxicity of nanomaterials. I. Benmessaoud, B. Vileno, A. Sienkiewicz, J. Tribollet, P. Turek, L. Forro, B. Vileno Conference of Nanophysics for health, Mittlewihr-Alsace, 2012.

Health hazards of the photovoltaic perovskite $CH_3NH_3PbI_3$: cytotoxicity studies. I. Benmessaoud, A-L. Mahul Mellier, E. Horvath, B. Maco, M. Spina, H. A. Lashuel, and L. Forro. Conference PSCO, Swisstech convention center EPFL, 2015.

Talks:

Scanning Infrared micro spectroscopy in neurodegenerative diseases. Infrared Beamline Workshop-One day meeting, ETH Zurich, 10th April 2015.

Toxicity effects of methylammonium halide perovskites. From solid state to biophysics conference, Dubrovnik, 4-11 June 2016

Technical Skills

Cell and molecular biology, Flow cytometry, Microscopy (Confocal, and Live imaging), FTIR measurements and analysis, AFM, *In vivo* manipulation of small organisms.

Software Skills

Office softwares, Illustrator, InDesign, FIJI, Zen, Cytometry softwares (Kaluza, FACSDIVA), FTIR (Opus, Omnic), Statistics and spreadsheets (Origin, Excel).

Languages

French (native), Arabic (native), English (advanced, C2), Italian (Intermerdiate, B2), German (Advanced beginner, A2/B1), Spanish (basic, A2)

Awards

Master research scholarship. Université des sciences et arts,*Nîmes, France.*